# UNIVERSIDAD COMPLUTENSE DE MADRID

FACULTAD DE CIENCIAS QUÍMICAS



## TESIS DOCTORAL

# Characterization and control of laser ablation plasmas for the synthesis of new materials and as optical nonlinear media

MEMORIA PARA OPTAR AL GRADO DE DOCTOR

PRESENTADA POR


**Ignacio López Quintás**

Directoras

**Marta Castillejo Striano**
**Margarita Martín Muñoz**


**Madrid, 2017**


**© Ignacio López Quintás 2016**

Universidad Complutense de Madrid

Facultad de Ciencias Químicas



Consejo Superior de Investigaciones Científicas

Instituto de Química Física Rocasolano

# CARACTERIZACIÓN Y CONTROL DE PLASMAS DE ABLACIÓN LÁSER PARA LA SÍNTESIS DE NUEVOS MATERIALES Y COMO MEDIOS ÓPTICOS NO LINEALES

Ignacio López Quintás

Tesis Doctoral

Directoras:

Dra. Marta Castillejo Striano

Dra. Margarita Martín Muñoz

Madrid 2016

Universidad Complutense de Madrid

Facultad de Ciencias Químicas



Consejo Superior de Investigaciones Científicas

Instituto de Química Física Rocasolano

# CHARACTERIZATION AND CONTROL OF LASER ABLATION PLASMAS FOR THE SYNTHESIS OF NEW MATERIALS AND AS OPTICAL NONLINEAR MEDIA

Ignacio López Quintás

Doctoral Thesis

Supervisors:

Dr. Marta Castillejo Striano

Dr. Margarita Martín Muñoz

Madrid 2016

*A mis padres...*

# Acknowledgments

This is going to be long... As in many other aspects of life this thesis would not have been possible without the contribution of other people.

First of all, I would like to thank specially Drs. Margarita Martín and Marta Castillejo, first off for having given me the opportunity to carry out my PhD thesis in their group and second for their guidance and help during the process. It was a pleasure and an honor to work under your supervision. I would like to thank also Prof. Enrique Verdasco, my tutor at the Complutense University for his help with all the administrative procedures.

I would not be at this point of my life without the contribution of my big family, specially without the patience and support of my parents, Joaquín and Amalia, who raised me and always encouraged me to persist in my academic career. All my siblings, Joaquín, Ana, Cristina, Marta, Antonio and Beatriz and the rest of my family, Margarita, Margarita Jr., Amalia, Guadalupe and Victoria, el tío Antonio and the others, also contributed with their support and served me as a mirror to look at in many occasions.

I would also like to thank specially the rest of the people of the LANAMAP group at the Instituto de Química Física Rocasolano. Drs. Rebeca de Nalda, Mohamed Oujja, Mikel Sanz and Esther Rebollar helped me and taught me a lot (really a lot!) regarding the scientific aspects but they also became very good friends during these years. Other people did it as well. Dr. Vincent Loriot and Antonio Benítez were two of the people of LANAMAP that also contributed directly to the success of the experiments described in my thesis. The same gratitude goes to the people at the administration and workshops of the IQFR-CSIC. I always got impressed by their effectiveness and readiness to help in any aspect I needed during these years. They demonstrated me that the “great science engine” is not running only thanks to the scientists.

Some other people contributed to this work, to a greater or lesser extent, with their help and advice. Sharing the 216 office with Dr. Luis Cerdán was a big pleasure. Chatting with him provided me a better insight into science. Thanks to René Rodriguez whose sense of humor really helped me during the final stage of the writing process. Thanks to the people at CLUR-UCM, specially to Prof. Luis Bañares who provided me access to the femtosecond laser systems used in a great part of my thesis and to Dr. Jesus Gonzalez-Izquierdo, who assisted me during long hours in the lab. I used many other services and techniques during these years and I would like to thank also those people; Prof. Tiberio

Ezquerra for providing me access to the AFM set-up, Dr. David Avila-Brande for his collaboration during these years and for the help with the TEM measurements, Prof. José Marco for the access to the XPS lab and for his help with the interpretation of results, Dr. Margarita Hernández for the assistance during the Raman measurements, Dr. José Miguel Vadillo for putting me in contact with Richard Chater, with whom I performed the FIB-SIMS measurements of this thesis at the Imperial College in London and finally the people at ICTP-CSIC for the use of SEM set-ups and for their help with the interpretation of the images.

During these years, I carried out several stays at the Imperial College London and at the University of Ottawa. First of all, I would like to thank Prof. Jonathan Marangos for having given me the opportunity of joining the QOLS group during more than six months. I met there a bunch of outstanding scientists and I had the opportunity to work and share a very special time of my life with them. Just to mention some of these people, thanks to Prof. John Tisch, Dr. Thomas Siegel, Dr. Christopher Hutchison, Dr. Felicity McGrath and Dr. Zara Abdelrahman. The same feeling of gratitude goes to Prof. Ravi Bhardwaj at the University of Ottawa and the rest of the people in the group. The long and deep conversations with Dr. Deepak Kallepalli and Hajar Al-Khazraji were fantastic and really helped me to feel like at home being roughly 6000 km away and 20 °C below. I would also like to thank specially Prof. Rashid Ganeev. I met him first in Madrid and then in London, and I got amazed about his enthusiasm and energy. His ideas on plasma harmonics were the seed for some of the experiments described in this thesis.

I probably would not be writing this without the contribution of two people; Dr. Ginés Nicolás and Dr. Victor Piñón. With their guidance, I immersed myself definitely into research and into the world of lasers and laser ablation plasmas. Thanks to Dr. Nicolás I joined the Quimiláser family, where I met a lot of interesting people which also contributed to my work in science. My gratitude is extensive to Dr. Anastasia Giakoumaki and the rest of the people I met during my days at the Lasers Applications Laboratory of UDC.

How could I skip my friends! I am specially proud to say that within this group I count on many of the people I mentioned before but also on others, who are very important in my life. The people of 16 Tons, all the Chemistry mates from the UDC days and the Gö Erasmus family...without you I would probably have finished earlier...but definitely it would not have been that fun. People from mountain biking, specially Alex Lage and Damian Barreiro and the rest of “Ambronians”, you cannot imagine how important your

contribution is to this thesis. Thanks to Pepe Valverde, not only for having mentored me in the mountains but also for having inspired me in many other aspects of life.

Last but not least, I would like to thank the funding agencies which made possible the materialization of this thesis. The economic support provided by the Spanish Ministry of Economy and Competitiveness through the FPI 2011 programme (BES-2011-044738) and through projects CTQ2010-15680 and CTQ 2013-43086-P is thanked.

Thank you all!

## Contents

# Resumen

El trabajo descrito en esta memoria de tesis titulada: *"Caracterización y control de plasmas de ablación láser para la síntesis de nuevos materiales y como medios ópticos no lineales"*, ha sido realizado en el grupo de Láseres, nanoestructuras y procesado de materiales del Instituto de Química Física "Rocasolano" perteneciente al Consejo Superior de Investigaciones Científicas, CSIC en Madrid.

El proceso de ablación láser tiene lugar cuando un haz lo suficientemente intenso interacciona con un material, generalmente designado como *blanco de ablación*. La radiación del láser es absorbida por el blanco, dando lugar a un aumento de su temperatura. Dependiendo de la intensidad de la radiación, pueden tener lugar procesos como la ruptura de enlaces, fundido y vaporización de las capas más próximas a la superficie y en última instancia la eyección de una pequeña cantidad de material formándose un *plasma de ablación*. El plasma generado se expande preferentemente en la dirección perpendicular a la superficie del material en forma de lo que se conoce como *pluma de ablación*. Como consecuencia del proceso, el material sufre una serie de cambios físicos observables en la superficie, siendo el más evidente la formación de un cráter. La ablación láser es por lo tanto un proceso muy complejo que depende de las propiedades de la radiación láser empleada y de las propiedades del material ablacionado.

Por este motivo, la investigación encaminada a profundizar en los mecanismos de ablación y a extender y mejorar su aplicación en distintos ámbitos científicos y tecnológicos es de gran interés. Una de las características más destacables de la ablación láser es su universalidad, ya que en principio cualquier material puede ser ablacionado. El proceso de ablación permite retirar una pequeña cantidad de material de forma controlada y transferir a la fase gas especies que de otra forma sería complicado obtener. Todo ello hace de la ablación láser un proceso muy atractivo en campos como el procesado y la síntesis de materiales o el análisis químico, entre otros.

El principal objetivo de la presente tesis es estudiar desde un punto de vista fundamental los mecanismos de ablación de materiales mediante láser pulsado y explorar métodos para ejercer un cierto control sobre propiedades específicas de plasmas de ablación en dos áreas de investigación distintas: la *generación de armónicos* usando dichos plasmas como medios no lineales y la síntesis mediante la técnica de *deposición por láser pulsado* de materiales micro y nanoestructurados.

En el primer campo de estudio, los plasmas de ablación se emplean como medio no lineal para la generación de radiación coherente de corta longitud de onda (armónicos) a partir de una radiación láser fundamental. Este nuevo enfoque ha sido propuesto recientemente para tratar de solventar algunas de las limitaciones de los medios no lineales usados tradicionalmente, típicamente jets supersónicos de gases nobles, en el proceso de generación de altos armónicos. La amplia disponibilidad de materiales sólidos, susceptibles de ser usados como blancos de ablación, hace que este método sea altamente atractivo para obtener de forma eficiente radiación coherente de corta longitud de onda en la región del ultravioleta extremo o de los rayos-X.

Más recientemente, se ha propuesto la generación de bajos armónicos en plasmas de ablación láser como un método que permite obtener información relativa a la composición y dinámica de dichos plasmas mediante el análisis espaciotemporal de la respuesta no lineal de los mismos. El análisis de plasmas de ablación láser mediante generación de armónicos, por sí solo o en combinación con otras técnicas espectroscópicas, permite obtener información de gran utilidad para guiar la síntesis de nuevos materiales mediante la técnica de deposición por láser pulsado. Adicionalmente este método basado en la generación de armónicos permite estudiar las propiedades no lineales de los plasmas y de esta forma seleccionar materiales adecuados para obtener de forma eficiente radiación coherente de corta longitud de onda.

Los plasmas de ablación generados a partir de materiales con carbono se presentan en la literatura como medios eficientes para la generación de armónicos. En los experimentos descritos en esta tesis se emplearon plasmas obtenidos a partir de blancos de grafito y carburo de boro mediante ablación con pulsos de nanosegundos a 1064 nm. Se emplearon pulsos de la misma longitud de onda y en el mismo régimen temporal como radiación fundamental para la generación de armónicos. En plasmas de grafito se generó de forma eficiente el 3º armónico de la radiación fundamental a 355 nm. En plasmas de carburo de boro se generaron el 3º y 5º armónicos de la radiación fundamental a 355 nm y a 213 nm respectivamente. Adicionalmente, en carburo de boro se obtuvo radiación a 266 nm mediante un proceso de combinación de frecuencias que involucran radiación fundamental de 1064 nm y 532 nm. La generación de armónicos se llevó a cabo en vacío y en atmósfera de gas inerte a fin de modificar las propiedades del plasma y poder estudiar cómo afectan estas condiciones ambientales a la eficiencia del proceso. La generación de armónicos se extendió a órdenes no lineales más elevados (en el rango del ultravioleta de vacío) en el semiconductor sulfuro de zinc. En este material se generaron

de forma eficiente los armónicos impares de la radiación fundamental hasta el 9º armónico a 118 nm en condiciones de alto vacío.

El comportamiento temporal de la señal de armónicos, junto con el análisis adicional de las emisiones espontáneas de los plasmas estudiados, revelaron la presencia de dos poblaciones de especies que son responsables del proceso no lineal a distintos tiempos con respecto a la ablación. Estas dos contribuciones se observaron en plasmas de grafito y carburo de boro generados en atmósfera de gas inerte (kriptón y xenón) y en plasmas de sulfuro de zinc obtenidos en vacío. La componente más rápida, observada a tiempos de retraso en torno a 300 ns, se atribuye a especies atómicas y moléculas de pequeño tamaño que son eyectadas a alta velocidad en el proceso de ablación. La segunda componente de la señal de armónicos, observada a tiempos de retraso más largos, en torno a los 10 µs, se atribuye a la presencia de nanopartículas en la pluma que son fragmentadas por la acción del pulso que ocasiona la generación de armónicos, dando lugar a un plasma secundario más ionizado constituido fundamentalmente por especies iónicas. Estos iones se proponen como los principales responsables del proceso no lineal en ese rango temporal. Las nanopartículas se forman por agregación de especies atómicas o clústeres en las plumas de ablación generadas en atmósfera de gas inerte en el caso del grafito o carburo de boro y están presentes en el plasma de ablación de sulfuro de zinc obtenido en vacío. Del estudio espacial de la respuesta no lineal de los plasmas se deduce que la eficiencia del proceso no lineal cambia considerablemente en función de la región explorada por el haz de generación de armónicos. Los resultados revelan la fuerte dependencia de la amplitud de la señal de armónicos con las condiciones del plasma, principalmente densidad de especies, relación de fase entre la radiación fundamental y los armónicos (*phase matching*) y la absorción en el medio de los armónicos generados.

Como se ha mencionado anteriormente, el segundo campo de estudio abordado en esta tesis es la deposición por láser pulsado. Este método de síntesis se basa en colectar sobre un sustrato apropiado, el material que es eyectado en el proceso de ablación láser. De esta forma se pueden obtener capas finas (típicamente sub-micrométricas) a partir de una gran variedad de materiales y en diversas formas como capas nano o microestructuradas, multicapas, materiales cristalinos etc., que pueden ser de gran utilidad en aplicaciones tecnológicas. A pesar de su aparente sencillez, el proceso de deposición por láser pulsado encierra una gran complejidad ya que además de los ya de por sí complicados mecanismos de interacción entre la radiación láser y el material, entran en juego la dinámica de expansión de la pluma de ablación y los procesos de

crecimiento sobre el sustrato. Por todo ello, resultan de gran interés los estudios encaminados a entender y controlar el proceso de ablación y deposición.

Los primeros experimentos de deposición por láser pulsado descritos en esta tesis están dirigidos a la obtención de depósitos microestructurados mediante ablación de carburo de boro con pulsos láser de nanosegundos a 1064 nm y 266 nm. Los depósitos se obtuvieron sobre sustratos de silicio cristalino a temperatura ambiente. En estas condiciones se estudió el proceso de deposición en distintas condiciones de vacío y en atmósferas de gas inerte. La caracterización morfológica de los depósitos revela que la ablación a 1064 nm bajo condiciones de alto vacío favorece la formación de estructuras en forma de columna, de tamaño micrométrico y con características típicas de los materiales cristalinos. En particular se obtuvieron estructuras micrométricas de forma regular, con una sección cuadrada delimitada por aristas nítidas y puntas facetadas, formándose en algunos casos microcolumnas huecas. El análisis de las microestructuras indica que están compuestas de un material fundamentalmente basado en boro, carbono y oxígeno. La peculiar morfología de las microestructuras obtenidas y las excepcionales propiedades del carburo de boro sugieren que estos depósitos son potenciales candidatos para futuras aplicaciones tecnológicas.

La última parte de esta tesis está dedicada al estudio de la dinámica de ablación y del proceso de deposición por láser pulsado de blancos mixtos de cobalto y sulfuro de zinc. El objetivo último que se persigue es obtener, de forma controlada, depósitos nanoestructurados donde el cobalto esté incluido como dopante en la red cristalina del sulfuro de zinc. Este tipo de materiales, conocidos como semiconductores magnéticos diluidos, pueden presentar, además de las propiedades ópticas y electrónicas asociadas al semiconductor, propiedades magnéticas, lo cual los hace de especial interés para su aplicación en ámbito de la tecnología de la información.

En una primera fase se estudió la dinámica de ablación de blancos de Co y ZnS mediante un esquema de irradiación de dos pulsos de femtosegundos separados temporalmente en el rango de 0 a 300 ps, en combinación con el análisis del plasma por espectrometría de masas de tiempo de vuelo. Con este esquema se persigue actuar sobre la interacción láser-material basándose en la suposición de que la absorción del primer pulso modifica las propiedades de la superficie irradiada y que dicha modificación puede afectar al mecanismo de acoplamiento del segundo pulso, dependiendo de la relación de energías entre los pulsos y su retraso temporal. Para todas las configuraciones de irradiación con doble pulso estudiadas, la energía de cada uno de los pulsos se mantuvo por debajo del

umbral de detección de señal de iones, de forma que solo la combinación de ambos produjo una señal medible.

El análisis del plasma de ablación producido en la irradiación con doble pulso mostró que las intensidades de los picos del espectro de masas son fuertemente dependientes de la energía relativa del par de pulsos. La diferencia más notable se observó para el caso de pares de pulsos de distinta energía, donde se obtuvo que la configuración en la que el primer pulso es el de menor energía produce intensidades de la señal de iones mucho mayores que en el caso opuesto. Asimismo se obtuvo que las intensidades correspondientes a $Co^+$, $Zn^+$ y $S^+$ evolucionan de forma diferente con el retraso entre el par de pulsos. Eso último sugiere que mediante un esquema basado en irradiación con láseres ultrarrápidos en configuración de doble pulso se puede establecer un cierto grado de control sobre la composición del plasma.

Finalmente, este esquema se trasladó a un experimento de deposición por láser pulsado con el objetivo de estudiar el efecto de la separación temporal entre los pulsos en la morfología (espesor) y composición del material depositado. Se prepararon depósitos mediante irradiación con secuencias de doble pulso a distintos tiempos de retraso. Adicionalmente el proceso de deposición por láser pulsado se monitorizó *in situ* midiendo los cambios de reflectividad sobre el sustrato de silicio empleado mientras se crece el depósito sobre éste. Estas medidas permiten obtener información relativa al espesor de la capa depositada. Usando el esquema de doble pulso en condiciones en las que los pulsos individuales no producen cambios significativos en la reflectividad, se comprobó que la velocidad de deposición depende del retraso entre ambos pulsos, observándose que para un mismo número de pulsos, el espesor de la capa obtenida con tiempos de retraso cortos es mayor. El análisis morfológico y composicional de los depósitos confirmó la presencia de nanopartículas cristalinas donde el cobalto está incluido en la red del semiconductor. Por último, los resultados del análisis composicional de los depósitos preparados a distintos tiempos de retraso entre pulsos indican pequeñas diferencias en el ratio Co/Zn pero la alta variabilidad de los resultados obtenidos hace difícil afirmar que se produzca un efecto significativo de dicho retraso en la sustitución de Zn por Co en el semiconductor.

# Abstract

The work described in this thesis, entitled: "*Characterization and control of laser ablation plasmas for the synthesis of new materials and as optical nonlinear media*", was carried out in the Lasers, nanostructures and materials processing group at the Institute of Physical Chemistry "Rocasolano" of the Spanish National Research Council, CSIC in Madrid.

Laser ablation is a physical process taking place as a consequence of the interaction of a sufficiently intense laser beam with a material, usually referred as *ablation target*. The energy deposited by the laser is absorbed by the target, leading to a temperature increase, which in turn, depending on the laser intensity, can lead to events like bond breaking, melting and vaporization of the surface layers and ultimately to ejection of a small amount of material generating a *laser ablation plasma*. The induced plasma expands preferentially in the direction normal to the target surface in the form of a *plasma plume*. As a consequence of the ablation, the material undergoes a series of observable physical changes. Laser ablation is therefore an extremely complex process, depending both on the properties of the laser radiation and on the properties of the target material.

For this reason, research aimed at studying the ablation mechanisms and to extend and improve its application in different fields of science and technology is of great interest. One of the main characteristics of laser ablation is its universality, as in principle, all materials can be ablated. This process allows the controlled removal of a small amount of material and to entrain in the gas phase species that otherwise would be difficult to obtain. All these characteristics make laser ablation a highly attractive process in fields such as materials processing and synthesis or chemical analysis among others.

The main objective of the present thesis is to study from a fundamental point of view the pulsed laser ablation of materials, and to explore ways to exert some control on specific properties of ablation plasmas in two different research fields: *harmonic generation* using plasmas as nonlinear media and synthesis of new micro and nanostructured materials by the *pulsed laser deposition* technique.

In the first topic, laser ablation plasmas are used as nonlinear media for the generation of coherent short wavelength radiation (harmonics) of a fundamental laser radiation. This new approach emerged recently to overcome some of the limitations of the traditional

nonlinear media employed in high-order harmonic generation (typically noble gas jets). The broad variety of materials that can be used as ablation targets makes this approach highly attractive to improve the efficiency of the harmonic generation process in order to obtain radiation in the extreme ultraviolet or X-ray regions.

More recently, low-order harmonic generation in laser ablation plasmas has been proposed as a diagnostic method of the composition and dynamics of those plasmas through the spatiotemporal analysis of their nonlinear response. The analysis of laser ablation plasmas by harmonic generation, alone or in combination with other spectroscopic techniques, allows obtaining valuable information to guide the synthesis of materials by pulsed laser deposition. Moreover, this method serves to select suitable materials that can efficiently generate coherent radiation of short wavelength through the study of the plasma nonlinear properties.

Plasmas generated from carbon containing materials are proposed in the literature as efficient nonlinear media. In this thesis, plasmas of graphite and boron carbide were generated by 1064 nm nanosecond ablation. As fundamental radiation for harmonic generation, pulses of the same wavelength and temporal range were used. In graphite plasmas, third harmonic generation was efficiently achieved. In boron carbide plasmas the $3^{rd}$ and $5^{th}$ harmonics of the fundamental radiation at their respective wavelengths of 355 nm and 213 nm were generated. Additionally, in this material, radiation at 266 nm was obtained by a frequency mixing process involving 1064 nm and 532 nm fundamental beams. Harmonic generation was carried out under vacuum and inert gas atmospheres in order to modify the expansion conditions of the plasma and to assess how these influence the generation process. Harmonic generation was extended to higher nonlinear orders (in the vacuum ultraviolet region) in plasmas of the semiconductor zinc sulfide. In this material, odd harmonics of the fundamental 1064 nm radiation were generated up to the $9^{th}$ order at 118 nm under vacuum conditions.

The temporal behaviour of the harmonics signal, together with the analysis of the spontaneous plasma emissions, revealed the presence of two populations of species which are responsible for harmonic generation at different times with respect to the ablation event. These two contributions were observed in graphite and boron carbide plasmas generated under inert gas atmospheres (krypton and xenon) and in plasmas of zinc sulfide obtained under vacuum. The fastest component, observed at delay times around 300 ns, is attributed to atomic and small molecular species ejected at high velocity in the ablation process. The second component, observed at longer times of around 10 μs, is attributed to the presence of nanoparticles in the plasma plume, which

are fragmented by the harmonics driving pulse, inducing a more ionized secondary plasma constituted mainly by ionic species. These ions are believed to be the responsible of the nonlinear process in this temporal range. The spatial study of the plasma plume reveals that the efficiency of the nonlinear process changes considerably as a function of the region explored by the harmonics driving beam. The results reveal the strong dependence of the amplitude of harmonics signal on the plasma conditions, mainly the density of species, phase mismatch and absorption of the newly generated radiation.

As mentioned earlier, the second topic treated in this thesis is pulsed laser deposition. This synthesis technique is based on collecting the material ejected from the ablation process on appropriate substrates. In this way, thin layers with thickness typically below the micrometre, can be obtained from a wide variety of materials and in different forms like nano or microstructured deposits, multilayers, crystalline material etc., which can be of high interest in technological applications. Despite its apparent simplicity, the pulsed laser deposition process entails a great complexity as it depends not only on the already complex ablation mechanisms but also on the expansion dynamics of the plasma plume and growth processes on the substrate. For all these reasons, research aimed at understanding and controlling the pulsed laser deposition process is of high interest.

The first pulsed laser deposition experiments described in this thesis deal with the growth of microstructured deposits by ablation of boron carbide targets with nanosecond laser pulses at 1064 nm and 266 nm. Deposits were obtained on crystalline silicon substrates at room temperature. In these conditions, the deposition process was studied in different atmospheres of vacuum and inert gas. The morphological characterization of the deposits reveals that ablation at 1064 nm under vacuum conditions favours the growth of micrometric columnar structures featuring typical characteristics of crystalline materials. In particular, regular micrometric structures exhibiting a square section delimited by sharp edges and ending with faceted tips were obtained. In some cases, hollow structures were observed. The compositional analysis of the microstructures indicates that these are formed by a material based on boron, carbon and oxygen. The latter is believed to be present as impurity in the target material. The characteristic morphology of the obtained structures and the exceptional properties of boron carbide suggest potential technological applications for these deposits.

The final part of this thesis deals with the study of the laser ablation dynamics and pulsed laser deposition of mixed cobalt/zinc sulfide material. The ultimate goal of these experiments is the controlled growth of nanostructured deposits with cobalt atoms included as dopant in the semiconductor crystalline lattice. This kind of materials, known

as diluted magnetic semiconductors, apart from the optical and electronic properties of the semiconductor can bare magnetic properties, which makes them suitable candidates for applications in the realm of the information technology.

In a first stage, the ablation dynamics of the mixed Co/ZnS material was studied using a scheme based on double pulse irradiation with femtosecond pulses delayed in the range from 0 to 300 ps, combined with the time-of-flight mass spectrometric analysis of the ablation plasma. The goal is to act on the laser-material interaction process under the assumption that the first pulse modifies the properties of the irradiated layer, affecting the coupling mechanism of the second pulse in a different way depending on the delay and relative energy of the pulses. For all the irradiation configurations, the energy of each individual pulse was kept below the threshold for ion detection, in such a way that only the combination of both pulses yielded a measurable ion signal.

The analysis of plasmas induced by double pulse irradiation revealed that the amplitude of the mass peaks were strongly dependent on the relative energy of the pulses. For irradiation with pairs of pulses having different energy, the maximum signal amplitude was obtained when the pulse carrying the lowest energy was ahead in time. Likewise, it was found that the corresponding amplitudes of $Co^+$, $Zn^+$ and $S^+$ peaks exhibit distinct behaviours when the interpulse delay was varied. The latter observation suggests that a certain degree of control over the plasma composition can be achieved with a scheme based on double pulse femtosecond irradiation.

Finally, this scheme was implemented in a pulsed laser deposition experiment with the objective of studying the effect of the interpulse delay on the morphology (thickness) and composition of the deposited material. For that purpose, deposits were prepared at different interpulse delays and the growth of the deposited layer was monitored *in situ* by measuring the reflectance changes on the substrate surface, providing an estimation of the deposit thickness. In the double pulse configuration with irradiation conditions where the individual pulses do not yield a significant reflectance change, it was observed that the deposition rate depends on the interpulse delay. Thicker deposits were obtained at short interpulse delays compared to those obtained at longer delays. The morphological and compositional analysis confirmed the presence of crystalline nanoparticles where cobalt is included in the semiconductor lattice. Finally, the results of the compositional analysis of deposits prepared at different interpulse delays revealed small differences in their Co/Zn ratio. Nevertheless, the high variability of results makes difficult to claim that there is a significant effect of the interpulse delay on the cobalt substitution in the deposited material.

# Chapter 1

# Introduction

# 1. Introduction

## 1.1 About this thesis

The work described in this thesis was carried out in the Lasers, nanostructures and materials processing group (LANAMAP) at the Institute of Physical Chemistry "Rocasolano" (IQFR) of the Spanish National Research Council (CSIC) in Madrid. Most of the experimental work was performed in the laboratories of the LANAMAP group and at the Ultrafast Lasers Centre (CLUR) of the Complutense University of Madrid (UCM).

In the following section, an overview of the work described in this thesis is provided. This encompasses the motivation behind this work and its main objective, as well as a brief note on the organization of this manuscript to guide the reader through its content.

### 1.1.1 Motivation and objective

Laser ablation is a process taking place as a consequence of the interaction of sufficiently intense laser radiation with a solid material (frequently referred to as "target"). Upon irradiation, the surface layer of the target absorbs part of the radiation of the laser, rising its temperature and, depending on the radiation intensity, causing events like bond breaking, melting, vaporization and ultimately ejection of a small fraction of the material and plasma formation [1]. It is thus an extremely complex process, governed by the properties of both the target material and the laser radiation, and characterized by the complex expansion dynamics of the induced plasma, which can be constituted of neutral and ionic species, free electrons and aggregates.

In the past decades, laser ablation has developed together with laser technology. The appearance of new pulsed laser sources such as Q-Switched solid state lasers, excimer lasers emitting in the UV region and, more recently, laser systems delivering ultrashort pulses in the femtosecond temporal regime, opened new possibilities for both the fundamental study of the laser ablation process and for its application in new technological areas. Nowadays, laser ablation constitutes a useful tool in many fields, primarily thanks to its wide range of applicability, since essentially *all* materials can be potentially ablated.

Analytical techniques based on laser ablation, such as laser induced breakdown spectroscopy (LIBS) [2-4], laser ablation inductively coupled plasma mass spectrometry

(LA-ICP-MS) [5, 6] or matrix-assisted laser desorption and ionization (MALDI) [7, 8], are good examples of the applicability of laser ablation to chemical analysis. Different methods for materials processing are also based on laser ablation. The rise of nanotechnology has expanded the number of applications towards nano and microstructuring of materials [9-12]. Recently, synthesis methods based on laser ablation, like pulsed laser deposition (PLD), have gained huge interest for the fabrication of thin films of a wide variety of materials and in different forms [13]. Industrial applications, such as laser cutting and welding [14] also take advantage of laser ablation of solid materials. Laser cleaning is widely used in the conservation of cultural heritage for the restoration of paintings, sculptures, buildings, etc. [15, 16]. Laser ablation is also the basis of several medical procedures, such as ophthalmological and dental surgery, among others [17, 18]. Recently laser ablation plasmas emerged as alternative media for high-order harmonic generation [19].

Despite the great effort dedicated to investigate and exploit laser ablation, many aspects of the process are still not well understood. Additionally, owing to the aforementioned universality, laser ablation of many interesting materials remains, to a greater or lesser extent, still unexplored. For these reasons, research aimed at delving into the mechanisms of laser ablation and to extend and improve its technological applications is of great interest.

The general objective pursued in this thesis is to achieve insight into the mechanisms of the ablation of solids and to explore ways to exert some control on specific properties of the ablation plasmas. The study is focused on two different processes: the first is the generation of coherent short wavelength radiation (harmonics of a fundamental laser frequency) using laser ablation plasmas as nonlinear media. The second deals with the factors influencing the transfer of the material ejected in the ablation from the target to an appropriate substrate in the form of a thin film.

In more detail, the first objective of this thesis is the study of the nonlinear response of plasmas generated in the semimetal graphite and the semiconductors boron carbide ($B_4C$) and zinc sulfide (ZnS). Here, the spatial and temporal behaviour of this nonlinear response is used to gain information about the plasma composition and dynamics. Laser ablation plasmas of carbon containing materials proved to be good candidates for efficient harmonic generation [20-26]. From these, graphite constitutes the simplest and most affordable form of pure carbon, and it is therefore a suitable model for the study of the nonlinear response of this kind of materials. Boron carbide constitutes a step forward

in terms of complexity, entraining boron species in the plume and adding an advantage related to its high hardness, which can improve the stability of plasma conditions upon repetitive ablation in the same position of the target. Semiconductors like ZnS have multiple applications in the fabrication of electronic and optical devices. Thin films and nanostructures of this compound are becoming of interest for the fabrication of electrodes for solar energy conversion, nonlinear optical devices, light emitting diodes, lasers and others [27]. Amongst the suitable techniques to fabricate ZnS thin films is PLD. The properties of materials fabricated by this technique depend on the generation and expansion of the ablation plasma, thus the complementary information provided by harmonic generation in plasmas of these materials is of great value.

The second objective of this thesis is the study of the ablation and deposition processes of pure $B_4C$ and of targets composed by Co and ZnS. The exceptional properties of $B_4C$ (further detailed in this chapter) lead to think that this material can be very interesting candidate for the fabrication of novel nano and microstructured borocarbides by PLD. In the case of the Co/ZnS mixed targets, a double pulse ultrafast laser ablation scheme is used, aimed to gain some knowledge on the ablation dynamics and plasma composition and to extract guidelines for the controlled synthesis of Co-doped ZnS nanostructured material by PLD.

### 1.1.2 Organization of this manuscript

A brief explanation regarding the organization of this manuscript is given below.

This thesis is divided into five chapters. The following sections of this introductory chapter deal with the basic aspects of the physical processes involved in the ablation studies described later, putting them in the context of the current research in the field. The second chapter provides a description of the experimental methods applied in this work. The third and fourth chapters can be considered as the core of this thesis. In each one, the results of the experiments regarding the use of laser ablation plasmas as nonlinear media for harmonic generation (HG) and for the synthesis of new nano and microstructured materials by PLD are described. The final chapter presents the conclusions reached after the analysis of the obtained results. A scheme of the different experiments described herein is given in figure 1.1. Additional information is provided in the appendices attached at the end of this manuscript.

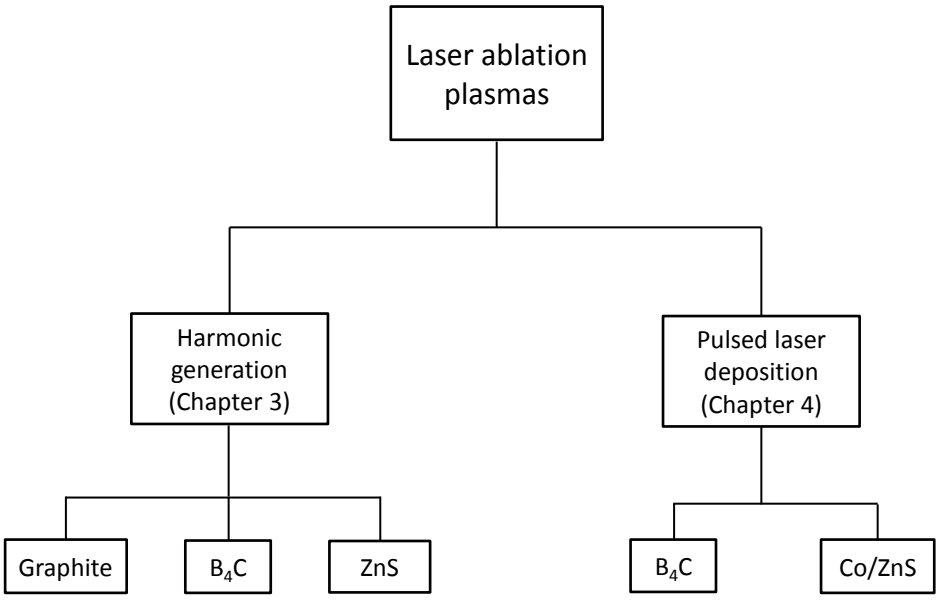


Figure 1.1 General scheme of the topics and materials studied in this thesis.

## 1.2 Laser ablation

As mentioned, the common thread of this thesis is the laser ablation of solid materials. In the following section, the basic principles of the physical processes involved are presented. The description is focused on the characteristics of the process that are most relevant to the experiments described in the next chapters.

### 1.2.1 Fundamentals of laser ablation

Soon after the discovery of the laser by T. Maiman in 1960 [28], laser ablation caught the attention of the scientific community. Early works of Breech *et al*. [29], Honig *et al.* [30] and Linlor [31] reported the first observations of particle emission when coherent intense radiation was aimed at a solid material. Since then, the physical mechanisms of laser ablation are still under study.

In the following, the description of laser ablation is focused on the interaction of pulsed laser radiation with solid matter, as this is the case of the experiments performed in this thesis. Continuous wave (CW) radiation also leads to ablation of solid materials and it is widely used in industrial applications but it is beyond the scope of this work.

When a laser pulse interacts with a solid target, the radiation is absorbed in the sub-femtosecond time scale by the electron sub-system (free or valence band electrons) of the material. The laser energy is deposited in a layer of thickness equal to the optical penetration depth (the inverse of the absorption coefficient $\alpha$). Absorption will depend on the intensity[1] and wavelength of the laser pulse and on the electronic structure of the material. The energy gained by the electrons is transferred to the lattice by the interaction of those with the quantized lattice vibrations (electron-phonon coupling), leading to a localized increase of the lattice temperature. This *thermal mechanism* can lead to melting and vaporization (or sublimation) of the material in the surface layer of the target and ultimately to the ejection of particles at high speed.

Besides thermal ablation, other mechanisms can take place. In the case of band gap materials, the absorption process depends on whether the photon energy of the laser pulse is higher or lower than the energy gap. In the first case single-photon absorption occurs by promotion of electrons from the valence band to the conduction band, while in the second, electron promotion takes place via multiphoton absorption. If a large number of carriers are excited from bonding states of the valence band to the conduction band, lattice destabilization can occur. Mechanisms as generation of defects and carrier confinement can contribute to energy localization in the solid, eventually leading to ablation of the material.

Other mechanisms leading to physical modification of the material should also be considered. The shock wave caused by the laser pulse propagates from the surface to deeper layers in the target, causing cracking or exfoliation of the material due to stress confinement. Formation of voids in a sub-surface region of the irradiated target caused by the relaxation of laser-induced thermoelastic stress can lead to *spallation* [32, 33] of the material and eventually to ejection of solid nanoparticles. At high laser pulse intensities, the rapid temperature increase can set the material in a situation characterized by the presence of a superheated liquid beyond the boiling temperature. As a result *phase explosion* (or explosive boiling) of the material can take place, causing the ejection of vapour and liquid droplets [34].

As mentioned, all the processes described above are strongly dependent on the characteristics of the laser pulse and the electronic structure of the target material [10]. In particular, the influence of the laser pulse duration in relation with the time needed for

[1] The correct term for power per unit area (usually given in W $cm^{-2}$) is *irradiance* but the term *intensity* is commonly accepted.

the complete energy transfer from the electron sub-system to the lattice is of extreme importance. Femtosecond irradiation involves a situation where the laser pulse ends before the electron-phonon energy transfer is completed, which occurs typically in a timescale of few picoseconds [35, 36]. The onset of material ejection takes place after the laser pulse ceases, and therefore no laser-plasma interaction is expected. In the case of irradiation with picosecond pulses, electrons begin to thermalize during the laser pulse. In nanosecond irradiation, the electronic sub-system and the lattice are in thermal equilibrium before the laser pulse ceases. In this thesis, either pulses in the femtosecond or nanosecond temporal regimes have been used in order to ablate the studied materials.

Laser ablation implies the ejection of a significant amount of material, leaving a detectable damage on the surface (usually referred to as *ablation crater*) and plasma formation. Ablation only occurs when a certain threshold intensity is surpassed, although it is common to express this ablation threshold in terms of *fluence*, defined as the energy per unit area (J $cm^{-2}$). Once the ablation threshold is overcome, the process is characterized by the generation of an incipient plasma over the target surface and by the subsequent formation of a *plasma plume*, which can be defined as the expanding vapour cloud formed by the partially ionized material ejected from the target. Beyond this rather simple definition lies an extremely complex gas dynamics and composition [37-40], ranging from neutral atoms, ions and free electrons to aggregates, such as small molecules, clusters or even nanoparticles. The relative abundance of these species depends once again on the material and laser pulse properties and also on the ambient conditions in which the plasma plume is expanding.

The plasma plume expansion dynamics has important implications in the two processes studied in this thesis. Variables like the velocity, density and spatial distribution of species can affect the nonlinear response of plasmas and the thickness profile and local composition of deposits obtained by PLD. From a general point of view, the plume is strongly forward peaked due to the pressure gradients in the direction normal to the target surface [37, 40]. The angular distribution of the expanding plume is dependent on factors such as the shape of the laser focal spot on the target, the density of the ablation plume and the expansion regime, that is, in vacuum or into an ambient gas.

Regarding the laser spot on the target, PLD experiments and calculations have shown that the vapour flow keeps some memory of its initial shape. A well-known example is the so called “flip-over effect” observed for elliptical focal spots, for which the deposited material has also an elliptic shape with the axes of the ellipse rotated by 90º [38].

The plume expansion under vacuum has been described by several models [37-40] that, despite their substantial differences, lead to a common description of the expansion as the superposition of two independent motions: the expansion along the *x* axis, perpendicular to the target surface and the expansion in the *y-z* plane. In some models the forward and transverse motions are respectively characterized by a flow velocity *u* and by a mean thermal velocity $v_{yz}$, with the $u/v_{yz}$ ratio giving the forward peaking of the plume [40, 41]. The above ratio is strongly affected by the density of species in the plume through its effect on the collisional regime of the expansion. High number of collisions and high collision rates can result in efficient cooling of the particle velocity distribution and enhanced forward peaking of the plume. Moreover, in multicomponent plasmas, due to the dependence of the collision rates with the mass, spatial distribution of heavy and light species can be different [40].

Strong narrowing (focusing) of the ablated flux distribution is also observed when the plume expands into an ambient gas. Some models to describe the complex expansion dynamics have been developed [38, 42]. In the initial stage, the evaporated material begins to expand and acts like a "piston" on the surrounding gas leading to successive shock waves arising in the ambient gas and in the vapor, which makes the position of the contact surface between plume and ambient gas to oscillate with the expansion time. The plume propagation length and plume focusing are affected by the molecular weight and pressure of the background gas respectively. Light background molecules allow an easier penetration of the cloud, allowing the contact surface to propagate to a larger distance. More pronounced focusing is obtained at higher ambient gas pressure [42].

Other processes related to the interaction of the laser radiation with the plasma, and to the interaction between the different plasma components must be taken into account. In the particular case of nanosecond ablation, absorption of the laser radiation by the incipient plasma through *inverse Bremsstrahlung* (IB) must be considered, as this absorption process can lead to shielding of the laser radiation by the plasma. Ionization of neutral species may also occur. The electrons accelerated as a consequence of IB can ionize neutral atoms by *impact ionization*. Moreover, *photoionization* of the neutral species is favoured at short wavelengths. Ionization can coexist with recombination of the free electrons with the generated ions. The deceleration suffered by free electrons through electron-electron collisions in the plume leads to *Bremsstrahlung*. This process yields a characteristic broad continuum emission resulting from the contributions of photons with energy equal to the difference between the initial and final kinetic energy of the involved electrons. *Bremsstrahlung* is particularly important at early times after the

ablation event, when the electron density is high. In the nanosecond regime, aggregates (small molecules, clusters and nanoparticles) generated upon ablation can be subjected to photo-fragmentation upon interaction with the trailing part of the laser pulse.

It should be noted that laser irradiation sets the material in a far from the equilibrium state. Therefore, the value of many physical constants (refractive index, thermophysical constants etc.), usually known for thermodynamical equilibrium conditions can only be approximate and subjected to variations during the laser irradiation, adding further complexity to the description of the laser ablation process.

### 1.2.2 Characterization of laser ablation plasmas

Characterization of laser ablation plasmas is crucial to understand the conditions in which the different ablation experiments performed in this thesis are taking place. The information gained through this characterization serves to guide the processes of HG and PLD by optimization of the ablation and expansion conditions.

Experimental characterization of laser-induced plasmas can be performed using different types of techniques [43]. At this point, it is important to remind that plasmas are characterized by a certain degree of ionization, thus involving the presence of free electrons, ions and neutrals and at least a fraction of these species can be found in an excited state in the hot plasma.

Spectroscopic techniques, such as optical emission spectroscopy (OES) [2, 44], absorption spectroscopy [45, 46] or laser induced fluorescence (LIF) [47], are widely used for the characterization of excited neutral and ionic species present in plasma plumes. The information retrieved by OES from the plasma spontaneous emission allows assessment of important parameters such as the electron temperature and density. Other methods based on different interferometric configurations (*e.g.* Michelson or Mach-Zehnder interferometry) are also used [48-50]. Other suitable techniques rely on the detection of charged particles. In this group one can find mass spectrometric techniques like time-of-flight mass spectrometry (TOF-MS) [51-53] or other methods based on ion collection devices like Langmuir probes [54]. Techniques like *shadowgraphy*, based on photographic methods, are also employed to investigate the plasma plume expansion dynamics [55].

In the following, we will focus on the techniques used in this thesis for the characterization of laser induced plasmas with particular emphasis on OES and TOF-MS.

In OES[2] the spontaneous emissions from excited plasma species returning to lower energy states are collected and analysed. Optical emission spectroscopy is considered an elemental analysis technique. The photons emitted as a consequence of the electronic transitions appear in the spectra as narrow emission lines at characteristic wavelengths for each neutral or ionic species. However, the presence of small molecules can also be revealed in the form of broader emission bands [56-59] and detection of the black body emission of nanoparticles present in the plasma plume is also possible [60-63]. Therefore, the optical emission spectra constitute fingerprints of the ablated material and the area behind the emission lines and bands provides information about the relative abundance of the atomic and molecular species. Nevertheless, it should be reminded that OES is only sensitive to electronically excited species.

In OES, temporal gating of the detection allows interrogation of the plasma plume at different times with respect to the ablation event, providing time-resolved information of the evolution of different emitters. Spatially-resolved information can also be obtained in different ways. By selecting a narrow spatial window, different zones of the plasma plume can be analysed with spectral resolution. On the other hand, the entire plasma volume can be imaged on the detection system in order to obtain a 2D image containing either spatial or combined spatial-spectral information.

We now move to the analysis of the ions present in laser ablation plasmas by TOF-MS. Charged particles can be steered, accelerated, focused and detected. This is the basic principle of mass spectrometry. From the range of mass spectrometric techniques, TOF-MS is probably the most versatile for the analysis of the ions produced directly by laser ablation, providing useful information regarding the plasma plume dynamics and composition at each laser shot [43, 53, 64, 65].

The fundamental principle of linear TOF-MS is based on the fact that ions with different mass to charge ratio ($m/q$) travel at different speeds after being accelerated in an electric field. The ions separate in groups according to this ratio when they fly along a field free flight tube kept under high-vacuum. The measurable magnitude is the time-of-flight that the ions need to travel from the ion source to an ion sensitive detector placed at the end of the flight tube, allowing the determination of the mass of each ion group. In this particular case, the ion source is the pulsed laser ablation process of the target material.

[2] Essentially OES and LIBS are equivalent techniques but the term LIBS is usually reserved for the use of OES as an analytical method.

The plasma is generated between a set of parallel plates, biased at a different potential to create the electric field used for extraction and acceleration of the plasma ions. The electric field can be applied continuously or can be pulsed. The latter operation mode allows for time-resolved analysis of the ion content. In TOF-MS, detection of neutral species is also possible by post-ionization of those neutrals generated in the ablation process [64, 66].

Alternative diagnostic methods can also provide information about the nature of the species present in the plume. The ejected material can be collected on appropriate substrates and analyzed in terms of morphology, composition, crystallinity etc. This method is the fundamental principle of the PLD technique, which is described in more detail in section 1.4 of this chapter. The analysis of the nonlinear response of laser ablation plasmas also provides information regarding the presence of different populations of species in the plasma plume. This method is treated more extensively in the next section.

## 1.3 Harmonic generation

The experiments described in Chapter 3 of this thesis are aimed to generate harmonics of a fundamental radiation using plasmas as nonlinear media. The following section provides an overview of the basic principles of this nonlinear optical process and a background of the presented experiments.

### 1.3.1 Fundamentals of harmonic generation

Harmonic generation [67] is a physical process in which a fundamental radiation of frequency $\omega$ interacts with a nonlinear medium. This interaction results in the generation of radiation with frequencies $n\omega$, that is, integer multiples of that of the fundamental radiation. This is illustrated schematically in figure 1.2. The generated frequencies are the *harmonics* of the fundamental radiation, and $n$ indicates the nonlinear order of the process. Typically only laser light has enough intensity to drive nonlinear processes, therefore the harmonics propagate collinearly with the fundamental beam and retain its coherence and directionality, at least to a certain extent.

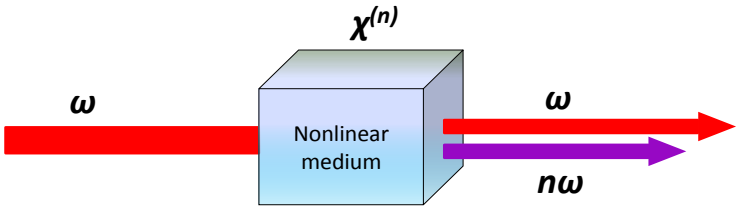


Figure 1.2 Schematic representation of the harmonic generation process where $\omega$ is the frequency of the fundamental radiation, $\chi^{(n)}$ is the nonlinear susceptibility of the medium and $n$ is the harmonic order.

The nonlinear process occurs as a consequence of the modification of the optical properties of the medium under the action of the intense laser field. Its nonlinearity derives from the fact that the response of the material scales to the $n^{\text{th}}$-order of the strength of the applied field [67].

To understand the nonlinearity of the harmonic generation process, one must consider the dependence of the polarization $\tilde{P}(t)$ of the medium, defined as the dipole moment per unit volume, on the applied optical field $\tilde{E}(t)$. In a linear process, the induced polarization depends linearly on the field and can be expressed as:

$$\tilde{P}(t) = \epsilon_0 \chi^{(1)} \tilde{E}(t) \tag{1.1}$$

where $\epsilon_0$ is the vacuum permittivity and $\chi^{(1)}$ is the linear susceptibility. The polarization for a given nonlinear process can be expressed as a power series expansion of the laser field[3]:

$$\tilde{P}(t) = \epsilon_0 \left[\chi^{(1)}\tilde{E}(t) + \chi^{(2)}\tilde{E}^2(t) + \chi^{(3)}\tilde{E}^3(t) + \cdots\right] \equiv \tilde{P}^1(t) + \tilde{P}^2(t) + \tilde{P}^3(t) + \cdots \tag{1.2}$$

where $\chi^{(2)}$ and $\chi^{(3)}$ are the second and third order nonlinear susceptibilities respectively, and $\tilde{P}^2$ and $\tilde{P}^3$ are the corresponding polarizations.

Besides the nonlinear susceptibility, the efficiency of the nonlinear process is determined by the *phase matching* between the wavevector of the incident radiation $k_1$ and the respective wavevectors of the generated harmonics $k_n$. The *wavevector mismatch* $\Delta k$ is then defined as:

$$\Delta k = k_n - nk_1 \tag{1.3}$$

[3] Although the polarization $\tilde{P}$ and the electric field $\tilde{E}$ are both vectorial quantities, in equations (1.1) and (1.2) these magnitudes are considered as scalar for the sake of simplicity.

In the ideal case of perfect phase matching, $\Delta k = 0$, that is, the newly generated photons have a fixed phase with respect to the incident photons. Thus, in this situation, the resulting radiation is the constructive sum of all the coherent contributions.

For low intensities, the harmonic generation process can be described in the framework of a *perturbative regime*, where harmonic radiation is emitted through low-order parametric processes, such as second harmonic generation (SHG) and third harmonic generation (THG) or sum- and difference-frequency mixing processes.

As an example, the lowest-order nonlinear process is SHG, observed for the first time by Franken *et al*. [68] and represented schematically in figure 1.3. Second harmonic generation can be understood as a process in which two photons of the incident radiation with frequency $\omega$ are destroyed and a new photon of frequency $2\omega$ is generated [67].

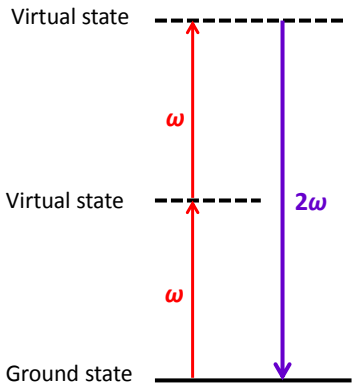


Figure 1.3 Scheme of energy levels and transitions involved in second harmonic generation.

The moderate intensity of the fundamental laser radiation used in the experiments described in this thesis ($\sim 10^{11}$ W cm$^{-2}$) leads to the generation of low-order harmonics, a process that can be described by the perturbative approach.

For higher intensities, harmonic generation can be described in the framework of a *non-perturbative regime.* Figure 1.4 shows a schematic representation of the spectrum of harmonics generated upon intense laser irradiation. In it, three different regions can be differentiated. In the first region the intensity of the successive harmonic orders decays exponentially. In the second region, usually referred to as the *plateau*, the intensity remains roughly constant with the harmonic order. Finally, the third region, known as the

*cut-off*, is the region of the spectrum where the intensity of the harmonic signal decays abruptly to zero or near zero.

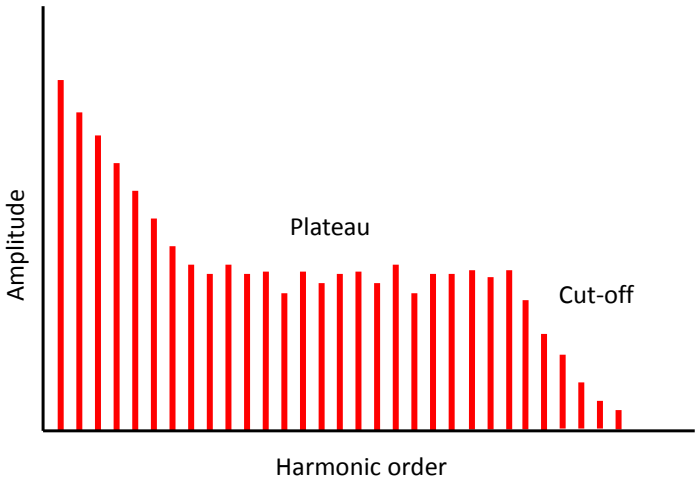


Figure 1.4 Scheme of the harmonics spectrum.

In this non-perturbative regime, the intensity of the incident radiation is high enough to modify the intra-atomic or intra-molecular electromagnetic fields within the nonlinear medium. This situation is described by the *three step model* proposed by Corkum [69]. In the first step the strong laser field interacts with an atom, lowering the Coulomb potential barrier and leading to tunnel ionization. In the second step, the freed electron oscillates in the laser field. The electron is driven away from the precursor ion, gaining kinetic energy. In the last step, when the direction of the driving field is reversed, there is a certain probability of recombination of the free electron with the parent ion, resulting in the emission of radiation of higher frequency, in the form of high-order harmonics. The position of the cut-off is determined by the maximum kinetic energy that the free electron can gain before it is recombined and by the ionization potential of the parent species.

It should be noted that due to symmetry considerations, generation of even-order harmonics only takes place in noncentrosymmetric media. Therefore, in media exhibiting inversion symmetry, such as liquids, gases, amorphous materials, some crystals and also in laser ablation plasmas, only odd harmonics are generated from a monochromatic laser light. Nevertheless, radiation of wavelength coincident with that of even harmonic orders

can be obtained through a frequency mixing process as described in Chapter 3, section 3.1.4, page 100.

### 1.3.2 Harmonic generation in laser ablation plasmas

Generation of coherent radiation of very short wavelength, in the extreme-UV (XUV) and X-ray regions, is of great interest for its application in many scientific and technological fields, such as spectroscopy, biology and medicine. Currently, coherent radiation in these spectral ranges is obtained mainly with free electron lasers [70, 71] or other kinds of X-ray lasers [72, 73] and through high-order harmonic generation (HHG), which has been successfully performed using gaseous media [74-77] and surfaces [78]. The main advantage of HHG compared to free electron or X-ray lasers resides in its simplicity and lower cost of operation, specially thanks to the availability of high-power, compact and stable laser sources emitting ultrashort pulses. Radiation beyond the so-called *water window* (2.3-4.6 nm) can be generated by HHG and finds application in biological or medical fields. More recently, HHG has gained additional interest as a way to obtain laser pulses in the attosecond range [79-81].

Despite the advantages of HHG compared to other sources of coherent short wavelength radiation, the limited conversion efficiency achieved has motivated research aimed at developing new approaches. Recently, laser ablation plasmas emerged as suitable media for high-order harmonic generation [19, 82-86] in an attempt to overcome the limitations of noble gases, which were the main media used in HHG. Nonetheless, the conversion efficiency achieved in the first experiments proved to be insufficient to compete with gas jets [83, 84, 87-90]. Efforts to optimize the ablation process, and hence the plasma conditions, have allowed to improve the conversion efficiency and extending the harmonics cut-off [91-94]. Nowadays, plasma harmonics have been extended up to the 101$^{st}$ order of 800 nm fundamental radiation [95] and the conversion efficiency has been improved by the use of new target materials like graphite [21, 22].

In a similar way that a nonlinear crystal or a gas jet can be used as nonlinear media, harmonic radiation can be generated when a sufficiently intense laser beam, frequently denoted as *driving beam*, is propagated through a laser ablation plasma. Figure 1.5 depicts a schematic representation of the HG process in the expanding laser ablation plasma plume.

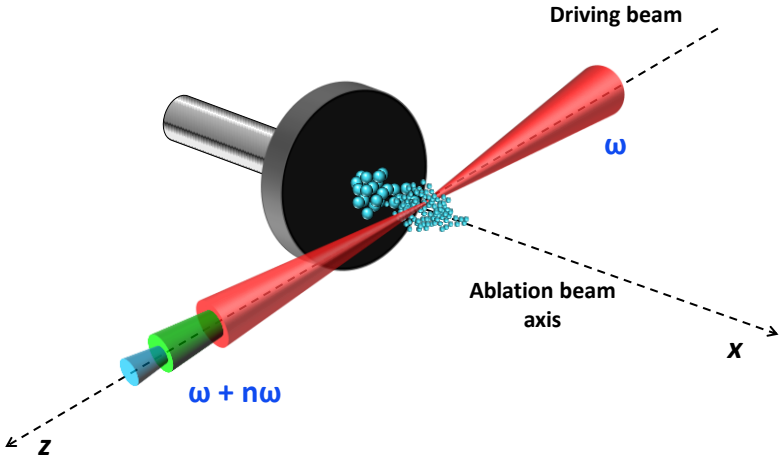


Figure 1.5. Schematic representation of the harmonic generation process in laser ablation plasmas. The ablation laser beam propagates at normal incidence towards the target surface along the *x* axis. The harmonics driving beam propagates parallel to the target surface along the *z* axis and is focused within the plasma volume.

In this diagram, the target is ablated with laser pulses delivered at normal incidence with respect to its surface. At a controllable delay, the driving pulse is propagated parallel to the target surface and focused within the plasma volume, allowing time-resolved assessment of the frequency up-conversion process. The control of the position of the driving beam focus with respect to the plasma volume allows the spatial scanning of its nonlinear response.

One of the great advantages of laser ablation resides in the possibility of transferring to the gas phase a wide variety of materials, which otherwise would be difficult to evaporate. This means that eventually all solids can be ablated and their laser induced plasmas are susceptible to be used for harmonic generation, opening an extremely wide range of possibilities of searching for materials that could efficiently generate coherent radiation of short wavelength. By selecting the appropriate ablation parameters, including laser wavelength, pulse duration, fluence, and spatial profile of the beam, the characteristics of the medium can be modified in order to optimize its nonlinear response. Moreover, HG in laser ablation plasmas can benefit by the presence of atomic or plasmon resonance effects, which can lead to an enhancement of the nonlinear optical response of the medium [96, 97].

In recent works, low-order harmonic generation (LHG) has been proposed as a method to reveal the presence of different populations of species in the plasma plume though the

spatiotemporal analysis of the plasma nonlinear response [98-103]. As mentioned earlier, the information provided by OES is usually restricted to excited atomic or simple molecular species. Harmonic generation in laser ablation plasmas has emerged as a method to obtain additional information of plasma species which otherwise would be difficult to retrieve by other spectroscopic techniques. This information is highly valuable to optimize the ablation conditions in thin film deposition processes.

Whit this goal in mind, the experiments described in Chapter 3 of this thesis focus on the use of the nonlinear response of plasmas of graphite, $B_4C$ and ZnS as a diagnostic tool to obtain information relative to their composition and dynamics. The experiments are restricted to the generation and study of low-order harmonics, from the $3^{rd}$ to the $9^{th}$ orders of a 1064 nm fundamental radiation using plasmas obtained by ablation with nanosecond pulses at 1064 nm.

## 1.4 Pulsed laser deposition

In the following sections an overview of the fundamentals of the pulsed laser deposition technique is provided together with a framework for the experiments described in Chapter 4.

### 1.4.1 Fundamentals of pulsed laser deposition

Pulsed laser deposition is a synthesis technique which basically consists on interposing an adequate substrate in the expansion path of the ablation plasma plume in such a way that a layer of the ejected material is grown on the substrate surface [13, 104-106]. Nonetheless, this rather simple description does not account for the complexity of the ablation and deposition processes involved. The PLD process is represented schematically in figure 1.6.

The development of PLD technique began right after the first ablation experiments performed in the 1960s as a way to deposit thin films [107-109] and was definitely driven in the late 1980s by the advent of new high-temperature superconductor materials and the need for suitable techniques for their fabrication [110].

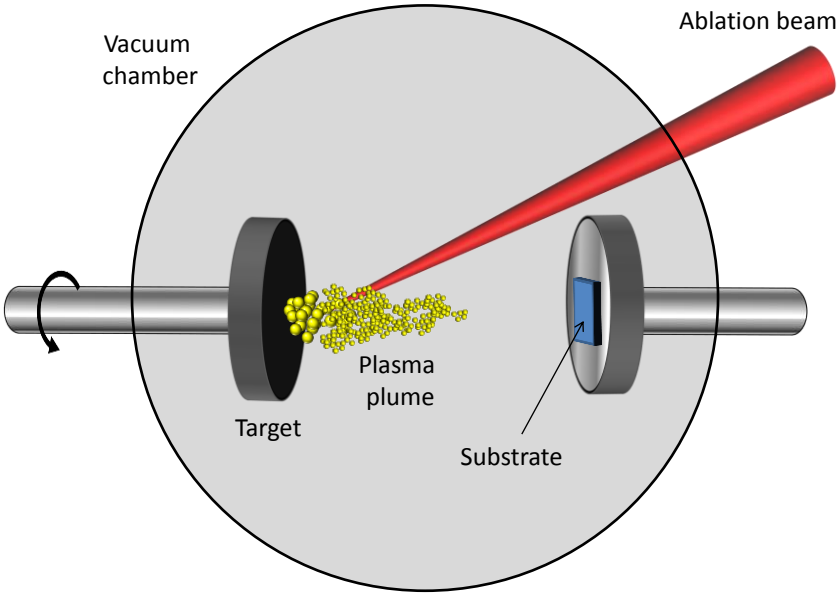


Figure 1.6. Schematic diagram of the pulsed laser deposition process.

The rapid success of PLD was motivated by its multiple advantages. The simplicity of its operation, together with the broad variety of target materials available, enables for a quick development of new deposition processes. Moreover, the flexibility of PLD allows fabricating deposits in multiple forms, from thin films to nano and microstructured deposits. It allows for multiple possibilities of optimization as the deposition outcome depends on many parameters, such as laser wavelength, pulse duration, fluence, atmosphere, substrate nature, target-substrate distance, substrate temperature etc. Under appropriate experimental conditions, stoichiometric transfer of the target material is possible [111] as well as deposition in reactive ambient conditions (*e.g.* oxidizing atmosphere) [112].

However, other characteristics of the PLD process can be detrimental for certain applications. These include the presence of particulates on the obtained deposits, which can be formed by material ejected directly in the ablation process, after solidification of droplets on the substrate surface or by aggregation of species in the plume. Another common drawback is the thickness inhomogeneity found in the deposits, caused by a distinct angular distribution of species that typically leads to a thicker deposit in the region close to the target normal [37, 113]. Nonetheless, all these limitations can be overcome by choosing appropriate experimental parameters.

The aforementioned advantages make PLD a very attractive method for the fabrication of thin films of many materials such as metals and metallic alloys [114-116], semiconductors [117-119], dielectrics [120, 121] or even biological materials [120, 122]. Deposits can be obtained in different forms, such as epitaxial layers [123, 124], multi-layered films [114, 117], nano and microstructured materials [125-129], crystalline layers [130, 131] etc. All these possibilities have been applied in many different fields, such as electronics, optics, sensoring and protective and biocompatible coatings. Nowadays, PLD is making way for being a suitable procedure in industrial environments [132, 133].

### 1.4.2 Nanosecond pulsed laser deposition of boron carbide

Boron carbide is a ceramic material exhibiting exceptional properties. It is the third hardest material known after diamond and cubic boron nitride, it displays a high resistance to chemical agents, high melting point, low density, thermoelectrical properties and a high neutron absorption cross section [134-136]. These outstanding characteristics make boron carbide a very interesting material for industrial applications, such as the fabrication of coatings, abrasive materials, cutting tools, armours, thermoelectrical devices, as well as applications for the nuclear industry, among others.

In the literature, several works have focussed on the fabrication of $B_4C$ thin films by different deposition techniques, including chemical vapour deposition (CVD) [137, 138], laser-assisted CVD [139, 140] and magnetron sputtering [141]. Pulsed laser deposition of $B_4C$ has been studied only to a limited extent, despite the fact that laser ablation can easily overcome the high melting point of the material (1768 K) and allows for a wide range of deposition conditions.

Several works have reported on thin film fabrication by nanosecond PLD of $B_4C$ under different experimental conditions. The majority of the reported experiments have been performed with ablation in the UV range [142-149]. In this region the deposits consisted on micrometric particles over a background film. In the visible range, Zemsky *et al*. [150] have described the deposition of $B_4C$ at 532 nm with several orientations of the substrates which led to deposits with different morphologies, from $B_4C$ crystalline material in the form of rounded particles on a continuous film to deposits characterized by densely packed nanocolumns. Deposits containing micro and nanometric particles embedded in a continuous film have been also observed upon ablation at 532 nm by Sun *et al*. [151]. Only few publications deal with nanosecond PLD of $B_4C$ in the IR region. Dietsch *et al*. [152, 153] have described the growth of nanometric layers of $B_4C$ for X-ray optics coating by 1064 nm ablation.

The nanosecond PLD experiments presented in Chapter 4 of this thesis are dedicated to the study of the deposition process of $B_4C$ using laser radiation at 1064 nm. The results set the conditions to grow novel borocarbide deposits containing micrometric regular structures.

### 1.4.3 Femtosecond pulsed laser deposition of Co/ZnS

Nowadays the quest for new information processing and storage methods is one of the main challenges of science and technology. While traditional electronic devices rely on the manipulation of electron charge in semiconductor materials for information processing and on electron spin manipulation in ferromagnetic materials for information storage, *spintronics* (from spin + electronics) has emerged as an alternative technology based on a combination of the two capabilities in one single material [154].

A family of materials known as *diluted magnetic semiconductors* (DMS) are considered promising candidates for the fabrication of spintronic devices [155]. In figure 1.7, an illustration of the structure of DMS is given. In these materials, the substitution of a small fraction of the cations in the semiconductor lattice by transition metal ions can endow magnetic properties to the semiconductor. Additionally, splitting of the metal atomic levels by interaction with the crystal field of the host also modifies the transition energies and luminescence lifetimes of the semiconductor as a function of the dopant concentration, making these materials candidates for magneto-optical applications [156-159].

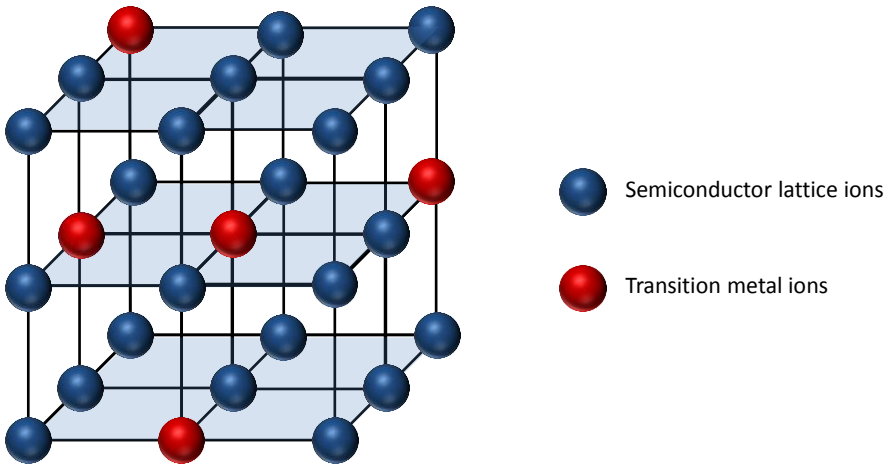


Figure 1.7. Schematic structure of diluted magnetic semiconductors.

Transition metal doped II-VI semiconductors are widely investigated for applications as DMS [160, 161]. The main advantage of these type of semiconductors is that the valence of the cations in the host lattice matches that of the common magnetic ions [154]. Several methods have been used to dope II-VI semiconductors with transition magnetic metals [162]. Amongst these methods, PLD has been chosen for preparation of thin films of ZnO and ZnS semiconductors doped with transition metal atoms [156-159, 162-164] thanks to its simplicity, to the relatively low temperatures reached in the ablation process and to the possibility of growth under a reactive atmosphere.

Ultrashort laser pulses have allowed the development of new strategies to control the synthesis and processing of materials. As mentioned earlier, the utility of pulses of some tens of femtoseconds resides in the fact that upon irradiation, the electronic excitation is completed in a time scale much faster than the characteristic times for energy transfer to the materials lattice. This property can be used for influencing the outcome of the ablation process by spatial or temporal shaping of the laser pulses. This approach has been applied for processing of dielectrics [165], metals [166-168], non-polar semimetals and semiconductors [169-171], following two different strategies, either by acting on the laser-material interaction dynamics [165, 166, 169] or on the laser-plasma interaction [167, 168, 170].

Temporal shaping of ultrashort pulses has been employed for transferring material from the target to a substrate by laser-induced forward transfer (LIFT) [166, 172] and PLD techniques either by irradiation with temporally stretched individual pulses or multiple consecutive pulses. In studies involving PLD, adaptive temporal control of femtosecond irradiation with pulses stretched in the range of few picoseconds has been used to influence the deposition process of brass [173]. Pulses stretched up to several hundreds of picoseconds and shaped into two successive pulses have been used to study the crystalline phase and particulate abundance of deposited SiC layers [174]. Several works rely on a scheme based on femtosecond ablation and deposition with sequences of detached pulses. Pulsed laser deposition of diamond-like carbon films has been investigated with sequences of two femtosecond pulses above the ablation threshold and delayed in the range of several tens of picoseconds [175]. In a similar temporal range, the double pulse femtosecond irradiation was investigated in germanium targets in order to obtain information relative to the absorption of the delayed pulse by the nascent plasma and to the ablation and deposition rates [176].

The experiments described in Chapter 4 of this thesis were motivated by the observation of mixed clusters in nanosecond ablation plasmas form Co/ZnS targets and by the deposition of $Co_{1-x}Zn_xS$ material demonstrated for the first time by Jadraque *et al*. [164]. Cobalt as transition metal dopant was chosen by its similar radius compared to that of Zn ions, which in principle facilitates its substitution in the ZnS lattice. These findings opened a door to the controlled synthesis of this kind of doped material by ablation of mixed targets of Co and ZnS. In the present thesis, in order to investigate new possible strategies to influence the ablation and deposition processes of the above doped semiconductors, a femtosecond double pulse irradiation scheme was used. The effect of the relative energy and delay between pairs of pulses on the ablation dynamics of Co/ZnS targets was studied together with its influence on the composition and properties of the deposited material obtained upon ablation.

## 1.5 References


1. J.C. Miller, R.F. Haglund, eds. Laser Ablation and Desorption, 1998, Academic Press.
2. D.A. Cremers, L.J. Radziemski, *Handbook of Laser-Induced Breakdown Spectroscopy*, 2013, John Wiley and Sons, Ltd.
3. A.W. Miziolek, V. Palleschi, I. Schechter, eds. Laser Induced Breakdown Spectroscopy, 2008, Cambridge University Press.
4. R.E. Russo, X. Mao, S.S. Mao, *Peer Reviewed: The Physics of Laser Ablation in Microchemical Analysis,* Analytical Chemistry, **74** (2002) p. 70 A.
5. A.L. Gray, *Solid sample introduction by laser ablation for inductively coupled plasma source mass spectrometry,* Analyst, **110** (1985) p. 551.
6. D. Günther, B. Hattendorf, *Solid sample analysis using laser ablation inductively coupled plasma mass spectrometry,* TrAC Trends in Analytical Chemistry, **24** (2005) p. 255.
7. K. Dreisewerd, *Recent methodological advances in MALDI mass spectrometry,* Analytical and Bioanalytical Chemistry, **406** (2014) p. 2261.
8. M. Karas, U. Bahr, U. Gießmann, *Matrix-assisted laser desorption ionization mass spectrometry,* Mass Spectrometry Reviews, **10** (1991) p. 335.
9. X. Liu, D. Du, G. Mourou, *Laser ablation and micromachining with ultrashort laser pulses,* IEEE Journal of Quantum Electronics, **33** (1997) p. 1706.
10. B.N. Chichkov, C. Momma, S. Nolte, F. von Alvensleben, A. Tünnermann, *Femtosecond, picosecond and nanosecond laser ablation of solids,* Applied Physics A, **63** (1996) p. 109.
11. F. Korte, J. Serbin, J. Koch, A. Egbert, C. Fallnich, A. Ostendorf, B.N. Chichkov, *Towards nanostructuring with femtosecond laser pulses,* Applied Physics A, **77** (2003) p. 229.
12. K. Sugioka, Y. Cheng, *Ultrafast laser processing: from micro-to nanoscale*, 2013, CRC Press.
13. R. Eason, *Pulsed Laser Deposition of Thin Films: Applications-Led Growth of Functional Materials*, 2007, Wiley.
14. J.F. Ready, *Industrial Applications of Lasers*, 1997, Academic Press.
15. C. Fotakis, D. Anglos, V. Zafiropulos, S. Georgiou, V. Tornari, *Lasers in the preservation of cultural heritage: Principles and applications*, 2006, CRC Press.
16. M. Castillejo, P. Moreno, M. Oujja, R. Radavan, J. Ruiz, *Lasers in the Conservation of Artworks: Proceedings of the International Conference Lacona VII*, 2008, CRC Press.
17. L.G. Pallikaris, M.E. Papatzanaki, E.Z. Stathi, O. Frenschock, A. Georgiadis, *Laser in situ keratomileusis,* Lasers in Surgery and Medicine, **10** (1990) p. 463.
18. R. Hibst, U. Keller, *Experimental studies of the application of the Er:YAG laser on dental hard substances: I. Measurement of the ablation rate,* Lasers in Surgery and Medicine, **9** (1989) p. 338.
19. R.A. Ganeev, *High-order harmonic generation in laser plasma plumes*, 2013, World Scientific.
20. R.A. Ganeev, T. Witting, C. Hutchison, F. Frank, P.V. Redkin, W.A. Okell, D.Y. Lei, T. Roschuk, S.A. Maier, J.P. Marangos, and J.W.G. Tisch, *Enhanced high-order-*

*harmonic generation in a carbon ablation plume,* Physical Review A, **85** (2012) p. 015807.
21. L.B.E. Bom, Y. Pertot, V.R. Bhardwaj, T. Ozaki, *Multi-μJ coherent extreme ultraviolet source generated from carbon using the plasma harmonic method,* Optics Express, **19** (2011) p. 3077.
22. Y. Pertot, L.B. Elouga Bom, V.R. Bhardwaj, T. Ozaki, *Pencil lead plasma for generating multimicrojoule high-order harmonics with a broad spectrum,* Applied Physics Letters, **98** (2011) p. 101104.
23. R.A. Ganeev, P.A. Naik, H. Singhal, J.A. Chakera, M. Kumar, M.P. Joshi, A.K. Srivastava, P.D. Gupta, *High-order harmonic generation in carbon-nanotube-containing plasma plumes,* Physical Review A, **83** (2011) p. 013820.
24. R.A. Ganeev, L.B.E. Bom, J. Abdul-Hadi, M.C.H. Wong, J.P. Brichta, V.R. Bhardwaj, T. Ozaki, *Higher-Order Harmonic Generation from Fullerene by Means of the Plasma Harmonic Method,* Physical Review Letters, **102** (2009) p. 013903.
25. R.A. Ganeev, M. Suzuki, M. Baba, H. Kuroda, *High-order harmonic generation from carbon plasma,* Journal of the Optical Society of America B, **22** (2005) p. 1927.
26. M. Oujja, A. Benítez-Cañete, M. Sanz, I. Lopez-Quintas, M. Martín, R. de Nalda, M. Castillejo, *Frequency mixing in boron carbide laser ablation plasmas,* Applied Surface Science, **336** (2015) p. 53.
27. *Wide Bandgap Semiconductors: Fundamental Properties and Modern Photonic and Electronic Devices*, 2007, Springer-Verlag.
28. T.H. Maiman, *Stimulated Optical Radiation in Ruby,* Nature, **187** (1960) p. 493.
29. F. Breech, L. Cross, *Optical Micromission Stimulated by a Ruby Maser,* Applied Spectroscopy, **16** (1962) p. 59.
30. R.E. Honig, J.R. Woolston, *Laser-induced emission of electrons, ions, and neutral atoms from solid surfaces,* Applied Physics Letters, **2** (1963) p. 138.
31. W.I. Linlor, *Energetic Ions Produced by Laser Pulse*, in *Laser Interaction and Related Plasma Phenomena: Proceedings of the First Workshop, held at Rensselaer Polytechnic Institute, Hartford Graduate Center, East Windsor Hill, Connecticut, June 9–13, 1969*, H.J. Schwarz and H. Hora, ed. 1971, Springer. p. 173.
32. E. Leveugle, L.V. Zhigilei, *Microscopic mechanisms of short pulse laser spallation of molecular solids,* Applied Physics A, **79** (2004) p. 753.
33. L.V. Zhigilei, *Dynamics of the plume formation and parameters of the ejected clusters in short-pulse laser ablation,* Applied Physics A, **76** (2003) p. 339.
34. A. Miotello, R. Kelly, *Laser-induced phase explosion: new physical problems when a condensed phase approaches the thermodynamic critical temperature,* Applied Physics A, **69** (1999) p. S67.
35. E.G. Gamaly, A.V. Rode, *Physics of ultra-short laser interaction with matter: From phonon excitation to ultimate transformations,* Progress in Quantum Electronics, **37** (2013) p. 215.
36. S.K. Sundaram, E. Mazur, *Inducing and probing non-thermal transitions in semiconductors using femtosecond laser pulses,* Nature Materials, **1** (2002) p. 217.
37. R.K. Singh, J. Narayan, *Pulsed-laser evaporation technique for deposition of thin films: Physics and theoretical model,* Physical Review B, **41** (1990) p. 8843.
38. S.I. Anisimov, B.S. Luk'yanchuk, A. Luches, *An analytical model for three-dimensional laser plume expansion into vacuum in hydrodynamic regime,* Applied Surface Science, **96–98** (1996) p. 24.

39. R. Kelly, *Gas dynamics of the pulsed emission of a perfect gas with applications to laser sputtering and to nozzle expansion,* Physical Review A, **46** (1992) p. 860.
40. K.L. Saenger, *On the origin of spatial nonuniformities in the composition of pulsed-laser-deposited films,* Journal of Applied Physics, **70** (1991) p. 5629.
41. R. Kelly, *On the dual role of the Knudsen layer and unsteady, adiabatic expansion in pulse sputtering phenomena,* The Journal of Chemical Physics, **92** (1990) p. 5047.
42. A.V. Bulgakov, N.M. Bulgakova, *Gas-dynamic effects of the interaction between a pulsed laser-ablation plume and the ambient gas: analogy with an underexpanded jet,* Journal of Physics D: Applied Physics, **31** (1998) p. 693.
43. S. Amoruso, R. Bruzzese, N. Spinelli, R. Velotta, *Characterization of laser-ablation plasmas,* Journal of Physics B: Atomic, Molecular and Optical Physics, **32** (1999) p. R131.
44. C. Aragón, J.A. Aguilera, *Characterization of laser induced plasmas by optical emission spectroscopy: A review of experiments and methods,* Spectrochimica Acta Part B: Atomic Spectroscopy, **63** (2008) p. 893.
45. D.B. Geohegan, *Time-Resolved Diagnostics of Excimer Laser-Generated Ablation Plasmas used for Pulsed Laser Deposition*, in *Excimer Lasers*, L.D. Laude, ed. 1994, Springer. p. 165.
46. S. Amoruso, M. Armenante, V. Berardi, R. Bruzzese, N. Spinelli, *Absorption and saturation mechanisms in aluminium laser ablated plasmas,* Applied Physics A, **65** (1997) p. 265.
47. K. Niemax, W. Sdorra, *Optical emission spectrometry and laser-induced fluorescence of laser produced sample plumes,* Applied Optics, **29** (1990) p. 5000.
48. D. Breitling, H. Schittenhelm, P. Berger, F. Dausinger, H. Huegel. *Shadowgraphic and interferometric investigations on Nd: YAG laser-induced vapor/plasma plumes for different processing wavelengths*, in *XIII International Symposium on Gas Flow and Chemical Lasers and High-Power Laser Conference*. 2001. International Society for Optics and Photonics.
49. R.E. Walkup, J.M. Jasinski, R.W. Dreyfus, *Studies of excimer laser ablation of solids using a Michelson interferometer,* Applied Physics Letters, **48** (1986) p. 1690.
50. R.F. Smith, J. Dunn, J. Nilsen, V.N. Shlyaptsev, S. Moon, J. Filevich, J.J. Rocca, M.C. Marconi, J.R. Hunter, T.W. Barbee, *Picosecond X-Ray Laser Interferometry of Dense Plasmas,* Physical Review Letters, **89** (2002) p. 065004.
51. D.M. Lubman, *Lasers and mass spectrometry*, 1990, Oxford University Press.
52. S. Amoruso, V. Berardi, R. Bruzzese, R. Capobianco, R. Velotta, M. Armenante, *High fluence laser ablation of aluminum targets: Time-of-flight mass analysis of plasmas produced at wavelengths 532 and 355 nm,* Applied Physics A, **62** (1996) p. 533.
53. A. Cavalleri, K. Sokolowski-Tinten, J. Bialkowski, M. Schreiner, D. von der Linde, *Femtosecond melting and ablation of semiconductors studied with time of flight mass spectroscopy,* Journal of Applied Physics, **85** (1999) p. 3301.
54. B. Doggett, J.G. Lunney, *Langmuir probe characterization of laser ablation plasmas,* Journal of Applied Physics, **105** (2009) p. 033306.
55. R.E. Russo, X.L. Mao, H.C. Liu, J.H. Yoo, S.S. Mao, *Time-resolved plasma diagnostics and mass removal during single-pulse laser ablation,* Applied Physics A, **69** (1999) p. S887.

56. A. Portnov, S. Rosenwaks, I. Bar, *Emission following laser-induced breakdown spectroscopy of organic compounds in ambient air,* Applied Optics, **42** (2003) p. 2835.
57. M. Baudelet, M. Boueri, J. Yu, S.S. Mao, V. Piscitelli, X. Mao, R.E. Russo, *Time-resolved ultraviolet laser-induced breakdown spectroscopy for organic material analysis,* Spectrochimica Acta Part B: Atomic Spectroscopy, **62** (2007) p. 1329.
58. L. Nemes, A.M. Keszler, C.G. Parigger, J.O. Hornkohl, H.A. Michelsen, V. Stakhursky, *Spontaneous emission from the $C_3$ radical in carbon plasma,* Applied Optics, **46** (2007) p. 4032.
59. F. Claeyssens, M.N.R. Ashfold, E. Sofoulakis, C.G. Ristoscu, D. Anglos, C. Fotakis, *Plume emissions accompanying 248 nm laser ablation of graphite in vacuum: Effects of pulse duration,* Journal of Applied Physics, **91** (2002) p. 6162.
60. S. Amoruso, R. Bruzzese, N. Spinelli, R. Velotta, M. Vitiello, X. Wang, G. Ausanio, V. Iannotti, L. Lanotte, *Generation of silicon nanoparticles via femtosecond laser ablation in vacuum,* Applied Physics Letters, **84** (2004) p. 4502.
61. S. Amoruso, G. Ausanio, R. Bruzzese, M. Vitiello, X. Wang, *Femtosecond laser pulse irradiation of solid targets as a general route to nanoparticle formation in a vacuum,* Physical Review B, **71** (2005) p. 033406.
62. D.B. Geohegan, A.A. Puretzky, *Species-resolved imaging and gated photon counting Spectroscopy of laser ablation plume dynamics During KrF- and ArF- laser PLD of amorphous diamond films,* MRS Online Proceedings Library Archive, **397** (1995) p. 55.
63. E.A. Rohlfing, *Optical emission studies of atomic, molecular, and particulate carbon produced from a laser vaporization cluster source,* The Journal of Chemical Physics, **89** (1988) p. 6103.
64. A.V. Bulgakov, I. Ozerov, W. Marine, *Cluster emission under femtosecond laser ablation of silicon,* Thin Solid Films, **453–454** (2004) p. 557.
65. F. Costache, S. Kouteva-Arguirova, J. Reif, *Sub–damage–threshold femtosecond laser ablation from crystalline Si: surface nanostructures and phase transformation,* Applied Physics A, **79** (2004) p. 1429.
66. M. Jadraque, M. Santos, L. Díaz, J. Álvarez-Ruiz, M. Martín, *Silicon Oxide Cluster Formation and Stability in the Laser Ablation of SiO Targets,* The Journal of Physical Chemistry A, **113** (2009) p. 10880.
67. R. Boyd, *Nonlinear Optics*, 2008, Academic Press.
68. P.A. Franken, A.E. Hill, C.W. Peters, G. Weinreich, *Generation of Optical Harmonics,* Physical Review Letters, **7** (1961) p. 118.
69. P.B. Corkum, *Plasma perspective on strong field multiphoton ionization,* Physical Review Letters, **71** (1993) p. 1994.
70. D.A.G. Deacon, L.R. Elias, J.M.J. Madey, G.J. Ramian, H.A. Schwettman, T.I. Smith, *First Operation of a Free-Electron Laser,* Physical Review Letters, **38** (1977) p. 892.
71. A. Hasegawa, *Free Electron Laser,* Bell System Technical Journal, **57** (1978) p. 3069.
72. J. Dunn, A.L. Osterheld, R. Shepherd, W.E. White, V.N. Shlyaptsev, R.E. Stewart, *Demonstration of X-Ray Amplification in Transient Gain Nickel-like Palladium Scheme,* Physical Review Letters, **80** (1998) p. 2825.
73. N. Rohringer, D. Ryan, R.A. London, M. Purvis, F. Albert, J. Dunn, J.D. Bozek, C. Bostedt, A. Graf, R. Hill, S.P. Hau-Riege, and J.J. Rocca, *Atomic inner-shell X-ray*

*laser at 1.46 nanometres pumped by an X-ray free-electron laser,* Nature, **481** (2012) p. 488.

74. A. McPherson, G. Gibson, H. Jara, U. Johann, T.S. Luk, I.A. McIntyre, K. Boyer, C.K. Rhodes, *Studies of multiphoton production of vacuum-ultraviolet radiation in the rare gases,* Journal of the Optical Society of America B, **4** (1987) p. 595.
75. G.P. Zhang, *High Harmonic Generation in Atoms, Molecules and Nanostructures,* International Journal of Modern Physics B, **21** (2007) p. 5167.
76. A. L'Huillier, P. Balcou, *High-order harmonic generation in rare gases with a 1-ps 1053-nm laser,* Physical Review Letters, **70** (1993) p. 774.
77. J.W.G. Tisch, R.A. Smith, M. Ciarrocca, J.E. Muffett, J.P. Marangos, M.H.R. Hutchinson, *Angularly-resolved High-order Harmonic Generation in Helium,* Journal of Modern Optics, **41** (1994) p. 1163.
78. D. von der Linde, T. Engers, G. Jenke, P. Agostini, G. Grillon, E. Nibbering, A. Mysyrowicz, A. Antonetti, *Generation of high-order harmonics from solid surfaces by intense femtosecond laser pulses,* Physical Review A, **52** (1995) p. R25.
79. M. Hentschel, R. Kienberger, C. Spielmann, G.A. Reider, N. Milosevic, T. Brabec, P. Corkum, U. Heinzmann, M. Drescher, F. Krausz, *Attosecond metrology,* Nature, **414** (2001) p. 509.
80. L.B. Elouga Bom, S. Haessler, O. Gobert, M. Perdrix, F. Lepetit, J.F. Hergott, B. Carré, T. Ozaki, P. Salières, *Attosecond emission from chromium plasma,* Optics Express, **19** (2011) p. 3677.
81. P.M. Paul, E.S. Toma, P. Breger, G. Mullot, F. Augé, P. Balcou, H.G. Muller, P. Agostini, *Observation of a Train of Attosecond Pulses from High Harmonic Generation,* Science, **292** (2001) p. 1689.
82. R.A. Ganeev, *High-order harmonic generation in a laser plasma: a review of recent achievements,* Journal of Physics B: Atomic, Molecular and Optical Physics, **40** (2007) p. R213.
83. S. Kubodera, Y. Nagata, Y. Akiyama, K. Midorikawa, M. Obara, H. Tashiro, K. Toyoda, *High-order harmonic generation in laser-produced ions,* Physical Review A, **48** (1993) p. 4576.
84. W. Theobald, C. Wülker, F.P. Schäfer, B.N. Chichkov, *High-order harmonic generation in carbon vapor and low charged plasma,* Optics Communications, **120** (1995) p. 177.
85. R.A. Ganeev, T. Witting, C. Hutchison, F. Frank, M. Tudorovskaya, M. Lein, W.A. Okell, A. Zaïr, J.P. Marangos, J.W.G. Tisch, *Isolated sub-fs XUV pulse generation in Mn plasma ablation,* Optics Express, **20** (2012) p. 25239.
86. R.A. Ganeev, C. Hutchison, T. Siegel, M.E. López-Arias, A. Zaïr, J.P. Marangos, *High-order harmonic generation from metal plasmas using 1 kHz laser pulses,* Journal of Modern Optics, **58** (2011) p. 819.
87. Y. Akiyama, K. Midorikawa, Y. Matsunawa, Y. Nagata, M. Obara, H. Tashiro, K. Toyoda, *Generation of high-order harmonics using laser-produced rare-gas-like ions,* Physical Review Letters, **69** (1992) p. 2176.
88. C.G. Wahlström, S. Borgström, J. Larsson, S.G. Pettersson, *High-order harmonic generation in laser-produced ions using a near-infrared laser,* Physical Review A, **51** (1995) p. 585.
89. R.A. Ganeev, V.I. Redkorechev, T. Usmanov, *Optical harmonics generation in low-temperature laser-produced plasmas,* Optics Communications, **135** (1997) p. 251.

90. K. Krushelnick, W. Tighe, S. Suckewer, *Harmonic generation from ions in underdense aluminum and lithium–fluorine plasmas,* Journal of the Optical Society of America B, **14** (1997) p. 1687.
91. R. Ganeev, M. Suzuki, M. Baba, H. Kuroda, T. Ozaki, *High-order harmonic generation from boron plasma in the extreme-ultraviolet range,* Optics Letters, **30** (2005) p. 768.
92. R.A. Ganeev, H. Singhal, P.A. Naik, V. Arora, U. Chakravarty, J.A. Chakera, R.A. Khan, I.A. Kulagin, P.V. Redkin, M. Raghuramaiah, and P.D. Gupta, *Harmonic generation from indium-rich plasmas,* Physical Review A, **74** (2006) p. 063824.
93. R.A. Ganeev, M. Baba, M. Suzuki, H. Kuroda, *Optimization of harmonic generation from boron plasma,* Journal of Applied Physics, **99** (2006) p. 103303.
94. R.A. Ganeev, M. Suzuki, M. Baba, H. Kuroda, *Generation of strong coherent extreme ultraviolet radiation from the laser plasma produced on the surface of solid targets,* Applied Physics B, **81** (2005) p. 1081.
95. R.A. Ganeev, L.B.E. Bom, J.C. Kieffer, M. Suzuki, H. Kuroda, T. Ozaki, *Demonstration of the 101st harmonic generated from a laser-produced manganese plasma,* Physical Review A, **76** (2007) p. 023831.
96. R.A. Ganeev, C. Hutchison, I. Lopez-Quintas, F. McGrath, D.Y. Lei, M. Castillejo, J.P. Marangos, *Ablation of nanoparticles and efficient harmonic generation using a 1-kHz laser,* Physical Review A, **88** (2013) p. 033803.
97. R.A. Ganeev, T. Witting, C. Hutchison, V.V. Strelkov, F. Frank, M. Castillejo, I. Lopez-Quintas, Z. Abdelrahman, J.W.G. Tisch, J.P. Marangos, *Comparative studies of resonance enhancement of harmonic radiation in indium plasma using multicycle and few-cycle pulses,* Physical Review A, **88** (2013) p. 033838.
98. M. Oujja, R. de Nalda, M. López-Arias, R. Torres, J.P. Marangos, M. Castillejo, *$CaF_2$ ablation plumes as a source of CaF molecules for harmonic generation,* Physical Review A, **81** (2010) p. 043841.
99. R. de Nalda, M. Lopez-Arias, M. Sanz, M. Oujja, M. Castillejo, *Harmonic generation in ablation plasmas of wide bandgap semiconductors,* Physical Chemistry Chemical Physics, **13** (2011) p. 10755.
100. I. Lopez-Quintas, M. Oujja, M. Sanz, M. Martín, R.A. Ganeev, M. Castillejo, *Low-order harmonic generation in nanosecond laser ablation plasmas of carbon containing materials,* Applied Surface Science, **278** (2013) p. 33.
101. M. López-Arias, M. Oujja, M. Sanz, R. de Nalda, R.A. Ganeev, M. Castillejo, *Generation of low-order harmonics in laser ablation plasmas,* Molecular Physics, **110** (2012) p. 1651.
102. M. López-Arias, M. Oujja, M. Sanz, R.A. Ganeev, G.S. Boltaev, N.K. Satlikov, R.I. Tugushev, T. Usmanov, M. Castillejo, *Low-order harmonic generation in metal ablation plasmas in nanosecond and picosecond laser regimes,* Journal of Applied Physics, **111** (2012) p. 043111.
103. I. Lopez-Quintas, M. Oujja, M. Sanz, A. Benitez-Cañete, C. Hutchison, R. de Nalda, M. Martin, R.A. Ganeev, J.P. Marangos, M. Castillejo, *Characterization of laser-induced plasmas of nucleobases: Uracil and thymine,* Applied Surface Science, **302** (2014) p. 299.
104. P.R. Willmott, J.R. Huber, *Pulsed laser vaporization and deposition,* Reviews of Modern Physics, **72** (2000) p. 315.

105. M.N. Ashfold, F. Claeyssens, G.M. Fuge, S.J. Henley, *Pulsed laser ablation and deposition of thin films,* Chem Soc Rev, **33** (2004) p. 23.
106. D.B. Chrisey, G.K. Hubler, eds. Pulsed Laser Deposition of Thin Films, 1994, Wiley.
107. G. Hass, J.B. Ramsey, *Vacuum Deposition of Dielectric and Semiconductor Films by a $CO_2$ Laser,* Applied Optics, **8** (1969) p. 1115.
108. H.M. Smith, A.F. Turner, *Vacuum Deposited Thin Films Using a Ruby Laser,* Applied Optics, **4** (1965) p. 147.
109. J.T. Cheung, H. Sankur, *Growth of thin films by laser-induced evaporation,* Critical Reviews in Solid State and Materials Sciences, **15** (1988) p. 63.
110. X.D. Wu, A. Inam, T. Venkatesan, C.C. Chang, E.W. Chase, P. Barboux, J.M. Tarascon, B. Wilkens, *Low-temperature preparation of high Tc superconducting thin films,* Applied Physics Letters, **52** (1988) p. 754.
111. J. Schou, *Physical aspects of the pulsed laser deposition technique: The stoichiometric transfer of material from target to film,* Applied Surface Science, **255** (2009) p. 5191.
112. W. Prellier, A. Fouchet, B. Mercey, C. Simon, B. Raveau, *Laser ablation of Co:ZnO films deposited from Zn and Co metal targets on (0001) $Al_2O_3$ substrates,* Applied Physics Letters, **82** (2003) p. 3490.
113. T. Donnelly, J.G. Lunney, S. Amoruso, R. Bruzzese, X. Wang, X. Ni, *Angular distributions of plume components in ultrafast laser ablation of metal targets,* Applied Physics A, **100** (2010) p. 569.
114. J.G. Lunney, *Pulsed laser deposition of metal and metal multilayer films,* Applied Surface Science, **86** (1995) p. 79.
115. H.U. Krebs, O. Bremert, *Pulsed laser deposition of thin metallic alloys,* Applied Physics Letters, **62** (1993) p. 2341.
116. J. Shen, Z. Gai, J. Kirschner, *Growth and magnetism of metallic thin films and multilayers by pulsed-laser deposition,* Surface Science Reports, **52** (2004) p. 163.
117. O. Akira, T. Atsushi, *Pulsed laser deposition of thin films and superlattices based on ZnO,* Semiconductor Science and Technology, **20** (2005) p. S1.
118. X.W. Sun, H.S. Kwok, *Optical properties of epitaxially grown zinc oxide films on sapphire by pulsed laser deposition,* Journal of Applied Physics, **86** (1999) p. 408.
119. K. Nomura, H. Ohta, A. Takagi, T. Kamiya, M. Hirano, H. Hosono, *Room-temperature fabrication of transparent flexible thin-film transistors using amorphous oxide semiconductors,* Nature, **432** (2004) p. 488.
120. D.B. Chrisey, A. Piqué, R.A. McGill, J.S. Horwitz, B.R. Ringeisen, D.M. Bubb, P.K. Wu, *Laser Deposition of Polymer and Biomaterial Films,* Chemical Reviews, **103** (2003) p. 553.
121. P. Balling, J. Schou, *Femtosecond-laser ablation dynamics of dielectrics: basics and applications for thin films,* Reports on Progress in Physics, **76** (2013) p. 036502.
122. C. Capuccini, P. Torricelli, F. Sima, E. Boanini, C. Ristoscu, B. Bracci, G. Socol, M. Fini, I.N. Mihailescu, A. Bigi, *Strontium-substituted hydroxyapatite coatings synthesized by pulsed-laser deposition: In vitro osteoblast and osteoclast response,* Acta Biomaterialia, **4** (2008) p. 1885.
123. E.M. Kaidashev, M. Lorenz, H. von Wenckstern, A. Rahm, H.-C. Semmelhack, K.-H. Han, G. Benndorf, C. Bundesmann, H. Hochmuth, M. Grundmann, *High electron mobility of epitaxial ZnO thin films on c-plane sapphire grown by multistep pulsed-laser deposition,* Applied Physics Letters, **82** (2003) p. 3901.

124. J.H. Kim, H. Kim, D. Kim, Y.E. Ihm, W.K. Choo, *Magnetic properties of epitaxially grown semiconducting $Zn_{1-x}Co_xO$ thin films by pulsed laser deposition,* Journal of Applied Physics, **92** (2002) p. 6066.
125. D. Valerini, A.P. Caricato, M. Lomascolo, F. Romano, A. Taurino, T. Tunno, M. Martino, *Zinc oxide nanostructures grown by pulsed laser deposition,* Applied Physics A, **93** (2008) p. 729.
126. M. Walczak, E.L. Papadopoulou, M. Sanz, A. Manousaki, J.F. Marco, M. Castillejo, *Structural and morphological characterization of $TiO_2$ nanostructured films grown by nanosecond pulsed laser deposition,* Applied Surface Science, **255** (2009) p. 5267.
127. M. Sanz, R.d. Nalda, J.F. Marco, J.G. Izquierdo, L. Bañares, M. Castillejo, *Femtosecond Pulsed Laser Deposition of Nanostructured CdS Films,* The Journal of Physical Chemistry C, **114** (2010) p. 4864.
128. Y. Sun, G.M. Fuge, M.N.R. Ashfold, *Growth of aligned ZnO nanorod arrays by catalyst-free pulsed laser deposition methods,* Chemical Physics Letters, **396** (2004) p. 21.
129. A.J. Pedraza, J.D. Fowlkes, D.H. Lowndes, *Silicon microcolumn arrays grown by nanosecond pulsed-excimer laser irradiation,* Applied Physics Letters, **74** (1999) p. 2322.
130. R.D. Vispute, V. Talyansky, Z. Trajanovic, S. Choopun, M. Downes, R.P. Sharma, T. Venkatesan, M.C. Woods, R.T. Lareau, K.A. Jones, and A.A. Iliadis, *High quality crystalline ZnO buffer layers on sapphire (001) by pulsed laser deposition for III–V nitrides,* Applied Physics Letters, **70** (1997) p. 2735.
131. D. Pergolesi, E. Fabbri, A. D'Epifanio, E. Di Bartolomeo, A. Tebano, S. Sanna, S. Licoccia, G. Balestrino, E. Traversa, *High proton conduction in grain-boundary-free yttrium-doped barium zirconate films grown by pulsed laser deposition,* Nature Materials, **9** (2010) p. 846.
132. J.M. Lackner, *Industrially-scaled large-area and high-rate tribological coating by Pulsed Laser Deposition,* Surface and Coatings Technology, **200** (2005) p. 1439.
133. D.H.A. Blank, M. Dekkers, G. Rijnders, *Pulsed laser deposition in Twente: from research tool towards industrial deposition,* Journal of Physics D: Applied Physics, **47** (2014) p. 034006.
134. V. Domnich, S. Reynaud, R.A. Haber, M. Chhowalla, *Boron Carbide: Structure, Properties, and Stability under Stress,* Journal of the American Ceramic Society, **94** (2011) p. 3605.
135. R. Lazzari, N. Vast, J.M. Besson, S. Baroni, A. Dal Corso, *Atomic Structure and Vibrational Properties of Icosahedral $B_4C$ Boron Carbide,* Physical Review Letters, **83** (1999) p. 3230.
136. F. Thévenot, *Boron carbide—A comprehensive review,* Journal of the European Ceramic Society, **6** (1990) p. 205.
137. B. Zeng, Z. Feng, S. Li, Y. Liu, L. Cheng, L. Zhang, *Microstructure and deposition mechanism of CVD amorphous boron carbide coatings deposited on SiC substrates at low temperature,* Ceramics International, **35** (2009) p. 1877.
138. A.O. Sezer, J.I. Brand, *Chemical vapor deposition of boron carbide,* Materials Science and Engineering: B, **79** (2001) p. 191.

139. O. Conde, A.J. Silvestre, J.C. Oliveira, *Influence of carbon content on the crystallographic structure of boron carbide films,* Surface and Coatings Technology, **125** (2000) p. 141.
140. Z. Guan, T. Gutu, J. Yang, Y. Yang, A.A. Zinn, D. Li, T.T. Xu, *Boron carbide nanowires: low temperature synthesis and structural and thermal conductivity characterization,* Journal of Materials Chemistry, **22** (2012) p. 9853.
141. L.G. Jacobsohn, R.D. Averitt, C.J. Wetteland, R.K. Schulze, M. Nastasi, L.L. Daemen, Z. Jenei, P. Asoka-Kumar, *Role of intericosahedral chains on the hardness of sputtered boron carbide films,* Applied Physics Letters, **84** (2004) p. 4173.
142. S. Zhang, Z. He, X. Ji, W. Lu, C. Wang, Q. Shen, L. Zhang, *Understanding the deposition mechanism of pulsed laser deposited B-C films using dual-targets,* Journal of Applied Physics, **115** (2014) p. 154906.
143. O. Derkach, S. Pentzien, W. Kautek, *Pulsed laser deposition of boron carbide: spectroscopic study of the laser ablation plasma,* SPIE proceedings, **2991** (1997) p. 48.
144. W. Kautek, S. Pentzien, A. Conradi, J. Krüger, K.-W. Brzezinka, *Pulsed-laser deposition and boron-blending of diamond-like caron (DLC) thin films,* Applied Surface Science, **106** (1996) p. 158.
145. T. Csákó, J. Budai, T. Szörényi, *Property improvement of pulsed laser deposited boron carbide films by pulse shortening,* Applied Surface Science, **252** (2006) p. 4707.
146. S. Aoqui, H. Miyata, T. Ohshima, T. Ikegami, K. Ebihara, *Preparation of boron carbide thin film by pulsed KrF excimer laser deposition process,* Thin Solid Films, **407** (2002) p. 126.
147. H.A. Castillo, E. Restrepo-Parra, J.M. Vélez, W. de la Cruz, *Substrate temperature influence on boron carbide coatings grown by the PLD technique,* Surface and Coatings Technology, **205** (2011) p. 3607.
148. F. Kokai, M. Taniwaki, K. Takahashi, A. Goto, M. Ishihara, K. Yamamoto, Y. Koga, *Laser ablation of boron carbide: thin-film deposition and plume analysis,* Diamond and Related Materials, **10** (2001) p. 1412.
149. F. Kokai, M. Taniwaki, M. Ishihara, Y. Koga, *Effect of laser fluence on the deposition and hardnessof boron carbide thin films,* Applied Physics A: Materials Science & Processing, **74** (2002) p. 533.
150. D. Zemsky, R. Shneck, P.J. Dagdigian, I. Bar, *Structure and morphology of pulsed laser depos ited boron carbide films: Influence of deposition geometry,* Journal of Applied Physics, **102** (2007) p. 104309.
151. J. Sun, H. Ling, W.J. Pan, N. Xu, Z.F. Ying, W.D. Shen, J.D. Wu, *Chemical structure and micro-mechanical properties of ultra-thin films of boron carbide prepared by pulsed-laser deposition,* Tribology Letters, **17** (2004) p. 99.
152. R. Dietsch, T. Holz, D. Weissbach, R. Scholz, *Large area PLD of nanometer-multilayers,* Applied Surface Science, **197-198** (2002) p. 169.
153. R. Dietsch, T. Holz, H. Mai, C.-F. Meyer, R. Scholz, B. Wehner, *High precision large area PLD of X-ray optical multilayers,* Applied Surface Science, **127-129** (1998) p. 451.
154. H. Ohno, *Making Nonmagnetic Semiconductors Ferromagnetic,* Science, **281** (1998) p. 951.

155. K. Sato, L. Bergqvist, J. Kudrnovský, P.H. Dederichs, O. Eriksson, I. Turek, B. Sanyal, G. Bouzerar, H. Katayama-Yoshida, V.A. Dinh, T. Fukushima, H. Kizaki, and R. Zeller, *First-principles theory of dilute magnetic semiconductors,* Reviews of Modern Physics, **82** (2010) p. 1633.
156. R.N. Bhargava, D. Gallagher, X. Hong, A. Nurmikko, *Optical properties of manganese-doped nanocrystals of ZnS,* Physical Review Letters, **72** (1994) p. 416.
157. N. Pradhan, D.D. Sarma, *Advances in Light-Emitting Doped Semiconductor Nanocrystals,* The Journal of Physical Chemistry Letters, **2** (2011) p. 2818.
158. R. Subha, V. Nalla, J.H. Yu, S.W. Jun, K. Shin, T. Hyeon, C. Vijayan, W. Ji, *Efficient Photoluminescence of $Mn^{2+}$-Doped ZnS Quantum Dots Excited by Two-Photon Absorption in Near-Infrared Window II,* The Journal of Physical Chemistry C, **117** (2013) p. 20905.
159. S.M.T. Otaqsara, *Tunable visible emission of TM-doped ZnS quantum dots (TM: $Mn^{2+}$, $Co^{2+}$, $Ag^{+}$),* The European Physical Journal - Applied Physics, **59** (2012) p. 10404.
160. T. Dietl, *A ten-year perspective on dilute magnetic semiconductors and oxides,* Nature Materials, **9** (2010) p. 965.
161. K.R. Kittilstved, W.K. Liu, D.R. Gamelin, *Electronic structure origins of polarity-dependent high-$T_C$ ferromagnetism in oxide-diluted magnetic semiconductors,* Nature Materials, **5** (2006) p. 291.
162. S.J. Pearton, W.H. Heo, M. Ivill, D.P. Norton, T. Steiner, *Dilute magnetic semiconducting oxides,* Semiconductor Science and Technology, **19** (2004) p. R59.
163. K. Ueda, H. Tabata, T. Kawai, *Magnetic and electric properties of transition-metal-doped ZnO films,* Applied Physics Letters, **79** (2001) p. 988.
164. M. Jadraque, A.B. Evtushenko, D. Ávila-Brande, M. López-Arias, V. Loriot, Y.G. Shukhov, L.S. Kibis, A.V. Bulgakov, M. Martín, *Co-Doped ZnS Clusters and Nanostructures Produced by Pulsed Laser Ablation,* The Journal of Physical Chemistry C, **117** (2013) p. 5416.
165. L. Englert, B. Rethfeld, L. Haag, M. Wollenhaupt, C. Sarpe-Tudoran, T. Baumert, *Control of ionization processes in high band gap materials via tailored femtosecond pulses,* Optics Express, **15** (2007) p. 17855.
166. A. Klini, P.A. Loukakos, D. Gray, A. Manousaki, C. Fotakis, *Laser Induced Forward Transfer of metals by temporally shaped femtosecond laser pulses,* Optics Express, **16** (2008) p. 11300.
167. S. Amoruso, R. Bruzzese, X. Wang, *Plume composition control in double pulse ultrafast laser ablation of metals,* Applied Physics Letters, **95** (2009) p. 251501.
168. M. Guillermin, J.P. Colombier, S. Valette, E. Audouard, F. Garrelie, R. Stoian, *Optical emission and nanoparticle generation in Al plasmas using ultrashort laser pulses temporally optimized by real-time spectroscopic feedback,* Physical Review B, **82** (2010) p. 035430.
169. F. Bourquard, T. Tite, A.-S. Loir, C. Donnet, F. Garrelie, *Control of the Graphite Femtosecond Ablation Plume Kinetics by Temporal Laser Pulse Shaping: Effects on Pulsed Laser Deposition of Diamond-Like Carbon,* The Journal of Physical Chemistry C, **118** (2014) p. 4377.
170. E.G. Gamaly, A.V. Rode, O. Uteza, V. Kolev, B. Luther-Davies, T. Bauer, J. Koch, F. Korte, B.N. Chichkov, *Control over a phase state of the laser plume ablated by*

*femtosecond laser: Spatial pulse shaping,* Journal of Applied Physics, **95** (2004) p. 2250.

171. H. Dachraoui, W. Husinsky, *Thresholds of Plasma Formation in Silicon Identified by Optimizing the Ablation Laser Pulse Form,* Physical Review Letters, **97** (2006) p. 107601.
172. E.L. Papadopoulou, E. Axente, E. Magoulakis, C. Fotakis, P.A. Loukakos, *Laser induced forward transfer of metal oxides using femtosecond double pulses,* Applied Surface Science, **257** (2010) p. 508.
173. M. Guillermin, A. Klini, J.P. Colombier, F. Garrelie, D. Gray, C. Liebig, E. Audouard, C. Fotakis, R. Stoian, *Tuning spectral properties of ultrafast laser ablation plasmas from brass using adaptive temporal pulse shaping,* Optics Express, **18** (2010) p. 11159.
174. C. Ristoscu, G. Socol, C. Ghica, I.N. Mihailescu, D. Gray, A. Klini, A. Manousaki, D. Anglos, C. Fotakis, *Femtosecond pulse shaping for phase and morphology control in PLD: Synthesis of cubic SiC,* Applied Surface Science, **252** (2006) p. 4857.
175. N. Jegenyes, Z. Toth, B. Hopp, J. Klebniczki, Z. Bor, C. Fotakis, *Femtosecond pulsed laser deposition of diamond-like carbon films: The effect of double laser pulses,* Applied Surface Science, **252** (2006) p. 4667.
176. P.P. Pronko, Z. Zhang, P.A. VanRompay, *Critical density effects in femtosecond ablation plasmas and consequences for high intensity pulsed laser deposition,* Applied Surface Science, **208–209** (2003) p. 492.

# Chapter 2

# Experimental methods

# 2. Experimental methods

This chapter describes the experimental systems and methods used in the present thesis.

Harmonic generation experiments were performed using different modifications of the same set-up. The PLD technique is used to generate micro and nanostructures from different target materials in the nano and femtosecond ablation regimes and the corresponding two PLD set-ups are described. Furthermore, as the ultimate goal of PLD is to produce deposits in the form of thin layers, analysis of the obtained samples is required. For this purpose, several microscopic and spectroscopic techniques have been applied and a brief account of these will be also presented in this section.

In both HG and PLD experiments, additional plasma characterization was conducted by OES and TOF-MS. The instrumentation required in these analytical techniques will be also described here.

Although in this chapter the main characteristics of the experimental set-ups are presented, the specific irradiation and detection parameters will be given in the corresponding results sections of Chapters 3 and 4.

## 2.1 Instrumentation for low-order harmonic generation experiments

Figure 2.1 depicts a general scheme of a set-up for harmonic generation in laser ablation plasmas. The basic components of the set-up are: the ablation and harmonics driving lasers, vacuum chamber, ablation target, separation system to filter the residual fundamental driving beam from the generated harmonics and detection system.

In this scheme, the ablation beam propagates through the *x* axis, perpendicular to the target surface. Ablation of the target is performed inside a vacuum chamber. The harmonics driving beam propagates parallel to the target surface along the *z* axis. The harmonic radiation ($n\omega$), generated upon interaction of the driving beam with the laser ablation plasma, is separated from the driving beam fundamental radiation ($\omega$). Finally, the filtered harmonic radiation is detected.

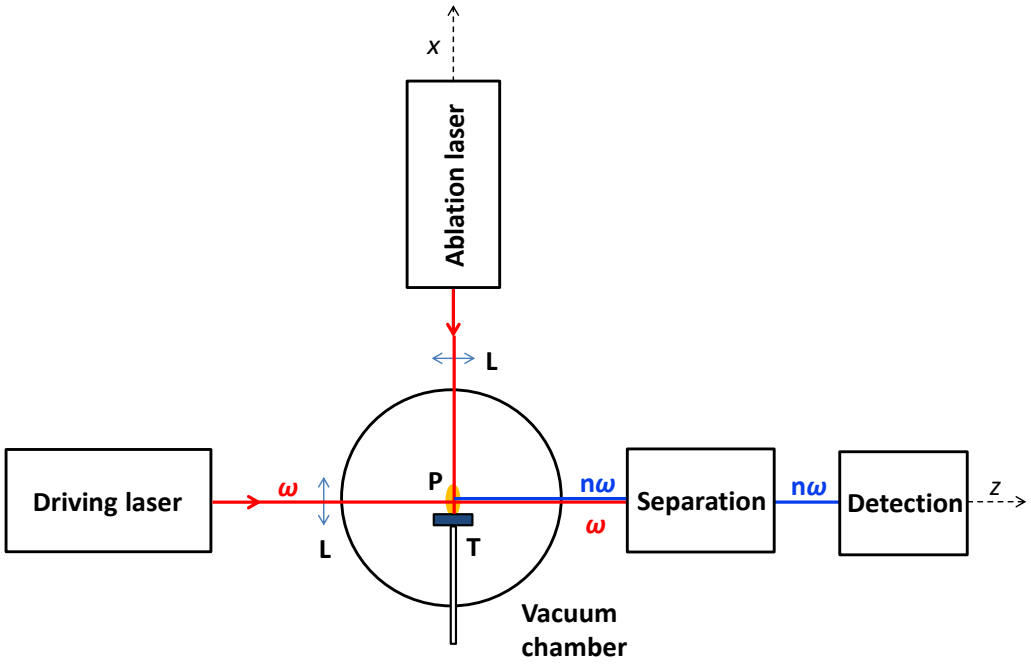


Figure 2.1 Scheme of the set-up for harmonic generation in laser ablation plasmas. The *x* and *z* axes coincide with the propagation directions of the ablation and driving beams respectively. Signs in the figure correspond to: T = target, P = plasma, L = focusing lens.

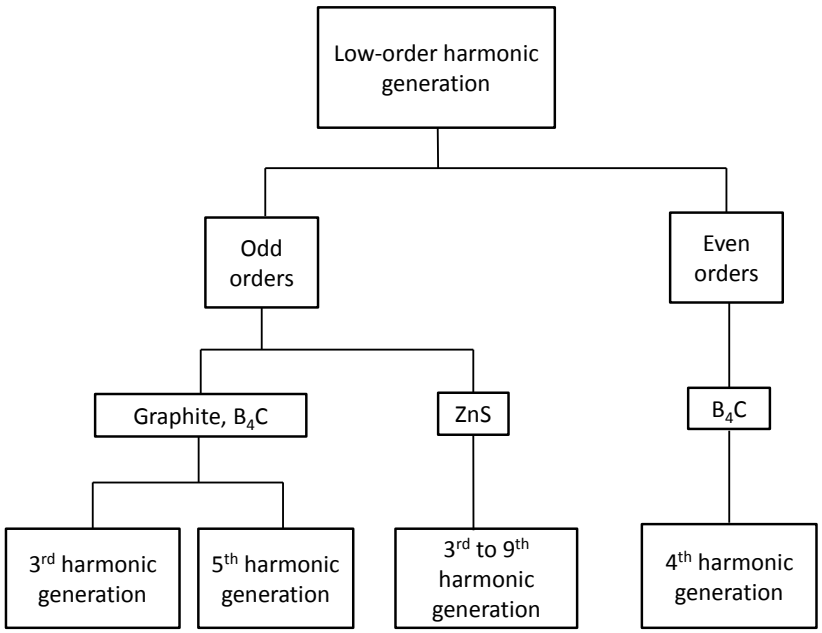


Figure 2.2 Diagram showing the four different types of low-order harmonic generation experiments described in this chapter.

Depending on the harmonic order studied, four configurations of the same experimental set-up have been used in this thesis. In figure 2.2 a scheme of the different harmonic generation processes studied in laser ablation plasmas of graphite, boron carbide and zinc sulfide is depicted.

The four experimental configurations share the same laser systems and ablation chamber, but differ in the specific detection system used. Also the optical layout needed to generate and bring the driving beams into the ablation chamber in the case of 4$^{th}$ harmonic generation differs from that needed to generate odd-order harmonics. All these differences will be described in more detail in the following sections.

### 2.1.1 Laser systems and optics

As mentioned, harmonic generation in laser ablation plasmas requires the use of two laser beams, coming from the same or different laser systems (see figure 2.1). In this thesis, we used two different laser systems for generating the ablation plasma and for driving the harmonic radiation.

Solid state Q-switched Nd:YAG lasers delivering pulses in the nanosecond temporal range are suitable for both target ablation and driving of the low-order harmonics. Their versatility, in terms of emitted wavelengths (by frequency doubling, tripling and frequency mixing), power and robustness, makes them appropriate for this kind of application. Table 2.1 summarizes the main characteristics of the lasers used in the experiments described in this chapter.

Table 2.1. Summary of the laser systems described in this chapter and their main characteristics.

| | Role | | |
|---|---|---|---|
| | Ablation | | Driving |
| Supplier | Spectra Physics | Quantel | Lotis |
| Model | Indi 30-HG | Brilliant B | TII LS-2147 |
| Laser type | Q-Switched Nd:YAG | | |
| Repetition rate | 10 Hz | | |
| Wavelength used (nm) | 1064 | 266 | 1064 |
| Pulse duration (ns) | 7 | 4 | 18 |
| Max. output (J) | 0.5 | 0.09 | 0.85 |
| Energy profile | Gaussian | | |
| Output polarization direction | Linear (horizontal) | | |

### Ablation lasers

Ablation of solid targets was performed in all cases with Q-switched Nd:YAG lasers emitting at 1064 nm and delivering pulses in the nanosecond range. Experiments involving ablation at this wavelength were carried out with a laser system from Spectra Physics, model Quanta Ray Indi 30-HG.

Some considerations regarding the laser ablation energy (or fluence) must be taken into account. First of all, for efficient plasma formation, ablation must be carried out with a fluence above the ablation threshold of the target material. As the energy of the ablation pulse has important effects on the composition and dynamics of the plasma plume, different ablation regimes were explored by varying the energy of the ablation laser beam. This energy was controlled using variable attenuators, suitable for the selected ablation wavelength, purchased from Laseroptik GMBH. The output energy was measured with a Gentec ED200 at the entrance of the ablation chamber (see figure 2.1).

The ablation laser beam was focused onto the target surface at normal incidence using a spherical quartz lens with a focal length $f$ = 17 cm. In order to avoid breakdown in front of the target surface, which can shield the laser pulse energy, the beam was focused beyond the target surface. This resulted in a typical spot size on the target surface of about 800 µm diameter.

### Driving laser

For the harmonics driving radiation, 1064 nm nanosecond pulses from a Q-switched Nd:YAG laser from Lotis, model TII LS-2147, were used (table 2.1). The driving laser beam was focused inside the plasma volume by means of a quartz spherical lens with a $f$ = 20 cm focal length. The spot radius $w_0$ on the focal plane is estimated in 60 µm, thus achieving a peak intensity of about $4 \times 10^{11}$ W cm$^{-2}$. The estimated confocal parameter of the driving beam under the focusing conditions used in the experiments is 4 mm.

In HG experiments, the ablation and driving pulses are used as “pump and probe” of the nonlinear response of the plasma at different times. Therefore, synchronization between both laser pulses is extremely important. For that purpose, the ablation and driving lasers are fired at 10 Hz repetition rate and are controlled by a Stanford SRS DG-535 delay generator. Figure 2.3 shows the synchronization scheme of the experiment.

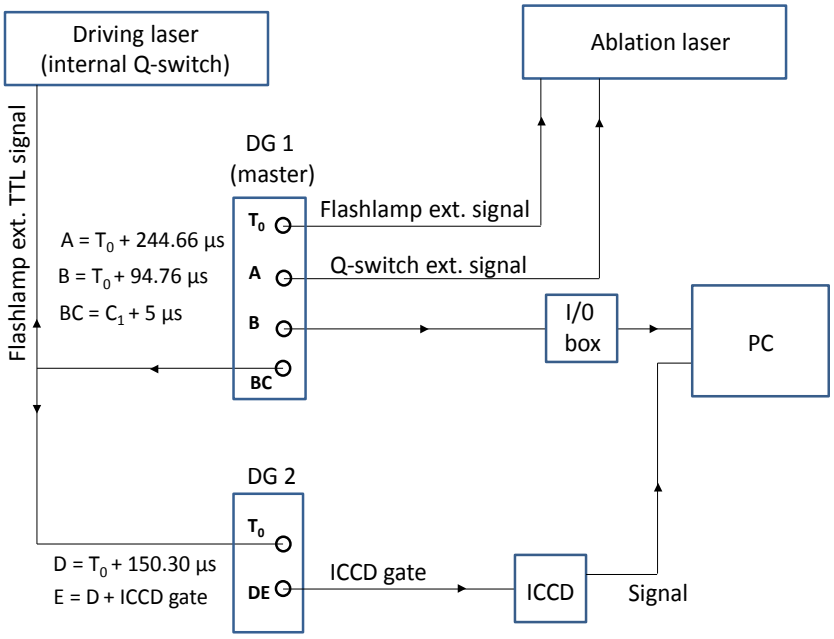


Figure 2.3 Synchronization scheme in low-order harmonic generation experiments using laser ablation plasmas as nonlinear medium. Synchronization is performed using two delay generators (DG1 and DG2), which trigger the ablation and driving lasers, the ICCD detector and the acquisition of the signal by a computer (PC). The optimized delay values for the triggering of the different components are given for each channel of the corresponding DG.

The delay generator DG1 was fired internally at 10 Hz and served for triggering the ablation laser at time zero. The time delay between the flashlamp and Q-switch triggering was optimized at 244.66 µs for yielding the maximum output energy (in order to minimize energy fluctuation). At a controllable delay (B), the driving laser, the PC acquisition card and the DG2 were fired simultaneously. The DG2 servers to control the ICCD opening time (observation window).

### 2.1.2 Ablation chamber and vacuum system

Two different ambient conditions were explored in low-order harmonic generation experiments, vacuum and inert gas atmosphere. For that purpose, targets were placed inside a homemade vacuum chamber pumped by a turbomolecular pump (Varian Turbo V-70 LP) backed by a Telstar 2G-6 rotary pump.

The pressure during the LHG experiments under vacuum conditions was selected in the range of $10^{-2}$-$10^{-5}$ mbar. These pressures can be easily achieved with only the rotary pump or by the combination of both pumps respectively.

In experiments involving inert gas atmosphere, the ablation chamber was filled with a continuous flow of inert gas, reaching a constant pressure inside the chamber of up to 1.5 mbar while the chamber was being pumped by the rotary pump. The gas inlet was equipped with a regulator and a needle valve in order to establish a controllable constant flux of the selected gas.

Pressures of the order of $10^{-2}$ mbar were measured with a Varian/Agilent Technologies ConvecTorr gauge, whereas below this pressure, a Varian 525 inverted magnetron cold cathode ionization gauge was used. Pressures above atmospheric were measured with a capacitive manometer MKS Baratron.

The ablation chamber was equipped with quartz windows (unless otherwise specified, see section 2.1.3.3 in page 47) through which the ablation and driving laser beams, as well as the generated harmonic radiation, can propagate. The solid targets were mounted at the end of a vacuum feedthrough that allowed rotation with the help of a step motor, and linear displacement, while holding the vacuum inside the chamber. Rotation of the targets is needed in order to prevent the formation of craters that could confine the plasma upon repetitive ablation. The feedthrough also allows the displacement of the target along the ablation axis, therefore the plasma plume can be interrogated by the perpendicularly propagating driving beam at a controllable distance with respect to the target surface. This distance was typically set to 0.6 mm from the target surface, except in the "*x*-scans", where it was gradually varied to study the expansion of the plasma species along the ablation axis.

## 2.1.3 Detection systems, optics and synchronization.

The experimental set-ups described in the following section are intended to generate and detect the coherent radiation of the different harmonics of the 1064 nm fundamental radiation. As mentioned, the main differences between the configurations of the set-up used in these experiments are related to the detection system and the optics required for generating and recording the signal of the different harmonic orders.

### 2.1.3.1 Detection up to the 5$^{th}$ harmonic

Experiments studying orders up to the fifth harmonic of the 1064 nm fundamental radiation (at $\lambda$ = 213 nm), the detection can be performed in air. At this point it is important to remember that the output radiation coming from the ablation chamber is constituted by the generated harmonic beams and by the transmitted fundamental

1064 nm beam, both propagating collinearly. Due to the relatively low efficiency of the nonlinear process, the intensity of the IR beam is high enough to damage the delicate optical components of the detector. Thus a method to separate the fundamental IR beam from the generated harmonics and, at the same time, drive the latter to the detection system, is required. In this case a set of two high damage threshold dichroic mirrors, suitable for the studied harmonic wavelength was chosen.

Figure 2.4 shows a scheme of the experimental set-up used for generation and detection of the 3$^{rd}$ harmonic of the 1064 nm fundamental radiation. More information about this set-up can be found in [1-4]. The detection system was constituted by a Czerny-Turner type spectrograph (Bentham model TMc300V) with a focal distance of 300 mm and an aperture of f/4.1, coupled to an ICCD detector (Andor DH501-25F-03). The spectrograph is equipped with an entrance slit with adjustable width from 10 µm to 13 mm. Further spectral separation of the incoming radiation was achieved by the use of either a 1200 or a 300 groves mm$^{-1}$ diffraction grating mounted on a motorized turret. Provided resolution values for the 1200 groves mm$^{-1}$ grating are 3 mm and 0.1 nm for the fully open and minimum slit widths respectively.

The ICCD detector provides an active area of 128 x 1024 pixels with pixel size of 24 x 24 µm$^2$. The main advantage of such an intensified detector is the possibility of performing time-gated detection, with resolution in the range of nanoseconds. This feature, together with the synchronization of both lasers, discussed later, is crucial for time resolved studies (and in some cases, like in OES/LIBS for avoiding the broad emission due to *Bremsstrahlung* at early times after ablation).

The spectrograph was connected through a GPIB interface card to a computer and was controlled using Andor MCD specific software. The same software serves to control the ICCD detector, which communicates with the computer via an acquisition card also from Andor Technologies. Using this software, some parameters such as number of accumulations or the acquisition mode can be set. For LHG experiments, full vertical binning acquisition mode was selected. With this setting, the software reads each pixel charge by columns in the 2D matrix of the sensor.

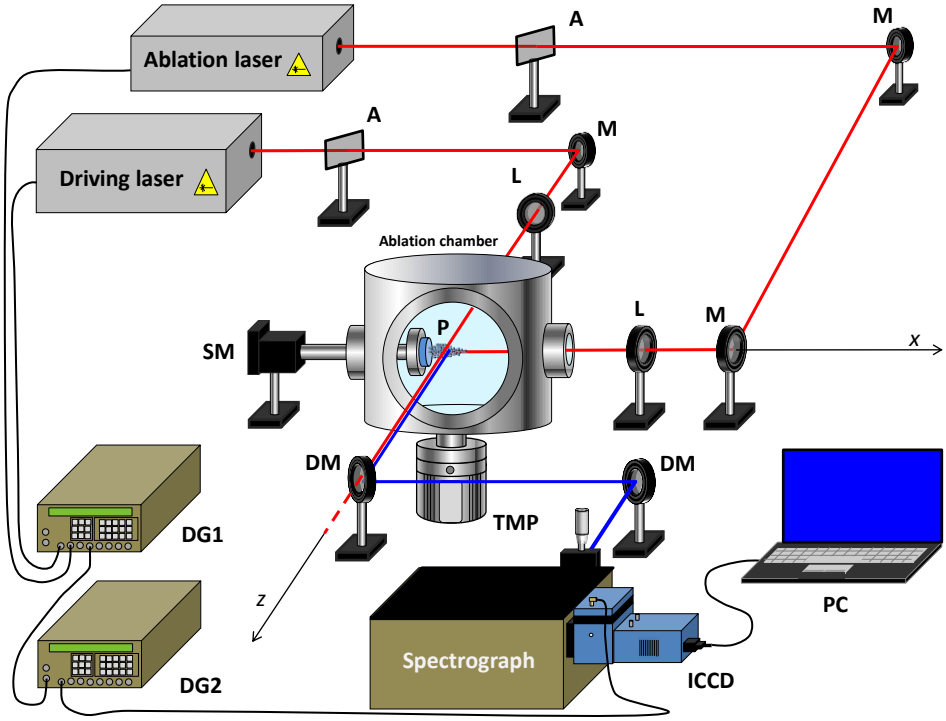


Figure 2.4 Experimental set-up for low-order harmonic generation in laser ablation plasmas. The detection system is configured for detection of the 3rd harmonic at 355 nm of the 1064 nm fundamental driving laser wavelength. Signs in the figure correspond to: A = variable attenuator, M = mirror, L = focusing lens, P = ablation plasma, DM = dichroic mirror (highly reflective at 355 nm), SM = step motor, TMP = turbomolecular pump, DG = delay generator, ICCD = intensified CCD camera, PC = computer.

Attempts were made to measure the 5th harmonic through detection of the second diffraction order at 426 nm. With this set-up this was possible in some experiments, but the low conversion efficiency required a more sensitive detection system. Figure 2.5 shows the modifications of the low-order harmonic generation set-up described previously. In this case highly reflective dichroic mirrors at 213 nm were employed in order to separate the 5th harmonic beam from the fundamental 1064 nm radiation. Detection was performed with a monochromator with a focal distance of 0.125 m (CVI SP CM110) coupled to a photomultiplier tube (Hamamatsu R928). The higher sensitivity of this detection system, compared to that composed by the Czerny-Turner spectrograph and the ICCD, described in figure 2.4, allowed us to detect a measurable signal at 213 nm, which was recorded with the help of a Tektronix DPO 3034 digital oscilloscope.

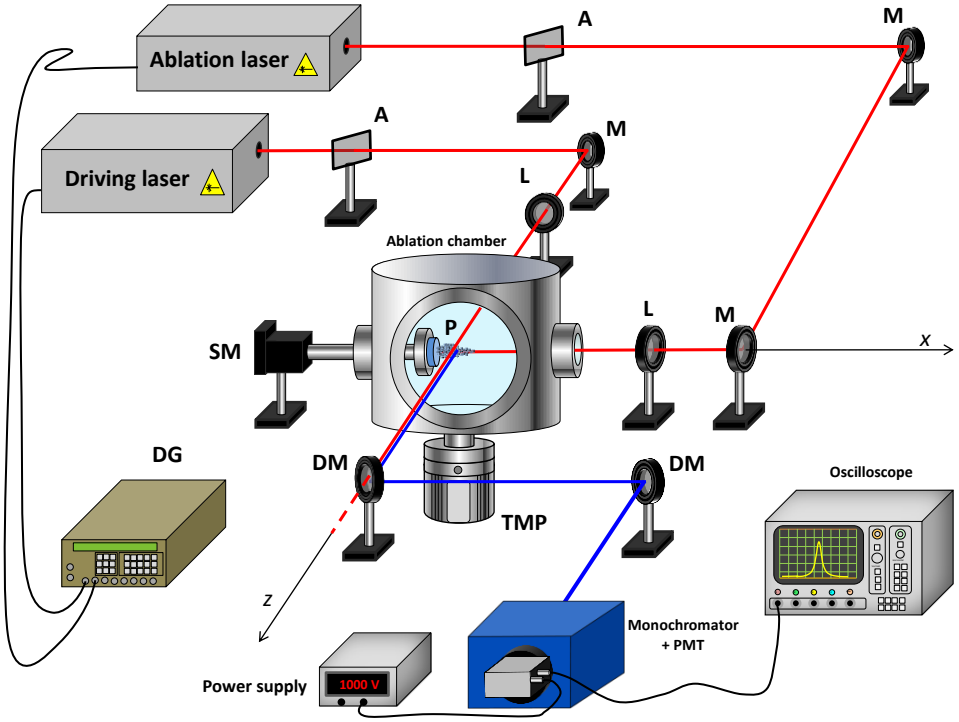


Figure 2.5 Scheme of the experimental set-up used for detection of the 5th harmonic of the 1064 nm fundamental radiation in laser ablation plasmas. Signs in the figure correspond to: A = variable attenuator, M = mirror, L = focusing lens, P = ablation plasma, DM = dichroic mirror (highly reflective at 213 nm), SM = step motor, TMP = turbomolecular pump, DG = delay generator, PC = computer.

### 2.1.3.2 Generation and detection of fourth-harmonic by frequency mixing

Radiation at the fourth harmonic wavelength (266 nm) of the 1064 nm fundamental radiation was generated in $B_4C$ laser ablation plasmas using a modification of the set-up depicted in figure 2.4. More information about this set-up can be found in [5].

In this case, harmonic generation was performed through a frequency mixing process involving a second driving beam which in turn was generated by doubling the frequency of the fundamental 1064 nm driving laser with a KDP nonlinear crystal through a type I SHG process. Figure 2.6 depicts a scheme of the optics implemented for 4th harmonic generation.

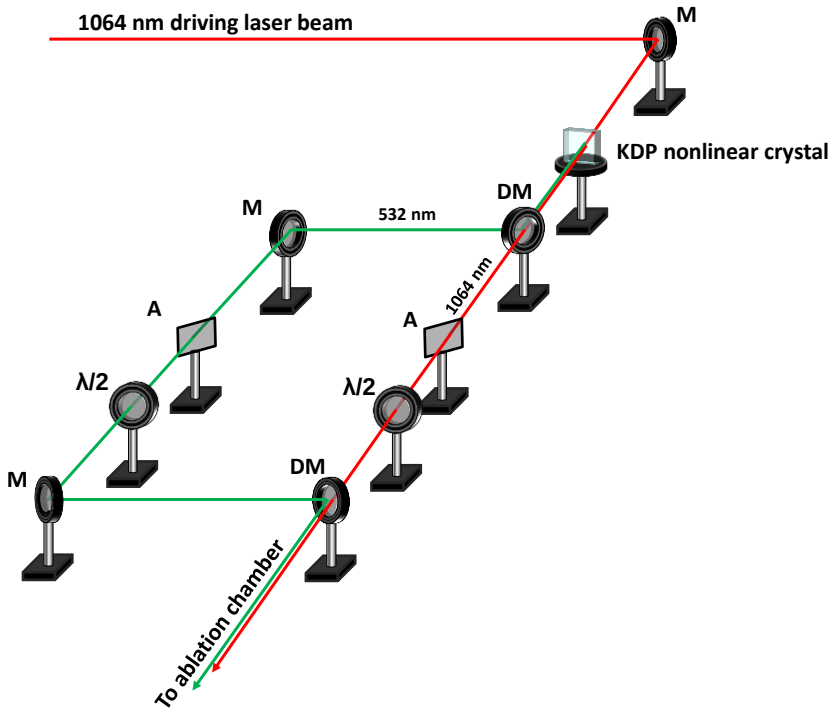


Figure 2.6 Two-color optical arrangement used for frequency mixing experiments. Signs in the figure correspond to: M = mirror, DM = dichroic mirror, A = variable attenuator, $\lambda/2$ = half wave plate.

After the KDP nonlinear crystal, the fundamental 1064 nm beam and its second harmonic at 532 nm propagate collinearly toward a highly reflective dichroic mirror at 532 nm where both wavelengths are separated. This arrangement allowed individual control of the energy and polarization of both beams by using a set of variable attenuators and half wave plates. Both beams were recombined with a second dichroic mirror. The recombined two-color beam was now driven to the ablation chamber and focused within the plasma volume as described previously.

The fourth harmonic signal was studied with the detection system shown previously in figure 2.4, by directing the 266 nm beam to the entrance slit of the spectrograph with the help of two dichroic mirrors, this time highly reflective at this wavelength.

### 2.1.3.3 Detection of higher-order harmonics in the vacuum ultraviolet region

Experiments to extend the study to higher-order harmonics ($3^{rd}$, $5^{th}$, $7^{th}$ and $9^{th}$ harmonics of the fundamental 1064 nm beam) were performed in the same ablation chamber and with the same lasers as previously described, but in this particular case, the detection had to be carried out under vacuum due to the strong absorption by air of wavelengths below 180 nm. Therefore, some modifications in the original set-up were implemented. A detailed scheme of this system is depicted in Figure 2.7.

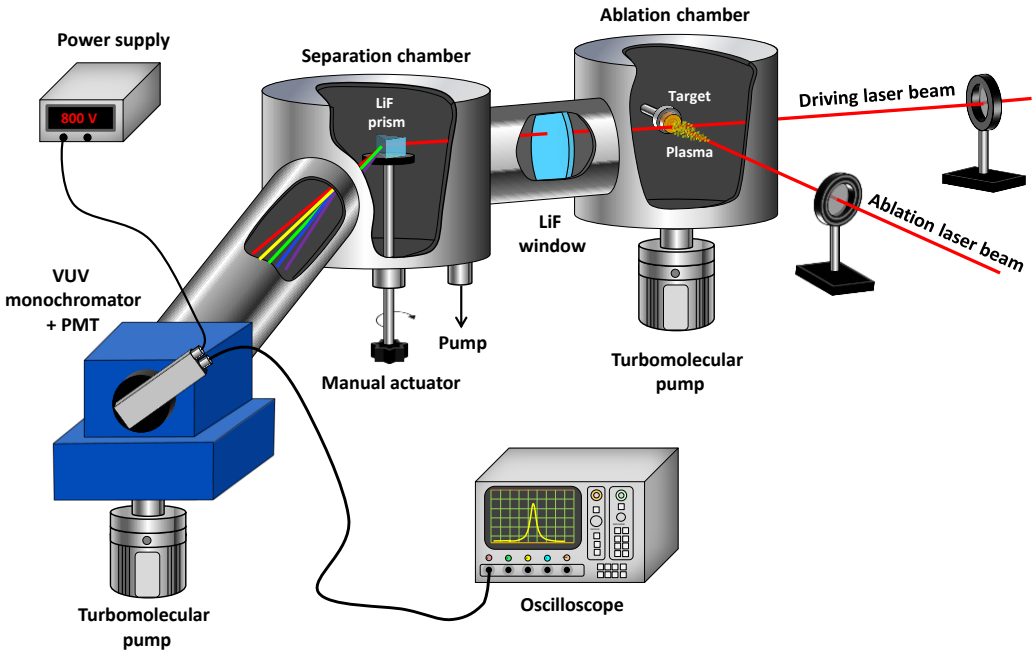


Figure 2.7 Scheme of the experimental set-up for detection of harmonic radiation in the vacuum ultraviolet region generated in laser ablation plasmas.

In this case, the separation of the generated harmonics from the residual IR beam was accomplished with a lithium fluoride prism, cut at 60° and mounted on a rotational stage inside a vacuum chamber (separation chamber). The prism can be manipulated externally with the help of a vacuum feedthrough in order to send the selected harmonic beam to the detection system. Both the ablation and separation chambers were isolated by a lithium fluoride window placed in between. This LiF window allows the transmission of shorter wavelengths (cut-off of 105 nm) as opposed to the standard quartz windows used in previous experiments. The separation chamber was connected to the detection system through a fitting attached at an angle of 47°. This particular angle was chosen as a trade-

off between all the propagation angles of the different harmonic beams after being dispersed by the LiF prism.

The detection system is composed by a 0.2 m Acton Research Corp. VM 502 VUV monochromator, equipped with a 1200 lines/mm grating, coupled to a sodium salicylate coated window and a photomultiplier tube (EMI 9781B). The PMT output signal was recorded with the help of a Tektronix DPO 3034 digital oscilloscope.

The separation chamber and the VUV monochromator were pumped with an additional turbomolecular pump, Agilent TV 81-M and a Telstar 2G-6 rotary pump down to a base pressure of $10^{-5}$ mbar or lower.

### 2.1.4 Plasma characterization in harmonic generation experiments by optical emission spectroscopy

Spontaneous emission of the plasmas obtained from the studied targets was characterized via OES. These experiments were performed with essentially the same set-up used in LHG, being the main difference the way in which the plasma emission is collected and detected. This modified set-up is shown in Figure 2.8. The radiation emitted by the ablation plasma is collected by a spherical quartz lens of focal length $f$ = 8 cm. The lens is placed at a distance equal to 2$f$ from the target and to 2$f$ from the entrance slit of the spectrograph in order to form the plasma plume image onto the slit plane.

One of the most important parameters to be controlled in OES experiments is the delay time between the ablation event and the onset of the signal acquisition. As mentioned, this is achieved by gating the ICCD detector.

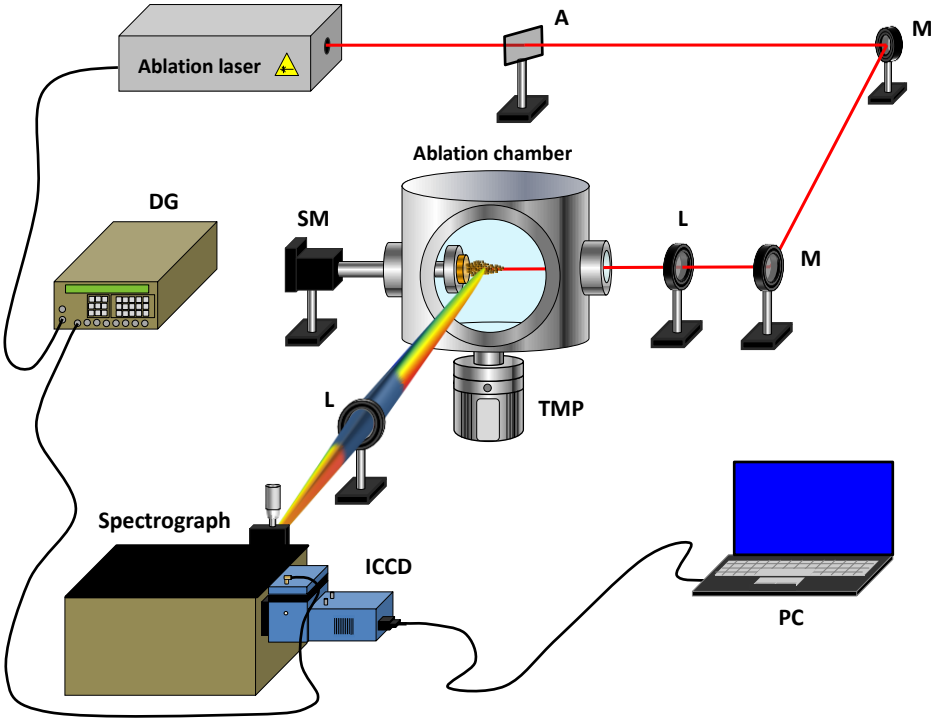


Figure 2.8 Experimental set-up for optical emission spectroscopy in laser ablation plasmas. Signs in the figure correspond to: A = variable attenuator, M = mirror, L = focusing lens, SM = step motor, DG = delay generator, TMP = turbomolecular pump, PC = computer.

## 2.2 Instrumentation for pulsed laser deposition experiments

In the present thesis, two different pulsed laser deposition experiments are described, being the main difference the duration of the ablation laser pulses used for ablation of the targets.

### 2.2.1 Nanosecond pulsed laser deposition

Pulsed laser deposition of $B_4C$ in the nanosecond laser ablation regime was carried out under vacuum and in inert gas atmospheres. A schematic view of the set-up is depicted in figure 2.9. Related additional information can be found in [3, 4, 6].

#### 2.2.1.1 Laser systems

Two laser systems were used for ablation of the $B_4C$ targets. Ablation at 1064 nm was performed with the same Spectra Physics Nd:YAG laser used in LHG experiments. Ablation at 266 nm was performed with a Quantel Brilliant B Q-switched Nd:YAG laser. Beams of both wavelengths were focused by means of a quartz $f$ = 17 cm focal length lens

resulting in a typical spot diameter of ~800 µm on the target surface. See table 2.1 and description in page 39 for more details on the laser systems.

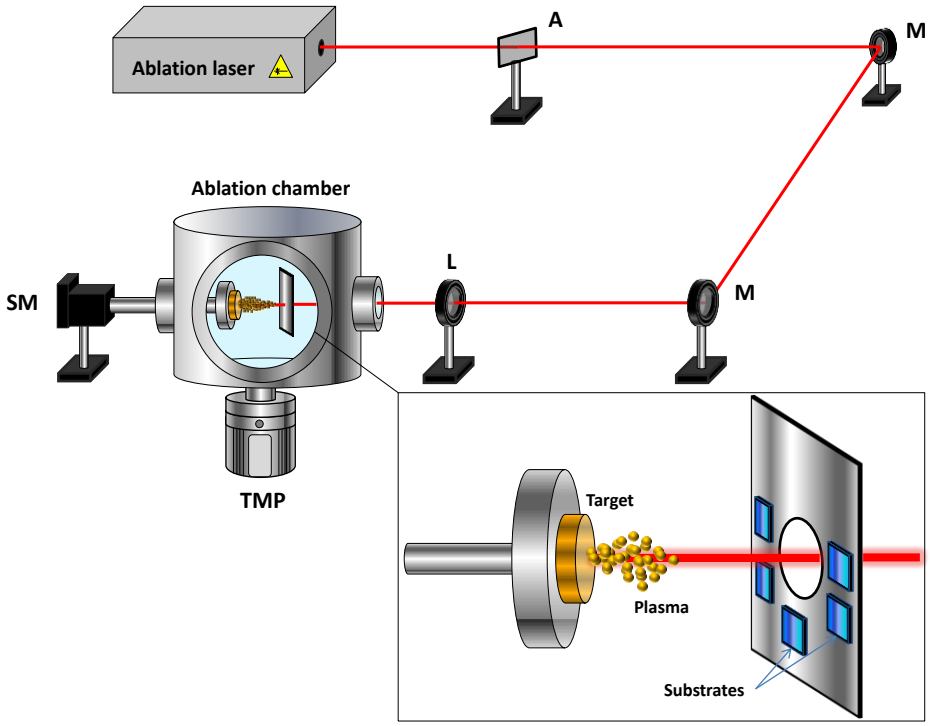


Figure 2.9. Scheme of the experimental set-up for nanosecond laser ablation and deposition. Signs in the figure correspond to: A = variable attenuator, M = mirror, L = focusing lens, SM = step motor, TMP = turbomolecular pump. The inset shows a detailed view of the ablation target, the expanding plasma and the holder accommodating several substrates.

### 2.2.1.2 Pulsed laser deposition chamber

The same vacuum chamber and target rotating holder described in the LHG (section 2.1.2) section of this manuscript were used in nanosecond ablation PLD experiments. Substrates were placed on a specially designed holder featuring an aperture through which the ablation laser beam can propagate, allowing the ablation of the target at normal incidence. This holder, and hence the substrates, were placed at 4 cm distance from the target surface. A scheme of this arrangement can be seen in the inset of figure 2.9. Deposition was performed at room temperature.

Experiments were carried out in low vacuum achieved by pumping out the chamber with the rotary pump down to about $10^{-2}$ mbar and under improved vacuum conditions by using the combination of a rotary and a turbomolecular pumps down to ~$10^{-5}$ mbar.

## 2.2.2 Femtosecond pulsed laser deposition

PLD experiments in Co/ZnS targets were performed using double pulse femtosecond ablation in the CLUR laboratory of the UCM.

Double pulse femtosecond ablation and deposition required a more sophisticated set-up than that used in nanosecond ablation PLD experiments. In the following section a detailed description of the laser system, optics and PLD chamber will be provided. Figure 2.10 depicts a general scheme of the set-up.

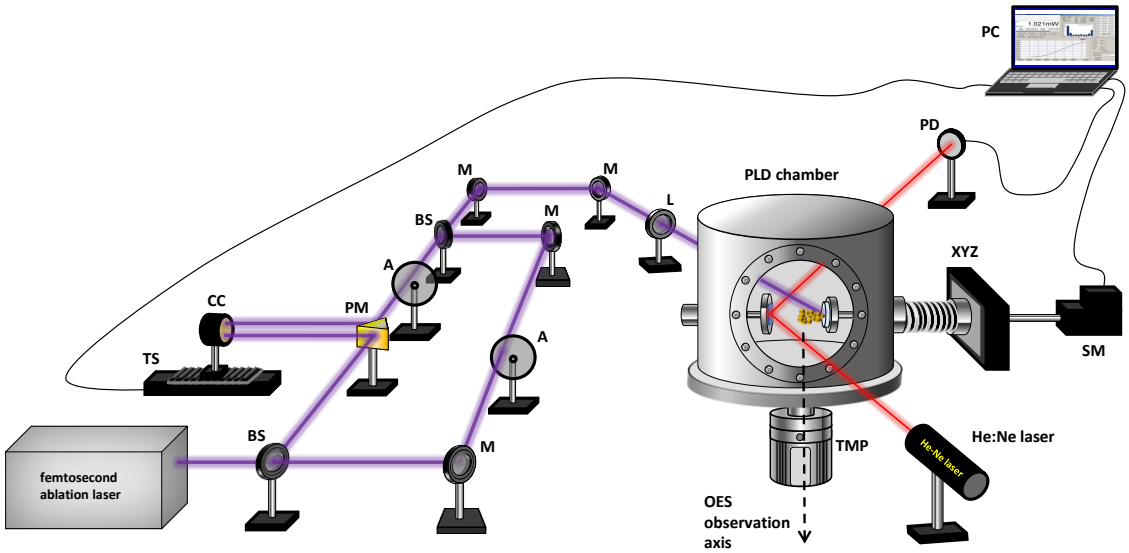


Figure 2.10 General schematic view of the femtosecond double pulse PLD experimental set-up. Signs in the figure correspond to: BS = beam splitter, M = mirror, A = variable attenuator, TS = translation stage, CC = corner cube, PM = prism mirror, L = focusing lens, PD = photodiode, XYZ = 3D positioning system, SM = step motor, TMP = turbomolecular pump, PC = computer. Optical emission spectroscopy analysis of the plasma plume was performed at the indicated observation axis.

### 2.2.2.1 Femtosecond laser system

Ti:Sapphire lasers, emitting at a wavelength around 800 nm, are nowadays the workhorse of femtosecond laser technology. Sapphire crystals ($Al_2O_3$) doped with $Ti^{3+}$ ions meet the desired mechanical, thermal and optical properties needed to be an ideal active medium for efficient generation of ultrashort laser pulses. Among these properties the operation simplicity offered by a solid state laser is an important advantage. Moreover, due to the

high thermal conductivity of the host sapphire crystal, the heat produced in the pumping stage can dissipate efficiently. Another advantage of Ti:Sapphire crystals resides in their absorption range, in the blue-green region, which makes it possible to pump them efficiently at the wavelengths of common powerful solid state nanosecond lasers such as frequency doubled Nd:YAG or Nd:$VO_4$. But the most important feature, crucial to produce ultrashort laser pulses, is a spectrally broad laser emission, which can support a short laser pulse. This is the case of the transition between the electronic ground state $^2T_g$ to the excited electronic state $^2E_g$ of the $Ti^{3+}$ ion in the sapphire matrix, responsible for the laser emission, which is broadened due to the coupling of the electronic energy levels of the $Ti^{3+}$ ions with the lattice phonons. This broad bandwidth makes Ti:Sapphire lasers widely tunable (from 660 to 1180 nm) with maximum emission intensity centered at around 800 nm and pulse durations that can be in the range of hundreds to few femtoseconds.

In the following, the basics of operation of the Ti:Sapphire laser system used for PLD experiments will be briefly described. Figure 2.11 shows a scheme of the laser system components.

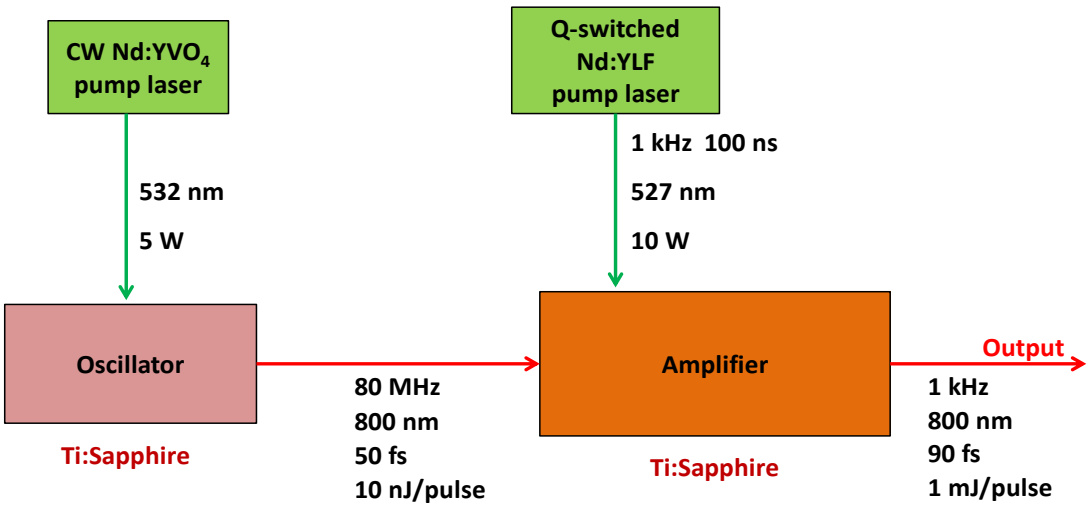


Figure 2.11 Scheme of the femtosecond laser system used in double pulse PLD experiments.

The system is constituted by a Ti:Sapphire oscillator (Spectra Physics Tsunami) operating in the mode locking[4] regime [7] and pumped by a CW frequency doubled Nd:$YVO_4$ laser (Spectra Physics Millennia). The output of the oscillator are 800 nm pulses of around 50 fs

[4] Actively mode locked with an acousto-optic modulator.

FWHM at a repetition rate of 80 MHz, with pulse energy of *ca*. 10 nJ and average power of around 0.8 W.

In the second module of this system (Spectra Physics Spitfire), the amplification of these pulses is performed by the Chirped Pulse Amplification technique (CPA) [8]. The amplification process consists of three consecutive steps: stretching, amplification and compression of the pulse.

In the first step, the 50 fs pulses are stretched to approximately 500 ps by using a set of diffraction gratings, delaying the higher frequencies with respect to the lower ones. The chirped 500 ps pulses are injected as seeds in a regenerative amplification stage, in which a resonant cavity with a second Ti:Sapphire crystal, pumped by a frequency doubled Q-Switched Nd:YLF laser (Spectra Physics Evolution) emitting at 527 nm, is used. By pumping this second active medium, a situation of population inversion in the active medium is achieved. Synchronously, one pulse out of $1 \times 10^5$ is picked using a Pockels cell as an optical switch. This allows the pulse to resonate in the cavity passing through the active medium several times (∼20) until the maximum gain is reached, then a second Pockels cell combined with a polarizer serves as an optical shutter to extract the pulse out of the cavity.

The last stage of the CPA process is the compression of the amplified pulse, which is essentially the reverse process of stretching before the regenerative amplification step.

The output of the system are pulses with an approximate duration of 90 fs at 1 kHz repetition rate (which can be reduced with the pockels cells), with a central wavelength around 800 nm and maximum pulse energy typically around 1 mJ. The diameter of the output beam is about 6 mm. The temporal characterization of the output femtosecond pulses was performed with a single shot second harmonic autocorrelator (Positive Light SSA).

#### 2.2.2.2 Optical layout for double pulse laser ablation

The main goal of these series of PLD experiments is to explore differences in the composition of deposits prepared by ablation with two consecutive femtosecond pulses separated in time by an adjustable delay.

Sequences of two pulses were generated via a modified Mach-Zehnder interferometer shown in figure 2.10. This optical arrangement consists of a first 50/50 beam splitter (BS) where the output beam coming from the laser is separated into two arms. One of the

arms goes through a delay line composed by a gold coated right-angled prism mirror (PM) and a gold coated corner cube (CC). The latter is mounted on a motorized linear stage (Newport, UTS150PP). By translating the corner cube, the optical length of this arm can be varied with respect to the other arm of the interferometer, therefore introducing a controllable delay between both pulses. The use of the corner cube ensures that the input and output beams are perfectly parallel. The beam coming out of the corner cube is reflected in the other face of the prism mirror towards a second 50/50 beam splitter where it is now recombined with the beam coming from the other arm of the interferometer. With this optical arrangement, the interpulse delay can be varied from 0 to 300 ps with a maximum temporal resolution of 1 fs. Variable neutral density reflective filters (A) served to control the energy of each pulse individually. The recombined beam, which is constituted of the two spatially overlapped arms, was now directed towards the PLD chamber and focused onto the target surface by a $f$ = 30 cm focal length lens (L). The incidence angle is estimated to be around 55° with respect to the normal of the target surface.

The beam profile was studied on focus and at several distances in front and beyond the focal plane with a Spiricon Sp630U camera beam profiler. The beams retained near Gaussian profiles, being the beam waist at the focus (radius at $1/e^2$) of 30 ± 2 μm.

At the beginning of each experiment the spatial overlap of both beams was checked in the far field and on focus using a CMOS camera and a set of suitable neutral density filters to avoid damage of the sensor. Images of the non-overlapped and overlapped foci acquired with the camera can be seen in figure 2.12a and 2.12b respectively.

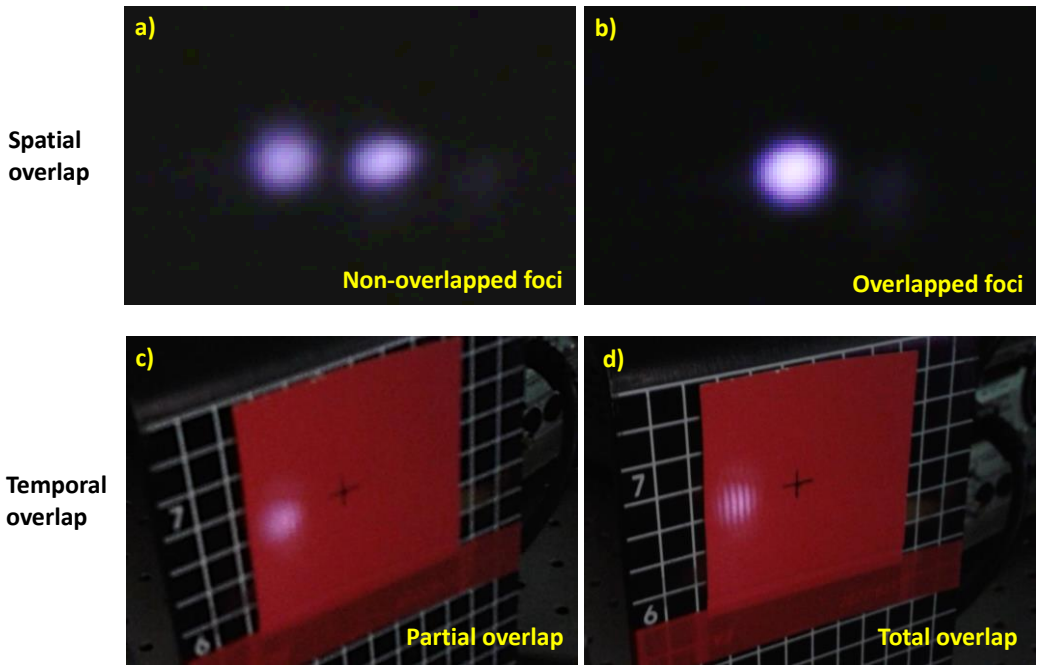


Figure 2.12 Images showing the spatially non-overlapped (a) and overlapped (b) foci of the beams corresponding to the two interferometer arms. In (c) a photograph of the partially overlapped pulses is shown and the characteristic diffraction fringes start to appear. In (d) the diffraction fringes arising when both pulses are temporally overlapped are clearly seen.

In the same way, the characteristic diffraction fringes arising when two pulses are temporally overlapped served to find the reference position of the translation stage corresponding to zero delay between both pulses. This diffraction pattern can be clearly observed in figure 2.12d. In the following, the region of ~200 fs width where there is total or partial overlap between both pulses will be referred as "zero delay" region.

### 2.2.2.3 PLD chamber

PLD was conducted under vacuum conditions ($10^{-5}$ mbar or better) while the substrates were kept at room temperature. The vacuum chamber used in the experiments is equipped with two holders that can be seen in figure 2.13, one for the substrates (figure 2.13a) and a second one for the target (figures 2.13b and 2.13c). The Co/ZnS pellet was mounted on the target holder with the help of a centring tool which was removed for the experiment in order to place the pellet always in the same initial position with respect to the ablation spot. The substrate holder is designed to accommodate several silicon substrates and one transmission electron microscopy (TEM) grid. The Si substrates were

fixed with double sided scotch tape. The target-substrate distance was fixed at 4 cm in all experiments.

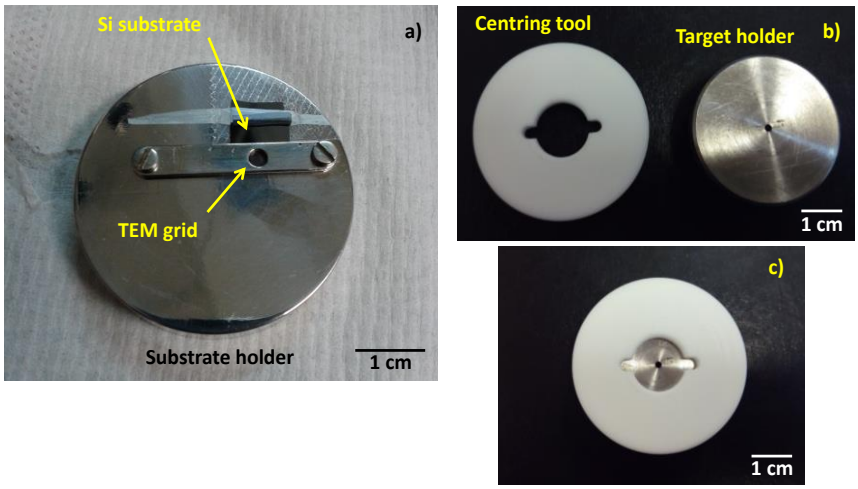


Figure 2.13 Images of the holders used in the PLD chamber to fix the substrates (a) and targets (b).

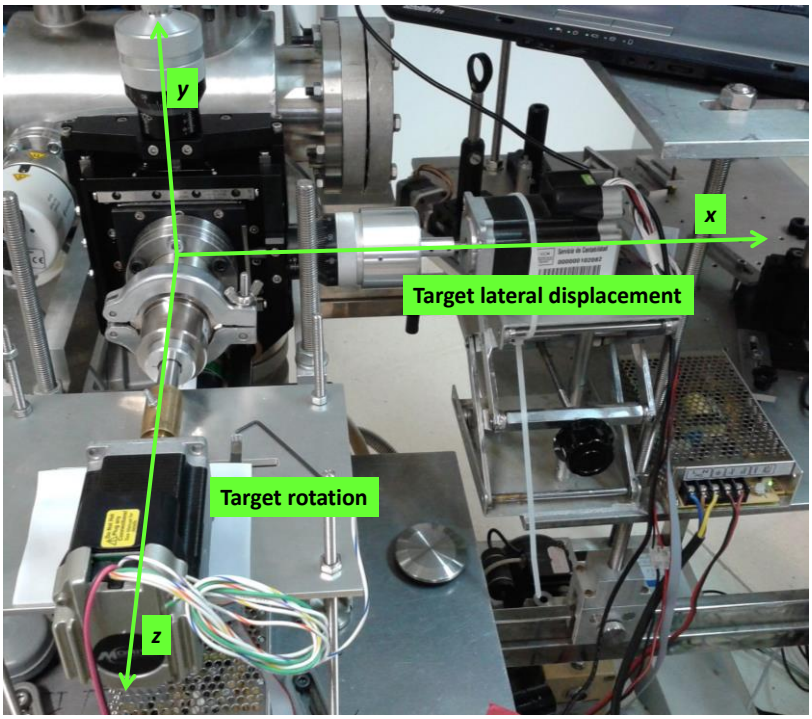


Figure 2.14 Photograph of the motorized 3D target displacement system.

One of the limitations of the experiment is the brittle nature of the Co/ZnS pellets. This fact makes critical its manipulation and the ablation conditions. In order to avoid as far as possible excessive cratering and in order to expose a fresh surface to the ablation beam after a certain number of laser shots, the ablation point must be moved during the deposition process. To overcome this limitation, a motorized XYZ positioning system was implemented. This system allows displacement of the target with respect to the focal point of the ablation beam without breaking the vacuum inside the PLD chamber. Two step motors connected to a computer and controlled by a LabVIEW based programme rotated and moved the target simultaneously. The outcome of these combined movements was a spiral ablation pattern. A picture of this positioning system can be seen in figure 2.14.

#### 2.2.2.4 Diagnostic of the pulsed laser deposition process based on *in situ* reflectance measurements

In order to obtain information about the deposition process, an *in situ* diagnostic method based on measurements of the reflectance changes on the Si substrate as the deposited layer growths, was implemented. Figure 2.15 depicts a scheme of the set-up. To that purpose, a He-Ne laser beam emitting at 633 nm was mildly focused on the Si substrate surface with an incidence angle of about 80°. During the deposition process, the power of the reflected beam after averaging 50 measurements was recorded every second (that is, every 1000 laser shots or double pulse sequences at 1 kHz repetition rate) with the help of a photodiode power sensor (Thorlabs S120C) connected to a computer.

These measurements provided information about the deposition rate and an estimation of the deposit thickness. More information about this reflectance measurement can be found in Chapter 4, page 178.

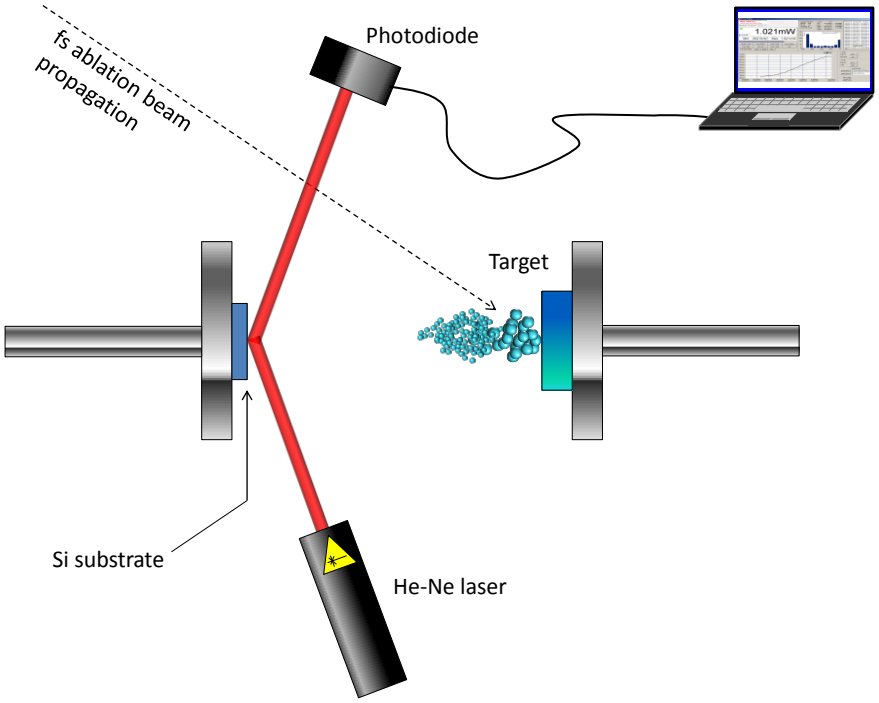


Figure 2.15 Schematic top view of the reflectance measurement system for *in situ* diagnosis of the pulsed laser deposition process.

## 2.2.3 Characterization of deposits

As mentioned, deposits prepared by PLD were characterized in terms of morphology and composition using different techniques, including SEM, TEM, EDX, XRD, XPS, Raman, FIB-SIMS and AFM. These are nowadays standard techniques, therefore a detailed description of these can be found elsewhere; only a brief account of each one is given below.

### Scanning Electron Microscopy (SEM)

Scanning Electron Microscopy [9] is one of the most important techniques for morphological characterization of samples. It allows obtaining topographic images with high spatial resolution (down to few nanometres or even higher). Large depth of field and great magnification are other powerful features of SEM. A large depth of field allows obtaining images with a three-dimensional appearance, while high magnification allows exploring small features, well beyond the optical microscopy capabilities. The principle of operation of SEM is based on the interaction of energetic electrons with the atoms of the sample. This interaction results in the emission of secondary or backscattered electrons

(among other types of emissions like X-rays or Auger electrons), which are commonly the two types of signal used to produce the images. The primary electrons are generated and accelerated by an electron gun in the form of a beam, which is focused onto the sample surface by electron lenses. By deflecting the electron beam, the sample surface is scanned and the variation of the signal of secondary or backscattered electrons arising from the sample is recorded to form the image of the surface.

SEM images shown in this thesis were acquired with two different SEM set-ups, a high-resolution FE-SEM Hitachi SU8000 and an environmental ESEM Philips XL30 located at the Instituto de Ciencia y Tecnología de Polímeros, ICTP-CSIC in Madrid.

### Transmission Electron Microscopy (TEM)

As in SEM, in Transmission Electron Microscopy [10] is the interaction of primary electrons with the specimen what provides the different signals suitable to form the images. In this case, primary electrons propagate through the sample, interacting with its atoms via elastic or inelastic scattering. The images are obtained after the analysis of the contrast (in amplitude or phase) of the transmitted electron wave. For that reason, samples have to be ultrathin in order to allow transmission of the impinging electrons. This requires in some cases previous preparation of the sample by, for instance, mechanical and/or ion etching. TEM can be operated in different modes, retrieving different types of information from the transmitted electron wave, bright field operation to obtain topographic images or electron diffraction to obtain diffraction patterns which reveal information about the crystallinity of the sample.

In this work, some deposits were prepared directly on copper TEM support mesh grids. These samples were obtained in a way that the deposited layers were thin enough to be analyzed by this technique, thus no further preparation was required. The samples were analyzed at the Centro Nacional de Microscopía Electrónica (CNME) in Madrid with a JEOL JEM 2100 microscope operating at 200 kV with a point resolution of 0.25 nm. Images were taken to assess the size of the deposited particles, and to obtain information about their crystallinity.

### X-ray Energy Dispersive Spectroscopy (XEDX)

Both SEM and TEM techniques can be coupled to X-ray Energy Dispersive Spectroscopy (also frequently abbreviated as EDS or EDX) [11]. As mentioned, one of the outcomes of the interaction between the primary electrons of a SEM or TEM apparatus and the sample is the emission of X-rays (consequence of inelastic scattering). The XEDX

technique provides the elemental chemical composition of the sample through the detection of the X-ray emission. In simple terms, when a high-energy electron from the microscope electron gun interacts with one atom of the sample, there is a probability of one electron being removed from an inner shell, leaving the atom in an excited state. To compensate for the excess of energy, one electron from an outer shell can "fall" into the hole left by the ejected electron and the excess of energy can be released in form of an X-ray photon (it can be also emitted as an Auger electron). As the energy difference between the shells is fixed (transitions between K, L or M shells are typically detected in XEDX) and it is characteristic for each atom, the X-rays will have well-defined element-specific energy. XEDX provides qualitative and quantitative analysis of the solid samples by analysing the peak energies and areas respectively.

In this work, deposits prepared on TEM grids were analysed by XEDX in an Oxford Inca system coupled to the aforementioned TEM microscope.

### Atomic Force Microscopy (AFM)

Atomic Force Microscopy [11] is an imaging technique based on the interaction of the sample surface with a very sharp tip mounted on a cantilever. The sample surface is scanned with the tip, revealing the topography with very high resolution (up to few nanometres). The principle of operation of an atomic force microscope is based on the measurement of the cantilever deflection under the interaction forces between the tip and the surface. Depending on the operation mode, these include mechanical contact, van der Waals, magnetic forces etc. Usually, the sample is placed on a precise piezoelectric scanner, in order to move it under the tip. AFM measurements can be performed in different modes. In "contact" mode, the tip is in physical contact with the sample surface. As the sample is moved under the tip, higher or deeper areas cause a vertical deflection of the cantilever. These height variations can be recorded directly using a diode laser aimed at the cantilever and the reflected beam is detected in a position sensitive device. More commonly, another procedure is employed in which the deflection setpoint is fixed, *i.e.* a constant force between tip and the sample. The system generates a feedback to keep the deflection constant, thus causing a vertical deflection on the cantilever. In "tapping" mode, the cantilever oscillates at a certain constant frequency being in intermittent contact with the sample surface. The amplitude of the cantilever oscillation varies as the tip scans the surface and the system feedback keeps it constant, thus causing a vertical deflection of the cantilever. These variations are used to form the image. In the "non-contact" mode the tip is kept oscillating at a certain distance

from the surface, and the non-contact long-range forces, *e.g.* van der Waals, decrease the oscillation frequency. This decrease combined with the feedback loop system maintains a constant oscillation frequency by adjusting the distance between tip and sample.

In this work AFM was used mainly to measure the thickness of the deposited layer obtained in PLD experiments. Measurements were carried out in the laboratories of the Soft and Polymeric Matter Group of the Instituto de Estructura de la Materia, IEM-CSIC in Madrid with a Bruker AFM Multimode 8 with Nanoscope V controller under tapping mode with NSG-30 probes (NT-MDT). Analysis was performed with the Nanoscope analysis 1.50 software (Bruker).

### X-ray Diffraction (XRD)

X-ray diffraction [12] is a powerful technique to study the structure of materials at the atomic level. As its name indicates, is based on the diffraction of incident radiation in the X-ray region by the electron cloud of the atoms in the studied material. In this way it is possible to determine their position in the material structure, and therefore assess the crystallinity of the sample.

The crystallinity of deposits obtained in this thesis by PLD of boron carbide was studied by XRD without further preparation (thin layers grown onto silicon substrates). The characterization was performed with a XRD (PANalytical XPert PRO MRD) using Cu Kα (1.54 Å) equipment using radiation in the θ/2θ configuration located at the Instituto de Ciencias Agrarias ICA-CSIC in Madrid. The study was complemented with XRD measurements at grazing incidence angle. These were performed with a Philips XPert diffractometer using Cu Kα (1.54 Å) radiation in the θ/2θ configuration located at the Centro Nacional de Microscopía Electrónica in Madrid.

### X-ray Photoelectron Spectroscopy (XPS)

X-ray photoelectron spectroscopy [13] is a surface analysis technique able to identify and quantify the elemental composition of the sample and reveal the chemical environment of the respective elements. The physical principle of XPS is the interaction of incident X-ray photons with the atoms in the sample material resulting in the emission of electrons (photoelectrons). The kinetic energy of these electrons is related to their binding energy and this magnitude is element and environmental specific. The interaction between the X-rays and the material takes place in the first 10 nm, this being the reason why XPS is considered a surface analysis technique.

XPS was employed in this work to perform analysis of deposits of $B_4C$ using a homemade spectrometer at the laboratories of Surface Analysis and Mössbauer Spectroscopy (SURFMOSS) group of IQFR-CSIC. This equipment consisted in a vacuum chamber pumped down to $10^{-9}$ mbar, coupled to a Leybold LHS-10XPS spectrometer using Mg Kα radiation (130 W).

### Raman spectroscopy

Raman spectroscopy [14] is a well-established analytical technique which allows for structural and compositional analysis of solid, liquid or gas samples. Its basic principle is the detection of scattered photons resulting from the interaction of an incident monochromatic radiation with the matter. Different scattering processes take place depending on the transitions involved. In molecules, the interaction with the incident radiation, results in the generation of short-lived "virtual states" which constitute the final state of the transitions involved in the scattering process. For this reason, Raman signals are normally very low, while Rayleigh scattering is the most intense process as it involves transitions from and to the same energy level (the ground or excited states). Therefore, scattered photons have the same wavelength than the excitation radiation. When the energy levels involved in the process correspond to vibrational excited states, the Raman scattering is either known as Stokes or anti-Stokes. In Stokes scattering, the transition departs from the ground state and ends in a vibrational excited state, thus the scattered photons have lower energy than those of the incident radiation. In anti-Stokes scattering the transition departs from a vibrational excited state and ends in the ground state, resulting in higher energy photons. At room temperature, the Stokes process is more probable as in these conditions population is mainly in the ground state. Raman spectra are obtained as a function of the Raman shift in $cm^{-1}$ units. This shift is the energy difference between the scattered and the excitation photons. The shift of the Raman bands observed in the spectra corresponds to transitions associated to vibrational modes of the molecule and therefore is characteristic for each species.

Analysis of deposits prepared by PLD of $B_4C$ was performed at the IEM-CSIC with a Raman spectrophotometer Renishaw inVia coupled to a Leica microscope. Irradiation of the *as prepared* samples was performed with a doubled Nd:YAG laser emitting at 532 nm with a maximum output power of 100 mW. The maximum lateral resolution of this equipment is around 1 μm.

#### Focused ion beam-secondary ion mass spectrometry (FIB-SIMS)

The FIB-SIMS [15, 16] technique is a type of mass spectrometry in which a focused ion beam serves to etch and ionize material of the sample. These etched ions are the species characterized in the mass spectrometer, hence the term “secondary ion” in contrast with the primary ions of the focused beam. One of the main advantages of FIB-SIMS is the high lateral resolution of the analyses. This advantage is provided by the FIB beam size that can be adjusted down to only few nanometres.

In this thesis, FIB-SIMS served to etch and analyse the micrometric-size features obtained by PLD of $B_4C$. Experiments were carried out at the Department of Materials of Imperial College London with a FEI FIB200 SIMS instrument. For morphology inspection, a high dose of the Ga ion beam, focused down to 7 nm, was used in order to etch the micrometric-size structures. For imaging purposes defocussing of the beam allowed further morphological characterization by SEM imaging.

### 2.2.4 Plasma characterization in pulsed laser deposition experiments

Laser ablation plasmas used in PLD experiments were characterized by time-of-flight mass spectrometry and optical emission spectroscopy. Time-of-flight mass spectrometry provides information about the ion content of the plasma. Optical emission spectroscopy is used to analyse its spontaneous emission.

#### 2.2.4.1 Time-of-flight mass spectrometry

The double pulse femtosecond ablation dynamics of Co/ZnS targets containing 2 % of Co was studied by analysing the plasma composition by time-of-flight mass spectrometry. The following section gives a detailed description of the experimental set-up used for this purpose.

#### Laser systems

Femtosecond ablation of Co/ZnS targets was performed using the laser system described in section 2.2.2.1, page 51. In this case, due to the limited response of the pulsed ion extraction mode used in TOF-MS experiments, the laser repetition rate was reduced from 1 kHz to 50 Hz.

## Reflectron time-of-flight mass spectrometer

The positive ion content of the Co/ZnS ablation plasma was analyzed with a commercial reflectron-type time-of-flight mass spectrometer (RETOF) from Jordan Products, model RETOF-MS D-850, located at the CLUR-UCM laboratories in Madrid. A scheme of this apparatus is shown in figure 2.16.

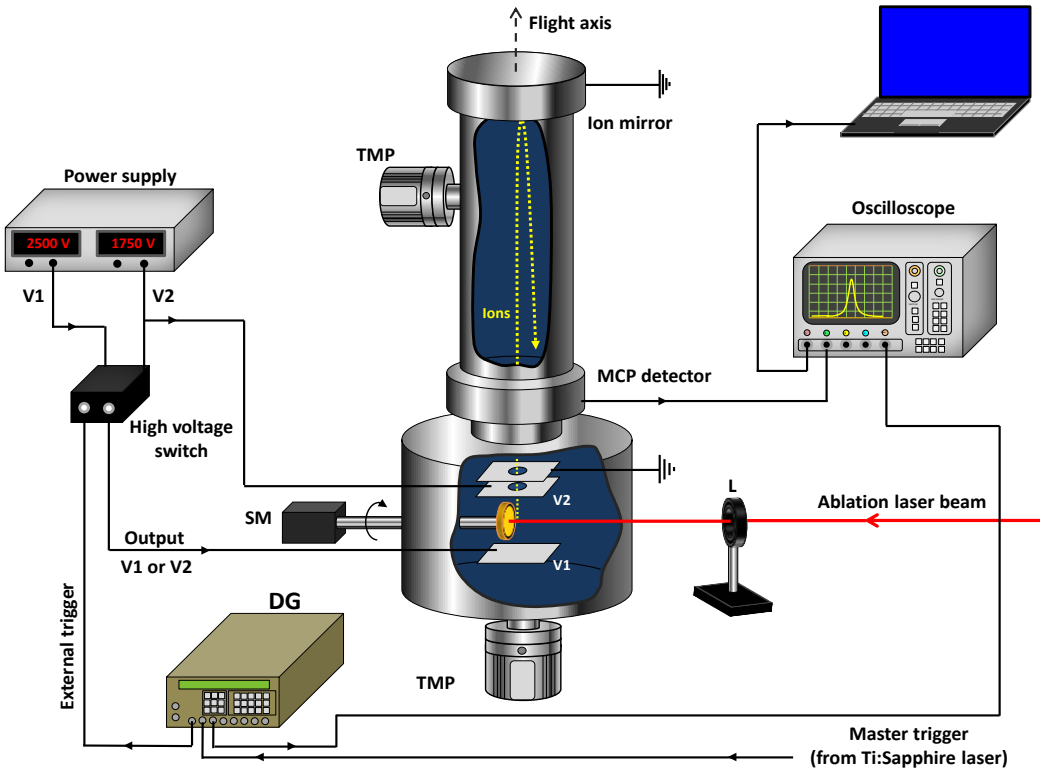


Figure 2.16 Scheme of the reflectron time-of-flight mass spectrometer used for the analysis of the Co/ZnS plasma ion content. The different components are labelled as: L = focusing lens, SM = step motor, TMP = turbomolecular pump, DG = delay generator.

Sequences of double pulses were generated using the optical arrangement (modified Mach-Zehnder interferometer) described previously (see figure 2.10 and description in page 53). Ablation of the Co/ZnS targets was performed under vacuum ($10^{-6}$ mbar) at normal incidence. The output recombined beam of the interferometer was focused onto the target surface with a $f$ = 30 cm focal length lens forming the focal point at 6-7 mm in front of the target surface. These focusing conditions resulted in a beam radius of 70-80 µm onto the target surface.

The targets were fixed at the end of an electrically isolated rotating holder placed between the repeller and the extractor plates of the spectrometer. In this configuration, the target surface is parallel to the time-of-flight axis. Ions produced in the ablation process were deflected perpendicularly to the plume expansion axis by an electric field generated between the two electrodes towards a field-free drift region, pumped by a turbomolecular pump down to a base pressure of about $10^{-6}$ mbar. The target holder allows displacement of the target with respect to the time of flight axis.

Ion extraction and acceleration were performed in pulsed mode using a high-voltage switch (Behlke GHTS 60). The device allows keeping the repeller and extractor plates at an identical voltage V2 for a selected time, after which, an external signal triggers the high-voltage switch, shifting the repeller plate voltage to a value V1, higher than V2. The electric field due to the bias voltage between repeller and extractor plates triggers the ions deflection and acceleration along the flight axis of the spectrometer. In this way, some control of the ion extraction conditions can be achieved by optimizing the time delay of the trigger signal with respect to the ablation pulse. This delay was found to be optimum at 500 ns after the ablation event. The total acceleration voltage was 2500 V.

The ions produced upon ablation were detected by a set of microchannel plates (MCP) located at the opposite side of the ion mirror and the signal was recorded in a digital oscilloscope Tektronix TDS 524A connected to a PC. The latter displayed an “on the fly” view of the mass spectra, averaged over 100 double pulse sequences, obtained at each delay and stored the spectra and time data in matrix form for further processing.

Synchronization of the experiment was controlled by a delay generation (Stanford SRS DG-535). As master trigger the signal of the Pockels cells in the laser amplifier was used as input signal for the delay generator which in turn triggers the oscilloscope and the high voltage switch.

#### 2.2.4.2 Optical Emission Spectroscopy

Nanosecond laser ablation plumes of boron carbide were studied by OES using the set-up described in section 2.1.4, page 48.

In femtosecond ablation experiments, plasma characterization was performed by studying the spontaneous emission from the plumes generated from Co/ZnS targets under the same conditions used in PLD experiments. For that purpose, the detection system, composed by a Czerny-Turner spectrograph and an ICCD detector, described previously in section 2.1.3.1, page 42, was combined with the femtosecond laser and PLD

chamber described in section 2.2.2. Plasma emission was collected at 90° with respect to the target surface normal (the observation axis is indicated in figure 2.10).

## 2.3 Materials and preparation methods

This section gives a brief account of the properties of materials used as targets to generate the ablation plasmas for LHG and PLD experiments.

### Graphite

Graphite is the most stable allotrope of carbon under standard conditions [17, 18]. Its characteristic crystalline structure consists of stacked parallel monolayers of graphene in which the C atoms are linked together by covalent trigonal $sp^2$ bonds ($\sigma$ bonds) forming a 2D lattice of hexagonal rings. A schematic representation of this structure is shown in figure 2.17. The series of monolayers interact between them through weak van der Waals bonds ($\pi$ bonds), being the interplanar spacing of 0.355 nm.

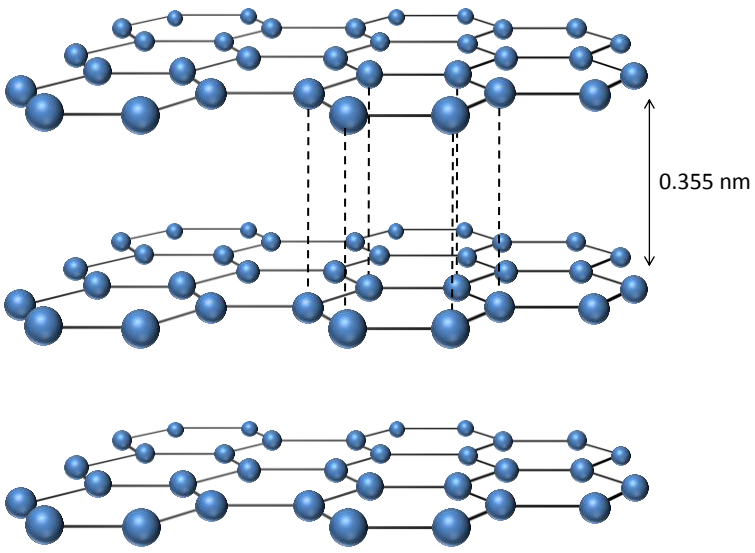


Figure 2.17 Structure of graphite. The blue spheres represent the C atoms forming the hexagonal rings of the graphene layers.

This description represents the ideal structure of graphite; however, there are many variations of this theoretical structure associated to the presence of defects in the lattice that give rise to the various polycrystalline forms of graphite found in natural and synthetic materials.

The anisotropy of graphite implies that some properties vary depending on the measurement direction. This is specially important in the case of electrical, optical and thermal properties. Attending to its electrical properties, graphite can be considered a semimetal. Due to the aforementioned anisotropy, graphite is a relatively good conductor in the direction parallel to the graphene planes but behaves as an insulator in the perpendicular direction with respect to these planes. Thermal conductivity exhibits a similar dependence with the parallel and perpendicular directions to the graphene planes.

### Boron carbide

Boron carbide [19, 20] is a ceramic material which is commonly named by the stoichiometric formula $B_4C$. However, other stoichiometries have been proposed and the structure of boron carbide still remains under debate, mainly due to the similar response of B and C atoms in crystallographic characterizations [19, 21]. As mentioned in the introduction chapter, boron carbide stands out among other materials for its combination of exceptional properties (see page 18).

This material has a complex crystalline structure, depicted in figure 2.18, which is still under discussion. The structural unit is frequently described in the literature as a rhombohedral unit cell containing 12-atom icosahedra linked by 3-atom linear chains ($B_{12}C_3$). It should be noted that, owing to the aforementioned technical limitations and the discrepancy between theoretical calculations, variations of the most accepted unit cell composed by $B_{11}C$ icosahedra linked by intericosahedral CBC chains are possible. Furthermore, this structure corresponds to the ideal case and in actual structures of synthesized boron carbide, vacancies, free carbon atoms, or other types of defects may play an important role.

Attending to its electronic properties boron carbide is a *p*-type semiconductor with an estimated band gap of 2.09 eV [22], although according to the different electronic structures proposed, lower band gap energies have been also reported [19].

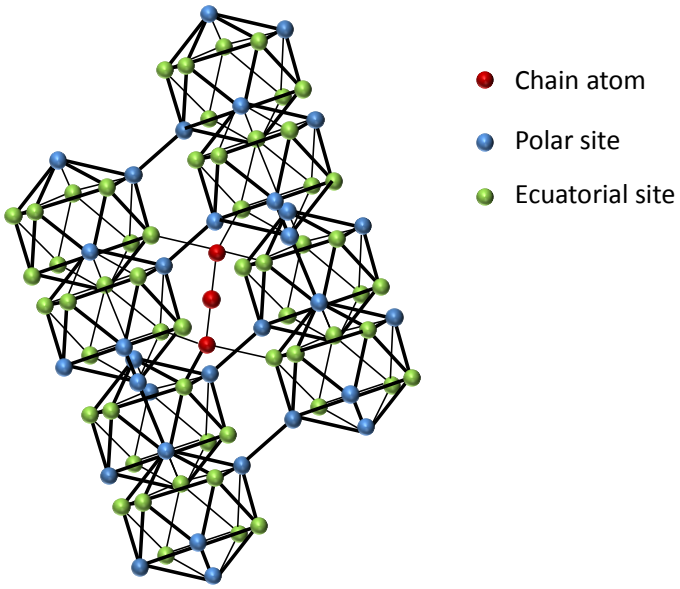


Figure 2.18 Atomic structure of boron carbide. Adapted from [21].

### Zinc sulfide

Zinc sulfide is a semiconductor material with formula ZnS. It exhibits polymorphism, being the most common crystal structures known as *zinc blende* and *wurtzite*. The most stable zinc blende has cubic symmetry, while wurtzite displays a hexagonal structure. Figure 2.19 illustrates the two forms of ZnS.

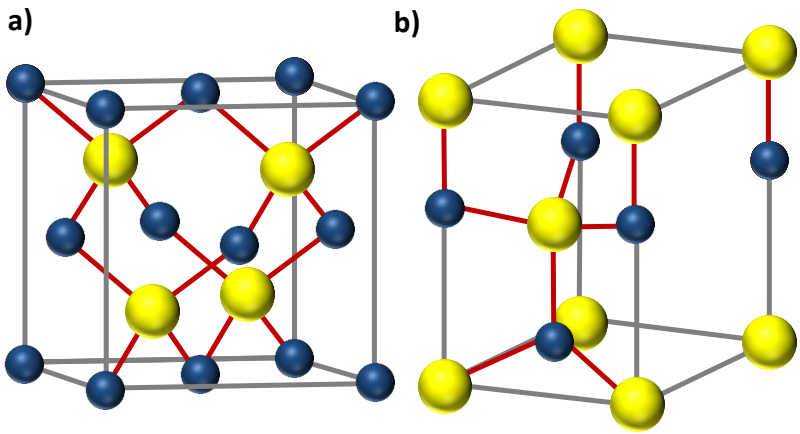


Figure 2.19 Crystalline structures of the most stable forms of zinc sulfide: a) zinc blende and b) wurtzite. The yellow and blue spheres represent the S and the Zn ions respectively.

Attending to its electronic properties, zinc sulfide is a II-VI wide band gap semiconductor with a direct band gap of 3.68 eV for the most stable zinc blende structure and 3.91 eV for the wurtzite structure.

### Cobalt

Cobalt is a transition metal with atomic number 27. The two most stable crystallographic structures are hexagonal close packed and face-centred cubic. Attending to its magnetic properties, cobalt is a ferromagnetic material.

### Ablation targets

Commercial graphite targets with 99.99 % purity were purchased from Tech Supplies LTD. Disks with thickness around 3 mm were cut from a 50 mm length rod of 12.7 mm diameter. No further preparation was performed as the targets exhibited a flat surface after cutting. Only after repetitive experiments, the targets were polished using grinding paper until the flatness of the surface was recovered.

Boron carbide targets were purchased from the same supplier with 99.9 % purity. In this case, the targets were 3 mm thick disks with a diameter of 10 mm. The same grinding procedure used for graphite was applied to eliminate the grooves caused by repetitive ablation.

Zinc sulfide targets were prepared from ZnS powder purchased from Sigma-Aldrich with 99.99 % purity and particle size of 10 µm. Targets were prepared in the form of 13 mm diameter and ~2 mm thick pellets by pressing a fixed amount of the commercial powder under 8000 kg $cm^{-2}$ during 10 minutes in a static press.

Co/ZnS mixed targets were prepared from the same commercial ZnS powder and metallic Co powder purchased from Alfa Aesar Puratronic series, with 99.998 % purity and -22 mesh size. Co/ZnS targets containing 2 % and 10 % of cobalt in weight were prepared in the following way. Fixed amounts of metallic Co and ZnS powders were weighted in an analytical scale, the Co powder was mechanically grinded in an agate mortar (to avoid agglomeration of particles) and then was mixed with the ZnS powder. The resulting mixture was grinded again in order to ensure homogeneity. A fixed amount of the Co/ZnS mixture was transferred to the static press and was pressed following the procedure described above.

### Substrates

In PLD experiments, the material ejected from the ablated targets was deposited on monocrystalline silicon (100) wafers purchased from ACM. The substrates were prepared by cutting pieces of approximately 1 x 1 $cm^2$ out of the commercial silicon wafers. These pieces were submerged in acetone and cleaned for 10 minutes in an ultrasonic bath in order to remove any organic contamination from the surface. Further cleaning in isopropanol was performed following the same procedure. Subsequently, the substrates were dried in air before starting the deposition process.

The material ejected from femtosecond laser ablation of Co/ZnS was simultaneously deposited on Si substrates and 200 mesh copper TEM grids with carbon film (Electron Microscopy Science, LC200-Cu). The latter are suitable substrates for analysing by this technique the particle size, crystallinity and composition of the deposits without the need of any further sample preparation.

## 2.5 References


1. M. Oujja, R. de Nalda, M. López-Arias, R. Torres, J.P. Marangos, M. Castillejo, *$CaF_2$ ablation plumes as a source of CaF molecules for harmonic generation,* Physical Review A, **81** (2010) p. 043841.
2. I. Lopez-Quintas, M. Oujja, M. Sanz, M. Martín, R.A. Ganeev, M. Castillejo, *Low-order harmonic generation in nanosecond laser ablation plasmas of carbon containing materials,* Applied Surface Science, **278** (2013) p. 33.
3. M. López-Arias, PhD Thesis: *Aplicaciones de plumas de ablación de semiconductores en óptica no lineal y síntesis de nuevos materiales*, Departamento de Química Física I, Complutense University, Madrid, 2013.
4. M. Walczak, PhD Thesis: *Deposition of $TiO_2$ nanostructures by short pulse laser ablation*, Departamento de Física de Materiales, Complutense University, Madrid, 2010.
5. M. Oujja, A. Benítez-Cañete, M. Sanz, I. Lopez-Quintas, M. Martín, R. de Nalda, M. Castillejo, *Frequency mixing in boron carbide laser ablation plasmas,* Applied Surface Science, **336** (2015) p. 53.
6. I. Lopez-Quintas, M. Oujja, M. Sanz, A. Benitez-Cañete, R.J. Chater, M.V. Cañamares, J.F. Marco, M. Castillejo, *Micrometric rods grown by nanosecond pulsed laser deposition of boron carbide,* Applied Surface Science, **328** (2015) p. 170.
7. C. Rulliere, *Femtosecond laser pulses*, 2005, Springer.
8. P. Maine, D. Strickland, P. Bado, M. Pessot, G. Mourou, *Generation of ultrahigh peak power pulses by chirped pulse amplification,* IEEE Journal of Quantum Electronics, **24** (1988) p. 398.
9. J. Goldstein, D.E. Newbury, D.C. Joy, C.E. Lyman, P. Echlin, E. Lifshin, L. Sawyer, J.R. Michael, *Scanning Electron Microscopy and X-ray Microanalysis*, 2003, Springer.
10. L. Reimer, *Transmission electron microscopy: physics of image formation and microanalysis*, 2013, Springer.
11. Y. Leng, *Materials Characterization: Introduction to Microscopic and Spectroscopic Methods*, 2013, Wiley.
12. Y. Waseda, E. Matsubara, K. Shinoda, *X-ray Diffraction Crystallography*, 2011, Springer.
13. J.F. Moulder, J. Chastain, *Handbook of X-ray Photoelectron Spectroscopy: A Reference Book of Standard Spectra for Identification and Interpretation of XPS Data*, 1992, Physical Electronics Division, Perkin-Elmer Corporation.
14. E. Smith, G. Dent, *Modern Raman spectroscopy: a practical approach*, 2013, Wiley.
15. L.A. Giannuzzi, F.A. Stevie, *Introduction to focused ion beams*, 2005, Springer.
16. A. Benninghoven, F. Rudenauer, H.W. Werner, *Secondary ion mass spectrometry: basic concepts, instrumental aspects, applications and trends*, 1987, Wiley.
17. H.O. Pierson, *Handbook of Carbon, Graphite, Diamonds and Fullerenes; Processing, Properties and Applications*, 1994, Noyes Publications.
18. D.D.L. Chung, *Review Graphite,* Journal of Materials Science, **37** p. 1475.
19. V. Domnich, S. Reynaud, R.A. Haber, M. Chhowalla, *Boron Carbide: Structure, Properties, and Stability under Stress,* Journal of the American Ceramic Society, **94** (2011) p. 3605.

20. F. Thévenot, *Boron carbide—A comprehensive review,* Journal of the European Ceramic Society, **6** (1990) p. 205.
21. R. Lazzari, N. Vast, J.M. Besson, S. Baroni, A. Dal Corso, *Atomic Structure and Vibrational Properties of Icosahedral $B_4C$ Boron Carbide,* Physical Review Letters, **83** (1999) p. 3230.
22. H. Werheit, H. Binnenbruck, A. Hausen, *Optical properties of boron carbide and comparison with β-rhombohedral boron,* physica status solidi (b), **47** (1971) p. 153.

# Chapter 3

# Harmonic generation in laser ablation plasmas

# 3. Harmonic generation in laser ablation plasmas

This chapter describes low-order harmonic generation experiments using laser ablation plasmas of graphite, boron carbide and zinc sulfide as nonlinear media [1-3].

The fundamental driving radiation is a 1064 nm laser delivering pulses of 18 ns with intensity around $10^{11}$ W cm$^{-2}$, propagating through the plasma plume. The energy dependence of the harmonic signal with the ablation and driving pulse energies, as well as its spatiotemporal behaviour constitute the core of this chapter. Additional characterization of the plasmas was performed by OES.

The spatiotemporal behaviour of the harmonic generation process was studied by probing the plasma plume with the driving beam at different times after the ablation event and at different positions with respect to the expanding plasma plume.

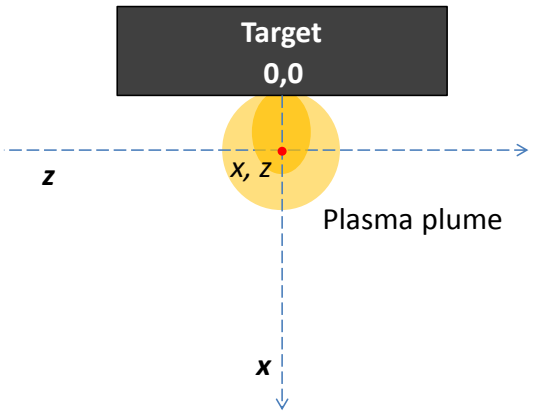


Figure 3.1 Schematic representation of the coordinates system used in harmonic generation experiments in laser ablation plasmas. The *x* axis corresponds to the propagation direction of the ablation laser beam. The *z* axis corresponds to the propagation direction of the harmonics driving beam. The position of the driving beam focus with respect to the plasma plume is described by *x*, *z* coordinates.

Some considerations regarding the spatial study of the harmonic radiation generated using ablation plasmas as nonlinear media must be taken into account. A coordinate system is established in order to define the position of the driving beam focus with respect to the plasma plume. Figure 3.1 depicts a scheme, showing the two axes *x* and *z*,

the target and the plasma plume. The *x* axis coincides with the propagation direction of the ablation laser beam, normal to the target surface. The *z* axis corresponds to the propagation direction of the harmonics driving beam, which is parallel to the target surface. In this way, the position of the driving beam focus with respect to the plasma plume is defined in the experiment by two coordinates *x*, *z*. In this system the origin of coordinates (*x* = 0 mm, *z* = 0 mm) corresponds to the ablation spot.

In the so called "*z*-scan", the plasma plume is explored by focusing the harmonics driving beam at different positions along the *z* axis (parallel to the target surface). A schematic representation of this measurement is shown in figure 3.2.

In a similar way, the plume was scanned by focusing the harmonics driving beam along the *x* axis (normal to the target surface). A schematic representation of the "*x*-scan" is depicted in figure 3.3. It is important to mention that ablation of the target by the driving beam may occur when it is focused at *x* = 0 mm. Due to this experimental limitation, the minimum *x* value achievable is around 0.6 mm.

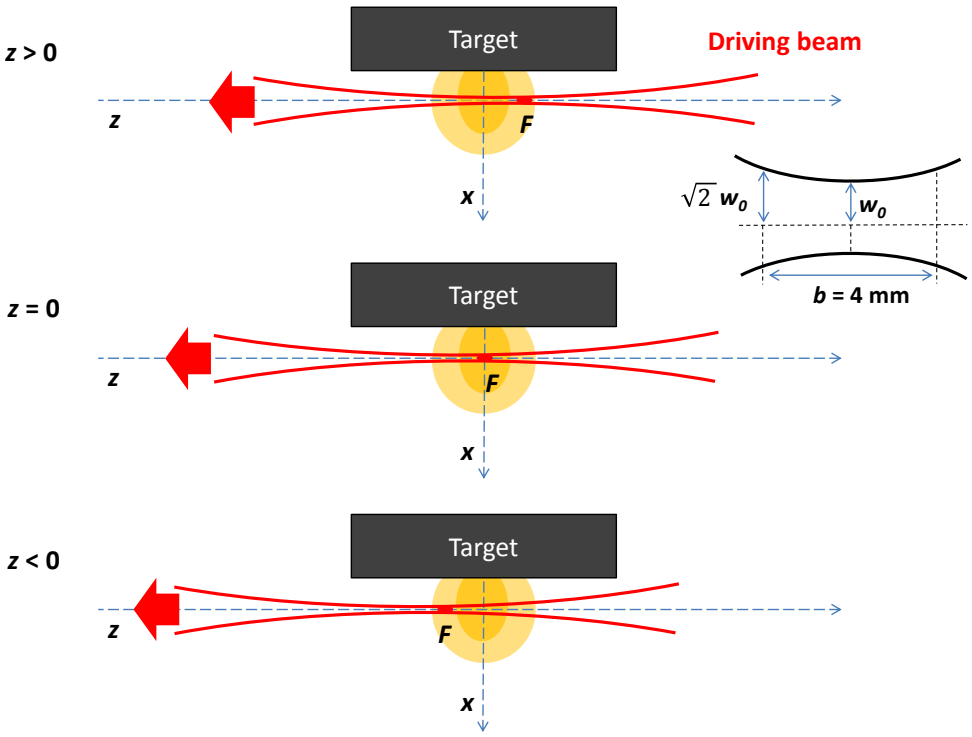


Figure 3.2 Schematic representation of the "*z*-scan" performed across the plasma plume. The focus of the driving beam *F* is moved along the *z* axis. The beam waist $w_0$ and the confocal parameter *b* of the driving beam are estimated in 60 µm and 4 mm respectively. The propagation direction of the driving beam is indicated by the red arrow.

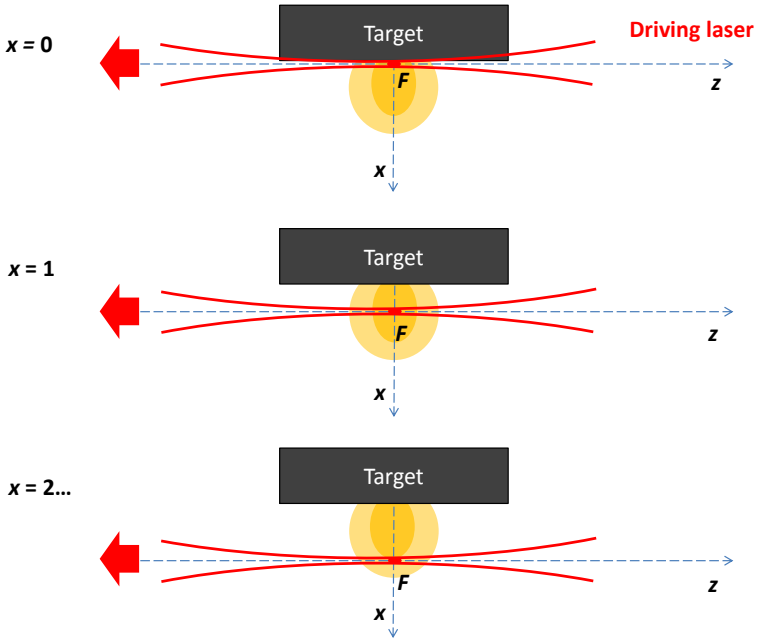


Figure 3.3 Schematic representation of the "*x*-scan" performed along the *x* axis. In it, the focus of the driving beam *F* is moved away from the target surface. The propagation direction of the driving beam is indicated by the red arrow.

## 3.1 Low-order harmonic generation in laser ablation plasmas of carbon containing materials

In this set of experiments, generation of the 3$^{rd}$ and 5$^{th}$ harmonics of the fundamental 1064 nm driving beam, at 355 and 213 nm respectively, was explored systematically in laser ablation plasmas obtained from two carbon containing materials, graphite and boron carbide. The nonlinear processes were studied in two different ambient conditions, vacuum and inert gas atmosphere.

### 3.1.1 Third harmonic generation in graphite ablation plasmas

Third harmonic generation was studied in graphite ablation plasmas obtained under vacuum conditions ($10^{-2}$ mbar) and under inert gas atmosphere (1 mbar of Ne, Kr or Xe). Ablation of the graphite targets was performed at normal incidence using nanosecond laser pulses of 1064 nm.

### Vacuum conditions

An example of the intense narrow peak detected at 355 nm corresponding to the 3rd harmonic (3H) of the 1064 nm fundamental driving beam is shown in figure 3.4. The driving beam, propagating parallel to the target surface, was focused at $x$ = 0.6 mm and $z$ = -2 mm (see figure 3.8). The signal detection was triggered 50 ns before the driving pulse and the signal was acquired in a temporal gate of 100 ns. Each data point in the following plots is the result of accumulating the intensity of 250 spectra.

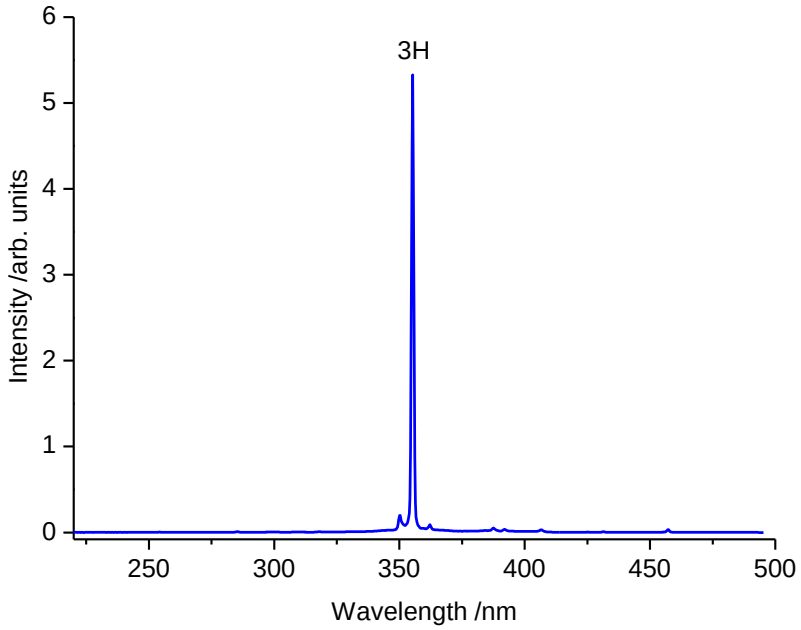


Figure 3.4 Emission at 355 nm corresponding to the 3H of the 1064 nm fundamental radiation generated in a graphite laser ablation plasma. Ablation of graphite targets was performed at 1064 nm under vacuum conditions ($10^{-2}$ mbar) with a fluence of 3 J cm$^{-2}$. The driving beam was focused at $x$ = 0.6 mm and $z$ = -2 mm (see figure 3.8). The delay between the ablation and driving pulses was set at 300 ns.

### Dependence of the third harmonic signal on the ablation pulse energy in graphite plasma

The dependence of the 3H signal with the ablation laser energy is plotted in figure 3.5. The driving beam was focused at $x$ = 0.6 mm and in the central region of the plasma plume ($z$ = 0 mm).

This dependence serves to choose the optimal ablation energy for the HG experiments. It can be observed that the evolution of the 3H signal with the ablation laser energy displays two different regions. Once a threshold is exceeded (~11 mJ) the signal increases

linearly up to a certain energy value. From that point, the 3H signal decreases due to several factors such as phase mismatch and absorption. In the following experiments an energy value of 18 mJ, close to the value which yields the maximum 3H signal, was chosen (unless otherwise specified). This energy results in a fluence of ~3 J $cm^{-2}$ in the applied focusing conditions and taking into account the losses due to the propagation of the ablation laser through the entrance window of the chamber.

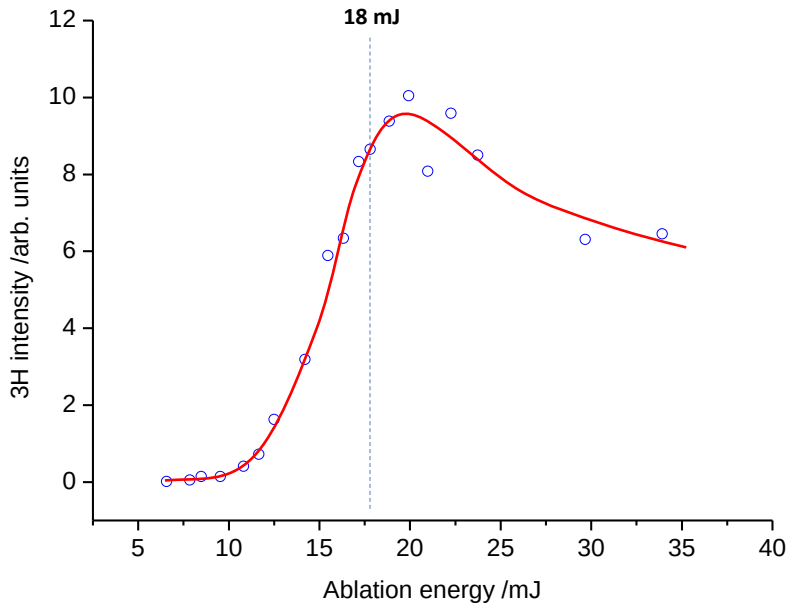


Figure 3.5 Dependence of the 3H signal with the ablation pulse energy obtained in a graphite laser ablation plasma. Ablation was performed at 1064 nm under vacuum conditions ($10^{-2}$ mbar). The 1064 nm driving beam was focused at $x$ = 0.6 mm and $z$ = 0 mm. The delay between the ablation and driving pulses was set to 200 ns. The red line serves as a visual guide.

Once a suitable value for the ablation energy is found, the dependence of the 3H signal with the driving laser pulse energy was studied. Figure 3.6 shows this dependence plotted in log-log form. The driving beam was focused at $x$ = 0.6 mm and $z$ = -2 mm (see figure 3.8).

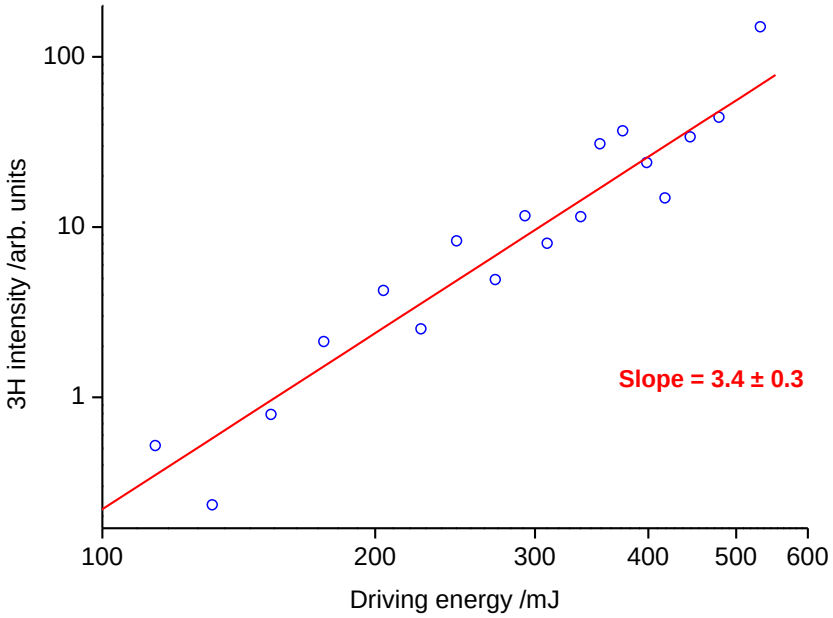


Figure 3.6. Intensity of the 3H signal as a function of the driving pulse energy ploted in log-log scale. The dependence was obtained in a graphite ablation plasma by focusing the 1064 nm harmonics driving beam at $x$ = 0.6 mm and $z$ = -2 mm (see figure 3.8). Ablation was performed at 1064 nm under vacuum conditions ($10^{-2}$ mbar) with a fluence of 3 J cm$^{-2}$. The delay between the ablation and driving pulses was set to 300 ns. The red line is a linear fit of the data.

From the linear fit of the data, a slope of 3.4 ± 0.3 is obtained. This nearly cubic dependence is in agreement with the expected power law in the perturbative regime, where the intensity of the generated $n^{th}$-harmonic order scales with the $n^{th}$ power of the laser intensity, thus confirming the third-order nonlinear nature of the process. In the experiments, the driving laser pulse energy was set to the maximum value achieved by the system of around 550 mJ per pulse. This ensures a good harmonic signal and increases the chances of detecting higher-order harmonics.[5]

### Spatiotemporal study of the 3$^{rd}$ harmonic emission in graphite plasma

The intensity of the 3H signal was measured as a function of the delay between the ablation and driving laser pulses. From the temporal evolution of the nonlinear response of the plasma, information about the relative importance of light and heavy species in the plasma composition can be inferred.

[5] With this experimental set-up it is also possible to observe the second order of the 5$^{th}$ harmonic at $\lambda$ = 213 nm.

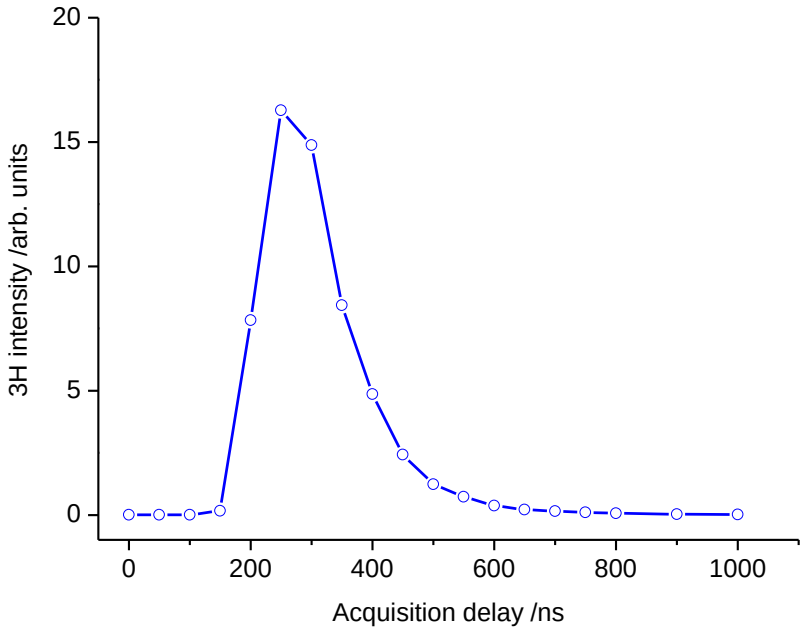


Figure 3.7 Intensity of the 3H signal as a function of the delay between the ablation and driving laser pulses acquired in a graphite plasma. Ablation was performed at 1064 nm under vacuum conditions ($10^{-2}$ mbar). The 1064 nm harmonics driving beam was focused at $x$ = 0.6 mm and $z$ = 2 mm (see figure 3.8).

Figure 3.7 shows an example of a delay scan performed in graphite plasma for an $x$ distance of 0.6 mm with respect to the target surface and focusing the driving laser in the central region of the plasma plume ($z$ = -2 mm in figure 3.8). The 3H signal is plotted against the delay between the ablation and driving pulses in steps of 50 ns. In the figure, a single maximum in the 3H signal evolution is observed, indicating the presence of a population of nonlinear emitters arriving at the explored position at early times. The onset of 3H signal is observed at 150 ns after the firing of the driving laser. The 3H emission is peaked at around 250 ns and then decays to almost zero at a delay time of around 600 ns. The estimated velocity of the peak of this population is around 2400 m $s^{-1}$.

In order to get more information regarding the spatial distribution of the nonlinear species, the 3H signal obtained in graphite plasma plume was scanned focusing the driving beam in different positions along the $x$ and $z$ axes.

Figure 3.8 shows the corresponding $z$-scan obtained in graphite plasma by scanning the plume in 1 mm steps along the $z$ axis at a distance $x$ = 0.6 mm. The direction of the driving beam propagation is indicated in the figure with a red arrow. The onset of 3H signal is detected when the focus of the driving laser approaches the boundaries of the expanding

plasma plume. In this case, the z-scan profile is highly asymmetric. In the direction of the driving beam propagation, a first maximum is observed at $z = 4$ mm, followed by a characteristic dip in the signal close to the central region of the plasma plume ($z = 3$ mm). A second maximum is observed at $z = -2$ mm.

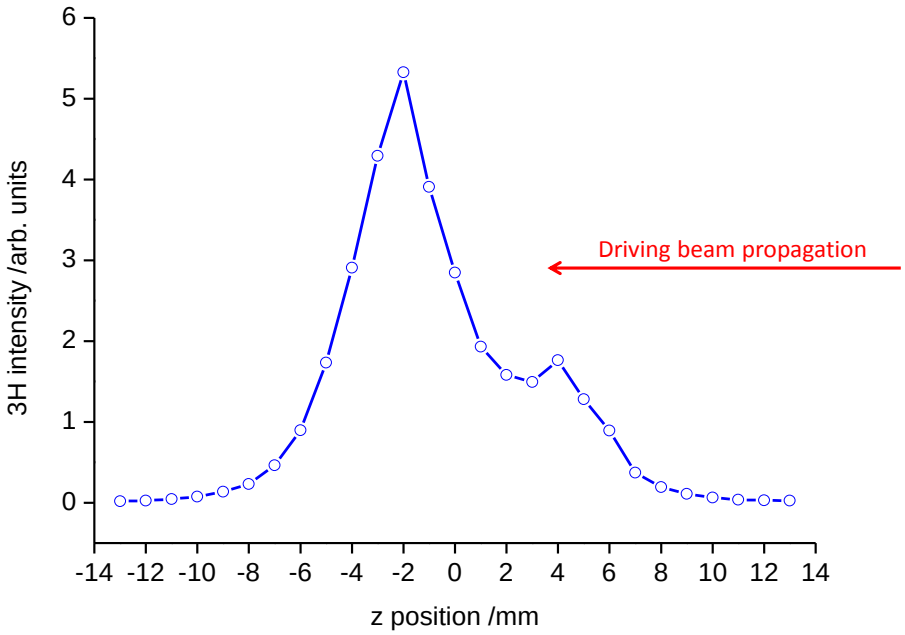


Figure 3.8. Intensity of the 3H signal as a function of the $z$ position of the 1064 nm driving beam focus with respect to the centre of the plasma plume ($z = 0$ mm) obtained in graphite plasma. The distance of the 1064 nm harmonics driving beam was fixed at $x = 0.6$ mm with respect to the target surface. Ablation was performed at 1064 nm with 3 J cm$^{-2}$ under vacuum ($10^{-2}$ mbar). The delay between the ablation and driving pulses was set to 300 ns.

A closer inspection of the atomic emissions detected simultaneously with the 3H signal provides more information about the plasma conditions upon irradiation by the driving beam. Figure 3.9 shows the $z$-scan previously displayed in figure 3.8 and the corresponding emission spectra recorded at $z = -2$ mm (maximum 3H signal) and $z = 3$ mm (minimum 3H signal). In the inset of figure 3.9c the atomic emission lines accompanying the intense 3H peak (which has been cut in the figure), appear superimposed on a relatively intense *Bremsstrahlung* emission. These lines are assigned to singly-charged C emissions at 245.3, 385.3, 300.3, 387.6, 392.0, 406.6 and 431.5 nm, which is indicative of a moderately ionized plasma.

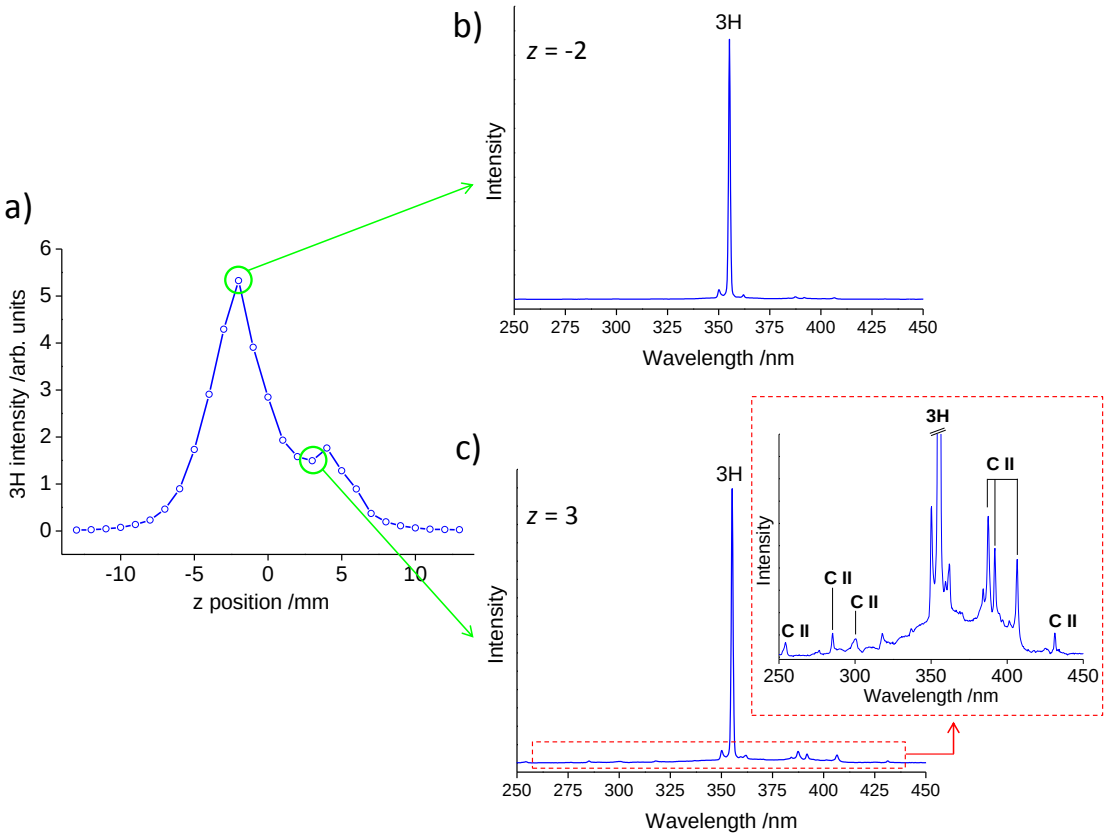


Figure 3.9 Analysis of the atomic emissions observed at different *z* positions a) 3H signal as a function of the *z* position (from figure 3.8), b) spectrum corresponding to the maximum 3H emission at *z* = - 2 mm, c) spectrum corresponding to the minimum 3H emission at *z* = 3 mm.

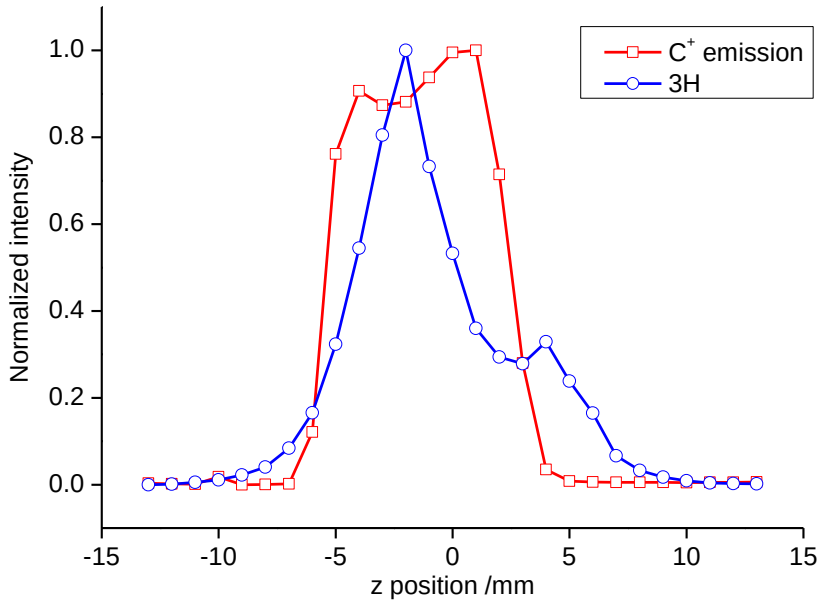


Figure 3.10 Comparison between the 3H signal and the $C^+$ integrated emission as a function of the *z* position (red squares). The z-scan (blue dots) corresponds to that shown in figure 3.8.

The integrated signal from the spectral region between 380 nm and 415 nm, including several $C^+$ emission lines, is plotted in figure 3.10 (red squares) together with the *z*-scan (blue dots) previously displayed in figure 3.8. As can be observed, carbon emissions maximize in the central region of the plume (z = 1 mm), coinciding with the 3H minimum.

Figure 3.11 shows an *x*-scan of the 3H signal performed at *z* = 4 mm (see figure 3.8) obtained by varying the driving laser focus position along the *x* axis in 0.4 mm steps. The data points represent the 3H intensity after optimizing the acquisition delay for each *x* value in order to have the maximum 3H signal. As can be seen in the figure, the maximum intensity corresponds to the closest position with respect to the target surface *x* = 0.6 mm. As the graphite plasma plume is explored at further positions, the 3H signal intensity decreases.

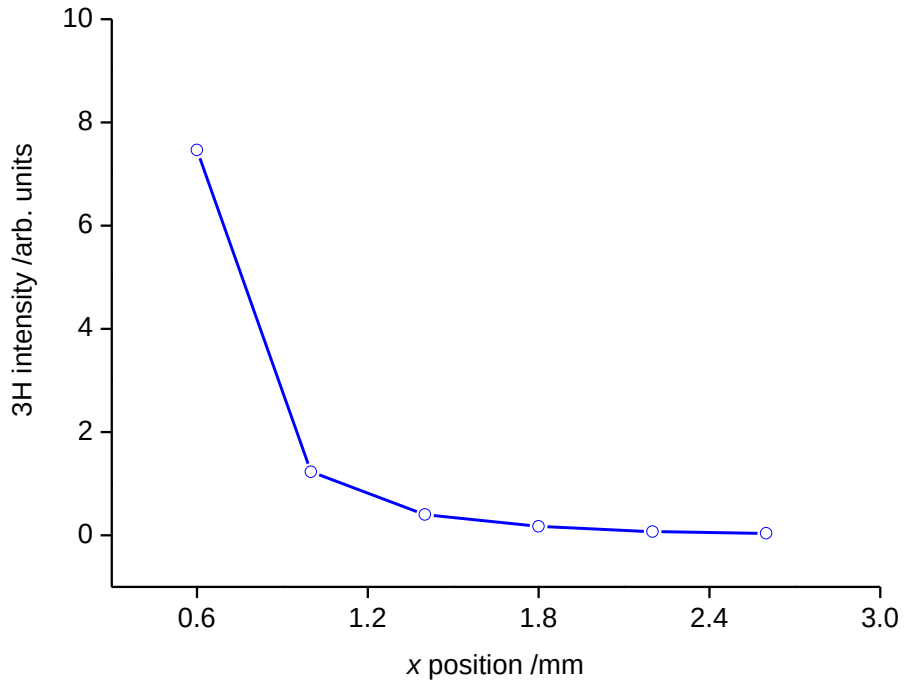


Figure 3.11 Dependence of the 3H signal with the *x* position of the 1064 nm driving laser beam focus with respect to the graphite target surface (*x* = 0 mm). The driving beam was focused at *z* = 4 mm (see figure 3.8). Ablation was performed at 1064 nm with 3 J $cm^{-2}$ under vacuum conditions ($10^{-2}$ mbar). The delay between the ablation and driving pulses was optimized for each data for obtaining the maximum signal.

### Inert gas atmosphere

Similar spatiotemporal study of the THG as described above was performed in the graphite laser ablation plasma under a flux of inert gas, keeping a constant pressure inside the ablation chamber in order to force the aggregation of species and to explore their effect on the nonlinear behaviour of the plasma. Figure 3.12, shows the corresponding log-log plot of the 3H intensity as a function of the delay between the ablation event and the arrival of the driving pulse for He, Kr and Xe atmospheres.

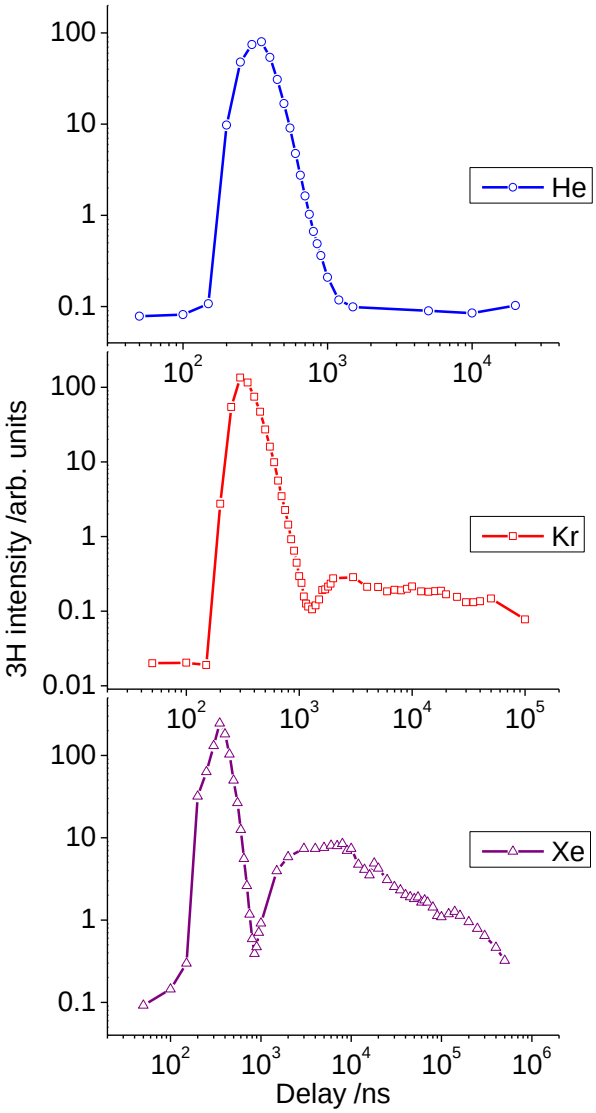


Figure 3.12 Intensity of the 3H signal as a function of the delay between the ablation and driving laser pulses acquired in a graphite plasma. Ablation was performed at 1064 nm under inert gas atmospheres of 1 mbar of He (blue circles), 1 mbar of Kr (red squares) and 1 mbar of Xe (purple triangles). The 1064 nm harmonics driving beam was focused at $x$ = 0.6 mm and $z$ =0 mm.

Under 1 mbar of Kr or Xe, the 3H signal reveals the presence of two maxima when the plasma is interrogated at $x$ = 0.6 mm. This observation is attributed to the presence of two different populations of nonlinear emitters in the plasma, arriving at the explored position at different times with respect to the ablation event. The first population is peaked at 250 ns for all atmospheres, therefore traveling with an average velocity of around 2400 m $s^{-1}$. This velocity value is in coincidence with that found for the distribution of nonlinear emitters obtained under vacuum conditions (see figure 3.7). For Kr and Xe, at delay times longer than 1 µs, the 3H signal rises again reaching a second broad maximum at around 3-5 µs after the ablation pulse. This second population, which was not observed under vacuum conditions or under He, confirms the presence of slower entities in the graphite plasma plume obtained under Kr or Xe atmospheres. The mean velocity of this population is estimated to be in the range of 120-200 m $s^{-1}$. The temporal evolution of the 3H signal, shown in figure 3.12, features a marked minimum at around 1 µs, indicating that the aforementioned populations are spatially separated by a gap from which third harmonic generation is less efficient.

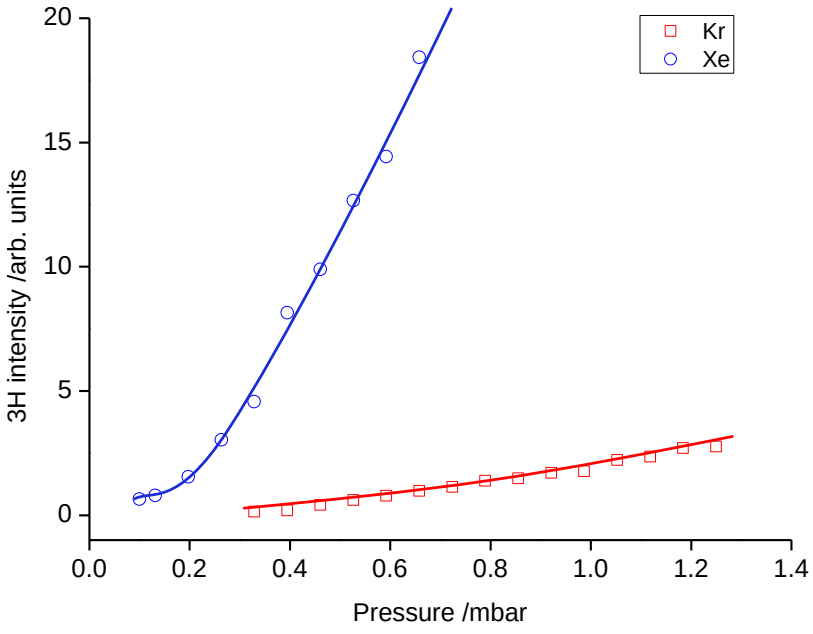


Figure 3.13 Evolution of the 3H intensity with the background pressure of krypton and xenon. Ablation of the graphite targets was performed at 1064 nm. The 1064 nm harmonics driving beam was focused at $x$ = 0.6 mm and $z$ =0 mm. The delay between the ablation and driving laser pulses was set to 3 µs.

The dependence of the 3H signal with the inert gas pressure was studied for the second population observed in Kr and Xe atmospheres (figure 3.12). For that purpose, the delay between the ablation and driving laser was set to 3 µs. The obtained dependence is displayed in figure 3.13. As shown, the 3H signal grows almost linearly with the inert gas pressure for the given experimental conditions.

The graphite plasma plume generated under atmospheres of 1 mbar of Kr and of 1 mbar of Xe was scanned along the *z*-axis by the driving beam. Figure 3.14 shows z-scans performed under these ambient conditions at a delay between ablation and driving laser pulses of 300 ns and 350 ns for Kr and Xe respectively and at $x$ = 0.6 mm. For both Kr and Xe atmospheres, the dependence of the 3H signal with the $z$ position is quasi-symmetric, in contrast with the assymmetric *z*-scan obtained in the case of vacuum conditions (see figure 3.8). A single maximum near the central region of the plasma plume at $z$ = -1 mm and $z$ = 1 mm for Kr and Xe respectively (with is consistent with the experimental error of the *z*-scan) is observed in both cases.

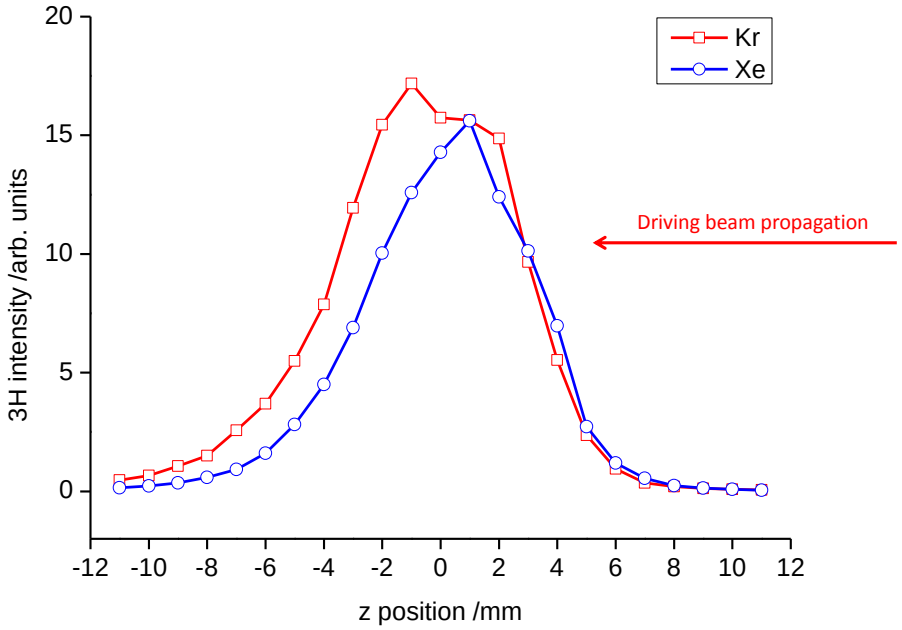


Figure 3.14 Intensity of the 3H signal as a function of the $z$ position of the 1064 nm driving beam focus with respect to the centre of the plasma plume ($z$ = 0 mm) obtained in graphite plasma. Ablation was performed at 1064 nm using pulses of 3 J cm$^{-2}$, under 1 mbar of Kr and 1 mbar of Xe. The harmonics driving beam was focused at $x$ = 0.6 mm. The delay between the ablation and driving pulses was set to 300 ns and 350 ns for Kr and Xe respectively.

Nevertheless, coinciding with this central region, the signal appears to level off (between $z$ = 2 mm and $z$ = 0 mm) in the case of Kr, suggesting that the attenuation observed under vacuum (figure 3.8) may also occur when the driving beam is focused in the central region of the graphite plume generated under inert gas atmosphere.

Figure 3.15 shows the $x$-scans obtained for Kr and Xe atmospheres. The position of the driving beam focus was varied along the $x$ axis in 0.4 mm steps and the delay between the ablation and driving pulses was optimized for each $x$ position explored. For Kr, the 3H signal increases in the first 0.4 mm, followed by the expected decay as the density of species decreases with the distance $x$. A constant decay of the signal is observed in the case of Xe atmosphere.

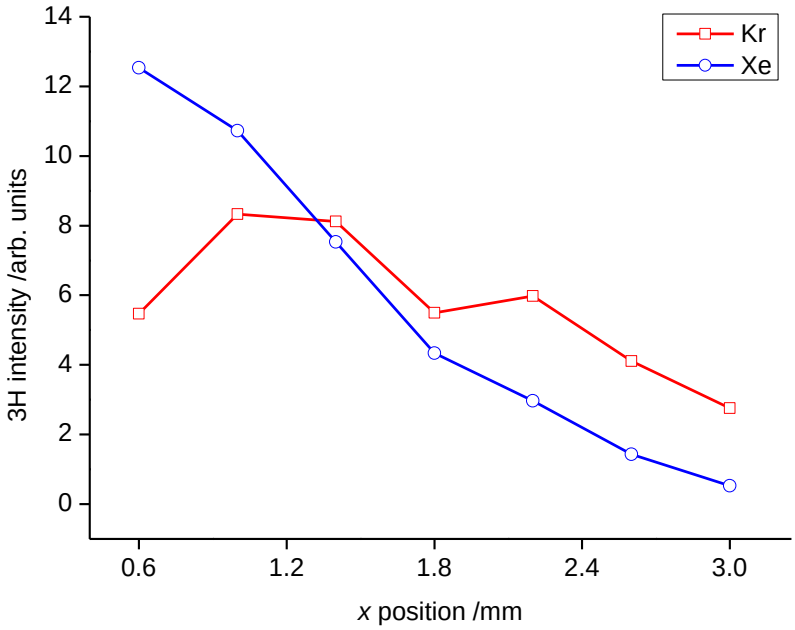


Figure 3.15 Dependence of the 3H intensity with the $x$ position of the 1064 nm driving laser beam focus with respect to the graphite target surface ($x$ = 0 mm). Ablation was performed at 1064 nm with pulses of 3 J cm$^{-2}$, under atmospheres of 1 mbar of Kr and Xe. The 1064 nm driving beam was focused at $z$ = 0 mm. The delay between the ablation and driving pulses was optimized for each position in order to obtain the maximum signal.

## 3.1.2 Third harmonic generation in boron carbide ablation plasma

The study of the THG from 1064 nm fundamental radiation was carried out in laser ablation plasmas of boron carbide. As in the case of graphite, ablation was performed at 1064 nm under different atmospheres, vacuum and inert gas.

### Vacuum conditions

Under vacuum ($10^{-2}$ mbar), the results are very similar to those obtained in graphite, but in the overall, $B_4C$ plasmas proved to be more efficient in the frequency up-conversion process. Figure 3.16 shows an example of the narrow 3H signal obtained at 355 nm using $B_4C$ plasma as nonlinear medium.

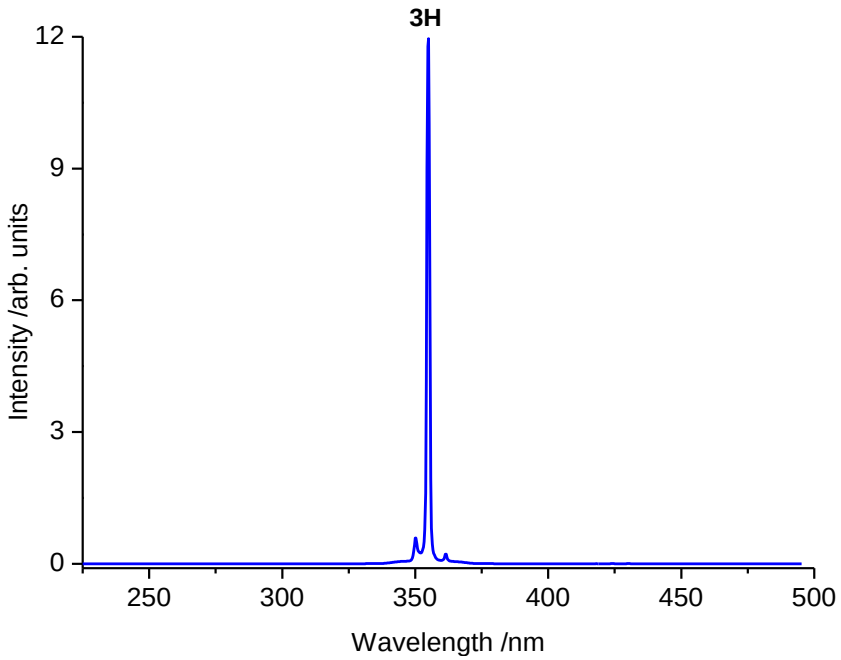


Figure 3.16 Emission at 355 nm corresponding to the 3H of the 1064 nm fundamental radiation generated in a boron carbide laser ablation plasma. Ablation of the $B_4C$ targets was performed at 1064 nm under vacuum ($10^{-2}$ mbar) with a fluence of 3 J $cm^{-2}$. The driving beam was focalized at $x$ = 0.6 mm and $z$ = 0 mm. The delay between the ablation and the driving pulses was set at 250 ns.

### Energy dependence of the 3rd harmonic emission in boron carbide plasma

The THG process was also studied in boron carbide plasmas as a function of the ablation laser pulse energy. This dependence is plotted in figure 3.17, where as in the case of graphite plasma (figure 3.5), it is observed that the 3H signal increases with the ablation

laser energy up to a certain value and then it levels off due to the aforementioned effects related to phase matching and absorption. For the sake of a better comparison with the graphite results, the same value of 18 mJ was chosen for the pulse energy of the ablation laser (unless otherwise specified) and ablation was performed in similar focusing conditions than those used for graphite ablation, therefore for this pulse energy the fluence on the target surface was about 3 J $cm^{-2}$.

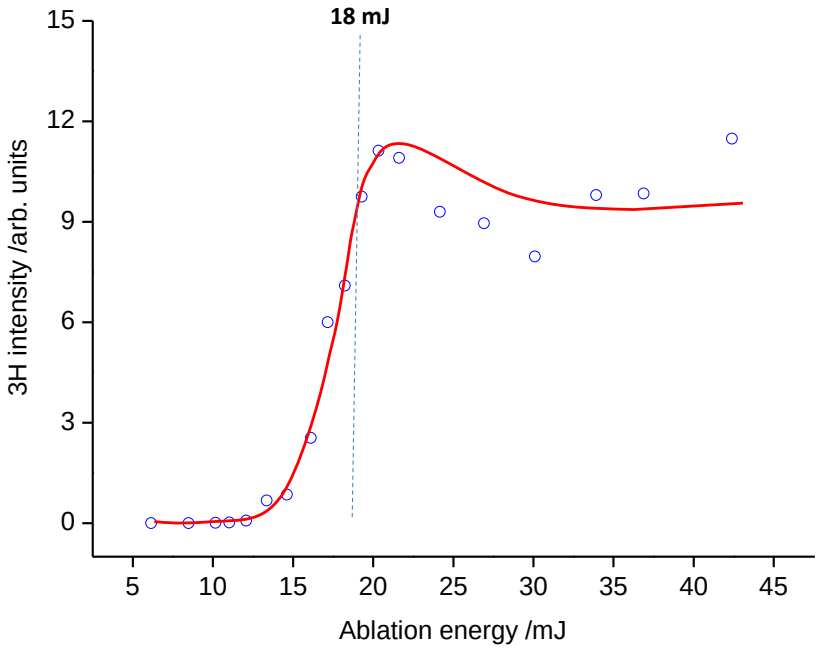


Figure 3.17 Dependence of the 3H signal with the ablation pulse energy obtained in a boron carbide laser ablation plasma. Ablation was performed at 1064 nm under vacuum ($10^{-2}$ mbar). The 1064 nm driving laser was focused at $x$ = 0.6 mm and $z$ = 0 mm. The delay between the ablation and driving pulses was set to 250 ns. The red line serves as a visual guide.

In order to check the nonlinear nature of the emission detected at 355 nm, the 3H signal intensity was plotted against the driving laser energy in a log-log plot. The result of this dependence is shown in figure 3.18. The delay between the ablation and driving pulses was set to 250 ns after performing a rough delay scan in order to find the value corresponding to the maximum 3H intensity. The resulting slope of the linear fit of the data is 2.8 ± 0.1, which is in agreement with the expected cubic dependence of the 3H signal with the driving laser energy.

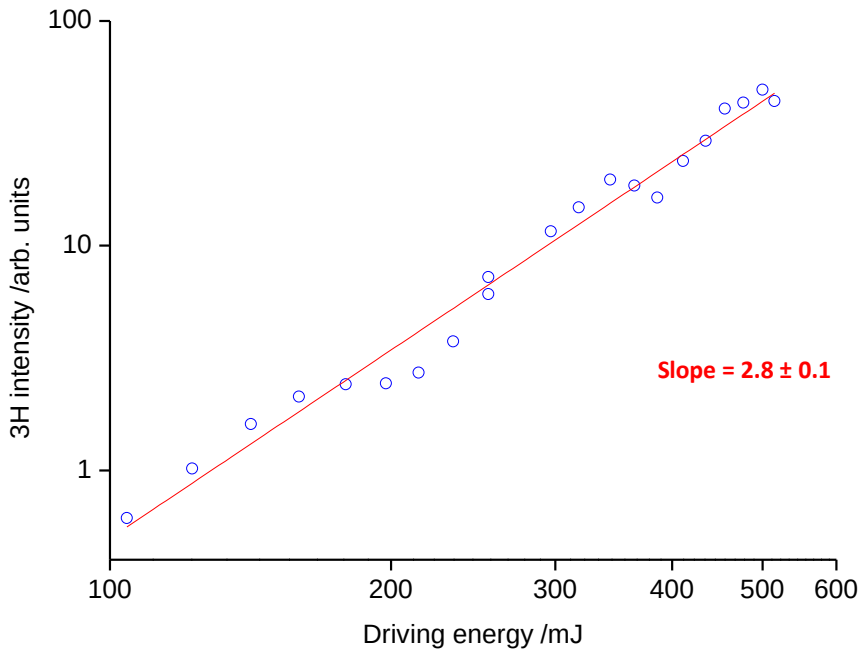


Figure 3.18 Intensity of the 3H signal as a function of the driving pulse energy ploted in log-log scale. Third harmonic generation was performed in a boron carbide ablation plasma by focusing the 1064 nm harmonics driving beam at $x$ = 0.6 mm far from the target surface and $z$ = 0 mm. Ablation was performed at 1064 nm under vacuum conditions ($10^{-2}$ mbar) with a fluence of 3 J cm$^{-2}$. The delay between the ablation and driving pulses was set to 250 ns. The red line is a linear fit of the data.

## Spatiotemporal study of the 3$^{rd}$ harmonic emission in boron carbide plasma

The dependence of the 3H on the delay between the ablation and the driving laser pulses obtained in $B_4C$ plasma is plotted in figure 3.19.

The plasma plume was probed at $x$ = 0.6 mm and $z$ = 0 mm in variable temporal steps. The delay scan reveals a single maximum in the 3H signal, found at 250 ns after the ablation pulse, indicative of a single population of species being responsible for harmonic generation under vacuum conditions.

The spatial behaviour of the 3H emission was studied in $B_4C$ plasma plumes. The obtained $z$-scan is shown in figure 3.20. The plot shows a symmetric distribution of the 3H signal with respect to the centre of the plume, where the intensity of the 3H emission reaches its maximum value. This is in contrast with the highly asymmetric dependence, featuring a minimum in the 3H signal, observed for graphite plumes generated under similar vacuum conditions (see figure 3.8).

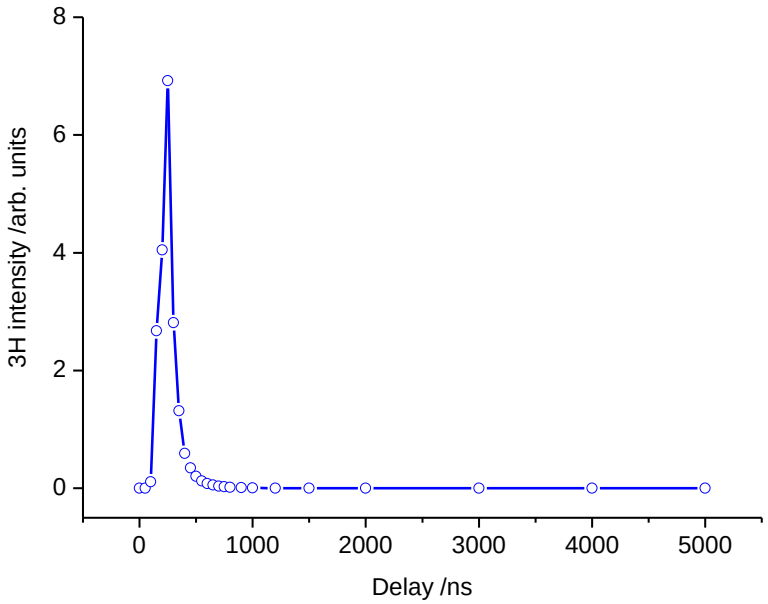


Figure 3.19 Intensity of the 3H signal as a function of the delay between the ablation and driving laser pulses acquired in a boron carbide plasma. Ablation was performed at 1064 nm under vacuum ($10^{-2}$ mbar). The 1064 nm driving beam propagates parallel to the target surface at a distance $x$ = 0.6 mm and is focused at $z$ = 0 mm.

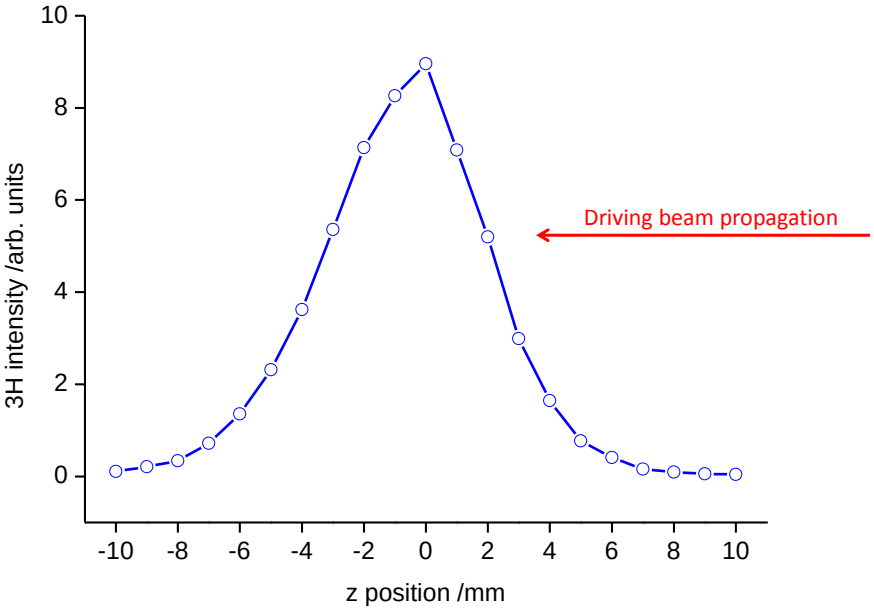


Figure 3.20 Intensity of the 3H signal as a function of the $z$ position of the 1064 nm driving beam focus with respect to the centre of the plasma plume ($z$ = 0 mm) obtained in a boron carbide plasma. The distance of the driving beam with respect to the target surface was fixed at $x$ = 0.6 mm. Ablation was performed at 1064 nm with 3 J $cm^{-2}$ under vacuum ($10^{-2}$ mbar). The delay between the ablation and driving pulses was set to 250 ns.

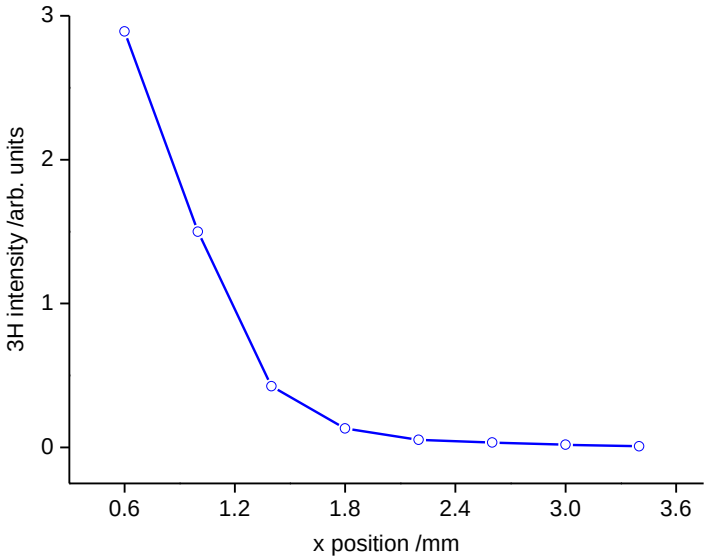


Figure 3.21 Dependence of the 3H signal with the *x* position of the 1064 nm driving laser beam focus with respect to the boron carbide target surface (*x* = 0 mm). The *z* position of the driving beam focus corresponds to *z* = 0 mm. Ablation was performed at 1064 nm with 3 J $cm^{-2}$ under vacuum ($10^{-2}$ mbar). The delay between the ablation and driving pulses was optimized for each data point in order to obtain the maximum signal.

The dependence of the 3H signal with the distance *x* obtained in a $B_4C$ plasma is plotted in figure 3.21. The *x*-scan shows the expected decay for the 3H signal as the plume is explored further away from the target surface.

### Inert gas atmosphere

Similarly to graphite, the delay scan obtained in boron carbide plasma under 1 mbar of Kr and 1 mbar of Xe, shown in figure 3.22, reveals the presence of an early component of the 3H signal at a delay of around 200 ns. The presence of a second component is also observed at longer delays for $B_4C$ plasmas generated under these ambient conditions, although the contribution of this population of species to the nonlinear process is more evident in the case of plasmas generated in the presence of Xe than those obtained under Kr atmosphere.

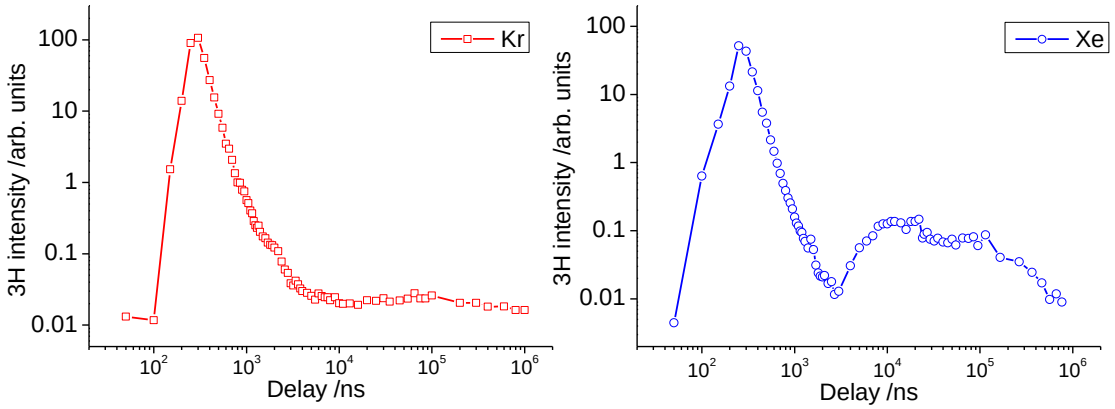


Figure 3.22 Intensity of the 3H signal as a function of the delay between the ablation and driving laser pulses acquired in a boron carbide plasma. Ablation was performed at 1064 nm under atmospheres of 1 mbar of Kr (red squares) and Xe (blue circles). The 1064 nm harmonics driving beam propagates parallel to the target surface at a distance $x = 0.6$ mm and is focused at $z = 0$ mm.

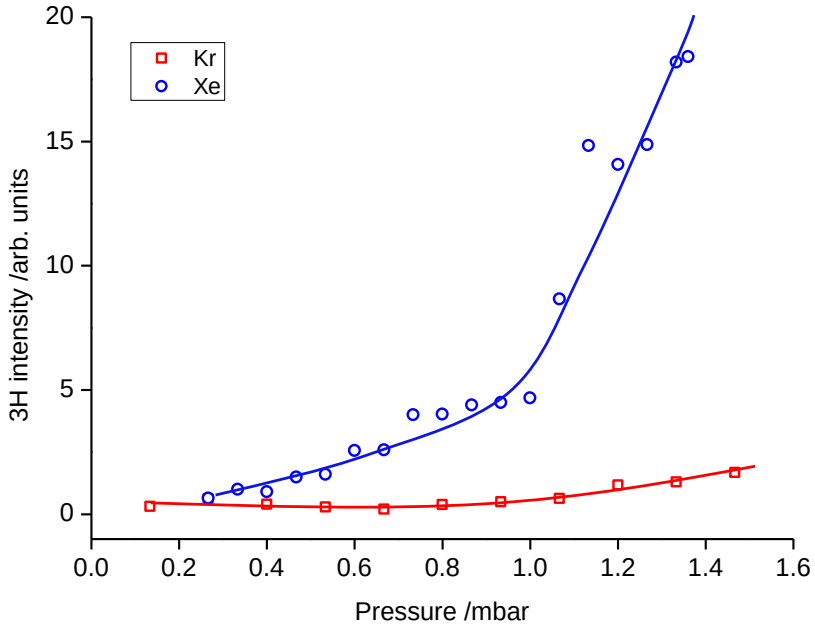


Figure 3.23 Evolution of the 3H intensity obtained in $B_4C$ plasmas with the background pressure of Kr and Xe. Ablation of the $B_4C$ targets was performed at 1064 nm. The 1064 nm harmonics driving beam propagates parallel to the target surface at a distance $x = 0.6$ mm and is focused at $z = 0$ mm. The delay between the ablation and driving laser pulses was set to 70 µs and 12 µs for Kr and Xe respectively. The blue and the red lines serve as visual guides.

Figure 3.23 shows the evolution of the 3H signal with the background gas pressure for the delayed component of the delay scan of figure 3.22. As expected, the 3H signal increases with the inert gas pressure. In the case of experiments performed under Xe, the evolution shows two components. The 3H intensity increases moderately up to 1 mbar followed by a sudden enhancement of the signal.

Figure 3.24 shows the results of the *z*-scans performed in $B_4C$ plasma under 1 mbar of Kr and 1 mbar of Xe. Similarly to the results obtained in graphite plasmas, a decrease in the 3H signal is observed when the driving beam is focused in the central region of the plasma plume.

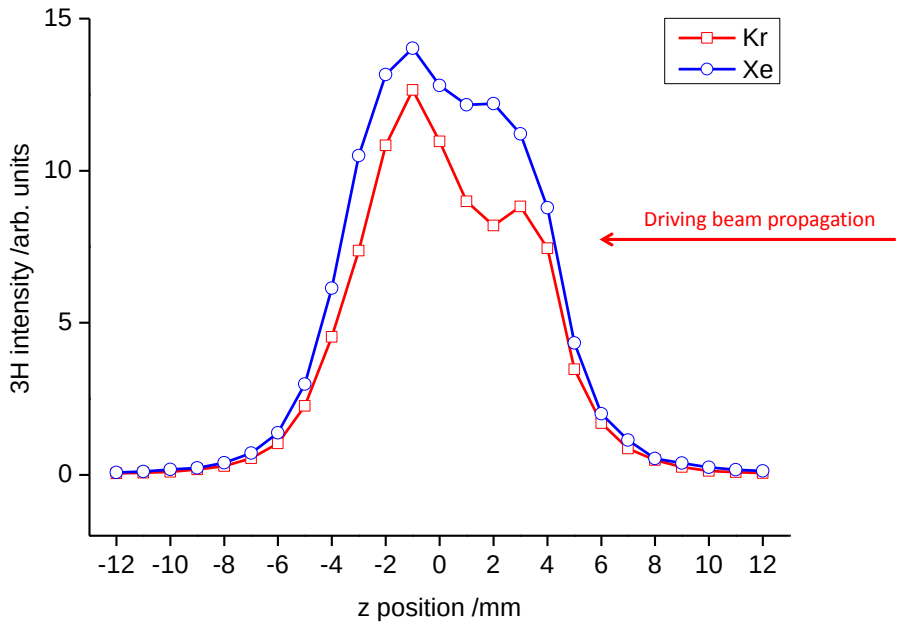


Figure 3.24 Intensity of the 3H signal as a function of the *z* position of the 1064 nm driving beam focus with respect to the centre of the plasma plume ($z$ = 0 mm) obtained in a boron carbide plasma. The distance of the harmonics driving beam with respect to the target surface was fixed at $x$ = 0.6 mm. Ablation was performed at 1064 nm with 3 J $cm^{-2}$ under atmospheres of 1 mbar of Kr and Xe. The delay between the ablation and driving pulses was set to 250 ns.

Figure 3.25 shows the *x*-scans obtained in $B_4C$ plasmas generated under 1 mbar of Kr and of 1 mbar of Xe. As expected, the 3H signal decays with the distance from the target surface, although some fluctuations are observed in the case of Xe.

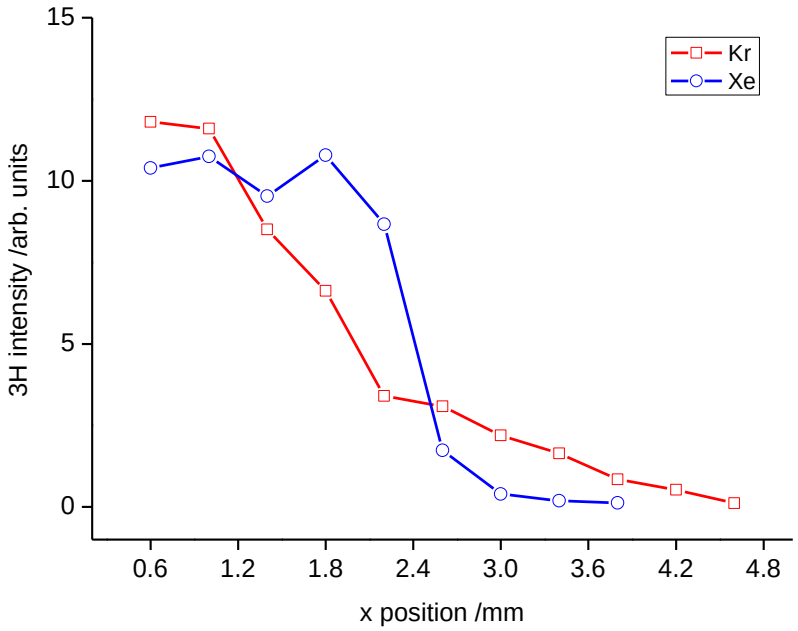


Figure 3.25 Dependence of the 3H intensity with the *x* position of the 1064 nm driving laser beam focus with respect to the boron carbide target surface (*x* = 0 mm). The *z* position of the driving beam focus corresponds to *z* = 0 mm. Ablation was performed at 1064 nm with 3 J cm$^{-2}$ under atmospheres of 1 mbar of Kr and Xe. The delay between the ablation and driving pulses was optimized for each data for obtaining the maximum signal.

### 3.1.3 Fifth harmonic generation in boron carbide plasmas

Fifth harmonic generation at 213 nm from the fundamental 1064 nm radiation was also studied in $B_4C$ plasma plumes generated by 1064 nm ablation under vacuum ($10^{-2}$ mbar). For that purpose, a different experimental set-up was required due to the limited spectral range of the ICCD detector used in the THG experiments described above. A detailed description of this set-up is given in the experimental section (Chapter 2, page 44). For comparison purposes, ablation was performed using the same fluence of 3 J cm$^{-2}$ chosen for THG experiments under vacuum conditions.

Detection of the fifth harmonic (5H) in the case of graphite plasma was not possible due to the overlapping of a strong spontaneous emission in the 5H region. The temporal decay of this signal, around 50 ns, indicates that its origin is related to atomic emissions induced by the driving pulse that can be attributed to $C^+$ lines at around 213.8 nm. This experimental limitation was less important in the case of $B_4C$ plasma, as atomic emission lines falling in the 5H region are weaker compared to the relatively intense 5H emission.

In this case, the temporal width of the signal detected at 213 nm, of around 15 ns, is in the order of the driving pulse temporal width.

Figure 3.26 shows the 5H signal obtained in a $B_4C$ plasma under vacuum ($10^{-2}$ mbar). From the fitting of the experimental data points to a Voigt function, the central wavelength of this emission is found to be around the expected wavelength of 213 nm.

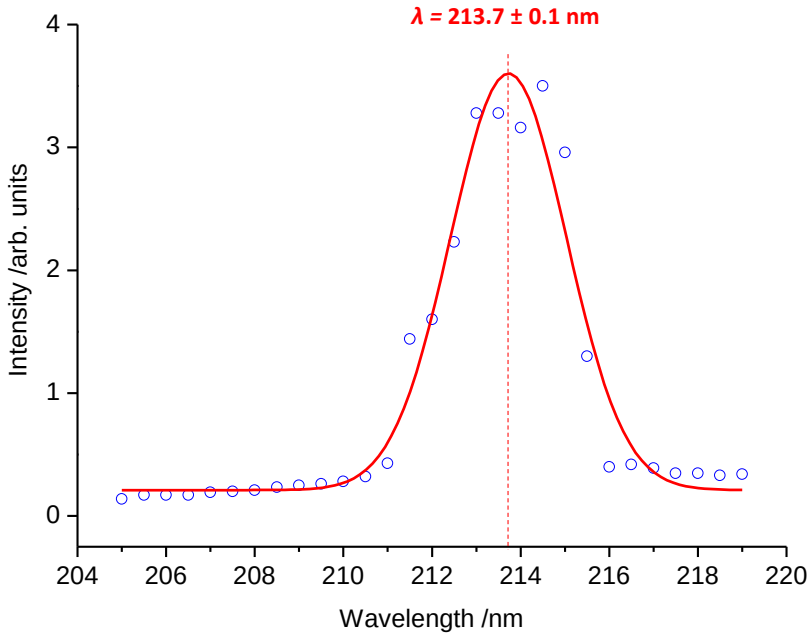


Figure 3.26 Emission at 213 nm corresponding to the 5H of the 1064 nm fundamental radiation generated in a boron carbide laser ablation plasma. Ablation of $B_4C$ targets was performed at 1064 nm under vacuum ($10^{-2}$ mbar) with a fluence of 3 J cm$^{-2}$. The driving beam was focalized at $x$ = 0.6 mm and $z$ = 0 mm. The delay between the ablation and driving pulses was set to 250 ns. The experimental data are fitted to a Voigt function (red line) in order to assess the central wavelength of the emission, which was found to be at 213.7 ± 0.1 nm.

### Energy dependence of the 5$^{th}$ harmonic emission in boron carbide plasma

Figure 3.27 shows the dependence of the 5H signal with the driving laser energy in log-log form. The slope obtained from the linear fit of the experimental data is 5.6 ± 0.5, close to the expected fifth-power dependence, thus confirming the nonlinear order of the emission.

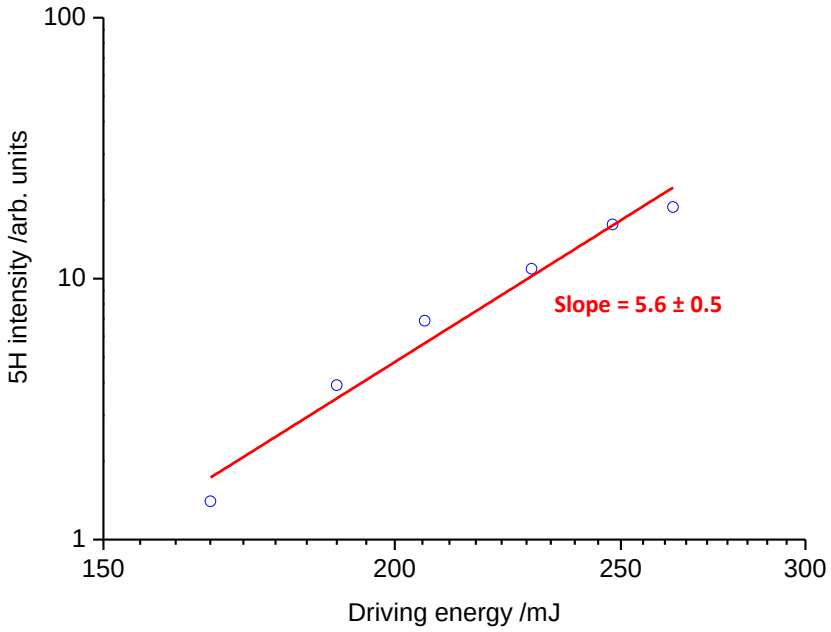


Figure 3.27 Intensity of the 5H signal as a function of the driving pulse energy ploted in log-log scale. Fifth harmonic generation was performed in a boron carbide ablation plasma by focusing the 1064 nm harmonics driving beam at $x = 0.6$ mm and $z = 0$ mm. The delay between the ablation and driving pulses was set to 250 ns. Ablation was performed at 1064 nm under vacuum ($10^{-2}$ mbar) with a fluence of 3 J cm$^{-2}$. The red line is a linear fit of the data.

## Spatiotemporal study of the 5$^{th}$ harmonic emission

The temporal evolution of the 5H signal was studied by varying the delay between the ablation and driving pulses. Figure 3.28 shows this dependence, in which a single maximum is observed at 250 ns, the same delay value observed in the case of the 3H generated in this plasma.

The evolution of the 5H signal with the position of the driving laser focus along the *z* axis is shown in figure 3.29 As can be observed, the *z*-scan is highly symmetric, featuring a single maximum coinciding with the central region of the plasma plume ($z = 0$ mm).

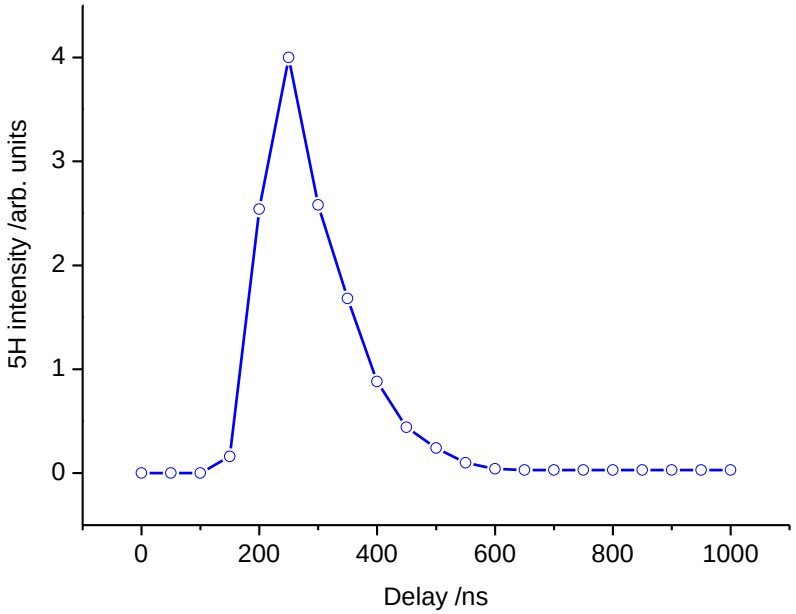


Figure 3.28 Intensity of the 5H signal as a function of the delay between the ablation and driving pulses acquired in a boron carbide plasma. Ablation was performed at 1064 nm under vacuum ($10^{-2}$ mbar). The 1064 nm harmonics driving beam propagates parallel to the target surface at a distance $x$ = 0.6 mm and is focused at $z$ = 0 mm.

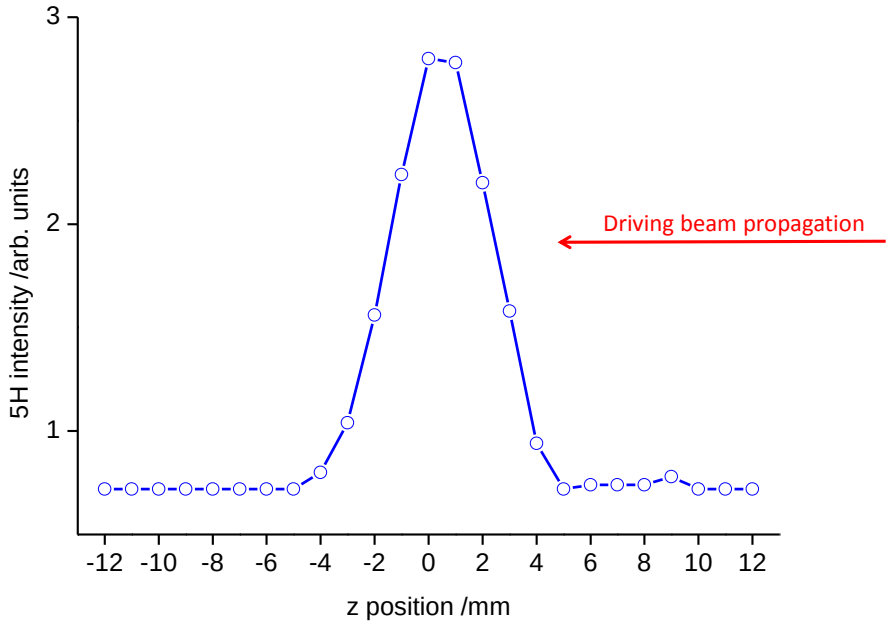


Figure 3.29 Intensity of the 5H signal as a function of the $z$ position of the 1064 nm driving beam focus with respect to the centre of the plasma plume ($z$ = 0 mm) obtained in a boron carbide plasma. The distance of the 1064 nm driving beam with respect to the target surface was fixed at $x$ = 0.6 mm. Ablation was performed at 1064 nm with 3 J cm$^{-2}$ under vacuum ($10^{-2}$ mbar). The delay between the ablation and driving pulses was set to 250 ns.

### 3.1.4 Frequency mixing in boron carbide ablation plasmas

The previous section contains results on 3$^{rd}$ and 5$^{th}$ harmonic generation in laser ablation plasmas. Due to the centrosymmetric character of the nonlinear medium (the plasma), only odd harmonics of the fundamental NIR radiation can be produced. In this section, a different nonlinear frequency mixing scheme is described. It involves two driving frequencies that correspond to that of the NIR, 1064 nm beam and to its second harmonic at 532 nm, generated by type I SHG in a KDP nonlinear crystal (see Chapter 2, page 45 for more details). This bichromatic configuration also introduces additional degrees of control over the irradiation conditions such as the relative energy and polarization of the two driving fields. Under this frequency mixing scheme, radiation at the wavelength of the fourth harmonic (4H) of the 1064 nm beam at 266 nm was detected. The $B_4C$ plasma was generated under vacuum ($10^{-2}$ mbar) using pulses at 1064 nm with a fluence of 3 J cm$^{-2}$ (unless otherwise specified).

Figure 3.30 shows an example of the intense narrow emission at 266 nm observed together with a peak that can be assigned either to B(I) at 249.7 nm or C(I) at 247.8 nm emissions.

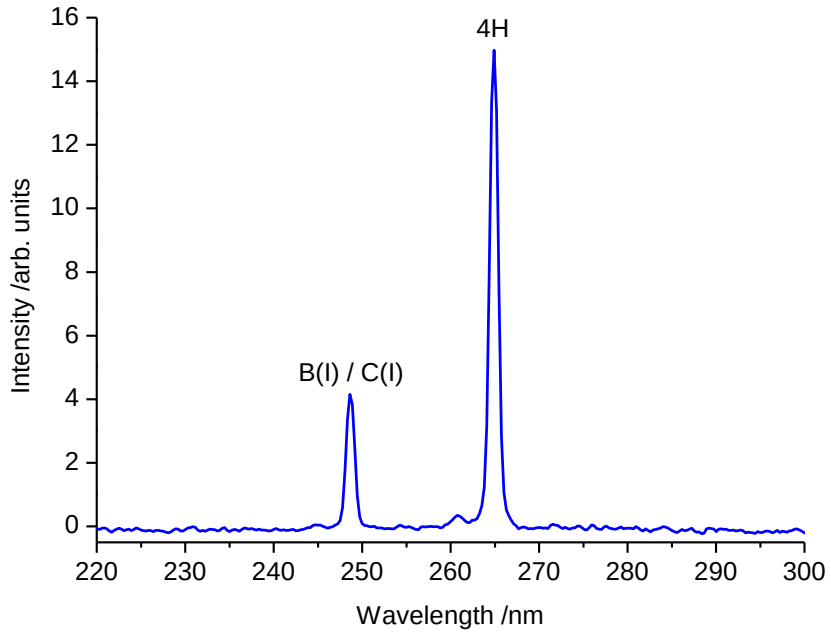


Figure 3.30 Emission at 266 nm obtained by frequency mixing of the fundamental 1064 nm and its second harmonic at 532 nm in a boron carbide laser ablation plasma. Ablation was performed at 1064 nm under vacuum ($10^{-2}$ mbar) using a fluence of 3 J cm$^{-2}$. The combined driving beam was focused at $x$ = 0.6 mm and $z$ = 0 mm. The delay between the ablation and driving pulses was set to 200 ns.

It is important to notice that 4H emission was detected exclusively in the presence of both parallel polarized 1064 nm and 532 nm driving beams.

### Energy dependence of the 4$^{th}$ harmonic emission

The dependence of the 4H emission at 266 nm with the energy of the 1064 nm and 532 nm driving beams is displayed in figure 3.31a and 3.31b respectively. In figure 3.31a, the energy of the NIR beam was varied while keeping the visible beam energy constant at 5 mJ. From the fitting of the data displayed in the log-log plot, a slope of 1.87 ± 0.08 is obtained. Conversely, in figure 3.31b, the energy of the visible driving beam was varied while keeping the NIR beam energy constant at 300 mJ. As can be seen in the log-log plot, the behaviour of the 4H signal is not characterized by a single power law.

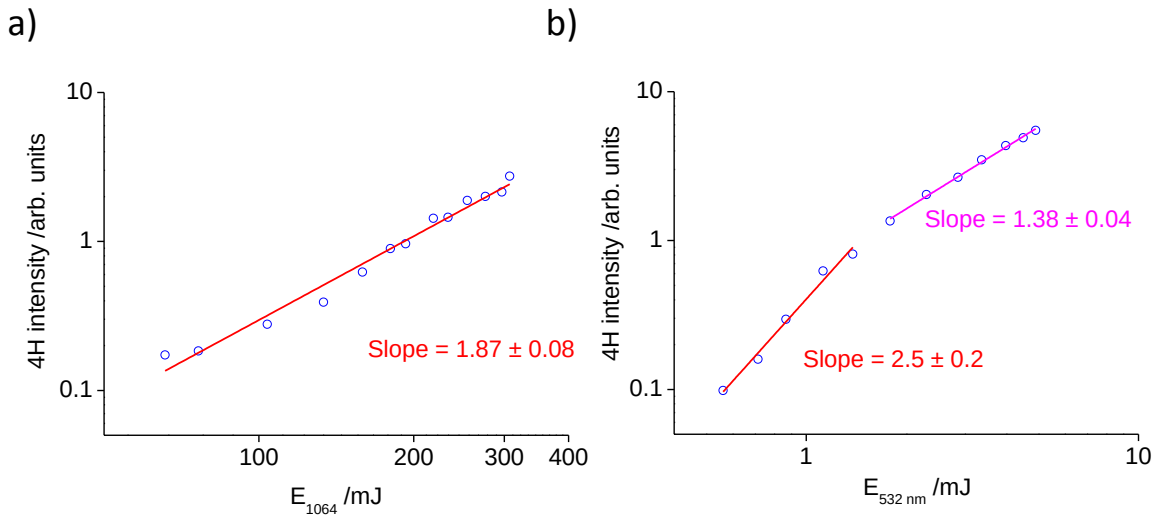


Figure 3.31 Intensity of the 4H signal as a function of the driving pulse energy ploted in log-log scale for: a) energy of the 1064 nm driving pulses ($E_{532}$ fixed at 5 mJ) and b) energy of the 532 nm driving pulses ($E_{1064}$ fixed at 300 mJ). Fourth harmonic generation was performed in a boron carbide ablation plasma by focusing the two-color harmonics driving beam at $x$ = 0.6 mm and $z$ = 0 mm. Ablation was performed at 1064 nm under vacuum ($10^{-2}$ mbar) with pulses of 3 J cm$^{-2}$. The red and the pink lines are linear fits of the data.

Fitting of the data corresponding to the lower energy values yields a slope of 2.5 ± 0.2, while that of the highest energy values is 1.38 ± 0.04. None of them are compatible with the lowest-order parametric processes:

$$\omega_{4H} = \omega_{vis} + 2\omega_{NIR} \tag{3.1}$$

which could yield the fourth harmonic frequency of the fundamental NIR beam. These energy dependences are crucial to unravel the type of parametric process responsible for fourth harmonic generation and will be treated in more detail in the discussion section (page 114).

### Spatiotemporal study of the 4$^{th}$ harmonic emission

The temporal behaviour of the 4H signal was explored by delaying the driving pulse with respect to the ablation event. Figure 3.32 shows the temporal dependence obtained for $x$ = 0.6 mm, $z$ = 0 mm, and energies of the 1064 nm and 532 nm beams of 450 mJ and 35 mJ respectively. The 4H emission maximizes at 200 ns and no late component was observed.

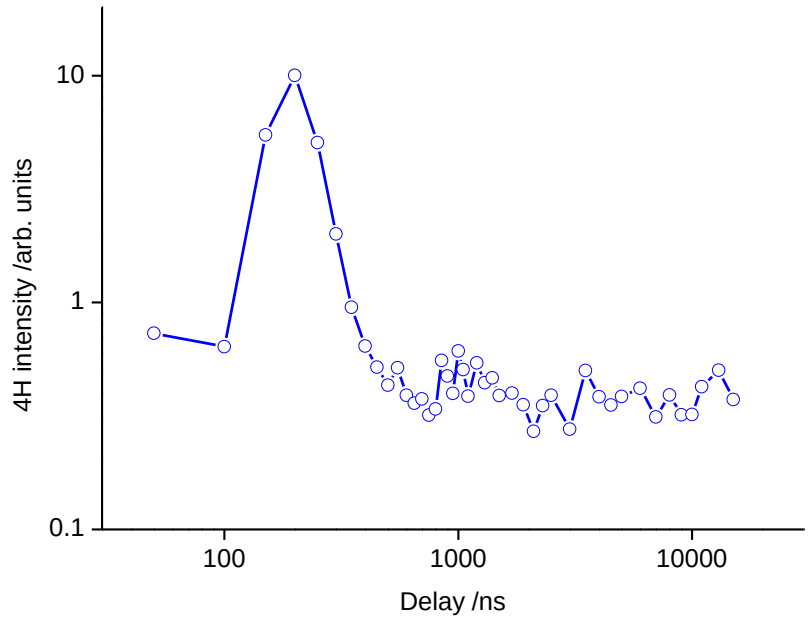


Figure 3.32 Intensity of the 4H signal as a function of the delay between the ablation and driving laser pulses acquired in a boron carbide plasma. Ablation was performed at 1064 nm under vacuum ($10^{-2}$ mbar). The 1064 nm harmonics driving beam propagates parallel to the target surface at a distance $x$ = 0.6 mm and is focused at $z$ = 0 mm.

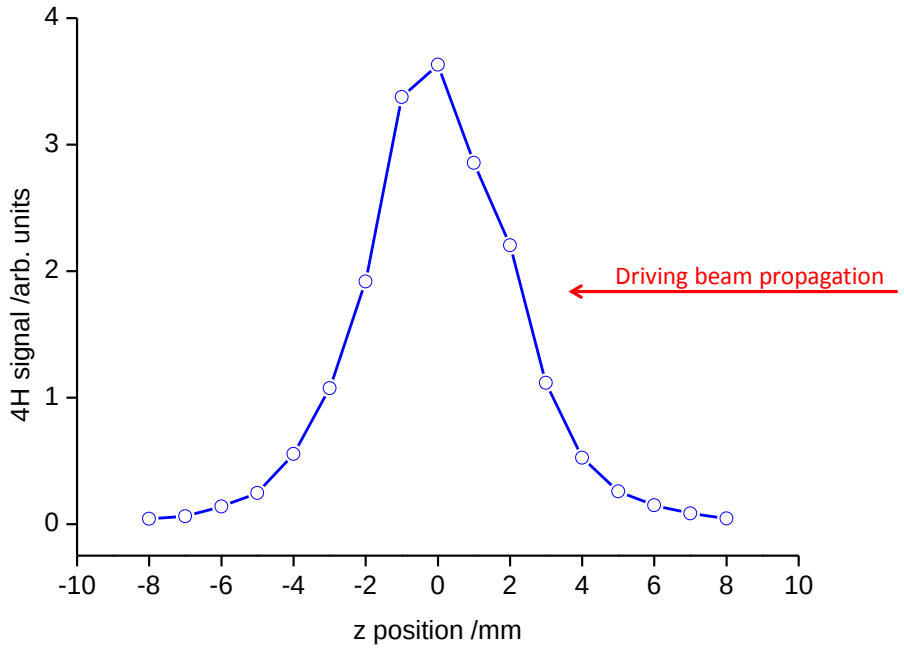


Figure 3.33 Intensity of the 4H signal as a function of the *z* position of the 1064 nm driving beam focus with respect to the centre of the plasma plume (*z* = 0 mm) obtained in a boron carbide plasma. The distance of the harmonics driving beam with respect to the target surface was fixed at *x* = 0.6 mm. Ablation was performed at 1064 nm with 3 J cm$^{-2}$ under vacuum (10$^{-2}$ mbar). The delay between the ablation and driving pulses was set to 200 ns.

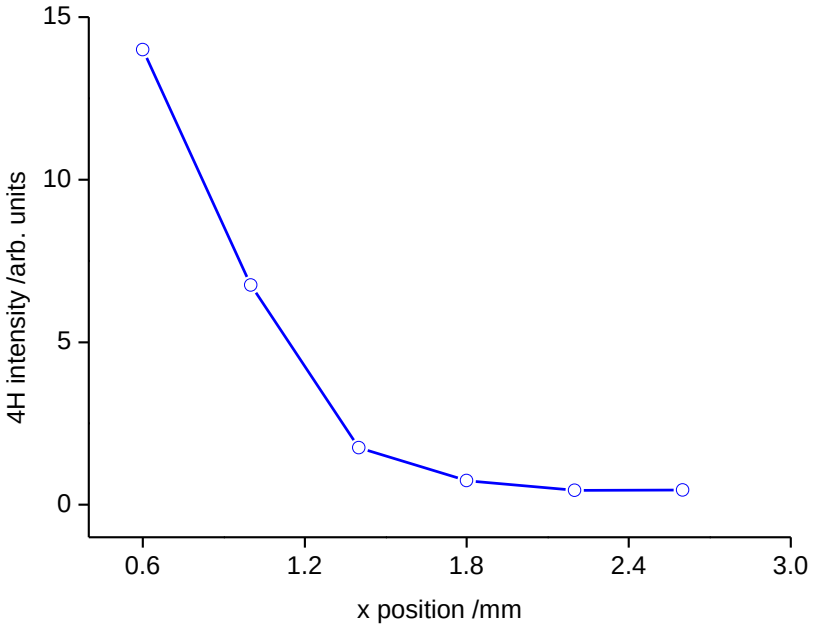


Figure 3.34 Dependence of the 4H signal with the *x* position of the 1064 nm driving laser beam focus with respect to the boron carbide target surface (*x* = 0 mm). The *z* position of the driving beam focus corresponds to *z* = 0 mm. Ablation was performed at 1064 nm with 3 J cm$^{-2}$ under vacuum (10$^{-2}$ mbar). The delay between the ablation and driving pulses was optimized for each data for obtaining the maximum signal.

The evolution of the 4H signal with the position of the driving beam focus along the *z* axis in $B_4C$ plasmas is plotted in figure 3.33. The *z*-scan shows a single maximum coinciding with the central region of the plasma plume (z = 0 mm). The signal displays a quasi-symmetric behaviour. The *x*-scan of the 4H signal, performed in similar conditions, is displayed in figure 3.34.

### Effect of the relative polarization of the driving beams

The results presented above were obtained in conditions where both driving beams have parallel polarization. In this section, the intensity of the 4H signal was studied as a function of the relative polarization directions of the linearly polarized fundamental and second harmonic driving beams. For that purpose the polarization of the 1064 nm beam was rotated with respect to that of the 532 nm with a half-wave plate before recombination (see figure 2.6 in page 46 of the experimental section). Figure 3.35 shows results obtained by varying the relative polarization angle between both beams. As can be seen in the figure, the maximum conversion efficiency is achieved when both driving beams have parallel polarizations (angles of 0° and 180°). For these measurements, the sensitivity of the detection system to parallel and perpendicular polarizations of a 266 nm linearly polarized laser beam was checked. The different response between polarization directions was found to be around 15 %, thus no significant bias is introduced in the results.

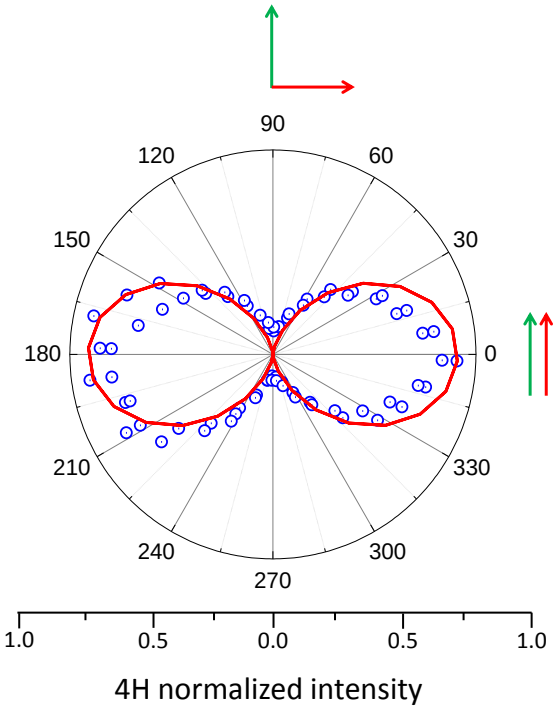


Figure 3.35 Fourth harmonic signal as a function of the relative polarizations of the 1064 nm and 532 nm driving beams. In the plot, 0° and 180° angles correspond to the situation where both beams (1064 nm and 532 nm) have parallel polarizations, whereas 90° and 270° correspond to a situation where the 1064 nm polarization is set perpendicular with respect to that of the 532 nm beam. The red line is a $\cos^2$ function which serves as a guide for the eye.

### 3.1.5 Characterization of the graphite and $B_4C$ laser ablation plasmas by optical emission spectroscopy and pulsed laser deposition

Optical emission spectroscopy was employed to obtain more information about the composition of the plasma plumes used in harmonic generation experiments. The information relative to the experimental details can be found in Chapter 2, page 48. With this aim, graphite and $B_4C$ targets were ablated under vacuum in the range of $10^{-2}$ mbar with pulses at 1064 nm in similar irradiation conditions than those used in HG experiments. In certain cases a slightly higher fluence was used to improve the signal intensity.

Figure 3.36a shows an example of the emission spectrum obtained in a graphite plasma generated under vacuum. In this case ablation was performed at a fluence of 3 J $cm^{-2}$. The spontaneous emission signal was acquired at zero delay after the ablation event and the integration time was set to 500 ns. In the spectrum, emissions assigned to vibrational

bands of the $C_2$ ($d^3\Pi_g - a^3\Pi_u$) Swan system and a broad emission of $C_3$ [4, 5] are observed. Only when increasing the ablation fluence, emissions from atomic C species appear, as can be seen in figure 3.36b, where a spectrum obtained upon ablation at a fluence of 16 J cm$^{-2}$ is shown. At this fluence, neutral and ionic carbon emission lines corresponding to C(I) 247.8 nm, C(I) 387.6 nm, and C(II) 387.6 nm are observed together with the $C_2$ Swan bands.

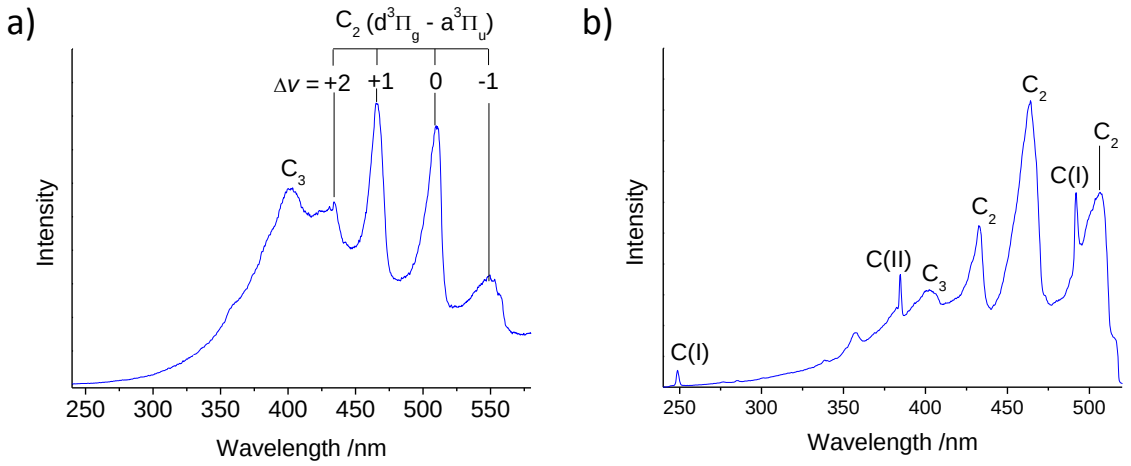


Figure 3.36 Optical emission spectra obtained by 1064 nm laser ablation of graphite under vacuum ($10^{-2}$ mbar) at: a) $F$ = 3 J cm$^{-2}$. The acquisition was performed at zero delay after the ablation pulse with an integration time of 500 ns and b) $F$ = 16 J cm$^{-2}$ with acquisition at zero delay and integration time of 100 ns.

Similar spectral features were found in OES measurements performed under 1 mbar of Kr and Xe. Emission from $C_2$ and $C_3$ molecular species can be observed in the spectra acquired in similar conditions, as shown in figure 3.37. Spectra obtained in $B_4C$ under Kr and Xe atmospheres yielded similar results than those obtained under vacuum.

Figure 3.38 shows the optical emission spectrum of $B_4C$ obtained by 1064 nm ablation at 4 J cm$^{-2}$ under vacuum ($10^{-2}$ mbar). The signal was acquired at zero delay with respect to the ablation pulse and was integrated during 1 µs. In the spectrum, emission lines assigned to B(I) 208.9 nm, B(I) 249.7 nm [6], and B(I) 348.9 nm [7] are observed together with $C_2$ Swan bands emissions.

[6] Possibly overlapped with C(I) at 247.8 nm
[7] Possibly overlapped with B(II) at 345.13 nm.

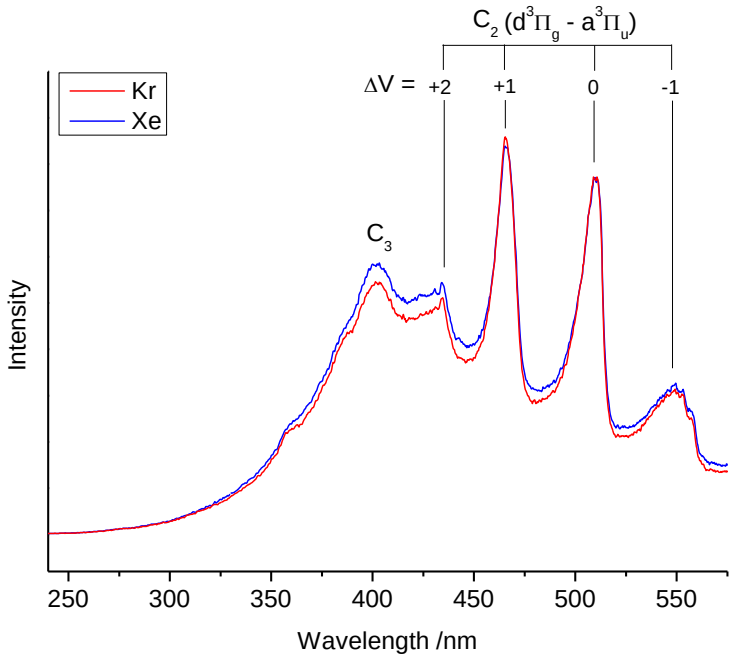


Figure 3.37 Optical emission spectra obtained by 1064 nm ablation of graphite targets under 1 mbar of Kr and 1 mbar of Xe. Ablation was performed at 3 J $cm^{-2}$. Spectra were acquired at zero delay after the ablation event and the signal was integrated during 500 ns.

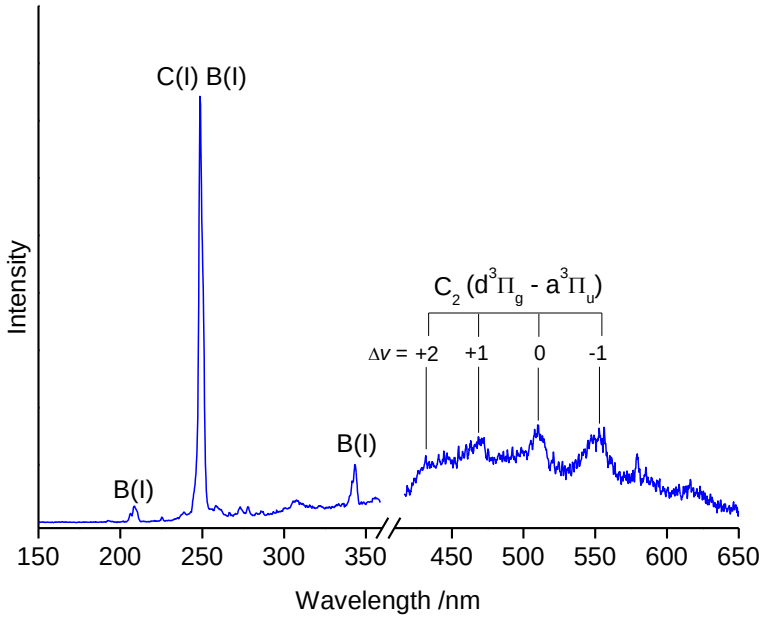


Figure 3.38 Optical emission spectrum obtained by ablation of $B_4C$ under vacuum ($10^{-2}$ mbar). Signal acquisition was performed at zero delay with respect to the ablation event and was integrated during 1 µs. The intensity of the signal after the break has been multiplied by a factor of 5 in order to better display the Swan bands system.

### Morphological characterization of the ejected material by PLD

At this point, PLD was used to obtain information about the morphology of the deposited material upon ablation in the different atmospheres studied: vacuum and inert gas [1].

Figure 3.39 shows SEM images of graphite deposits obtained under vacuum at $10^{-2}$ mbar (figure 3.39a), 1 mbar of Kr (figure 3.39b) and 1 mbar of Xe (figure 3.39c). Deposition was carried out at room temperature on Si substrates placed at 4 cm from the target. The differences in morphology of the deposits are patent. While under vacuum highly uniform thin layers are obtained, under inert gas atmosphere the formation of dendritic structures characterizes the morphology of deposits.

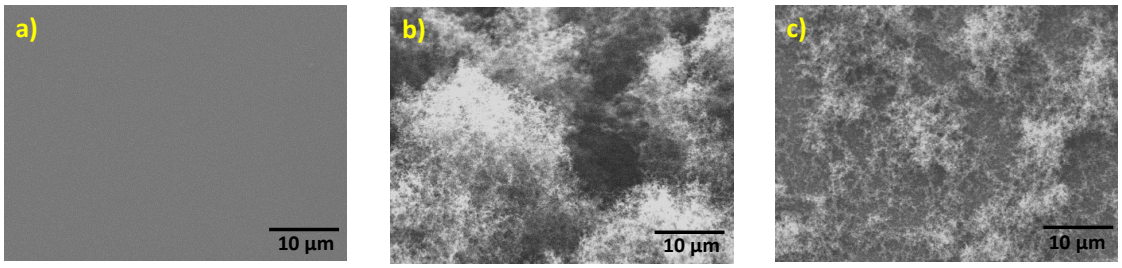


Figure 3.39 SEM images of deposits obtained by PLD of graphite under: a) vacuum ($10^{-2}$ mbar), b) Kr (1 mbar), c) Xe (1 mbar). Deposition was performed at room temperature on Si (100) substrates placed at 4 cm from the target surface.

The morphology of deposits obtained by ablation of $B_4C$ under the different atmospheres also differs, as can be seen in figure 3.40. Interestingly, deposits prepared under vacuum feature nano and micrometric sized particles that emerge from the continuous background film (figure 3.40a). The observation of these singular structures motivated a series of PLD experiments which constitute one of the two main topics described in Chapter 4 of the present thesis (page 133). Similarly to graphite ablation and deposition, dendritic structures are formed under Kr atmosphere (figure 3.40b) while under Xe (figure 3.40c) only isolated spherical particles lay on the background film.

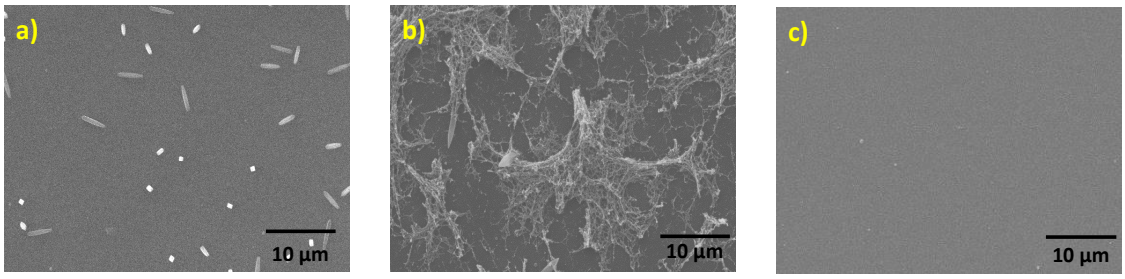


Figure 3.40 SEM images of deposits obtained by PLD of $B_4C$ under: a) vacuum ($10^{-2}$ mbar), b) Kr (1 mbar), c) Xe (1 mbar). Deposition was performed at room temperature on Si (100) substrates placed at 4 cm from the target surface.

## 3.1.6 Discussion of results

### Generation of odd harmonics in carbon containing materials

Third harmonic generation was studied in graphite and $B_4C$ laser ablation plasmas generated under vacuum and inert gas ambient conditions. The 3H signal at 355 nm was detected in experiments carried out in plasmas of both materials as a narrow intense peak, exclusively when the focused driving laser beam was propagated through the plasma volume. The nonlinear nature of this light was further confirmed through the analysis of the 3H signal response to the variation of the driving laser energy, plotted in figure 3.6 and figure 3.18 for graphite and $B_4C$ respectively. Analysis of the data yielded a third-order power dependence in both cases, as expected for a third-order nonlinear process. Regarding the frequency up-conversion efficiency, $B_4C$ plasmas systematically proved to be more efficient, yielding 3H signal amplitudes approximately twice larger than those measured in graphite plasmas.

The temporal behaviour of the 3H signal obtained in graphite and $B_4C$ plasmas is very similar. Under vacuum conditions, the signal is characterized by a single component observed at delays around 300 ns after the ablation pulse (see figures 3.7 and 3.19). At the explored distance of $x$ = 0.6 mm this delay would correspond to an average velocity of the species responsible for THG of about 2400 m $s^{-1}$. OES results (figure 3.36) indicate the presence of excited $C_2$ as well as $C_3$ molecules in graphite plasmas obtained under similar conditions than those used in the THG experiments. The presence of the $C_2$ molecules was also observed in $B_4C$ plasmas, as can be seen in figure 3.38. The estimated average velocity of particles in the early component of the delay scans is compatible with the

velocities of $C_2$ molecules, of about 3000 m $s^{-1}$, reported by Clayssens et al. [6] in 248 nm ablation plumes. Therefore this early contribution to the 3H signal can be attributed to atomic and small molecular species.

With regard to the results involving different ambient conditions, the early component of the 3H signal was also observed under Kr and Xe atmospheres at delay times around 300 ns. Additionally, under these ambient conditions, a second contribution to the 3H signal is observed at longer delays (see figures 3.12 and 3.22). The presence of an inert gas inside the ablation chamber is known to affect dramatically the expansion dynamics of the plasma plume. Under these conditions, aggregation of atomic species is strongly favoured due to the kinetic energy loss of the expanding species through collisions with surrounding gas atoms. This aggregation processes would explain the appearance of the late maximum in the delay scans performed under Kr and Xe atmospheres. This contribution to the THG process, observed at time delays > 3 μs after the ablation event, can be attributed to heavier species like clusters and/or nanoparticles arriving at the exploration position ($x$ = 0.6 mm) with an average velocity of the order of 120-200 m $s^{-1}$. The inert gas atoms are believed to have a minor contribution to the THG process at the moderate pressures used in the experiments.

The noble gas mass is found to play a role in the efficiency of the nonlinear process. In graphite plasmas, under 1 mbar of helium (figure 3.12) no signal enhancement has been found at long delays. On the other hand, the relative intensity of the 3H signal observed in this case is higher for experiments performed under 1 mbar of Xe, compared to that observed under Kr atmosphere. This enhancement can be related to the distinct collision efficiency reached in He, Kr and Xe due to their different collisional cross sections. As expected, increasing the background inert gas pressure also leads to an enhancement of the 3H signal at longer delays as demonstrated in figures 3.13 and 3.23. Increasing the pressure implies a higher collisions rate, thus favouring aggregation.

The participation of aggregation processes is supported by the morphological analysis of the material deposited on Si substrates. Although diffusion and aggregation can take place upon deposition, the totally different expansion dynamics of the plasma plume expected under vacuum and inert gas atmospheres, should lead to remarkably different aspect of the material. As an example, by comparing figures 3.39a and 3.39b, the different aspect of the deposited material collected under vacuum and under inert gas atmosphere is patent. In figures 39b, 39c and 40b, the formation of characteristic dendritic structures is observed in graphite and $B_4C$ deposits. These structures have been

observed previously in PLD experiments and its formation is attributed to the assembling of clusters upon deposition in the presence of a background gas [7, 8].

In the following, the observed spatial behaviour of the 3H signal generated in graphite and $B_4C$ plasmas will be discussed. Some considerations regarding the relative geometry of the driving beam and the plasma plume must be taken into account. In the experiments, the 1064 nm driving beam is focused by means of a 20 cm focal length lens. In these conditions the estimated confocal parameter is ~4 mm. The FWHM of the 3H signal distribution observed in *z*-scans performed in graphite and $B_4C$ ablation plumes is around 6-7 mm.

Interestingly, some *z*-scans performed in graphite and $B_4C$ plasmas generated under vacuum and inert gas for the early component (delay between ablation and driving pulses around 300 ns) and $x$ = 0.6 mm, exhibit a characteristic dip in the 3H signal when the driving beam is focused in the central region of the plasma plume, around $z$ = 0 mm (see figures 3.8 and 3.24).

This observation can be partially explained on the basis of the formalism described by Lago *et al*. [9] for harmonic generation in gaseous media with arbitrary density distributions. In this formalism, the density dependence of the intensity of *n*-order harmonics is determined by a dimensionless function $G_n$ of the form:

$$G_n = (b\Delta k_0)^2 F_n \tag{3.2}$$

where $b$ is the confocal parameter of the driving beam, $\Delta k_0$ is the wave vector mismatch between the generated harmonic radiation and the driving polarization at the centre of the density distribution ($z$ = 0 mm) and $F_n$ is the phase matching function, which in turn depends on the nonlinear medium density distribution *N(z)* across the propagation direction and on the $b/L$ ratio, being $L$ the width of the density distribution in the medium.

The theoretical dependence of $G_n$ (and therefore of the *n*-order harmonic intensity) on the position of the driving laser focus $z$, predicts that its maximum value is achieved at $z$ = 0 mm for a mismatch $b\Delta k$ corresponding to a certain plasma conditions. The mismatch $\Delta k$ depends on the plasma density accordingly to (3.3).

$$\Delta k(z) = C(\lambda)N(z) \tag{3.3}$$

where $C(\lambda)$ accounts for the wavelength dependence of $\Delta k$ per atom caused by dispersion in the medium.

For a situation where the driving beam is focused in a region of high density of species, different phase matching conditions and therefore a different value of $b\Delta k$ can be expected. In this situation it is observed that the function $G_n$ can feature a minimum at $z$ = 0 mm and two symmetrical maxima with respect to this position.

The analysis of the plasma emissions acquired at a $z$ position corresponding to the central region of the graphite plasma plume reveals the presence of $C^+$ ions together with *Bremsstrahlung* emission which is indicative of the presence of free electrons (see figure 3.9c). Visually, the aspect of the plasma changes to a bright white colour due to the background emission when the driving beam is focused at this position. The contribution of free electrons to the dispersion of harmonics is known to play a major role [10, 11]. These findings suggest that the dip in the harmonics signal observed in some of the $z$-scans corresponds to a situation in which a higher density of species, including free electrons, leads to a larger phase mismatch, thus causing a decrease in the harmonics signal. Nevertheless, other factors such as the presence of different types of species across the plume, can also contribute to spatial non-uniformities in the efficiency of the nonlinear process.

In a situation where there is no significant absorption of the harmonic radiation in the plasma, the $z$-scan profile is expected to be symmetric with respect to the centre of the plasma plume [9]. In order to explain the marked asymmetry observed in some of the $z$-scans obtained (*i.e.* in figure 3.8), one must have in mind the picture of the driving laser focus probing the plasma plume before and after the central region of the plasma (see figure 3.2). When the driving beam is focused before the centre of the plasma ($z$ > 0 mm), the generated harmonic photons must travel through most of the plasma length, including its densest part. Therefore, the newly generated harmonic beam can be partially absorbed by the plasma, leading to a local maximum with lower 3H intensity at $z$ = 4 mm as in figure 3.8. This is in contrast with the situation where the driving beam is focused after the centre of the plume ($z$ < 0 mm). In this case, harmonic photons travel a shorter distance through the plasma, thus absorption processes are less important, yielding the maximum 3H intensity in the $z$-scan at $z$ = -2 mm in figure 3.8.

The evolution of the 3H signal with the distance from the target surface was evaluated. In the $x$-scans, a fast decay of the 3H signal intensity is observed. Under vacuum the efficiency of the THG process in graphite and $B_4C$ plasmas decays to almost zero at around 3 mm.

In the absence of resonance effects, the conversion efficiency decreases with the harmonic order in the perturbative regime [12, 13]. For that reason, the 5H generation efficiency is expected to be lower than that of THG. This is the case observed in the described experiments. In graphite plasmas, the low conversion efficiency of the 1064 nm fundamental radiation into its 5H at 213 nm was evidenced by the fact that detection was not possible in the same experimental conditions used for THG. The detection of the weak 5H emission was hindered by spontaneous emissions in the 213 nm region. These emissions are favoured by the action of the driving beam, inducing fragmentation and re-excitation processes in the plasma.

With regard to the experiments concerning 5H generation, the nonlinear nature of the 213 nm emission detected in $B_4C$ plasmas was confirmed by the driving energy dependence shown in figure 3.27. From the fit of the data, the slope value close to 5 is in agreement with the expected power law for a 5H generation process.

The temporal dependence of the 5H (see figure 3.28) reveals, as in the case of THG experiments performed under vacuum, the presence of a single component contributing to fifth harmonic generation at a delay time of 250 ns. This delay value coincides with that observed in THG experiments, indicating a common origin for the $3^{rd}$ and $5^{th}$ harmonic signals in $B_4C$ plasmas. The analysis of graphite emissions by OES reveals the presence of molecular ($C_2$ and $C_3$) carbon species and in $B_4C$ plasmas, atomic (neutral) species appear to be the main constituents of the emission. This fact supports the hypothesis of small molecules, like $C_2$ and $C_3$, being the precursors of C atoms and ions which constitute the main nonlinear emitters. In this picture, upon irradiation with the relatively long pulses of the driving beam (18 ns), the pulse front can induce fragmentation of small molecules and clusters giving rise to atomic C species. The trailing part of the nanosecond pulse can interact with those C atoms and as a consequence harmonic radiation can be emitted.

The spatial behaviour of the 5H signal in $B_4C$ is similar to that observed for the $3^{rd}$ harmonic order in the same material. As shown in figure 3.29, the *z*-scan performed in $B_4C$ plasma exhibits a highly symmetric profile with a single maximum at $z = 0$ mm.

### Fourth harmonic generation in $B_4C$ plasmas by frequency mixing

The 4H of the 1064 nm driving beam at 266 nm has been also generated in $B_4C$ ablation plasmas by a frequency mixing process which is discussed below.

The intensity of the 4H was measured as a function of the pulse energy of the driving beams. In the particular case of harmonic generation through a parametric process, this measurement is crucial to reveal the order of the nonlinear process responsible for fourth harmonic generation. This dependence is plotted in figure 3.31a and figure 3.31b for the 1064 nm and 532 nm driving beams respectively.

In figure 3.41 possible schemes of the processes responsible for fourth harmonic generation are depicted, including sum- and difference-frequency mixing. Figure 3.41a, refers to the scheme of the lowest-order frequency mixing process that can generate 266 nm radiation with the bichromatic field (1064 nm + 532 nm), a sum-frequency mixing process involving four waves:

$$\omega_{4H} = \omega_{vis} + 2\omega_{NIR} \tag{3.4}$$

In the absence of saturation, this process would be characterized by a linear behaviour of the signal with the 532 nm beam intensity and a quadratic dependence for the intensity of the NIR beam. The experimental power law for the 1064 nm beam, shown in figure 3.31a, with a slope value of 1.87 ± 0.08, is in reasonable agreement with a quadratic dependence. Differently, the experimental power law obtained for the 532 nm beam, shown in figure 3.31b, displays a behaviour characterized by two different power laws (slopes of 2.5 ± 0.2 and 1.38 ± 0.04). The slope corresponding to lower pulse energy values would be compatible with a cubic dependence, therefore in disagreement with the proposed four-wave sum-frequency mixing process.

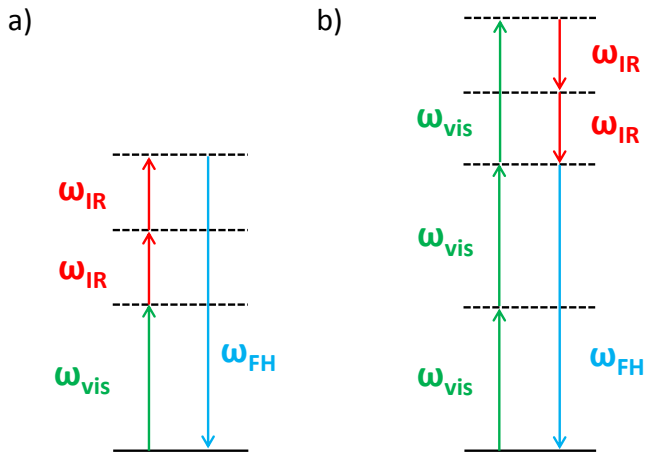


Figure 3.41 Schemes of possible parametric processes for fourth harmonic generation. a) four-wave sum-frequency mixing and b) six-wave difference frequency mixing.

In harmonic generation processes, parity conservation requires that the total number of driving photons of the two laser fields must be odd [14]. Therefore, besides the four-wave mixing process described above, the lowest order process allowed by symmetry would be a six-wave difference frequency mixing process of the form:

$$\omega_{4H} = 3\omega_{vis} - 2\omega_{NIR} \tag{3.5}$$

A scheme of this process is depicted in figure 3.41b. Such a higher order process should be in principle less probable, specially taking into account that the intensity of the 532 nm driving beam is relatively low (7 % of the total energy of the fundamental 1064 nm beam). Nevertheless, the power law obtained in figure 3.31b is more consistent with this six-wave difference frequency mixing process that the four-wave mixing process mentioned above.

The reason why a fifth-order process would dominate over a third-order process still remains unclear. There are several factors that could favour the latter, but these factors do not explain unambiguously why the experimental results are more consistent with a higher-order process. A factor that could favour a fifth-order, or be detrimental for a third-order process, is a resonance effect. As demonstrated by OES, $C_2$ molecules are present in the $B_4C$ plasma plumes obtained in similar conditions than that of the 4$^{th}$ harmonic generation experiments, and are potential candidates for HG at short times after the ablation event. The 532 nm driving beam radiation would be in resonance with the excited robrivational transitions of the $\Delta v$ = -1 bands of the $C_2$ Swan system. Similar

resonance effects have been reported in $C_2$ molecules present in flames [15]. This possibility should not be disregarded. In B and C atoms (either ions or neutrals) no resonance processes that can play a role in the nonlinear process have been identified.

Other aspect that should be taken into account is the collective response of the media, instead of that of individual species. Phase matching is known to be more favourable for difference frequency mixing than for sum frequency mixing processes [16, 17]. Nevertheless, as explained previously, there is no evidence that supports the prevalence of the fifth-order process over the third-order one. Further investigations should be required to clarify this point.

The temporal and spatial behaviour of the 4H radiation obtained in $B_4C$ plasmas is very similar to that found for lower harmonic orders. The temporal dependence of the 4H signal obtained at $x$ = 0.6 mm, shown in figure 3.32, yields a single maximum at 200 ns. This delay is in the order of the values found for the early component of the 3$^{rd}$ and 5$^{th}$ emission in graphite and $B_4C$ plasmas, reinforcing the idea of a population of atoms or small molecules, such as $C_2$, responsible for 3$^{rd}$ to 5$^{th}$ generation at early times in both materials. The spatial distribution of 4H nonlinear emitters investigated across the ablation plume is comparable to that found for the 3$^{rd}$ and 5$^{th}$ harmonics in graphite and $B_4C$ plasmas with a rather symmetric maximum at $z$ = 0 mm.

Regarding the effect of the relative polarization of the two driving beams, our results have shown an enhancement of the harmonic yield when both beams have parallel polarizations (figure 3.35). In the literature, there are several works reporting higher conversion efficiencies for parallel polarizations of the driving beam with respect to perpendicular polarizations [18, 19]. Nonetheless, Kim *et al*. [20] published results pointing towards the opposite behaviour, where a higher conversion efficiency is obtained for perpendicular polarizations via the relative phase matching of the driving beams and the better or worse phase matching due to the different degree of ionization in the medium.

## 3.2 Third to ninth harmonic generation in zinc sulfide plasma

The study of harmonic generation in laser ablation plasmas was extended to higher orders by implementing an important modification in the detection system (see Chapter 2, page 47 for more details). Odd harmonics up to the $9^{th}$ order of the fundamental 1064 nm radiation, have been studied in ZnS laser ablation plasmas [3]. Ablation of the ZnS targets was performed at 1064 nm under vacuum ($10^{-5}$ mbar).

### 3.2.1 Energy and spatiotemporal dependence of the harmonics signal

As in the previous materials, a systematic study of the energy and the spatiotemporal dependences of the harmonic signal was carried out here.

#### Energy dependence of the harmonic emission

The plots in figure 3.42 show the dependence of the $3^{rd}$, $5^{th}$, $7^{th}$ and $9^{th}$ harmonic signals, at 355 nm, 213 nm, 152 nm and 118 nm respectively, with the ablation pulse energy. Following the same nomenclature used before, the $7^{th}$ and $9^{th}$ harmonics will be denoted as 7H and 9H respectively. The driving beam was focused within the plasma volume at $x$ = 0.6 mm and $z$ = 0 mm and the delay between the ablation and driving laser pulses was optimized for each harmonic order. In the following figures, each data point is the result of averaging 64 acquisitions.

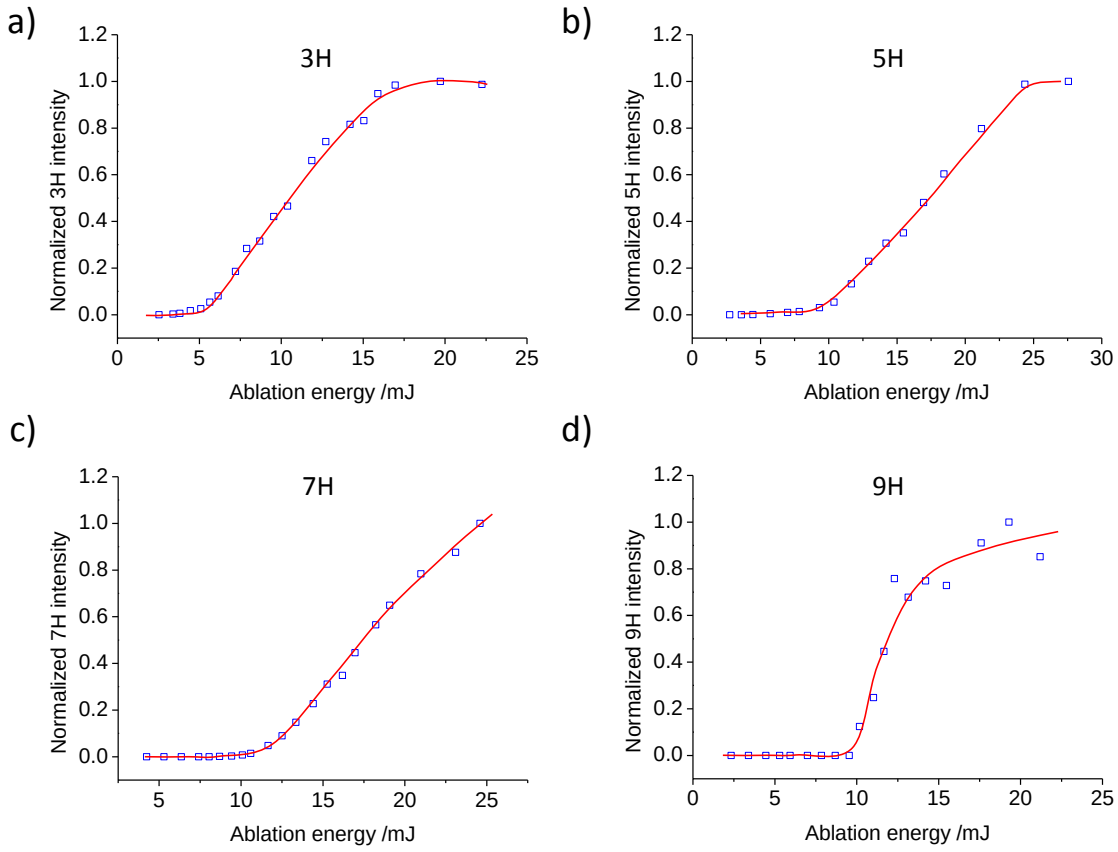


Figure 3.42 Dependence of the normalized harmonic signal with the ablation pulse energy obtained in zinc sulfide laser ablation plasmas for: a) 3H, b) 5H, c) 7H, d) 9H. The driving laser was focused at $x$ = 0.6 mm and $z$ = 0 mm and the delay between the ablation and driving pulses was optimized for each harmonic order. Ablation was performed at 1064 nm under vacuum conditions ($10^{-5}$ mbar). The red lines are visual guides.

The intensity of the different harmonics strongly depends on the ablation pulse energy, as this controls the amount of ejected material and thus the plasma density. The behaviour is shown in figure 3.42 for the early component of the harmonic signal for 3H, 5H and 7H and for the late component of the 9H signal (see figure 3.44). A sharp increase at pulse energies above 4, 8 and 11 mJ is observed for the 3H, 5H and 7H respectively. Above these values the signals grow linearly with pulse energy until a certain value, where saturation occurs. This behaviour can be attributed to several effects, including the dependence of the harmonics amplitude on phase mismatch and scattering or absorption of the driving and harmonics beam by the plasma.

The dependence of the harmonics signal with the driving laser energy was studied for the different harmonic orders. The results of these measurements are shown in the log-log plots of figure 3.43.

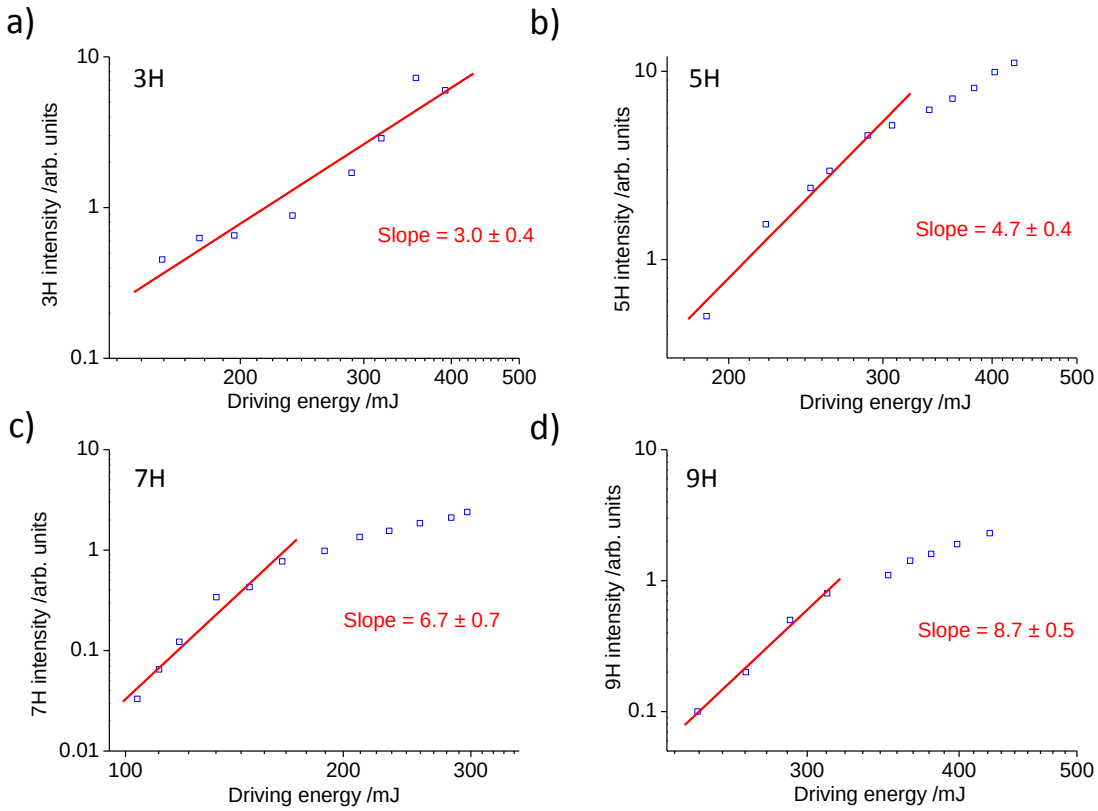


Figure 3.43 Intensity of the harmonic signal as a function of the driving pulse energy ploted in log-log scale. Harmonic generation was performed in a zinc sulfide ablation plasma by focusing the 1064 nm harmonics driving beam at $x = 0.6$ mm and $z = 0$ mm. The delay between the ablation and driving pulses was optimized for each harmonic order. Ablation was performed at 1064 nm under vacuum conditions ($10^{-5}$ mbar) with a fluence of ~2 J cm$^{-2}$. The red line is a linear fit of the data.

As can be seen in the plots, the slopes of the fitted data are in agreement with expected power laws for 3$^{rd}$, 5$^{th}$, 7$^{th}$ and 9$^{th}$ harmonic generation. However, over a certain value of the driving pulse energy, a change in the slope of the data is observed for the 5$^{th}$ to the 9$^{th}$ harmonics. As in the case of the ablation energy, above a certain pulse energy, fragmentation and ionization of species due the effect of the drivging pulse can lead to conditions in which larger phase mismatch and absorption of the generated harmonics are expected.

### Spatiotemporal study of the harmonic emission

The temporal behaviour of the studied harmonics is plotted in figure 3.44 in log-log form. The resulsts indicate the presence of two temporal components of the signal in the case of 3H, 5H and 7H. The early component maximizes in the region of 250 ns, while the

much broader second component, is observed at delays around 10 µs. Only this late component was observed for the 9H. As can be seen in the figure, the relative intensity of the early to late component of the signal decreases as the harmonic order increases. Direct comparison of the generation efficiency of the different harmonic orders is not straightforward due to the broad spectral range where the harmonics are emitted. However, taking into account the response of the detection system, it is expected that the generation efficiency follows a quasi-logarithmic decay with the harmonic order in the absence of resonances. On the contrary, the late component shows an anomalous behaviour and its signal intensity increases with the harmonic order up to the 7H.

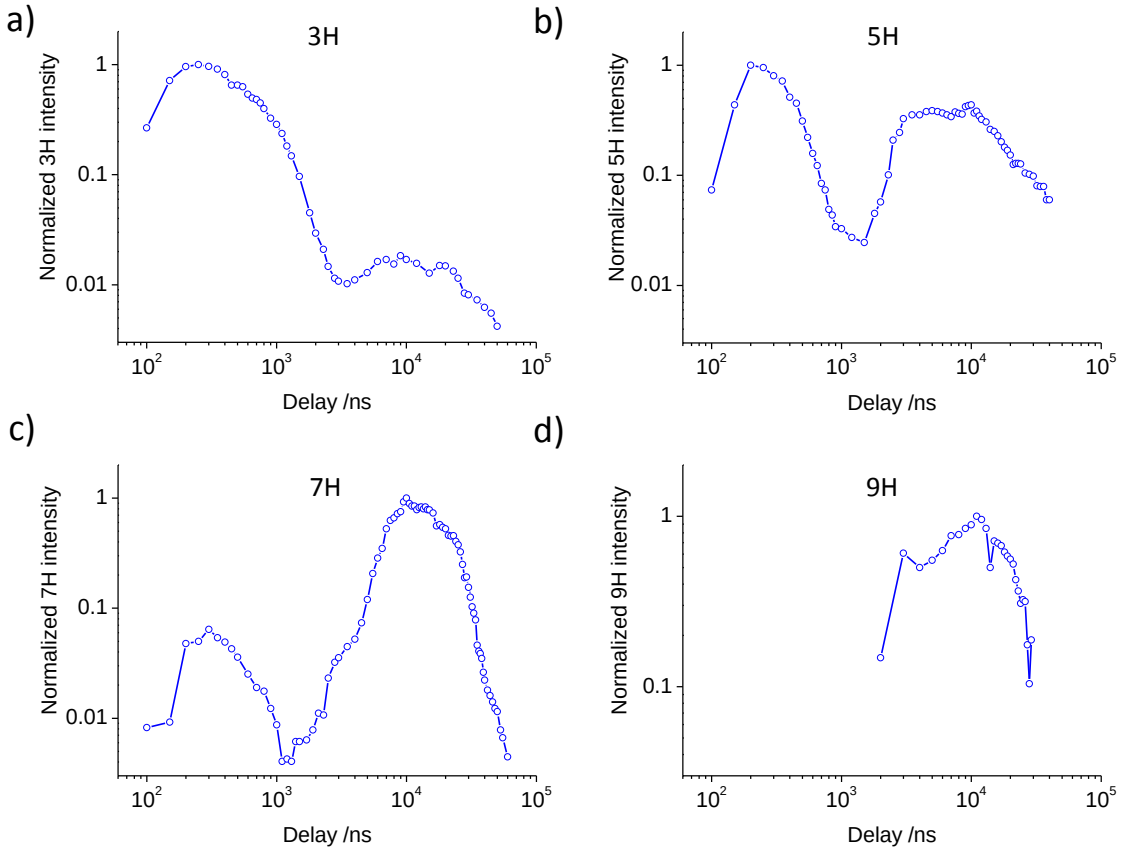


Figure 3.44 Temporal dependence of the harmonic signal with the delay between the ablation and driving laser pulses acquired in a zinc sulfide plasmas for: a) 3H, b) 5H, c) 7H, d) 9H. The 1064 nm harmonics driving beam propagates parallel to the target surface at a distance $x = 0.6$ mm and is focused $z = 0$ mm. Ablation was performed at 1064 nm under vacuum conditions ($10^{-5}$ mbar) using a fluence of ~2 J cm$^{-2}$.

The spatial behaviour of the harmonic signal was studied across the plasma plume by focusing the 1064 nm driving beam along the *x* and *z* axes. The results of the *z*-scans are shown in figure 3.45. The delay between the ablation and driving pulses was optimized in each case to observe the harmonics signal generated by the early component (see figures 3.44a, 3.44b and 3.44c), except in the case of the 9H (figure 3.44d), where this component was not observed. Therefore in this particular case the *z*-scan was performed at 10 μs delay.

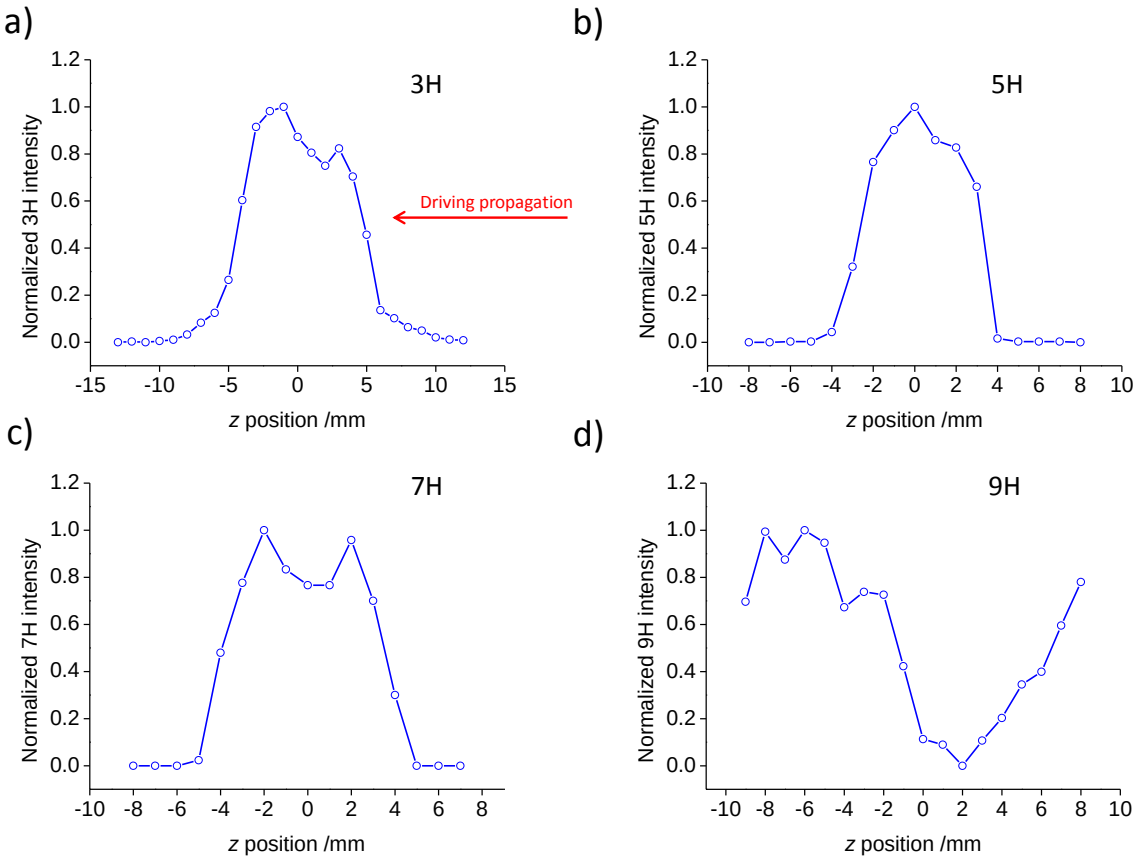


Figure 3.45 Harmonic signal intensity as a function of the *z* position of the 1064 nm driving beam focus with respect to the centre of the plasma plume (*z* = 0 mm) obtained in zinc sulfide plasmas for: a) 3H, b) 5H, c) 7H, d) 9H. The distance of the harmonics driving beam with respect to the target surface was fixed at *x* = 0.6 mm. Ablation was performed at 1064 nm with ~2 J cm$^{-2}$ under vacuum ($10^{-5}$ mbar). The delay between the ablation and driving pulses was optimized for each harmonic order. The red arrow indicates the propagation direction of the driving beam with respect to the plasma plume.

Figure 3.46 shows the *z*-scans of the 5H signal for the early and late components (see figure 3.44b) plotted together. As can be seen, a different spatial behaviour is found depending on the delay between the ablation and driving pulses. The *z*-scan acquired at 250 ns delay exhibits a rather symmetric maximum coinciding with the *z* = 0 mm position. On the contrary, the *z*-scan obtained at 10 μs delay has a minimum close to the central region.

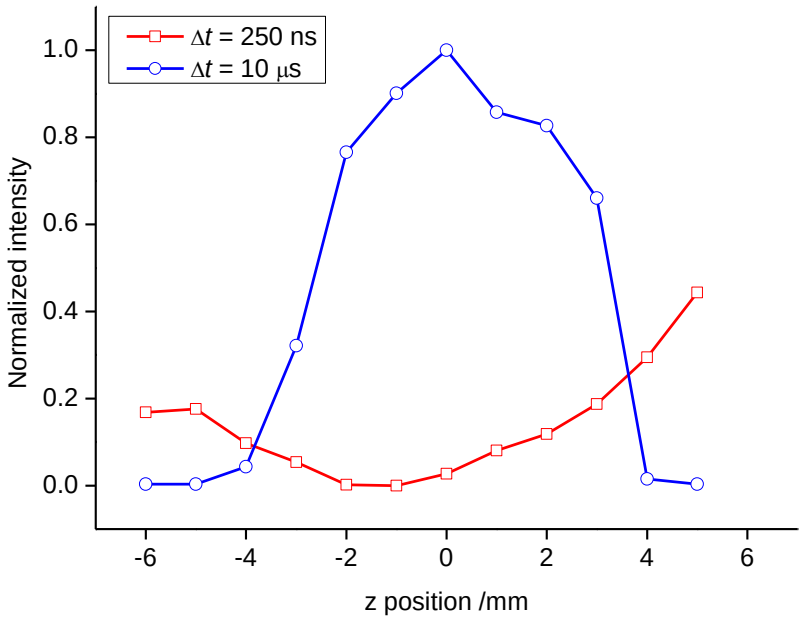


Figure 3.46 Dependence of th 5H with the *z* position of the driving beam focus along the *z* axis in a zinc sulfide laser ablation plasma for the early (250 ns) and late (10 μs) components of the 5H signal observed in figure 3.44b.

In the same way, the behavior of the harmonics signal with the distance of the driving beam focus whith respect to the target surface was explored. Figure 3.47 shows the obtained *x*-scans for each harmonic order. The same fast decay observed in plasmas of graphite and $B_4C$ generated under vacuum (see figures 3.11 and 3.21 in pages 84 and 93 respectively) is observed in ZnS.

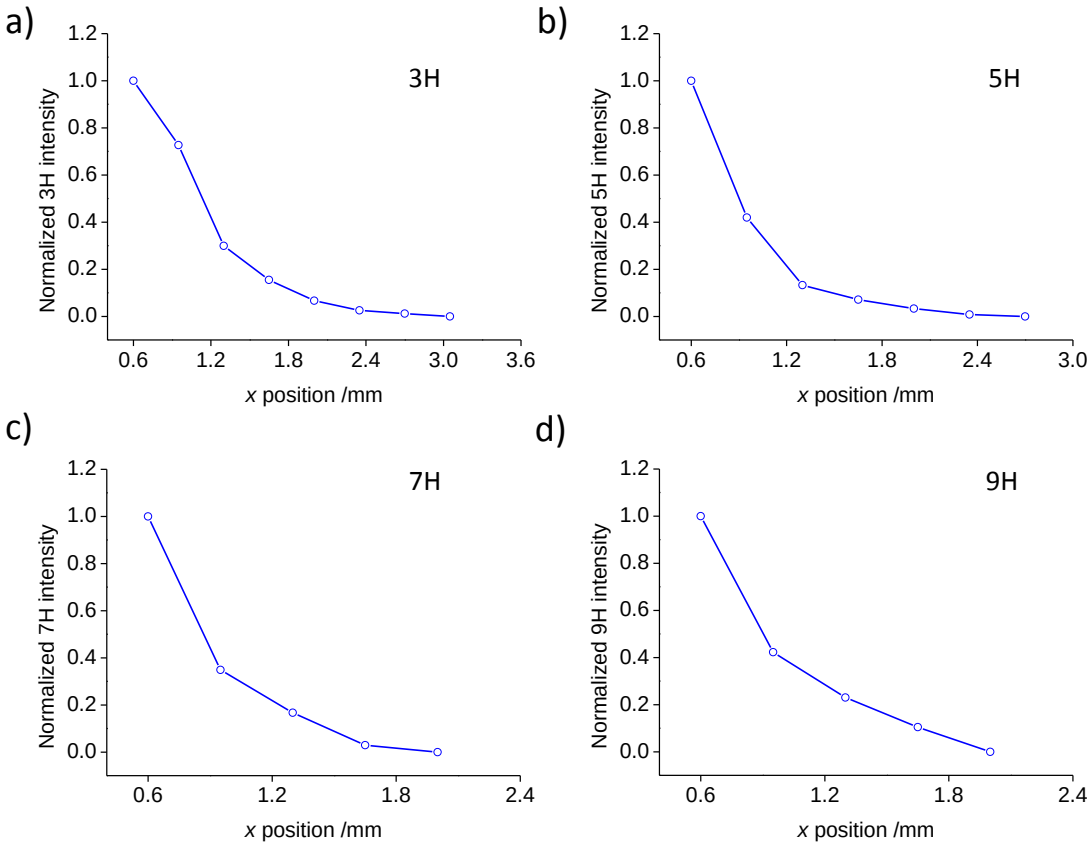


Figure 3.47 Harmonic intensity as a function of the *x* position of the 1064 nm driving laser beam focus with respect to the zinc sulfide target surface (*x* = 0 mm) for: a) 3H, b) 5H, c) 5H, d) 9H. The *z* position of the driving beam focus corresponds to *z* = 0 mm. Ablation was performed at 1064 nm with ~2 J cm$^{-2}$ under vacuum (10$^{-5}$ mbar). The delay between the ablation and driving pulses was optimized for each data for obtaining the maximum signal.

## 3.2.2 Characterization of ZnS laser ablation plasmas by OES

The spontaneous emission of the ZnS ablation plasma was studied by OES, both in the absence and in the presence of the driving beam, using different acquisition delays and temporal gate widths. Figure 3.48 shows the spectra aquired in the absence of the driving beam for the early and late components of the harmonics signal. The spectrum corresponding to the early component (figure 3.48a), acquired 200 ns after the ablation event in a temporal window of 200 ns, is enterely constituted by atomic emission lines mostly assigned to neutral Zn(I) species, indicating the formation of a low ionized plasma upon ablation. On the contrary, the spectrum corresponding to the late component (figure 3.48b), acquired 1 µs after the ablation event in a temporal window of 20 µs, is characterized by a broad emission which can be attributed to hot plasma nanoparticles [21-23]. A fit of the continuous emission spectrum to Planck´s law after correction by the

spectral response of the detection system, yielded a temperature around 2500 K. In this case, the atomic Zn lines are weak compared to those of the early component.

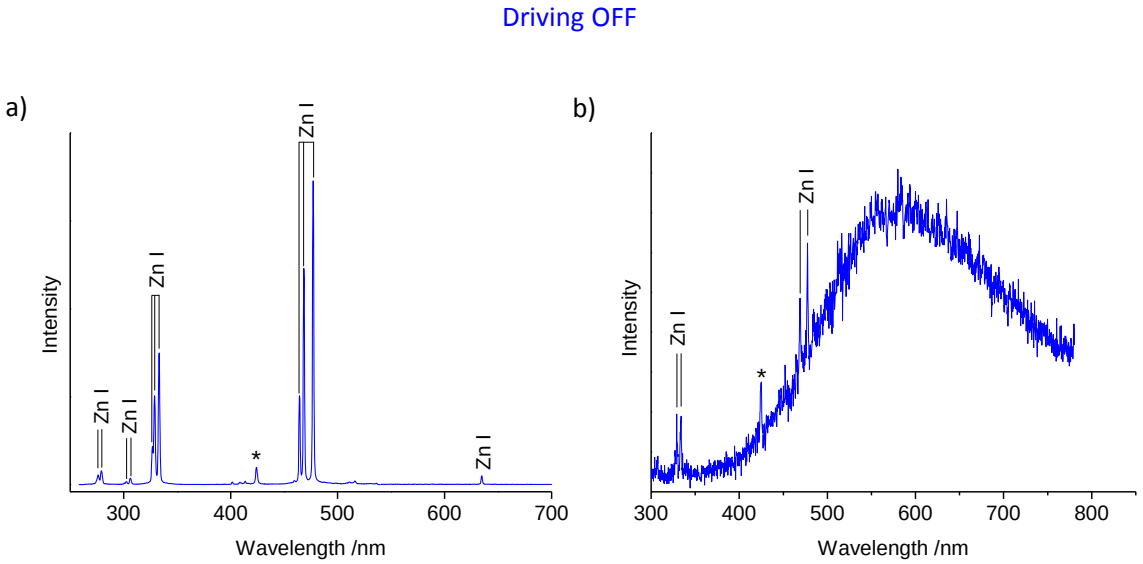


Figure 3.48 Optical emission spectra of laser ablation ZnS plasma aquired in the absence of the harmonics driving beam at: a) 200 ns of acquisition delay and temporal gate of 200 ns b) 1 µs acquisition delay and temporal gate of 20 µs. The star sign indicates that the line is a second order of Zn (I) emission at 213.86 nm.

The effect of the driving beam over the plasma emission can be observed in the spectra shown in figure 3.49. When the ablation and the driving lasers temporally overlap, the plasma emission is comparable to that shown in figure 3.48a. However, as soon as the driving beam is delayed by 100 ns or more with respect to ablation, the spectrum changes markedly. Figure 3.49a shows the corresponding spectrum of the early component of the harmonics signal, acquired by delaying the driving pulse by 400 ns with respect to the ablation event. New atomic lines, attributed mainly to ionic $Zn^{+}$, are observed and there is hardly any indication of *Bremsstrahlung* emission. In contrast, the spectrum corresponding to the late component obtained by delaying the driving beam at 12 µs and shown in figure 3.49b, is two orders of magnitude more intense and includes intense lines of ionic Zn and *Bremsstrahlung* emission. This situation corresponds to a much denser and ionized plasma.

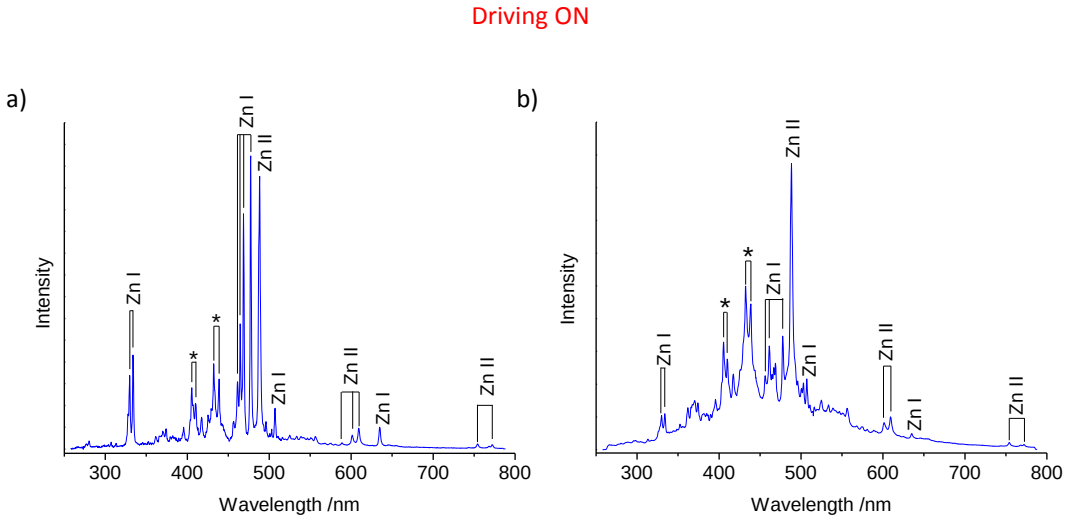


Figure 3.49 Optical emission spectra of laser ablation ZnS plasma acquired in the presence of the harmonics driving beam at a delay between the ablation and driving pulses of: a) 400 ns and b) 12 µs. Both spectra were acquired in a temporal gate of 200 ns at zero delay with respect to the driving pulse. The star sign indicates that the line is a second order of Zn (II) emission.

Finally, the intensities of the neutral Zn(I) at 477.5 nm and ionic Zn(II) at 488.4 nm emission lines are plotted against the delay between the ablation and driving pulses in figure 3.50.

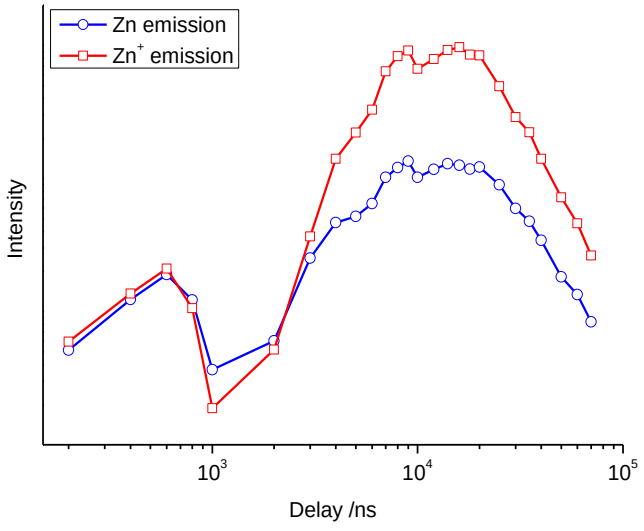


Figure 3.50 Intensities of the neutral and ionic Zn emission lines at 477.5 nm and 488.4 nm respectively plotted against the acquisition delay obtained in the presence of the driving beam. The signal was acquired in a temporal gate of 200 ns and the delay between the ablation and driving pulses was set to 10 µs.

The temporal structure of these atomic emissions clearly resembles that of the harmonic emission (see figure 3.44), with a rapid component peaking at few hundreds of nanoseconds and a delayed intense component at around 10 µs. It must be also emphasized that the degree of ionization of this second component is almost one order of magnitude higher than that of the first component.

### 3.2.3 Discussion of results

In the experiments described above, the 3H, 5H, 7H and 9H of the fundamental 1064 nm beam have been detected at their respective wavelengths of 355 nm, 213 nm, 152 nm and 118 nm. As mentioned, the power laws obtained (figure 3.43) correspond to the expected values, thus confirming the nonlinear nature of the emissions observed.

As shown in figure 3.44, the $3^{rd}$ to $7^{th}$ harmonic signal is characterized by the presence of two contributions to the nonlinear process at different delays time with respect to the ablation event. This multicomponent behaviour has been observed in HG experiments performed under inert gas atmospheres in graphite and $B_4C$ plasmas previously described in this chapter. In the case of ZnS, the late component was observed under vacuum conditions, indicating the presence of heavier species, such as clusters and/or nanoparticles generated upon ablation.

The relative intensity of the early and late components was found to vary with the harmonic order. For the early component, the maximum signal was obtained for the 3H and its intensity is found to drop with the harmonic order, becoming undetectable for the 9H. For the late component, an anomalous behaviour was observed. The signal increases with the harmonic order, maximizing for the 7H and is still clearly visible for the 9H. Therefore, the ratio of the harmonic intensities of the early to late component, measured at the centre of the plasma plume, suffers a decrease from the 3H to the 9H of more than two orders of magnitude.

The analysis of the ZnS plasma emissions by OES helps to clarify the nature of the nonlinear species that are the origin of HG in the plasma plume. The first temporal maximum observed in the harmonic signal at around 250 ns, would correspond with species moving away from the target at velocities around 3400 m $s^{-1}$. This velocity value is compatible with the propagation of fast atomic species in nanosecond laser ablation plumes [6, 24]. According to the OES analysis of the plume emission, at this time delay the plasma is mainly composed by atomic Zn species (see figure 3.48a). The role of

neutral Zn atoms is expected to be significantly more important than that of the S atoms due to their larger polarizability [25].

The temporally delayed component of the plasma has been shown by OES to be mainly constituted by nanoparticles (see figure 3.48b). This nanoparticle population, propagating at velocities in the range of 100-200 m $s^{-1}$, is believed to be the precursor of species responsible for HG at delay times around 10 μs upon interaction with the driving beam. The spectrum shown in figure 3.49b indicates that the driving beam causes extensive fragmentation and ionization of these nanoparticles, inducing a secondary plasma. The generated neutrals and ions act as delayed nonlinear species and yield a particularly intense harmonic emission. In this situation, the $Zn^+$ ions are believed to be the main responsible species for harmonic generation. Ions are known to present lower harmonic generation efficiency due to their lower polarizability, but it is also known that they tend to extend the cut-off compared to neutrals, at least in the strong field regime [26]. Under this assumption, it can be concluded that the first component of the harmonic signal can be attributed mainly to neutral species and the late component mainly to ionic species. This fact is supported by the temporal behaviour of the Zn and $Zn^+$ signals (see figure 3.50) which follow a similar temporal evolution than the harmonics signal and provides evidence of a higher degree of ionization for the late component. Moreover, resonance effects can play a role in the enhancement of the conversion efficiency for certain harmonic orders. The particularly intense 7H emission at long delays can be related to a seven-photon resonant $3d^{10}4s$-$3d^9 4s^2$ transition of the singly-charged Zn ions at 65441.41 $cm^{-1}$.

Regarding the spatial behaviour of the harmonics signal, the *z*-scan profiles obtained for the early component at delay of 250 ns for a $x$ = 0.6 mm distance exhibit the aforementioned minimum in the signal around $z$ = 0 mm, indicative of a situation in which the plasma conditions in the central part of the plume involve a detrimental phase matching. This minimum around $z$ = 0 mm is patent in the case of the 9H signal (figure 3.45d).

Additionally, the spatial behaviour of the harmonic signal has been found to be dependent on the delay between the ablation and driving pulses. This dependence is patent by comparison of *z*-scans of the 5H signal obtained from the faster and slower populations and plotted in figure 3.46. The marked differences observed for the early and late components, are related to the higher density of species in the secondary plasma induced by the driving laser upon interaction with the nanoparticle population. As

discussed previously, the presence of a minimum in the *z*-scan profile is attributed to conditions where there is a larger phase mismatch caused by the contribution of the dispersion of the radiation and of the presence of free electrons in the medium. This highly ionized plasma is characterized by a strong Bremsstrahlung emission (see figure 3.49b), indicative of a high density of free electrons.

The behaviour of the harmonic signal with the distance from the target surface reveals a faster decay for higher order harmonics in the case of the early component. The signal vanishes at around $x$ = 3 mm for the $3^{rd}$ and $5^{th}$ harmonics, while for the $7^{th}$ and $9^{th}$ orders becomes near zero at distances shorter than 2 mm. This observation can be attributed to the relative efficiency of the nonlinear processes. The less efficient low-order processes require a higher density of species and therefore the signal will decay faster as the plume is explored away from the ablation spot.

## 3.3 References


1. I. Lopez-Quintas, M. Oujja, M. Sanz, M. Martín, R.A. Ganeev, M. Castillejo, *Low-order harmonic generation in nanosecond laser ablation plasmas of carbon containing materials,* Applied Surface Science, **278** (2013) p. 33.
2. M. Oujja, A. Benítez-Cañete, M. Sanz, I. Lopez-Quintas, M. Martín, R. de Nalda, M. Castillejo, *Frequency mixing in boron carbide laser ablation plasmas,* Applied Surface Science, **336** (2015) p. 53.
3. M. Oujja, I. Lopez-Quintas, A. Benítez-Cañete, M. Martín, R. de Nalda, M. Castillejo, *Harmonic generation by atomic and nanoparticle precursors in a ZnS laser ablation plasma*, (Submitted 2016).
4. L. Nemes, A.M. Keszler, C.G. Parigger, J.O. Hornkohl, H.A. Michelsen, V. Stakhursky, *Spontaneous emission from the $C_3$ radical in carbon plasma,* Applied Optics, **46** (2007) p. 4032.
5. P. Monchicourt, *Onset of carbon cluster formation inferred from light emission in a laser-induced expansion,* Physical Review Letters, **66** (1991) p. 1430.
6. F. Claeyssens, M.N.R. Ashfold, E. Sofoulakis, C.G. Ristoscu, D. Anglos, C. Fotakis, *Plume emissions accompanying 248 nm laser ablation of graphite in vacuum: Effects of pulse duration,* Journal of Applied Physics, **91** (2002) p. 6162.
7. W. An, X. Zhao, Z. Zhang, R. Su, *Carbon dendrite formation induced by pulsed laser irradiation,* Applied Surface Science, **256** (2010) p. 2304.
8. P.M. Ossi, A. Miotello, *Control of cluster synthesis in nano-glassy carbon films,* Journal of Non-Crystalline Solids, **353** (2007) p. 1860.
9. A. Lago, G. Hilber, R. Wallenstein, *Optical-frequency conversion in gaseous media,* Physical Review A, **36** (1987) p. 3827.
10. W. Theobald, C. Wülker, F.P. Schäfer, B.N. Chichkov, *High-order harmonic generation in carbon vapor and low charged plasma,* Optics Communications, **120** (1995) p. 177.
11. A.B. Fedotov, N.I. Koroteev, A.M. Zheltikov, *Phase-Matching Effects in the Generation of the Third and Fifth Harmonics of Nd:YAG-Laser Radiation in a Low-Temperature Laser-Produced Plasma,* Laser Physics, **5** (1995) p. 812.
12. R. Boyd, *Nonlinear Optics*, 2008, Academic Press.
13. A. L'Huillier, P. Balcou, *High-order harmonic generation in rare gases with a 1-ps 1053-nm laser,* Physical Review Letters, **70** (1993) p. 774.
14. M.B. Gaarde, P. Antoine, A. Persson, B. Carré, A.L. Huillier, C.G. Wahlström, *High-order tunable sum and difference frequency mixing in the XUV region,* Journal of Physics B: Atomic, Molecular and Optical Physics, **29** (1996) p. L163.
15. C.F. Kaminski, I.G. Hughes, P. Ewart, *Degenerate four-wave mixing spectroscopy and spectral simulation of $C_2$ in an atmospheric pressure oxy-acetylene flame,* The Journal of Chemical Physics, **106** (1997) p. 5324.
16. P.L. Shkolnikov, A.E. Kaplan, A. Lago, *Phase matching for large-scale frequency upconversion in plasma,* Optics Letters, **18** (1993) p. 1700.
17. S. Meyer, H. Eichmann, T. Menzel, S. Nolte, B. Wellegehausen, B.N. Chichkov, C. Momma, *Phase-Matched High-Order Difference-Frequency Mixing in Plasmas,* Physical Review Letters, **76** (1996) p. 3336.

18. M.D. Perry, J.K. Crane, *High-order harmonic emission from mixed fields,* Physical Review A, **48** (1993) p. R4051.
19. H. Eichmann, A. Egbert, S. Nolte, C. Momma, B. Wellegehausen, W. Becker, S. Long, J.K. McIver, *Polarization-dependent high-order two-color mixing,* Physical Review A, **51** (1995) p. R3414.
20. I.J. Kim, C.M. Kim, H.T. Kim, G.H. Lee, Y.S. Lee, J.Y. Park, D.J. Cho, C.H. Nam, *Highly Efficient High-Harmonic Generation in an Orthogonally Polarized Two-Color Laser Field,* Physical Review Letters, **94** (2005) p. 243901.
21. K. Sasaki, T. Wakasaki, K. Kadota, *Observation of continuum optical emission from laser-ablation carbon plumes,* Applied Surface Science, **197–198** (2002) p. 197.
22. D.B. Geohegan, A.A. Puretzky, *Species-resolved imaging and gated photon counting Spectroscopy of laser ablation plume dynamics During KrF- and ArF- laser PLD of amorphous diamond films,* MRS Online Proceedings Library Archive, **397** (1995) p. 55.
23. E.A. Rohlfing, *Optical emission studies of atomic, molecular, and particulate carbon produced from a laser vaporization cluster source,* The Journal of Chemical Physics, **89** (1988) p. 6103.
24. O. Albert, S. Roger, Y. Glinec, J.C. Loulergue, J. Etchepare, C. Boulmer-Leborgne, J. Perrière, E. Millon, *Time-resolved spectroscopy measurements of a titanium plasma induced by nanosecond and femtosecond lasers,* Applied Physics A, **76** (2003) p. 319.
25. S. Fähler, H.-U. Krebs, *Calculations and experiments of material removal and kinetic energy during pulsed laser ablation of metals,* Applied Surface Science, **96–98** (1996) p. 61.
26. J.L. Krause, K.J. Schafer, K.C. Kulander, *High-order harmonic generation from atoms and ions in the high intensity regime,* Physical Review Letters, **68** (1992) p. 3535.

# Chapter 4

# Pulsed laser deposition for the synthesis of micro and nanostructured materials

# 4. Pulsed laser deposition for the synthesis of micro and nanostructured materials

This chapter describes two different experiments intended to understand and improve the laser ablation and deposition processes for the synthesis of two types of materials.

The aim of the first experiment, described in section 4.1, is to study the growth process of micrometric-size structures from boron carbide targets by nanosecond PLD under different atmospheric conditions and ablation wavelengths [1].

The second experiment, described in section 4.2, deals with the fundamentals of double pulse femtosecond laser ablation dynamics of Co/ZnS targets in order to search for control mechanisms for the synthesis via fs-PLD of DMS based on cobalt-doped zinc sulfide [2].

## 4.1 Nanosecond pulsed laser deposition of boron carbide: fabrication of micrometric size columns

As mentioned in the introduction chapter, boron carbide is a material exhibiting special properties which make it a very interesting starting compound for PLD experiments. Nevertheless, our first approach to PLD of $B_4C$ was related to the harmonic generation experiments described in Chapter 3.

In HG experiments, PLD served to study the differences of the ejected material upon ablation of $B_4C$ targets under different ambient conditions: low vacuum and inert gas atmosphere. At this point, it is important to bear in mind that PLD was used more as a diagnostic method for the characterization of the structure and dimensions of the deposited material than as a synthesis technique.

For this reason, the first deposits obtained by PLD of $B_4C$ were produced simultaneously with low-order harmonic generation experiments and therefore in optimized experimental conditions (irradiation parameters, pressure etc.) for obtaining a good harmonic signal.

The first PLD/HG experiments, performed under low vacuum, revealed the formation of well-defined structures over a continuous film (figure 4.1). The observation of these features motivated a new set of PLD experiments, this time under improved vacuum, which yielded larger and better defined structures. In these conditions, more typical of a PLD experiment, the influence of the deposition time and ablation laser wavelength on the collected material was studied. The most characteristic deposits, containing micrometric-size columns were characterized in terms of morphology and composition. Table 4.1 summarizes the main experimental conditions explored in the experiments.

Table 4.1 Summary of experimental conditions used in PLD of boron carbide.

<table>
<tr><th colspan="2">Atmosphere</th><th>Pressure (mbar)</th><th>Ablation wavelength (nm)</th><th>Fluence (J cm$^{-2}$)</th><th>Deposition time (minutes)[a]</th><th>Substrate</th></tr>
<tr><td rowspan="5">Vacuum</td><td>Low vacuum</td><td>$10^{-2}$</td><td>1064</td><td rowspan="3">3</td><td>60</td><td rowspan="7">Monocrystalline silicon</td></tr>
<tr><td rowspan="4">High vacuum</td><td rowspan="3">$10^{-5}$</td><td rowspan="2">1064</td><td>20</td></tr>
<tr><td>60</td></tr>
<tr><td rowspan="2">266</td><td>1</td><td>20</td></tr>
<tr><td rowspan="2">Inert gas</td><td>Krypton</td><td rowspan="2">1</td><td rowspan="2">1064</td><td rowspan="2">3</td><td rowspan="2">60</td></tr>
<tr><td>Xenon</td></tr>
</table>

[a] at 10 Hz repetition rate.

### 4.1.1 Pulsed laser deposition experiments under low-vacuum conditions

Ablation of $B_4C$ was performed using 7 ns laser pulses at 1064 nm with a fluence of ~3 J $cm^{-2}$. The focused ablation beam was driven at normal incidence with respect to the target surface. The deposition time was set to 60 minutes at a repetition rate of 10 Hz (unless otherwise specified). The 1064 nm driving laser for harmonic generation was fired at a controllable delay after the ablation event and was focused within the plasma volume (see Chapter 3, section 3.1). No external heating of the substrates was performed and the chamber was pumped down to a pressure in the order of $10^{-2}$ mbar. Silicon substrates were placed in front of the target at 4 cm from its surface on a specially designed holder that allows propagation of the ablation laser beam at normal incidence (see experimental section for more details on the PLD experimental configuration).[8]

In the above conditions, a set of deposits were obtained and analyzed by SEM. The obtained images, shown in figure 4.1, revealed the formation of regular structures scattered all over the substrate (see figure 4.1a). Some of the structures appear lying on the substrate surface (figure 4.1b) while others appear standing on it (figure 4.1c). The structures exhibit an elongated shape with a typical length of about 3 µm (see figure 4.1b). Inspection of the standing structures reveals a square-shaped section with typical side dimensions of 500 nm (figure 4.1c). These elongated particles appear over a continuous film, which can be observed in figure 4.2 in contrast with the clean silicon surface that was masked before deposition. The particles described previously can be seen as bright spots onto the background layer (above the dashed line). The clear region below the dashed line corresponds to the masked area of the Si substrate. A more detailed view of this nanostructured film is shown later in this section (see the high-resolution SEM image of figure 4.11).

[8] Samples were prepared in batches obtained in different days. In the following, the designation of each sample appears in the figures as “sample #n”.

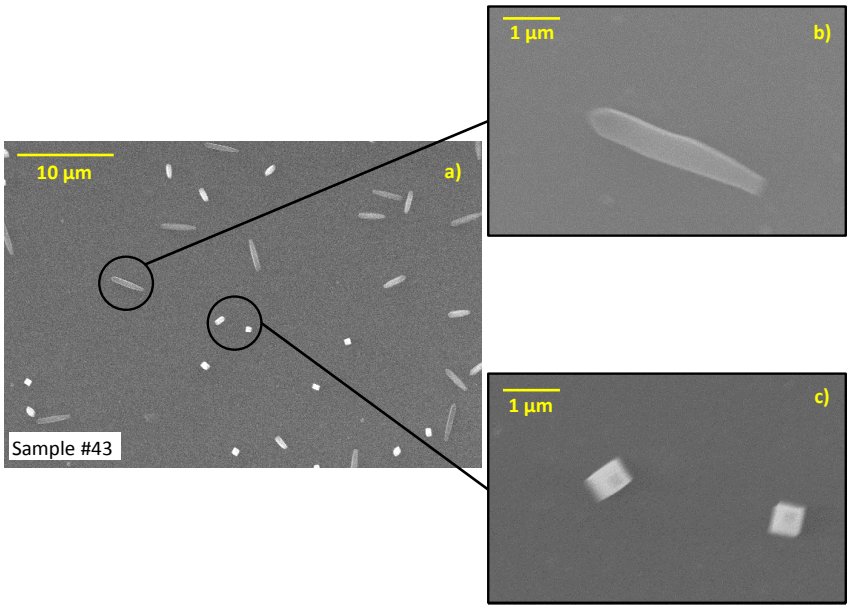


Figure 4.1 SEM images of deposits obtained by PLD of $B_4C$ simultaneously with LHG experiments. Ablation was performed at 1064 nm under low vacuum ($10^{-2}$ mbar) using a fluence of 3 J $cm^{-2}$.

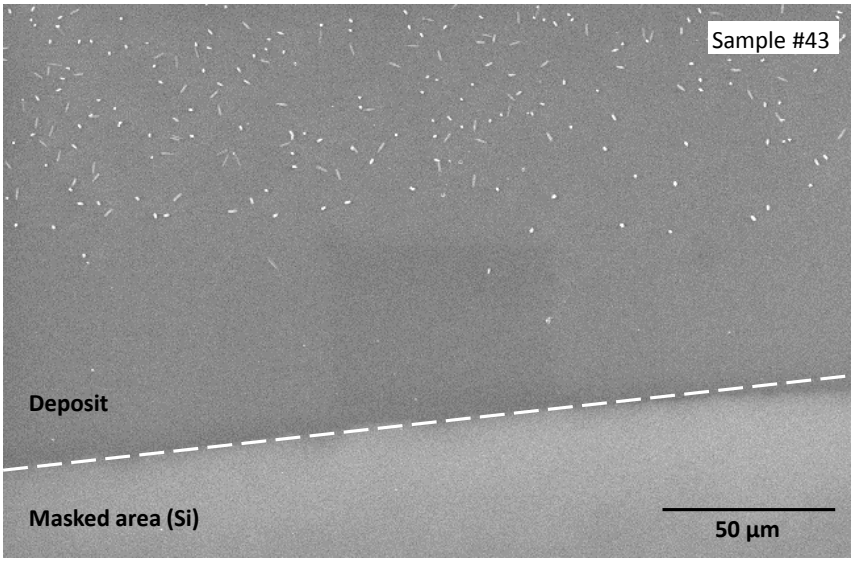


Figure 4.2 SEM image of a general top view of a PLD deposit obtained from $B_4C$ simultaneously with LHG experiments. Ablation was performed at 1064 nm under low vacuum ($10^{-2}$ mbar) using a fluence of 3 J $cm^{-2}$.

### 4.1.2 Pulsed laser deposition experiments under inert gas atmosphere

In order to study the influence of the background atmosphere on the ablation process, Kr gas was flowed maintaining a constant pressure of 1 mbar inside the chamber. The irradiation conditions were the same (for both the ablation and driving laser) than those described in the previous section for experiments under low vacuum. In figure 4.3, SEM images of the obtained deposits differ strongly from those obtained under low-vacuum conditions. Here, the features that characterize the deposits exhibit a spherical shape with diameters below 1 µm, as those observed in the high magnification image of figure 4.3b, or filamentous structures, similar to dendritic carbon, grown on top of the background film, as can be observed in detail in figure 4.3d.

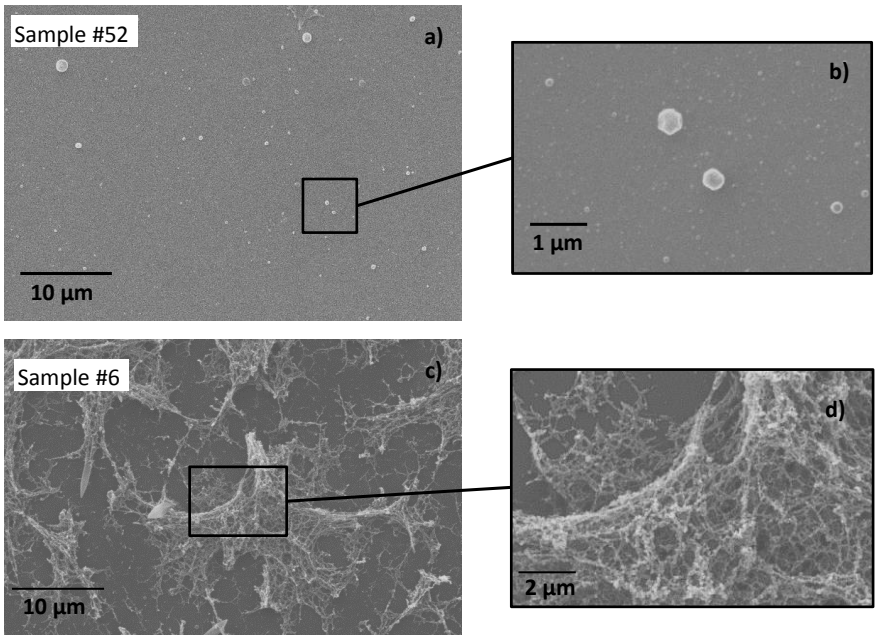


Figure 4.3 SEM images of deposits obtained by PLD of $B_4C$ simultaneously with LHG experiments under 1 mbar of Krypton. Ablation was performed at 1064 nm using a fluence of 3 J $cm^{-2}$.

Deposits were also grown under a flux of Xe, maintaining a constant pressure of 1 mbar inside the ablation chamber and using the same irradiation conditions. SEM images of the obtained deposits, shown in figure 4.4, display a lower density of particles compared to those obtained under 1 mbar of Kr. As in the previous experiment performed under Kr atmosphere, some sub-micrometric spherical particles can be observed onto the background film. Dendritic structures were not observed in this case.

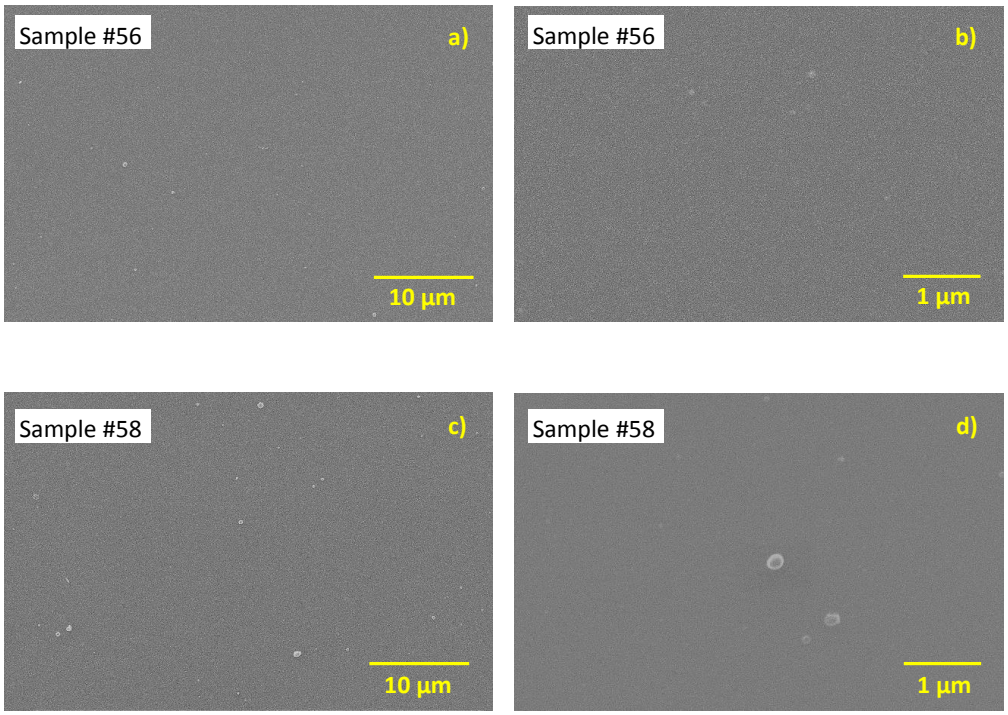


Figure 4.4 SEM images of deposits obtained by PLD from $B_4C$ targets simultaneously with LHG experiments under 1 mbar of Xenon. Ablation was performed at 1064 nm using a fluence of 3 J $cm^{-2}$.

### 4.1.3 Pulsed laser deposition experiments under improved vacuum conditions

After the observation of the regular structures obtained under low vacuum, experimental conditions aimed to enhance their growth were chosen. For that purpose two changes were made in the experimental parameters and set-up: first the vacuum conditions were improved from $10^{-2}$ to $10^{-5}$ mbar and second, the deposits were fabricated in a dedicated PLD experiment with a simpler configuration, this time in the absence of the harmonics driving laser. Additionally, the influence of the ablation laser wavelength and of the deposition time was studied under these improved ambient conditions. The rest of experimental parameters were kept identical to those of the previous experiments.

### 1064 nm ablation

Ablation and deposition at 1064 nm under improved vacuum conditions yielded deposits that differ dramatically from those obtained under low vacuum. In this case, the morphological analysis of the deposits by SEM revealed the presence of slightly larger and better-defined structures, exhibiting a square profile with sharp edges and in some cases a hollow core, as can be seen in figure 4.5.

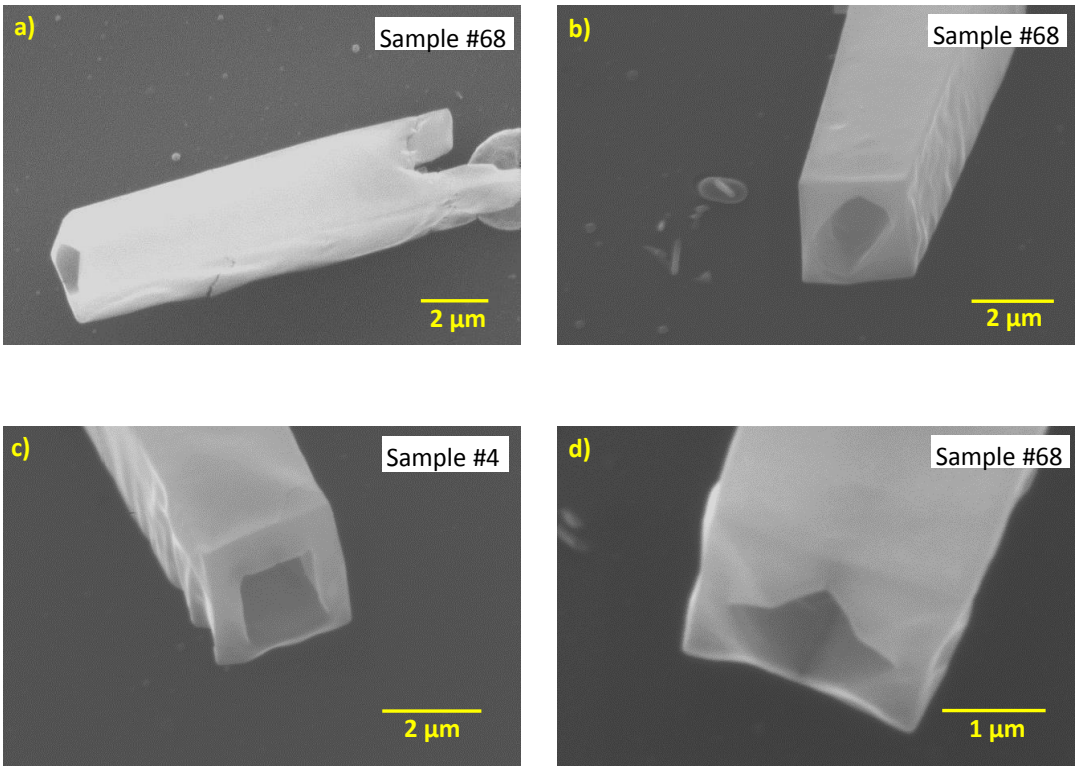


Figure 4.5 SEM images of the structures obtained by PLD of $B_4C$ under improved vacuum conditions ($10^{-5}$ mbar). Ablation was performed at 1064 nm using a fluence of 3 J $cm^{-2}$.

High-resolution SEM images allowed a better inspection of the structures. In figure 4.6 four of the hollow square-shaped columns are displayed in more detail. The elongated structures appear standing on the substrate surface, which is indicative of a vertical growth. In the first two HR-SEM images of figure 4.6a and 4.6b, the structures display sharp edges and faceted tips. These features can be observed in more detail in figure 4.7, where some solid (not hollow) structures are shown.

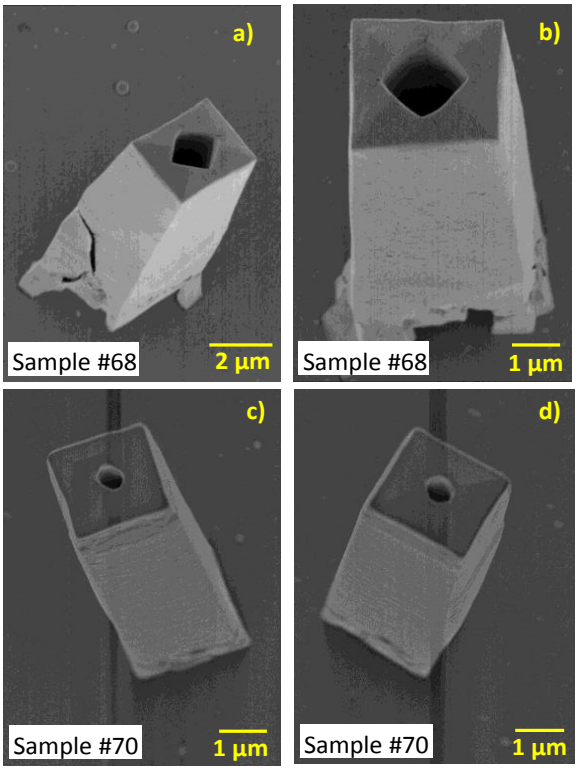


Figure 4.6 HR-SEM images of four microcolumns obtained by PLD of $B_4C$ under high-vacuum conditions ($10^{-5}$ mbar). Ablation was performed at 1064 nm using a fluence of 3 J $cm^{-2}$.

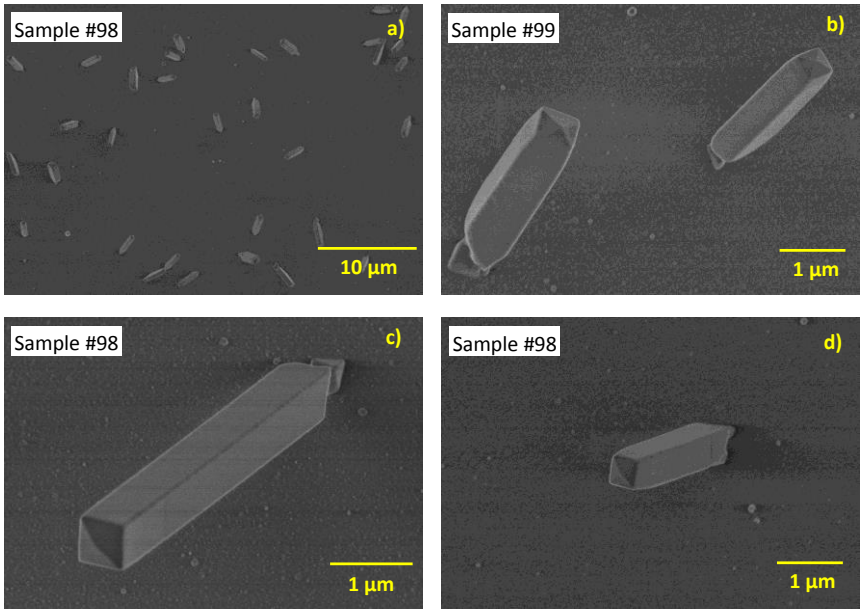


Figure 4.7 HR-SEM images of microcolumns obtained by PLD of $B_4C$ under high-vacuum conditions ($10^{-5}$ mbar). Ablation was performed at 1064 nm using 3 J $cm^{-2}$. a) General view of the deposit. b-d) High magnification images of individual microcolumns.

Comparing figures 4.6 and 4.7, elongated structures with different shapes and sizes were obtained in experiments performed under the same nominal conditions. While the structures in figure 4.6 have a hollow core, the columns obtained in deposits shown in figure 4.7 are solid.

At this point it was reasonable to think that both types of elongated structures (hollow and solid) could be the result of a different degree of evolution of the growth process, and the structures that appear hollow in some of the deposits could be closed as the growth evolves.

For this reason, the FIB technique was applied to obtain more information on the morphology of the microcolumns. As described in the experimental section, this technique can be used to accurately cut an individual structure and therefore was appropriate to find if the solid microcolumns were solid all along their length. The aspect of the structures after the successive cuts from the tip to the base is shown in the sequence of FIB-SEM images of figure 4.8.

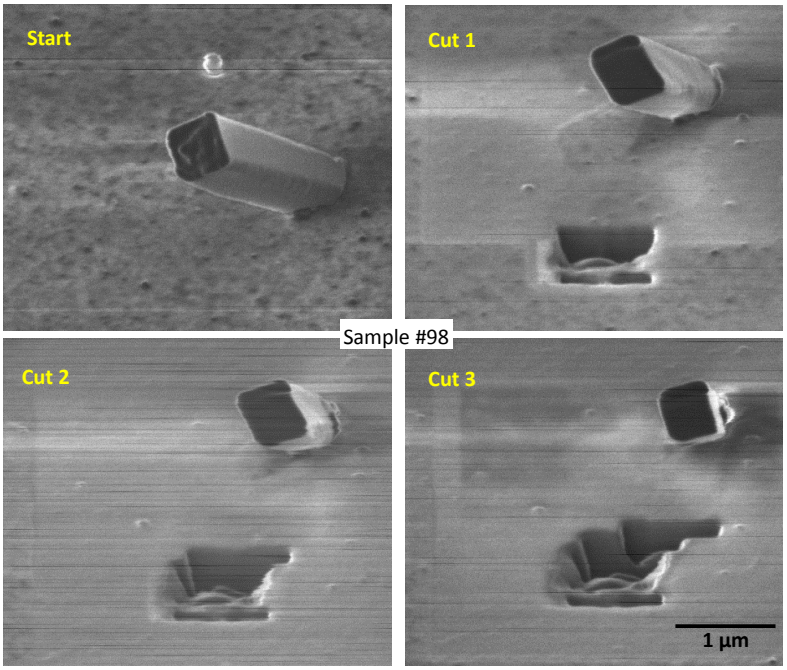


Figure 4.8 FIB-SEM images of one of the solid microcolumns successively etched with the FIB. The deposit containing the structure was prepared by PLD of $B_4C$ at 1064 nm ablation wavelength under high vacuum ($10^{-5}$ mbar) using a fluence of 3 J $cm^{-2}$. The images correspond to a sequence of three cuts from the top of the structure (top left) towards the base.

From the images, it can be concluded that the analyzed structure is solid from the tip to the base. In the same way, a hollow structure was etched with the FIB. As observed in figure 4.9, after several cuts starting from the tip, the dimensions of the hole decrease and the structure appears to be solid close to its base.

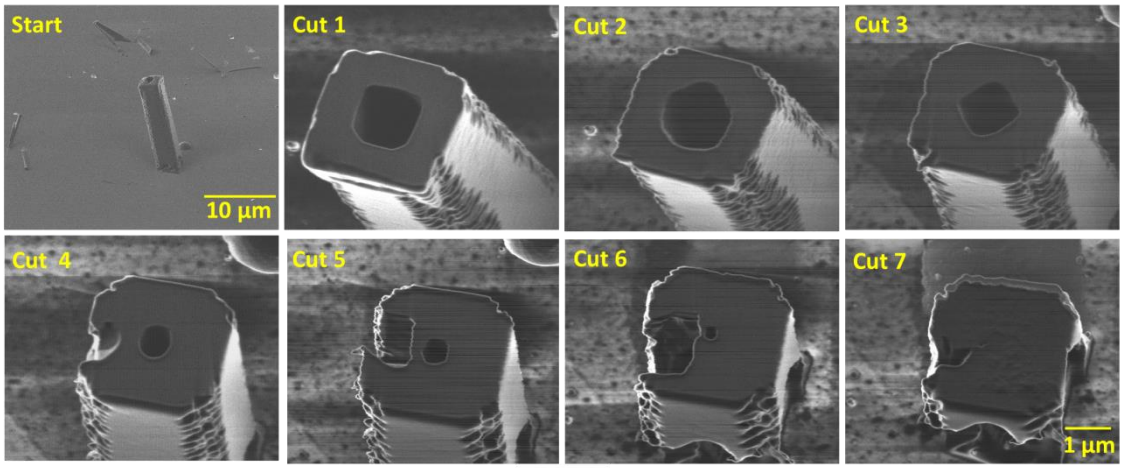


Figure 4.9 FIB-SEM images of the etching sequence of one of the hollow microcolumns from the tip to the base. The deposit was obtained by PLD of $B_4C$ at 1064 nm under high-vacuum conditions ($10^{-5}$ mbar) using a fluence of 3 J $cm^{-2}$.

The different orientation of the hole with respect to the external faces of the structure is also remarkable. These differences can be observed in figures 4.5b-d, as well as in figure 4.6a and 4.6b. By comparison of these images, it can be noted that in some structures, the sides of the hole appear parallel to the outer walls, whereas in some others the hole is rotated by 45°. This rotation can be also observed in the FIB-SEM images of figure 4.9. After the first cut, it appears parallel to the outer faces, while after the third cut, the hole appears rotated.

Other aspect that can be noticed after the inspection of some of the SEM images is the possibility of a stratigraphic or layer by layer growth of the structures. Several microcolumns observed in HR-SEM images, as the ones shown in figures 4.6c, 4.6d and 4.10, appear to be formed by multiple staked layers.

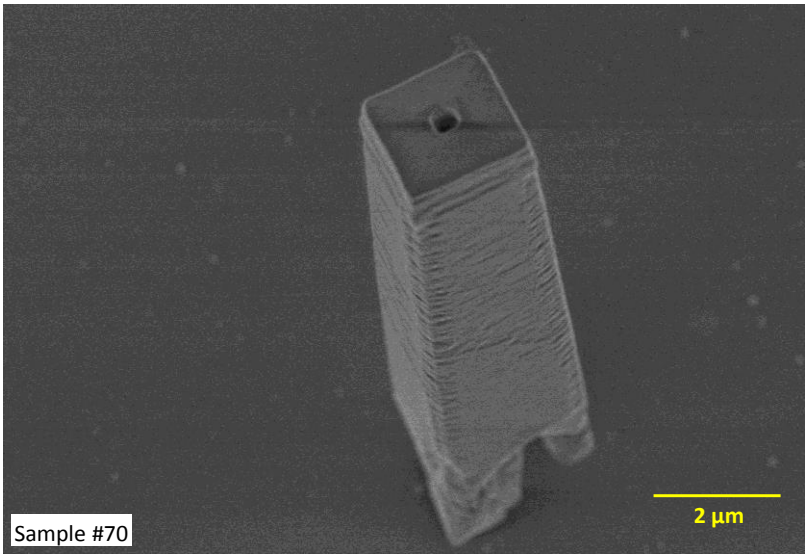


Figure 4.10 HR-SEM image showing a detailed view of one of the microcolumns obtained by PLD of $B_4C$ by ablation at 1064 nm under high vacuum ($10^{-5}$ mbar) using a fluence of 3 J $cm^{-2}$.

Other types of structures were also found in the deposits prepared by ablation at 1064 nm under high-vacuum conditions. Figure 4.11 shows a detailed view of the aforementioned background film composed by nanometric-size rounded particles.

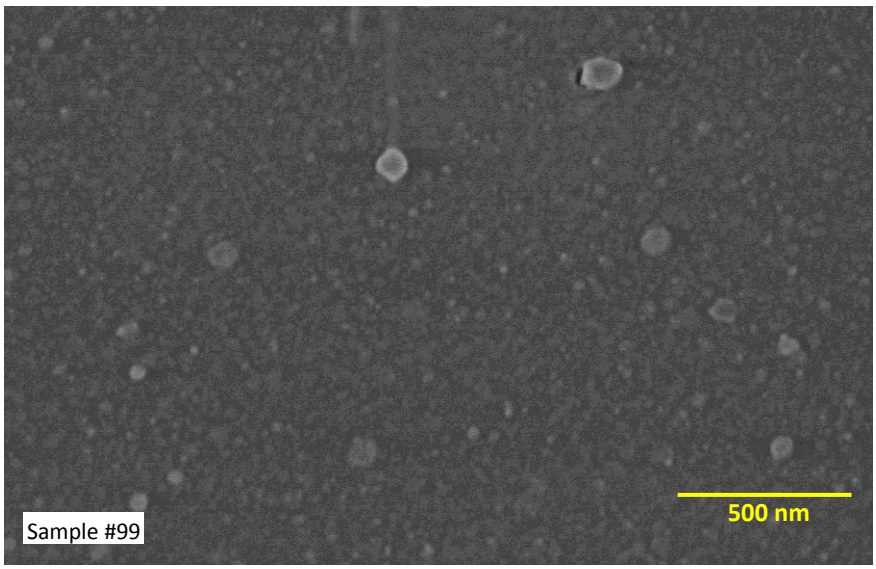


Figure 4.11 HR-SEM image of the nanostructured background film observed on the silicon substrate after PLD of $B_4C$ at 1064 nm under high-vacuum ($10^{-5}$ mbar) using a fluence of 3 J $cm^{-2}$.

Figure 4.12 shows a high magnification HR-SEM image of a spherical sub-micrometric particle form which several nanorods emerge.

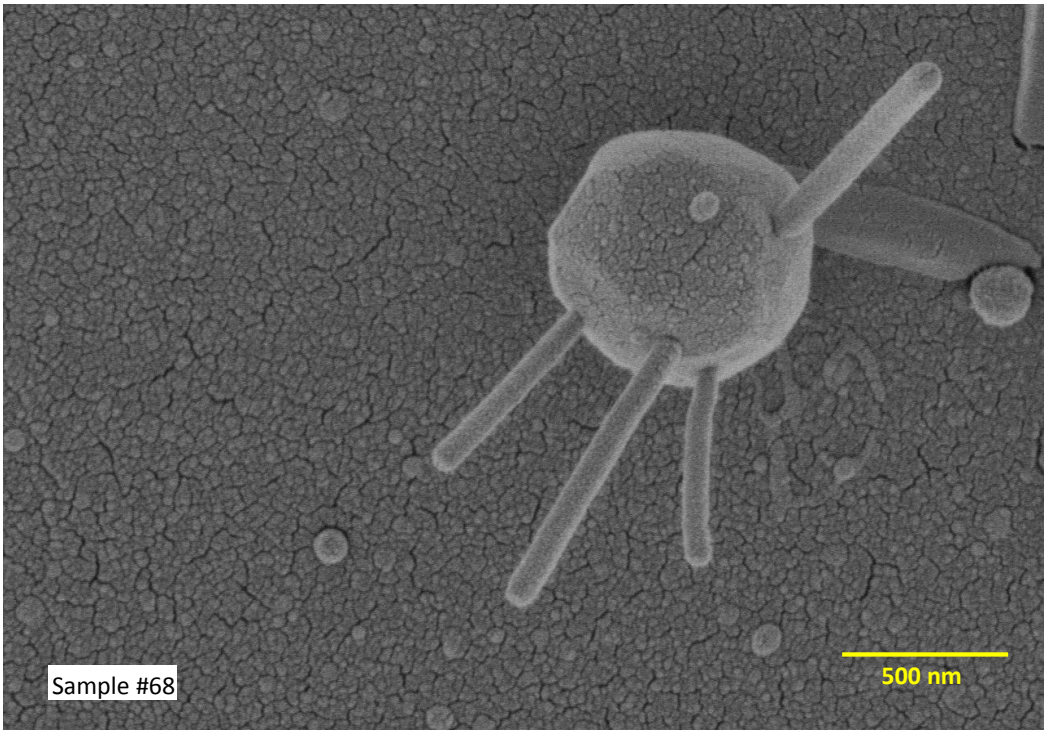


Figure 4.12 HR-SEM image of one of the sub-micrometric structures found in PLD deposits obtained by ablation of $B_4C$ at 1064 nm under high-vacuum ($10^{-5}$ mbar) using a fluence of 3 J $cm^{-2}$.

### Effect of the deposition time in 1064 nm PLD

The effect of the deposition time was studied by preparing deposits by 1064 nm ablation of the $B_4C$ target during 20, 40 and 60 minutes (equivalent to $12 \times 10^3$, $24 \times 10^3$ and $36 \times 10^3$ pulses respectively at 10 Hz repetition rate) in the same conditions of previous experiments.

Figure 4.13 shows SEM images of deposits obtained by ablation at 1064 nm under high vacuum after 20 minutes (figure 4.13a) and 60 minutes of irradiation (figures 4.13b and 4.13c). The images after 20 minutes show that the films are characterized by the presence of sub-micrometric spherical particles scattered all over the background film surface and the formation of microcolumns was not observed. Differently, deposits obtained after 60 minutes contain columnar structures with a typical length of about 2-3 µm and side dimensions of about 500 nm.

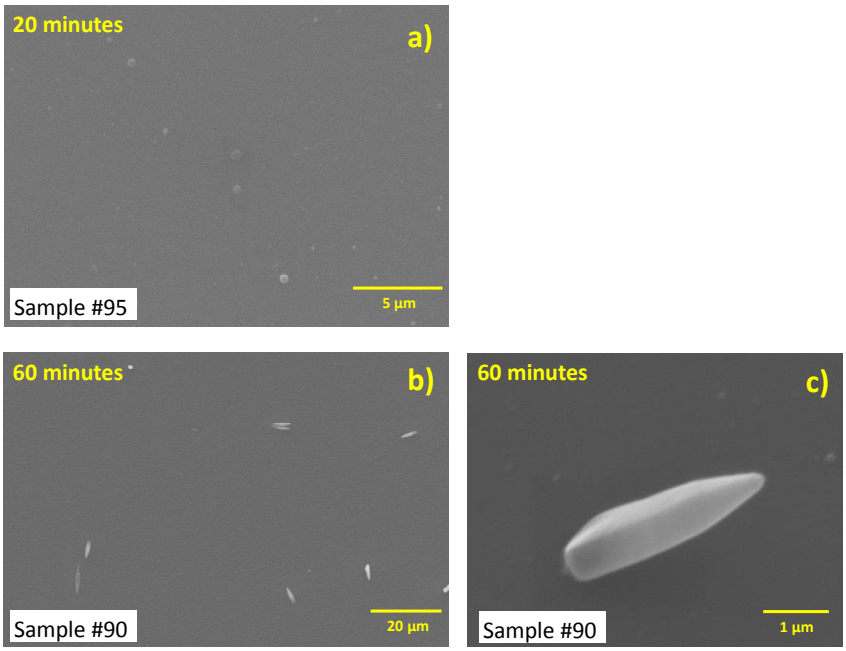


Figure 4.13 SEM images of deposits obtained by ablation of $B_4C$ at 1064 nm under high vacuum ($10^{-5}$ mbar) using a fluence of 3 J $cm^{-2}$ after: a) 20 minutes of deposition time and b, c) 60 minutes of deposition time.

## 266 nm ablation

Under high-vacuum conditions, the influence of the ablation laser wavelength in the PLD process was studied. Experiments were performed using an ablation laser wavelength in the UV region (266 nm), and a fluence of about 1 J $cm^{-2}$, while keeping the rest of the experimental parameters identical to those of the 1064 nm experiments. After the analysis of the deposits by SEM, we found that the results differ from those obtained by ablation in the IR region. In this case, a lower yield of structures is observed and these have a smaller size compared to that of those obtained by IR ablation, as can be observed in figures 4.14b and 4.14c. The shape of the structures obtained upon 266 nm ablation also differs from that of the well-defined microcolumns obtained upon IR ablation. As can be seen in figure 4.14c, upon 266 nm ablation the structures exhibit a more globular shape with conical tips, in contrast with the flat or faceted tips observed in the microcolumns obtained by 1064 nm ablation.

### Effect of the deposition time in 266 nm ablation PLD

As for the 1064 nm ablation case, the influence of the deposition time on the morphology of the deposits obtained upon 266 nm ablation was studied. Figure 4.14 illustrates the different aspect of the deposits prepared after 20 minutes (figure 4.14a) and 60 minutes of deposition time (figures 4.14b and 4.14c).

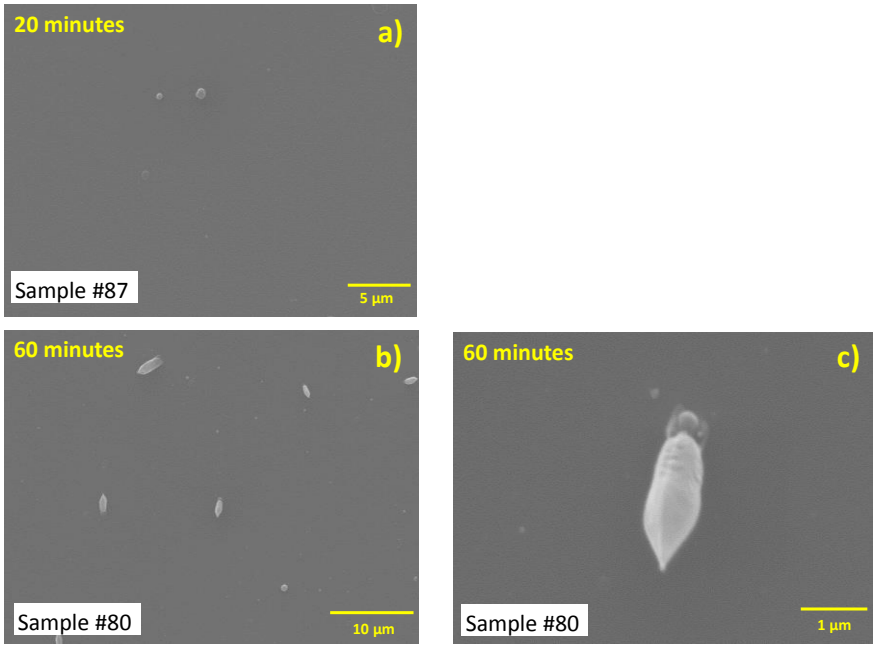


Figure 4.14 SEM images of deposits obtained by 266 nm ablation of $B_4C$ under high-vacuum conditions ($10^{-5}$ mbar) using a fluence of 1 J $cm^{-2}$ after: a) 20 minutes of deposition time and b) and c) 60 minutes of deposition time.

After 20 minutes, only few spherical particles are observed on the background film and no elongated structures were observed. After 60 minutes, deposits exhibit elongated structures with typical lengths of about 2 µm and lateral dimensions below 1 µm.

### 4.1.4 Compositional characterization of deposits

According to the results shown above, ablation at 1064 nm in vacuum at $10^{-5}$ mbar are the experimental conditions favouring the growth of micrometric-size, high aspect ratio structures. For that reason, the compositional characterization has been focused on deposits obtained under these conditions. The characterization was tackled using several analytical techniques, including micro-Raman spectroscopy, XPS, XRD and FIB-SIMS. Additionally, the $B_4C$ ablation plasma obtained under the aforementioned experimental conditions was also characterized by OES.

#### Micro-Raman

To find compositional differences between the microcolumns and the bulk boron carbide, micro-Raman point analysis was performed on the deposits and on the $B_4C$ target used for the PLD experiments. A clean Si wafer piece was also analyzed in order to distinguish bands that could belong to the substrate. In these analyses the excitation wavelength was set at 532 nm, being the spectral and lateral resolutions around 2 $cm^{-1}$ and 1 µm respectively.

Figure 4.15 shows the obtained Raman spectra of bulk $B_4C$ (black line), of a single microcolumn (red line) and of a silicon substrate (blue line). The intense band at 521 $cm^{-1}$ corresponding to the crystalline Si of the substrate was cut in order to better display other bands with lower intensity, which provide more information about the composition of the microcolumns. In the spectrum corresponding to pure $B_4C$, the bands at 275, 320, 478, 533, 715, 809, 1001 and 1084 $cm^{-1}$ are attributed to crystalline $B_4C$ [3], the band at 1587 $cm^{-1}$ corresponds to the G-band of graphitic carbon originated by the stretching of $sp^2$ atoms in the rings and usually present in sintered microcrystalline targets [4] . The D-band corresponding to the breathing of aromatic rings in graphitic domains, although weak, can be also observed at 1331 $cm^{-1}$ [5].

On the other hand, in the spectrum corresponding to one of the microcolumns (red line), the band observed at 472 $cm^{-1}$ can be compared to that found at 478 $cm^{-1}$ in the boron carbide target, which is attributed to the linear stretching and/or rotation of the 3-atom chains linking the boron icosahedra [3, 6] (see figure 2.18 in page 68 for more details). This band indicates the presence of crystalline $B_4C$ units in the structure. Its counterpart at 533 $cm^{-1}$ is possibly masked by the intense silicon band at 521 $cm^{-1}$. Additionally, new bands found at 679, 800, 1433, 2833, 2924 and 2958 $cm^{-1}$, which do not appear in the corresponding spectrum of the bulk $B_4C$ are also observed. This fact is indicative of a

change in the chemical composition of the microstructures with respect to that of the starting material. The origin of the band observed at 679 $cm^{-1}$ could be attributed to the presence of a high pressure, high temperature phase of boron (γ-boron) [7, 8]. The presence of B-B bonds, confirmed by the XPS experiments described further in this section, reinforces this assignment but some other bands with Raman shifts in this range, assigned to other B-C compounds, can be found in the literature as well [9]. Therefore, the assignment of this band should be considered as tentative. The band at 800 $cm^{-1}$ can be assigned to the symmetric vibrations of boroxol rings of boron oxide ($B_2O_3$) [10]. Bands at 1433, 2833, 2924 and 2958 $cm^{-1}$ are related to the presence of CH bonds. The first band can be attributed to δ(CH), while the other three are due to ν(CH) of groups $CH_2$ and/or $CH_3$.

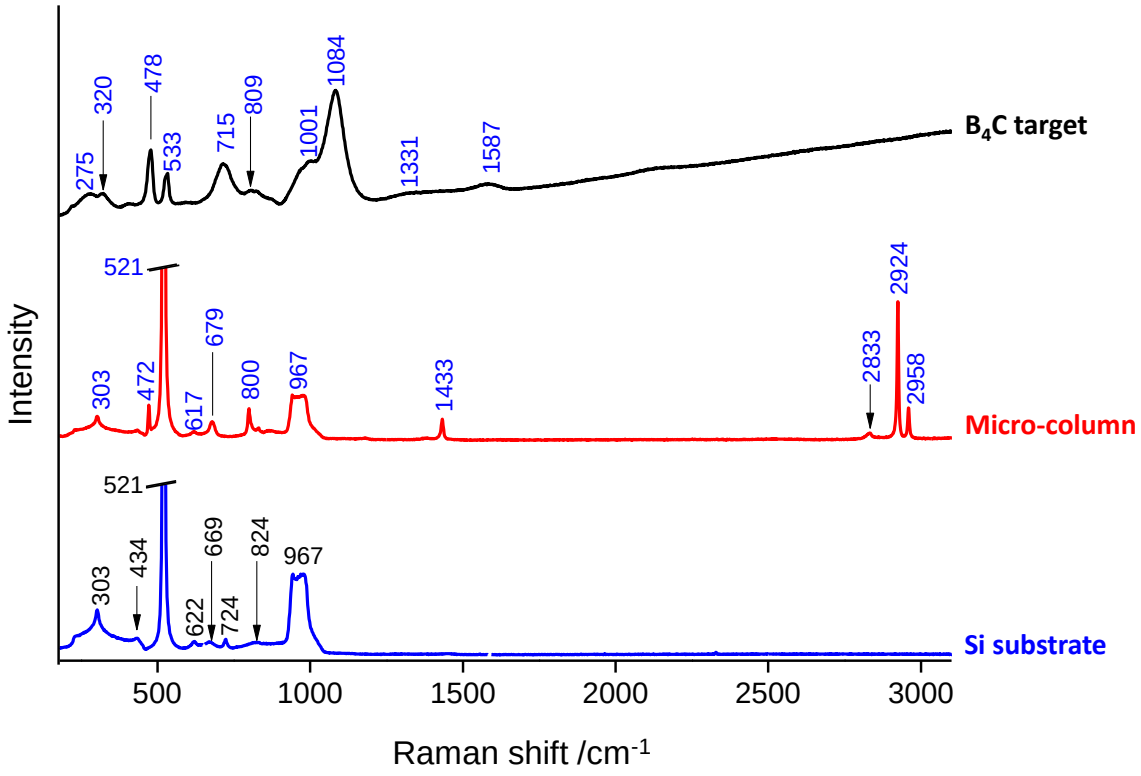


Figure 4.15. Micro-Raman point analysis obtained by excitation at 532 nm on: $B_4C$ target (black line), individual microcolumn (red line) prepared by PLD of $B_4C$ at 1064 nm under high vacuum ($10^{-5}$ mbar) using a fluence of 3 J $cm^{-2}$ (sample #69), clean Si substrate (blue line).

## XPS

XPS analysis provided more information on the deposits composition. Nevertheless, the low spatial resolution of this technique, of the order of the sample size, should be noted. In this case, the obtained information is an average of the deposit composition in the top few nanometres of the sample, including contributions from the microstructures (scattered all over the surface) and from the background film. The analyser transmission energy was set at 200 and 20 eV for the wide and narrow scan spectra respectively. Spectra were recorded at take-off angles of 90°. All binding values were charge-corrected to the adventitious C1s signal which was set at 284.6 eV and are accurate to ± 0.2 eV [11].

From the XPS analysis, boron and carbon appear as the main constituents of the studied deposits. Figure 4.16 shows the B1s core-level spectra recorded on a $B_4C$ target and on the deposits obtained by 1064 nm ablation under high-vacuum.

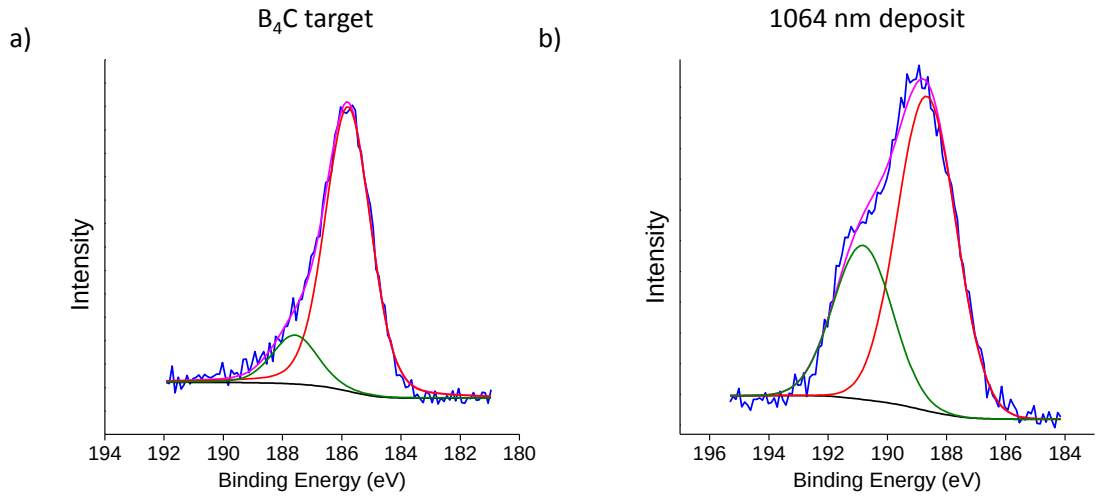


Figure 4.16. XPS spectra corresponding to the B1s level of: a) $B_4C$ target, b) deposit fabricated by PLD of $B_4C$ at 1064 nm under $10^{-5}$ mbar vacuum using a fluence of 3 J $cm^{-2}$ (samples #97 and #99).

Deconvolution of the signal using XPSPEAK 4.1 free software reveals, for the B1s level of the target (figure 4.16a), the presence of two possible chemical states of boron with binding energies centred at 185.8 and 187.5 eV. The obtained spectra are in agreement with those found in the literature for $B_4C$ [12], where the main peak at 187.0 eV is characteristic of C-B bonds in boron carbide [12, 13], whilst the band at 188.9 eV can be attributed to B-C bonds in graphitic structure [12, 14].

The XPS B1s spectrum of the deposit sample obtained at 1064 nm (figure 4.16b) shows the presence of two possible chemical states of boron with bands centred at 188.7 and 190.8 eV. The peak at 188.7 eV can be attributed to the aforementioned B-C bonds in graphitic structure but as in the case of the μ-Raman analysis, the possible presence of B-B bonds should not be disregarded, as a binding energy of 188.5 eV has been attributed to metallic boron [15]. Oxygen and nitrogen signals are also observed as impurities. The second contribution at higher binding energy can be associated to oxy-boron carbide species, *i.e.* to boron species with mixed B-C and B-O bonding [12, 14], favoured by the oxidation of $B_4C$.

### FIB-SIMS

The composition of the deposits was further investigated via FIB-SIMS. The first analysis was performed by selecting a large area of about 40 x 40 $\mu m^2$, which included several microcolumns and background film, in order to have a general picture of the deposit composition. The sputtered area can be inspected in figure 4.17a and the corresponding SIMS signal is presented in figure 4.18. In the spectrum, intense peaks assigned to the two isotopes of boron, $^{10}B^+$ and $^{11}B^+$, together with $C^+$, $BO^+$ and $Si^+$ species are present.

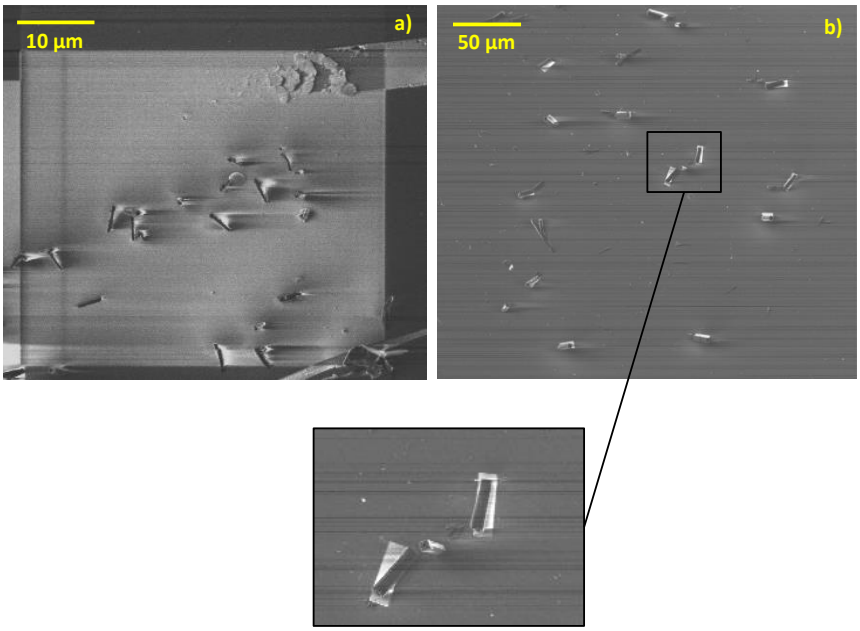


Figure 4.17. FIB-SEM images of the studied areas of a PLD deposit obtained by 1064 nm ablation of $B_4C$ under high vacuum ($10^{-5}$ mbar) using a fluence of 3 J $cm^{-2}$: a) sputtered ~40 x 40 $\mu m^2$ box containing several microcolumns and background film of sample #98 and b) sputtered boxes of a collection of thirteen individual microcolumns present in sample #72.

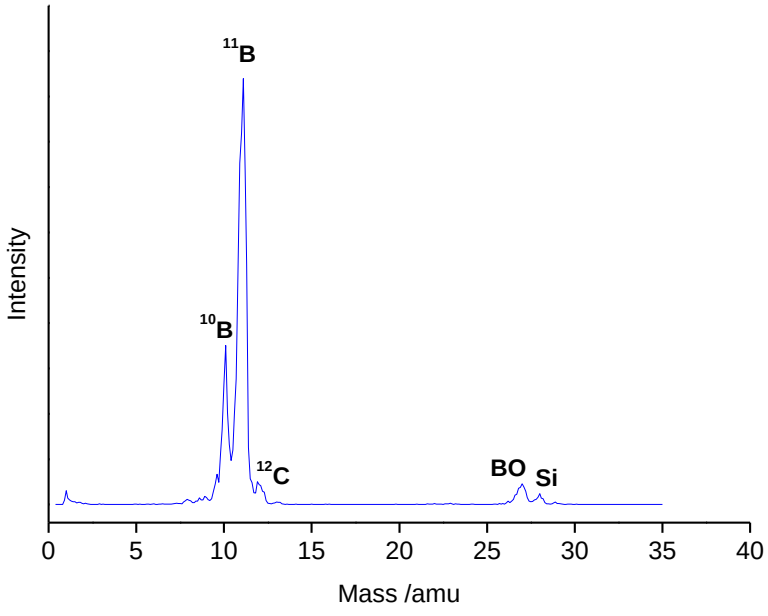


Figure 4.18. SIMS spectrum corresponding to a large area (approximately 40 x 40 $\mu m^2$) etched with the FIB in one deposit prepared by PLD of $B_4C$ at 1064 nm under high vacuum ($10^{-5}$ mbar) using a fluence of 3 J $cm^{-2}$ (sample #98). The area analyzed contains several microcolumns and background film.

The high spatial resolution of FIB-SIMS allows the analysis of the individual microstructures. Figure 4.19 shows the averaged SIMS spectrum obtained from a collection of thirteen individual microcolumns. The sputtered areas consisted on boxes of about the size of each microcolumn as seen in figure 4.17b. As in the previous spectrum, the main constituents of the microcolumns appear to be boron, carbon and boron oxide species. In this case, the observation window was extended to higher masses, as a consequence, peaks corresponding to Si and Ca impurities can now be observed. More interestingly, a peak at mass 56 amu appears in the spectrum (see insert in figure 4.19). This value corresponds to the mass of $B_4C$, corroborating the presence of this species in the composition of the microcolumns, as shown by micro-Raman spectroscopy.

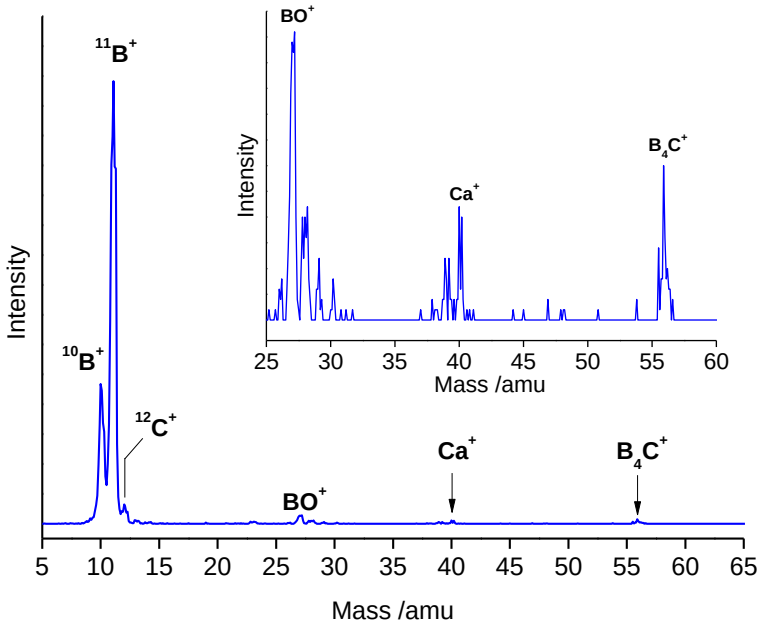


Figure 4.19 SIMS spectrum obtained by FIB etching of a collection of thirteen individual microcolumns present in a PLD deposit prepared by 1064 nm ablation of $B_4C$ under high-vacuum conditions ($10^{-5}$ mbar) using a fluence of 3 J $cm^{-2}$ (sample #72).

## XRD

The features observed in the microcolumns, such as a regular geometry and sharp edges, are typical of crystalline materials. This fact led us to try obtaining information on the crystallinity of the deposits by XRD. The first test was performed in one of the samples obtained by 1064 nm ablation under high vacuum using Cu Kα (1.54 Å) radiation in the

θ/2θ configuration. Figure 4.20 shows the resulting XRD pattern, where a single strong peak corresponding to the crystalline silicon of the substrate is observed. This result could be explained by the low thickness of the deposited layer and the high penetration depth of the X-rays. The combination of these two factors could preclude the observation of peaks related to the deposited material.

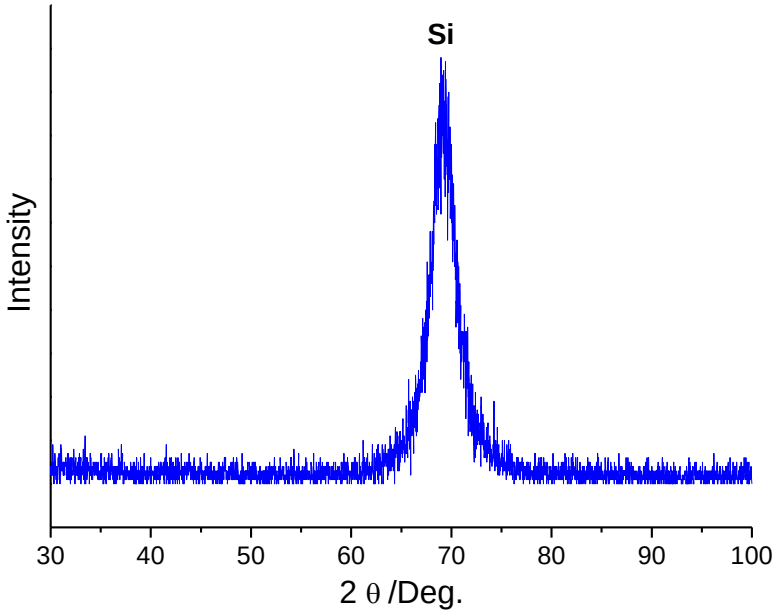


Figure 4.20. X-ray diffractogram of a PLD deposit obtained on a Si substrate by ablation of a $B_4C$ target at 1064 nm under high-vacuum conditions ($10^{-5}$ mbar) using a fluence of 3 J $cm^{-2}$ (sample #98).

In order to overcome this limitation, a further attempt to characterize the crystalline structure of the films was made by grazing incidence X-ray diffraction (GIXRD). The obtained diffractograms of the $B_4C$ target and of the studied deposit are shown in figure 4.21a and 4.21b respectively. The diffraction peaks appearing in the case of the target can be attributed to polycrystalline boron carbide [16]. In the case of the deposit, a broad band and a narrow peak centred around 55.5 and 54.3 degrees respectively are observed. Although the appearance of these features in the GIXRD spectrum suggests certain degree of crystallinity in the deposits, the assignment of these still remains unclear.

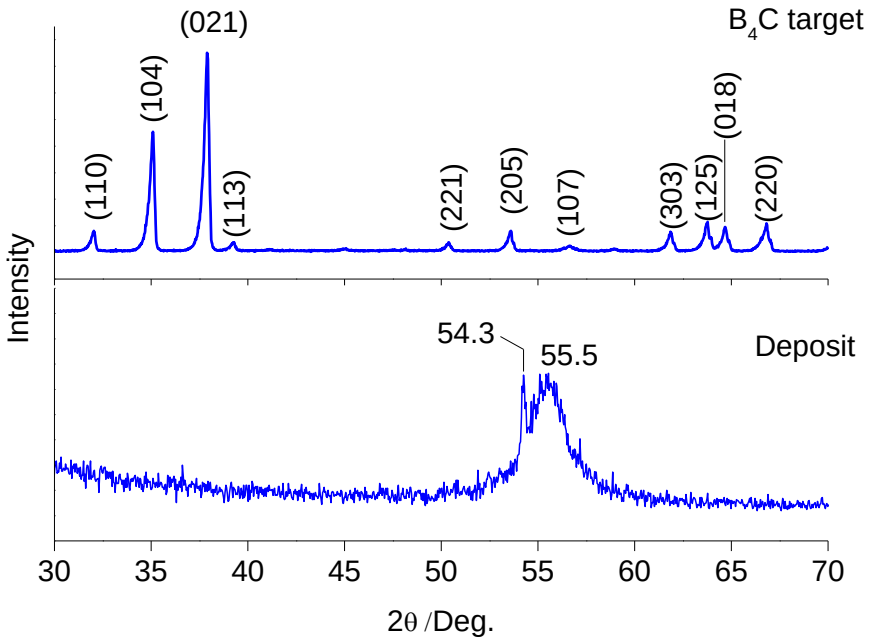


Figure 4.21 Grazing incidence X-ray diffractogram of the $B_4C$ target (upper panel) and PLD film on sample #98 obtained by 1064 nm ablation of $B_4C$ under high vacuum ($10^{-5}$ mbar) using a fluence of 3 J $cm^{-2}$ (lower panel).

## OES

Additionally, the composition of the plasma obtained by 1064 nm ablation of the $B_4C$ target under high-vacuum conditions was investigated by OES. Detection was performed at zero delay with respect to the ablation event in a time window of 1 µs.

The result of the spectroscopic analysis is shown in figure 4.22, where intense atomic emission lines corresponding to neutral species of boron and carbon, B(I) 208.9 nm, B(I) 249.7 nm (possibly overlapped with C(I) 247.9 nm) and B(I) 348.9 nm, can be observed. The features around 500 nm can be assigned to the emission of $C_2$ molecules (Swan bands). These bands, though weak compared to the intensity of the atomic lines, indicate the presence of this molecular species in the plasma plume.

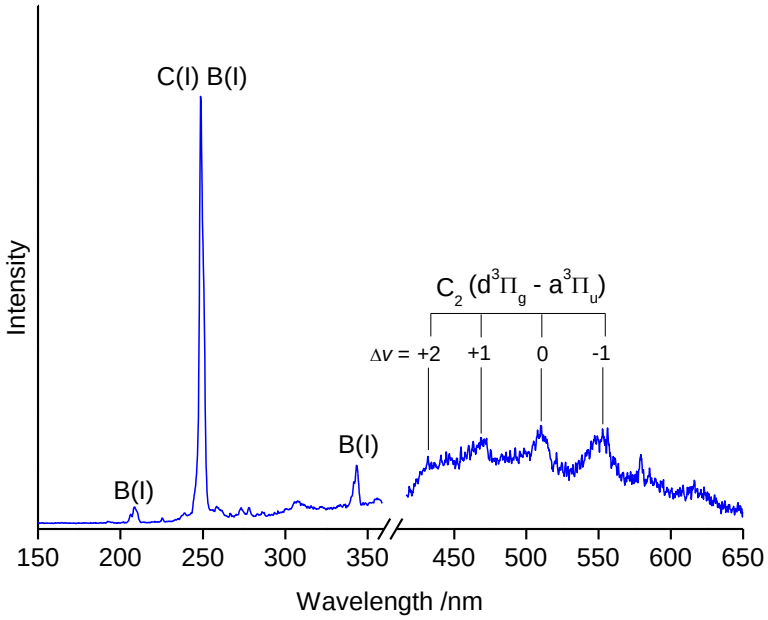


Figure 4.22 Optical emission spectrum of $B_4C$ plasma obtained by ablation at 1064 nm under vacuum ($10^{-2}$ mbar). From figure 3.37.

### 4.1.5 Discussion of results

From the results described above, it can be concluded that the conditions favouring the formation of structures with larger size and with the most regular shape are the combination of irradiation at 1064 nm and high-vacuum atmosphere. Deposits obtained under these conditions are characterized by the presence of high aspect ratio structures with typical sizes in the micrometric range. These structures feature sharp edges, square-shaped cross section and faceted tips, all of them typical characteristics of crystalline materials. Additionally, some of the structures display a hollow core.

In the literature, one can find studies using several fabrication techniques for the preparation of pure and homogeneous boron carbide films with amorphous and polycrystalline structures [3, 17, 18]. These include chemical vapour deposition (CVD) [18, 19], laser-assisted CVD [20, 21], magnetron sputtering [22] and PLD [23-35].

Studies involving nanosecond PLD of $B_4C$ have reported a dependence of the morphology and composition of deposits on the experimental parameters such as ablation laser wavelength, pulse duration and energy, type, orientation and temperature of the substrate and atmosphere of deposition. In the particular case of $B_4C$ (and other sintered

ceramic targets), the results appear to be influenced by repetitive ablation of the target, as found by Szörényi *et al*. [23]. According to their results, cumulative ablation in the same spot of the material may cause boron enrichment in the target surface, leading to a high variability of the films composition. In the same direction, the orientation of the substrate with respect to the target surface also plays an important role in the PLD outcome, as demonstrated by Zemsky *et al*. [24].

To date, references to PLD experiments using 1064 nm ablation of $B_4C$ appear only in a publication by Dietsch *et al*. [25]. In this work the authors focus on the methodology for depositing highly uniform alternate multilayers of Ni or Mo and $B_4C$ for X-ray optics applications. The authors provide only few details regarding the experimental conditions in which the ablation of $B_4C$ targets was performed. According to the stated aim of this study, it is clear that the ablation conditions were optimized for the fabrication of nanometric layers with very low roughness, in contrast with the micrometric structures obtained by 1064 nm ablation in our case. One of the main factors that could lead to these significant differences is the target to substrate distance, which in the case of Dietsch *et al*. was set to 15 or 25 cm, compared to the 4 cm distance in our experimental set-up. The relatively long distances affect the kinetic energy and density of species arriving to the substrate inducing a low deposition rate (which is interesting for thin films deposition under highly controlled conditions). On the other hand, in a previous work presented also by Dietsch *et al*. [26], the authors report typical energy per pulse values used in the same PLD set-up in the range of 500 and 1800 mJ, well beyond our energy per pulse figures (but in some cases in the same range of mean power density on the target surface of about $5 \times 10^8$ W cm$^{-2}$).

Zemsky *et al*. [24] reported on PLD of $B_4C$ by ablation at 532 nm. Deposition was carried out using fluences of 2-3 J cm$^{-2}$, under low-vacuum conditions, on Si (100) substrates at room temperature. The deposition time was set to 60 minutes. The Si substrates were placed at different orientations with respect to the target surface. The target to substrate distance was set to 5-10 mm. With substrates parallel to the target surface, they obtained crystalline deposits (being the first time that crystalline boron carbide films were prepared by PLD on room temperature Si substrates) characterized by the presence of round particles with diameters in the order of 1 µm on a continuous film. The authors attribute the formation of the crystalline phase of $B_4C$ to the high kinetic energy of the impinging boron and carbon species on the target, consequence of placing the substrates at a relatively short distance. Interestingly, a different morphology appears when the substrates are placed at different angles with respect to the target surface. In this case

deposits are formed by closely packed nanometric columns, tilted with respect to the substrate surface. At the same ablation wavelength of 532 nm, Sun *et al*. [27] described PLD experiments on Si substrates at room temperature and at 600 °C. Boron carbide ablation was carried out using a fluence of 5 J $cm^{-2}$. The morphology of the obtained deposits at room temperature is described as a smooth continuous film with embedded nanometric size particles, together with some scattered sub-micrometric particles.

Several PLD studies involving ablation in the UV range have been reported. Zhang *et al*. [28] describe experiments in which ablation of B/C dual targets was carried out at 355 nm with the aim of producing boron carbide thin films. The deposits are characterized by the presence of micrometric boron-rich droplets on a film surface. Ablation of $B_4C$ targets at 308 nm was used for the deposition of DLC films by Derkach *et al*. [29] and Kautek *et al*. [30]. Csákó *et al*. [31] performed PLD experiments ablating $B_4C$ targets at 248 nm with a KrF laser using 9.6 J $cm^{-2}$ and collecting the ejected material on Si substrates at room temperature. Deposits with a significant density of droplets with diameters > 1 µm on a smooth film were obtained. In the same spectral region, Aoqui *et al.* [32] describe the PLD process of $B_4C$ by 248 nm ablation using a fluence of 5 J $cm^{-2}$. Deposition was performed under high vacuum in a range of substrate temperatures from room temperature to 500 °C and applying a DC bias voltage to the substrate. Deposits are characterized by the presence of micrometric particles on the film surface when performing the PLD experiment with a target to substrate distance of 2 cm. At 4 cm, no film formation was observed; instead isolated particles were the only features of the deposits. BC films were obtained by Castillo *et al*. [33] by PLD with ablation at 248 nm at different substrate temperatures. Kokai *et al*. [34, 35] reported similar results on PLD under high-vacuum of $B_4C$ targets with irradiation at 266 nm using fluences of 1 and 3 J $cm^{-2}$ (conditions that can be compared to those presented in this thesis regarding UV ablation experiments). The target to substrate distance was set at 3-5 cm. PLD experiments yielded deposits containing spherical particles with diameters ranging from 0.5 to 5 µm, depending on the ablation fluence.

In all, most of PLD work reported to date deal with nanosecond ablation of $B_4C$ in the UV region. The majority of the deposits obtained by UV ablation are characterized by nano or micrometric-size spherical particles on a continuous film. To the best of our knowledge only few papers report on PLD via IR ablation of this material and the irradiation conditions are not clearly stated. The plethora of experimental conditions that can dramatically influence the deposition outcome, such as irradiation parameters like laser wavelength or fluence, target to substrate distance, substrate temperature, vacuum etc.,

lead to a broad spectrum or results. This, together with the lack of studies performed by ablation at 1064 nm (or any other wavelength in the IR range), makes the comparison with our results quite difficult and suggests that under the experimental conditions described above it is possible to grow a novel microstructured material from $B_4C$. In the following, different aspects of our results will be discussed in more detail.

### 1064 nm vs 266 nm ablation

The remarkable differences in size and morphology found in deposits obtained from $B_4C$ at the ablation wavelengths studied in this thesis (1064 and 266 nm) point out toward the different response of the target material to the incident radiation. While ablation at 1064 nm yielded well-defined columns with sizes in the range of micrometres, ablation at 266 nm produced smaller and less regular structures.

Deposits containing structures of different size may be originated by different deposition rates (considering a fixed number of laser pulses), which in turn are affected by the amount of ejected material and the degree of focusing of the ablation plume (the higher the plume focusing the higher the amount of material deposited on a given area of the substrate). In order to describe the possible factors influencing the angular distribution of the plume, the laser interaction with the $B_4C$ at 1064 nm and 266 nm will be briefly discussed.

Boron carbide is considered a *p*-type semiconductor with a band gap of 2.09 eV [3, 36]. While linear absorption is highly effective at 266 nm ($E_{photon}$ = 4.66 eV), absorption at 1064 nm ($E_{photon}$ = 1.17 eV) requires a multiphoton process in order to overcome the band gap. The density of energy deposited on the target at each wavelength depends on the laser fluences and on the optical penetration depths, which can be evaluated as the reciprocal of the linear absorption coefficient. In the present experiments, the fluence at 1064 nm is three times larger than at 266 nm. The absorption coefficient at 266 nm exceeds that at 1064 nm in polycrystalline ceramic targets as the one used in the experiments [3]. Therefore, a higher deposited energy density is expected at 266 nm compared to that at 1064 nm. This situation would favour a higher density of ejected species at 266 nm, but also a higher mean velocity of those and a larger fraction of ions in the plume, which under vacuum conditions, could result in a broad angular distribution and therefore in a lower deposition rate.

Other factors that should also be considered are related to the laser-plasma interaction. The different absorption of the ejected material in the UV and IR regions should also be

taken into account. In nanosecond laser ablation, the tail of the pulse interacts with the already formed plasma. The enhanced absorption of particles ejected after ablation would lead to a higher degree of photofragmentation in the case of UV irradiation and in turn to a smoother film surface [37]. Although a higher fragmentation of species in the plasma plume could not be directly related to different size of the microstructures, the presence of particulates in the background film can be involved in the growth mechanism as discussed later. On the other hand, fragmentation of the species impinging on the substrate is favoured in the case of UV ablation due to their higher kinetic energy compared to that of species produced upon IR ablation [38]. Moreover, this higher kinetic energy can lead to resputtering of the already deposited material [39].

### Vacuum and inert gas atmospheres

Experiments performed at 1064 nm under vacuum and inert gas atmospheres yielded structures with different morphology. In low and high vacuum experiments (at $10^{-2}$ and $10^{-5}$ mbar respectively) the formation of elongated structures with different sizes in the micrometric range is observed. Differently, under inert gas atmosphere (1 mbar of Kr or Xe), spherical particles or dendritic structures were obtained.

The role of the atmosphere inside the ablation chamber is known to be critical for the outcome of the PLD process, as the ambient in which the plasma is generated alters dramatically its expansion dynamics leading to changes in kinetic energy, spatial distribution and aggregation of the species present in the plasma. The pressure inside the chamber determines the collision rate between the ejected material and the ambient gas, being the main consequence of these collisions the variation of the kinetic energy of the ejected particles which in turn can have implications in the different deposition rate achieved at different pressures.

At reduced pressure, a lower collision rate is expected, thus the ejected particles will preserve most of their original kinetic energy. On the contrary, under inert gas atmosphere, the high density of gas atoms interacting with the ejected particles, leads to a decrease in the kinetic energy of the latter, favouring aggregation processes in the plume and/or on the substrate. This fact would explain the formation of the characteristic cluster-assembled dendritic structures [40-42] observed in figures 4.3c and 4.3d when ablation is performed in the presence of 1 mbar of Kr.

Furthermore, the deposition rate will also depend on either the scattering or focusing of the ejected particles on their way towards the substrate [43, 44]. These two competing

processes depend on the background pressure. The deposition rate increases with the background pressure as long as the particles preserve part of their initial kinetic energy and focusing of the plume dominates, but when the background pressure increases over a certain value, deceleration and scattering dominate the situation leading to a reduction in the deposition rate [44].

However, due to the complex expansion dynamics of the plasma plume, affected by interrelated processes, a quantitative assessment of the factor governing the process is difficult.

### Composition of the deposits

The analysis performed by OES revealed the presence of B and C neutral atoms as well as $C_2$ molecules in the $B_4C$ ablation plasma.

From the analysis of the obtained deposits, the first conclusion that can be extracted is their dissimilar composition with respect to the starting material. The composition of the microcolumns, instead of being pure $B_4C$, appears as a complex mixture of boron, boron oxide, boron carbide and aliphatic hydrocarbon species. Among the factors that could lead to non-stoichiometric deposits obtained by PLD is the re-deposition of species on the target surface after repetitive ablation [45]. The different spatial distribution of the ejected species could also lead to an incongruent composition of the prepared deposits [46].

On the other hand, Raman spectroscopy, XPS and SIMS analyses revealed the presence of oxygen containing species as constituents of the deposits. These measurements were performed in separated vacuum chambers, therefore the deposits were exposed to air prior to the analysis. The high affinity of boron for oxygen can explain the presence of this element in the analyzed deposits and individual microcolumns [27]. The origin of these oxygen atoms can be due to impurities present in the $B_4C$ target, residual air in the chamber or due to superficial oxidation of the deposits after exposure to air. However, FIB-SIMS spectra were obtained after repetitive etching of the structures and oxygen was detected at the different depths analyzed. It is therefore more likely to attribute the presence of oxygen to contamination in the target rather than superficial contamination of the deposits or to the residual gas present in high-vacuum conditions. The analysis also reveals the presence of other impurities, like aliphatic species, in the deposited material.

### Growth mechanism

The morphological characterization of the structures suggests that the obtained microcolumns are formed by a crystalline material. In the literature, several growth mechanisms have been proposed for explaining the formation of elongated structures by PLD.

Elongated nanostructures of $B_4C$ have been obtained following several procedures based on thermal evaporation [16, 47, 48]. The growth of such structures can be described by the vapor-liquid-solid (VLS) and solid-liquid-solid (SLS) mechanisms [47, 49, 50]. Both mechanisms usually involve the contribution of a catalytic liquid material (normally metal atoms alloyed with the compound forming the nanostructures). A typical evidence of VLS mechanism is the presence of catalyst nanoparticles at the end of the grown nanostructures, which are not observed in the present case. However, figure 4.12 shows a HR-SEM image of several nanorods emerging from the surface of a nanoparticle found in one of the deposits containing microcolumns. The formation of similar structures is described in the literature as a particular case of VLS growth denoted as *multiple prong* growth [51, 52]. Although evidences of nanorods formation trough VLS mechanism are observed, VLS and SLS mechanisms can hardly be extrapolated to the growth of the larger micrometric structures obtained in this thesis on substrates at room temperature and in the absence of an external catalyst.

Other mechanisms, such as vapour-solid (VS) growth mechanism appear more appropriate for explaining the formation of elongated structures in the present conditions [51, 53]. The VS mechanism has been proposed as the growth model of ZnO nanorods via PLD and CVD on thin films pre-deposited with ZnO nanoparticles, which act as nucleation sites [54, 55]. Microcolumns of $SnO_2$ and $TiO_2$ with very similar aspect than those obtained in the present thesis have been obtained in the absence of any external catalyst and their growth is explained through a VS mechanism [56, 57]. In our case, the morphological analysis of the background film observed in all deposits (see figure 4.11) reveals the presence of nanometric particulates which could act as nucleation sites for the growth of the elongated micrometric structures through a VS mechanism as long as the pulsed flux of vaporized material continues. Some SEM images also suggest a layer by layer growth (see figures 4.6 and 4.10) this observation supports a VS growth mechanism.

## Applications and future work

In this thesis we explored a range of conditions which yielded high aspect ratio microstructures with characteristic features in PLD experiments of $B_4C$. All the knowledge gained can serve to set the basis for the controlled synthesis of coatings containing structures with tailored size and/or shape by fine tuning the ablation and deposition experimental conditions.

Despite the fact that the experiments described in this thesis are aimed mainly to the study of the PLD process of $B_4C$ from a fundamental point of view, the exceptional properties of boron carbide and the interesting features of the deposits obtained upon 1064 nm ablation under high vacuum, suggest promising potential applications for the obtained material.

The intrinsic properties of boron carbide can guide the quest for applications of the deposits described in this thesis. Taking into account the exceptional hardness of $B_4C$ [3, 58], this is one of the most important physical properties to study in the deposited material (*e.g.* via nanoindentation tests). These studies will help to elucidate the potential of these deposits in applications involving the need of wear resistant coatings or abrasive properties. Provided the high neutron absorption cross section of boron carbide and boron rich compounds [58], applications towards the nuclear industry should also be borne in mind. This neutron absorption capability, together with the high specific surface of deposits containing hollow microcolumns is also a point that could be exploited in different future applications, such as particle sensors [59] or coatings. Other aspect that should be considered is the exceptional thermoelectric properties of boron carbide [60]. Thin film-based high-temperature thermoelectric devices are of great interest for recovering waste heat produced in many industrial processes for turning it into electricity. The study of thermoelectrical properties of the obtained material would shed some light on its potential application in energy conversion devices. Nevertheless, a better knowledge of the physical and chemical properties of the deposits and in particular of the microcolumns is desirable in order to propose possible applications.

## 4.2 Double pulse femtosecond pulsed laser deposition of Co/ZnS

In this section a detailed investigation on the ablation dynamics and deposition process of Co/ZnS material, irradiated by pairs of femtosecond laser pulses, is described.

The ultimate goal of the experiment is to search for control mechanisms over the plasma composition which can be transferred to a PLD process for the tailored synthesis of Co-doped ZnS nanostructured deposits. To modify the ablation plasma composition two different strategies, aimed at acting either on the laser-material interaction dynamics or on the laser interaction with the ablated material, can be followed. The approach taken in this work makes use of a double pulse (DP) femtosecond laser irradiation scheme in which two variables, the interpulse delay ($\Delta t$) and the relative energy between pulses, can be modified to influence the laser-material ablation dynamics.

The proposed DP scheme allows studying the ablation dynamics in the following way: the first pulse arriving to the target material, acts as a "pump" and the delayed pulse acts as a "probe" of the transient changes caused in the material by the first pulse.[9]

The obtained results regarding the DP ablation dynamics indicate that the relative abundance of the ion species ejected in the ablation is dependent on the interpulse delay. Therefore the possibility of controlling the plasma composition and in turn the composition of Co/ZnS deposits was explored by translating the same DP femtosecond ablation approach to a PLD experiment. Deposits of Zn/S/Co were prepared on silicon substrates and TEM grids at different interpulse delays and analysed by several characterization techniques. Additionally, the ablation plasma composition was studied by OES in similar DP irradiation conditions than those used in PLD experiments.

### 4.2.1 Study of the femtosecond double pulse ablation dynamics of Co/ZnS targets by time-of-flight mass spectrometry

The relative yield of the ion species present in the DP ablation plasma of Co/ZnS targets containing 2 % of cobalt was studied by TOF-MS. The analysis of the plasma was carried out as a function of the delay and relative energy between the two 100 fs pulses.

[9] This "pump and probe" notation will be used in the following sections.

The fluence of each individual pulse was kept below the ion detection threshold (unless otherwise specified). This resulted in a situation where only the combination of both pulses produced a measurable ion signal. This is exemplified in figure 4.23, where TOF mass spectra corresponding to single pulse (SP) irradiation acquired by blocking either of the two interferometer arms are shown in figure 4.23a and 4.23b. The absence of ion signal in the SP case is in contrast to the intense peaks observed in the spectrum shown in figure 4.23c, which corresponds to DP ablation with pulses of equal fluence of 0.2 J $cm^{-2}$ delayed by 5 ps.

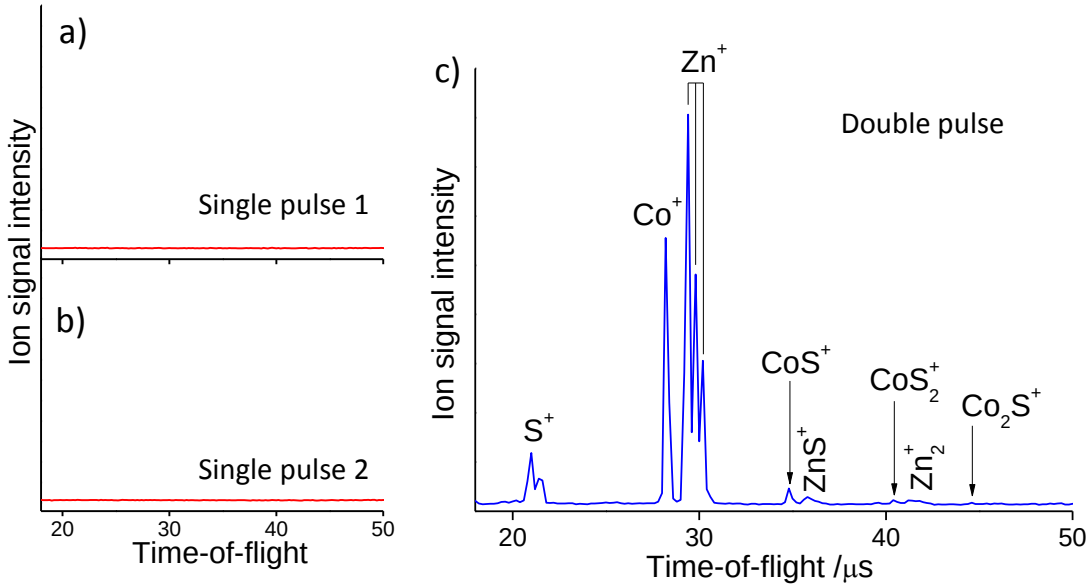


Figure 4.23 Time-of-flight mass spectra obtained upon femtosecond laser ablation of Co/ZnS targets: a) and b) single pulse irradiation with under-threshold fluence for signal detection ($F$ = 0.2 J $cm^{-2}$), c) double pulse irradiation combining both under threshold pulses ($F_{total}$ = 0.2 + 0.2 J $cm^{-2}$) at $\Delta t$ = 5 ps.

The composition of the Co/ZnS plasma can be better inspected in figure 4.24. In it, the TOF mass spectrum obtained by SP ablation at a fluence of ~ 0.3 J $cm^{-2}$ (above the ion detection threshold) is displayed together with a DP spectrum obtained by combination of two under threshold pulses of ~ 0.2 J $cm^{-2}$ separated by 1.5 ps.

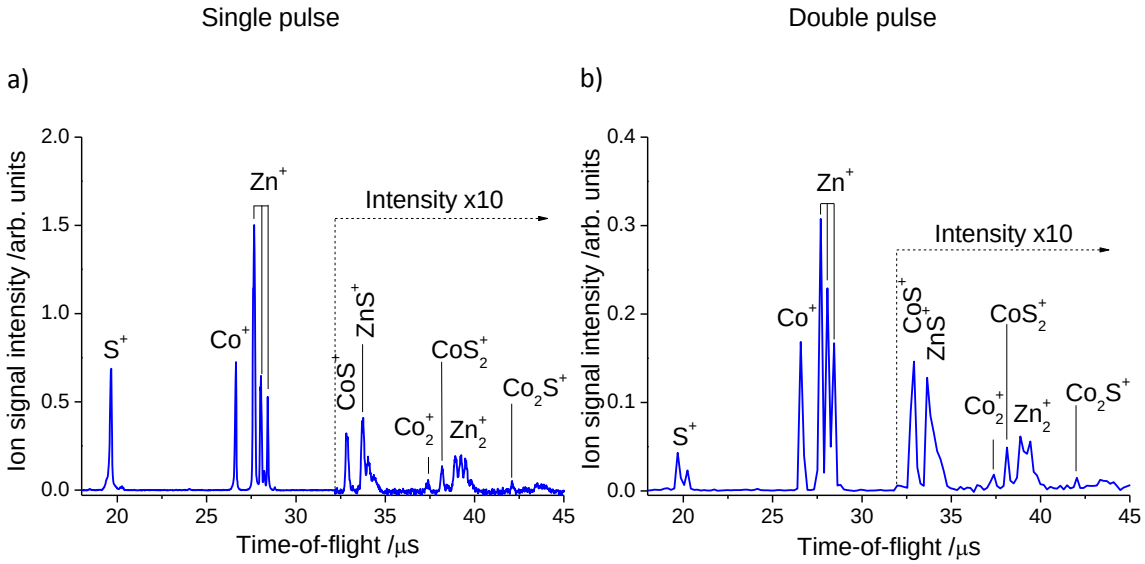


Figure 4.24 Time-of-flight mass spectra obtained by ablation of Co/ZnS targets. a) Single pulse ablation at fluence ~ 0.3 J cm$^{-2}$, b) double pulse ablation with two equal pulses of ~ 0.2 J cm$^{-2}$ delayed by 1.5 ps. Signal intensities corresponding to time-of-flight values longer than 32 μs are multiplied by a factor of 10.

Both DP and SP (above-threshold) spectra share similar features, being the most intense mass peaks assigned to $S^+$, $Co^+$ and $Zn^+$ ions. Other peaks with lower intensity can be assigned to $CoS^+$, $ZnS^+$, and $Co_nS_m{}^+$ and $Zn_nS_m{}^+$ clusters. The presence of $CoS^+$ and $Co_nS_m{}^+$ points toward ion-neutral reactions in the plume, showing indirect evidence of the formation of neutral species upon SP and DP ablation. Signal intensities corresponding to time-of-flight values longer than 32 μs were multiplied by a factor of 10 for better inspection.

The temporal dependence of the plasma composition was studied by scanning the interpulse delay in the picosecond range at fixed temporal steps in two different scenarios: symmetric and asymmetric double pulse ablation. Symmetric ablation refers to the situation where both femtosecond laser pulses (pump and probe) have the same fluence ($F_{pump} = F_{probe}$). On the contrary, in asymmetric double pulse ablation one of the two pulses (either the pump or the probe) is set to a lower fluence ($F_{pump} \neq F_{probe}$).

In the following "high" and "low" fluences will be labelled as H and L, respectively. Consequently, the symmetric configuration will be denoted as HH (from "high-high"). The asymmetric configuration will be denoted as HL for $F_{pump} > F_{probe}$ or LH for $F_{pump} < F_{probe}$. The fluence of the H pulse was set to ~ 0.2 J cm$^{-2}$. This value was found to be below the ion detection threshold (see figure 4.23). It represents approximately a 60% of the

reported ablation threshold for Co under comparable irradiation conditions [61] and is slightly higher than the reported value of 0.15 J $cm^{-2}$ for ZnS at 527 nm in air [62]. Nevertheless, the ablation threshold is expected to increase at the longer wavelength of 800 nm and under the vacuum conditions used in this work. The fluence of the L pulse was ~ 0.1 J $cm^{-2}$.

### Symmetric double pulse ablation

Symmetric DP ablation was performed using the aforementioned fluence of ~ 0.2 J $cm^{-2}$ for both individual pulses. Figure 4.25 shows the contour plots obtained from representing the TOF-MS intensities at a given interpulse delay. The assignment of each mass peak is shown in the mass spectrum obtained by DP ablation ($\Delta t$ = 285 ps) depicted in the figure. The intensity of peaks exhibiting a weak signal (from time-of-flight 32 µs upwards) was multiplied by a factor of 10 for the sake of a better comparison with other intense peaks in the same plot.

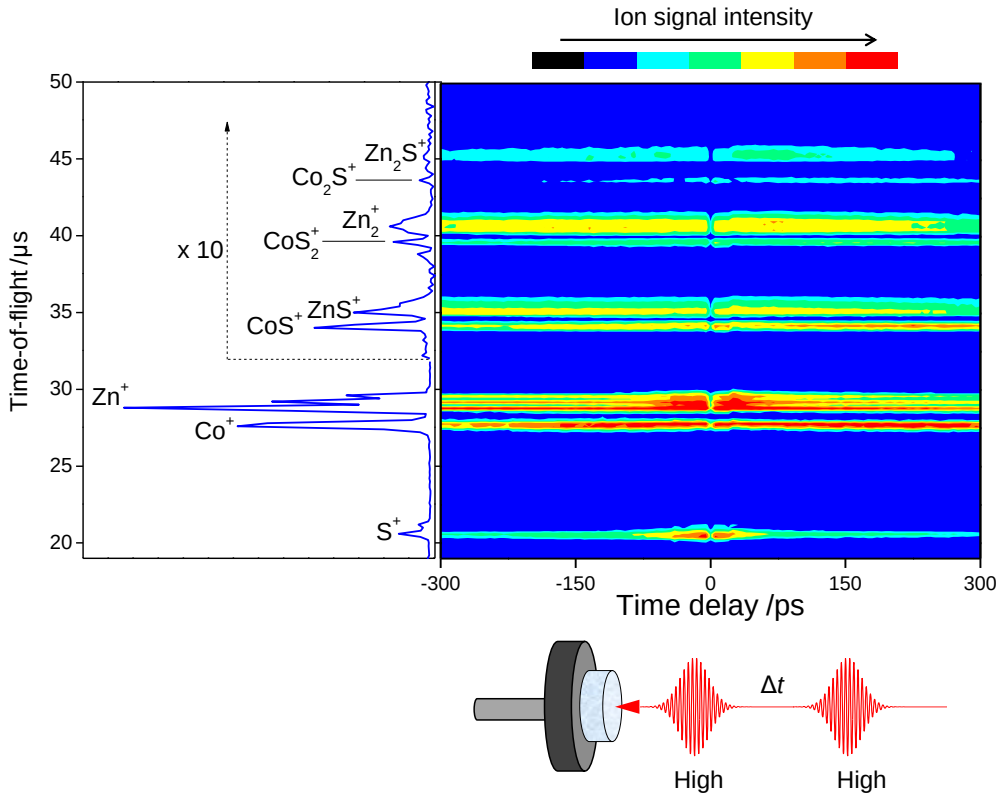


Figure 4.25 Contour plot of the TOF-MS signal obtained by symmetric DP femtosecond ablation of Co/ZnS as a function of the interpulse delay. The mass spectrum on the left, corresponding to $\Delta t$ = 285 ps, shows the peaks assignment. The panel below illustrates the sequence of equal fluence pulses (~ 0.2 J $cm^{-2}$) impinging on the target. The intensities of peaks with TOF longer than 32 µs have been multiplied by a factor of 10 for better comparison.

Mass spectra were recorded scanning the interpulse delay from -300 to 300 ps in 5 ps steps. In this situation, the role of the pump and probe pulses is exchanged in the negative (from -300 ps to zero delay) and positive (from zero delay to 300 ps) branches of the scan. As both pulses have equal fluence the outcome of both branches should be equivalent. In any case, it should be considered that both pulses are not identical, having slightly different energy distributions or temporal profiles. The fact of scanning the negative and positive branches provides a way to account for small differences in the irradiation conditions of the target.

In the region of partial or total temporal overlap between both 100 fs pulses (in the following referred as "zero delay"), there is either constructive or destructive interference between them. This means that, in a region of ∼200 fs the laser intensity ($I$) could take random values from 0 to 4$I$, thus affecting the ion signal obtained under these irradiation conditions. At both sides of the zero delay region, it is observed that the ion signal intensity of all peaks changes with the interpulse delay in a quasi-symmetric way, as expected for two pulses of equal fluence. From the plot it can be concluded that the signal intensity of the mass peaks corresponding to $S^+$, $Co^+$ and $Zn^+$ ions depends on the interpulse delay.

Additionally, the region of short delays (from -15 to 15 ps) was studied in more detail for the HH case by performing scans with higher temporal resolution. In these, interpulse delays were scanned from -15 to 15 ps in 100 fs steps. The results of these scans are shown in figure 4.26. The intensity represented in the figure is the value integrated over the whole range spanned by the isotopic masses of the respective species. The data were fitted with the exponential function:

$$A\left(1 - exp\left(\frac{-\Delta t}{\tau}\right)\right) + b \tag{4.1}$$

where $A$, $\tau$ and $b$ are adjustable parameters. The figure shows that after the zero time region the intensities of $S^+$, $Co^+$ and $Zn^+$ mass peaks increase with the interpulse delay but $Co^+$ signal levels off at shorter times compared to that of $Zn^+$ and $S^+$. Rising times $\tau$ of 10 ps, 2 ps and 5 ps are obtained for $Zn^+$, $Co^+$ and $S^+$ respectively.

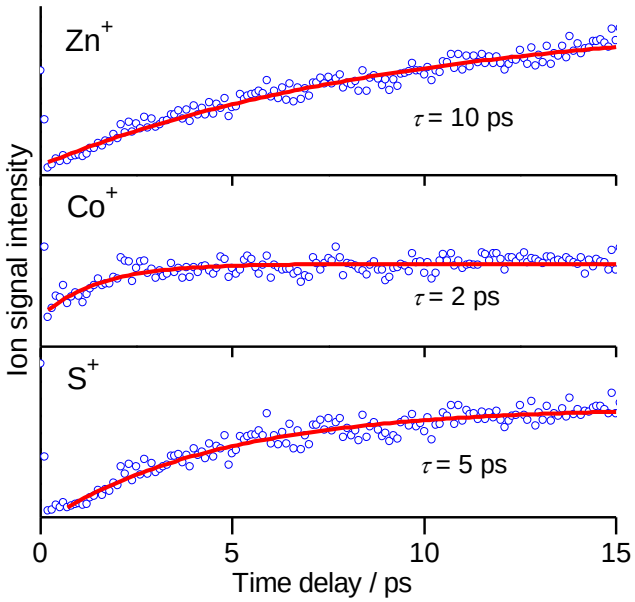


Figure 4.26 Integrated signal intensities for $S^+$, $Co^+$ and $Zn^+$ mass peaks as a function of the interpulse delay for HH DP ablation. Scans were performed at 100 fs steps. The red lines are the best fit of the obtained data to function (4.1).

### Asymmetric double pulse ablation

Figures 4.27a and 4.27b show the scans performed with pulses of different energy at the fluences of 0.2 J $cm^{-2}$ and ~ 0.1 J $cm^{-2}$ for H and L pulses respectively. In this case, and in contrast with results obtained in symmetric DP ablation (see figure 4.25), the asymmetry between HL and LH branches of the scan is patent. As it should be expected, the figures 4.27a and 4.27b are mirror images of each other. The figure shows that a more efficient ion ejection is achieved when the lowest fluence pulse is ahead in time (LH situation).

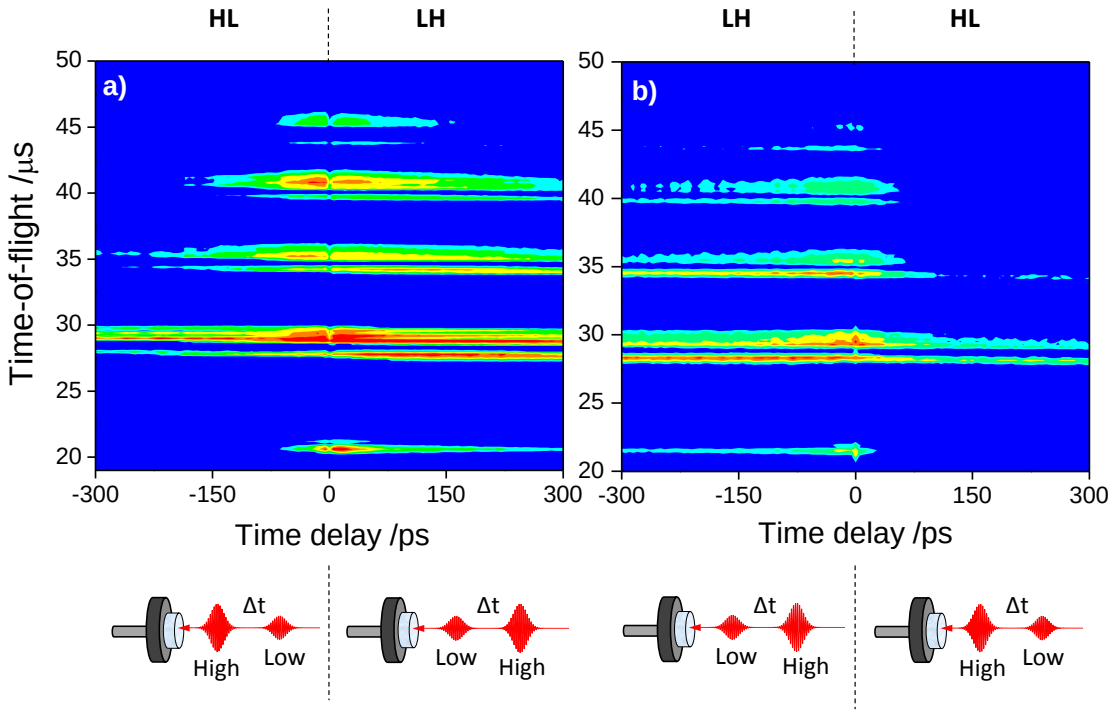


Figure 4.27 Contour plots of the TOF MS signal obtained by asymmetric DP femtosecond ablation of Co/ZnS targets. a) HL and LH branches of the scan at negative and positive interpulse delays respectively and b) LH and HL branches of the scan at negative and positive interpulse delays respectively. The panels below each plot illustrate the sequence of pulses impinging on the target.

The different interpulse delay dependence of $S^+$, $Co^+$ and $Zn^+$ signals for symmetric and asymmetric DP ablation can be inspected in more detail using the plots shown in figure 4.28a and 4.28b. In these, the mass signal intensities are integrated over the range spanned by their isotopic distributions and the positive and negative branches of the scan are plotted versus the interpulse delay. As in HH configuration the negative and positive branches should be equivalent. The average of both branches is shown as a solid line in figure 4.28a.

For HH DP ablation, shown in figure 4.28a, $S^+$ and $Zn^+$ signals reach the maximum intensity at delays shorter than 20 ps and then decrease. The decay shows a biexponential behavior, with a faster decay up to ~ 100 ps and a slower decay at longer times. Compared to $S^+$ and $Zn^+$, the $Co^+$ signal intensity shows a faster rise, reaching its maximum at about 5-10 ps. Then the signal remains roughly constant up to 150 ps and it is followed by a smooth decay at longer delays. These results are compatible with those shown in figure 4.26 for the HH configuration at short delays.

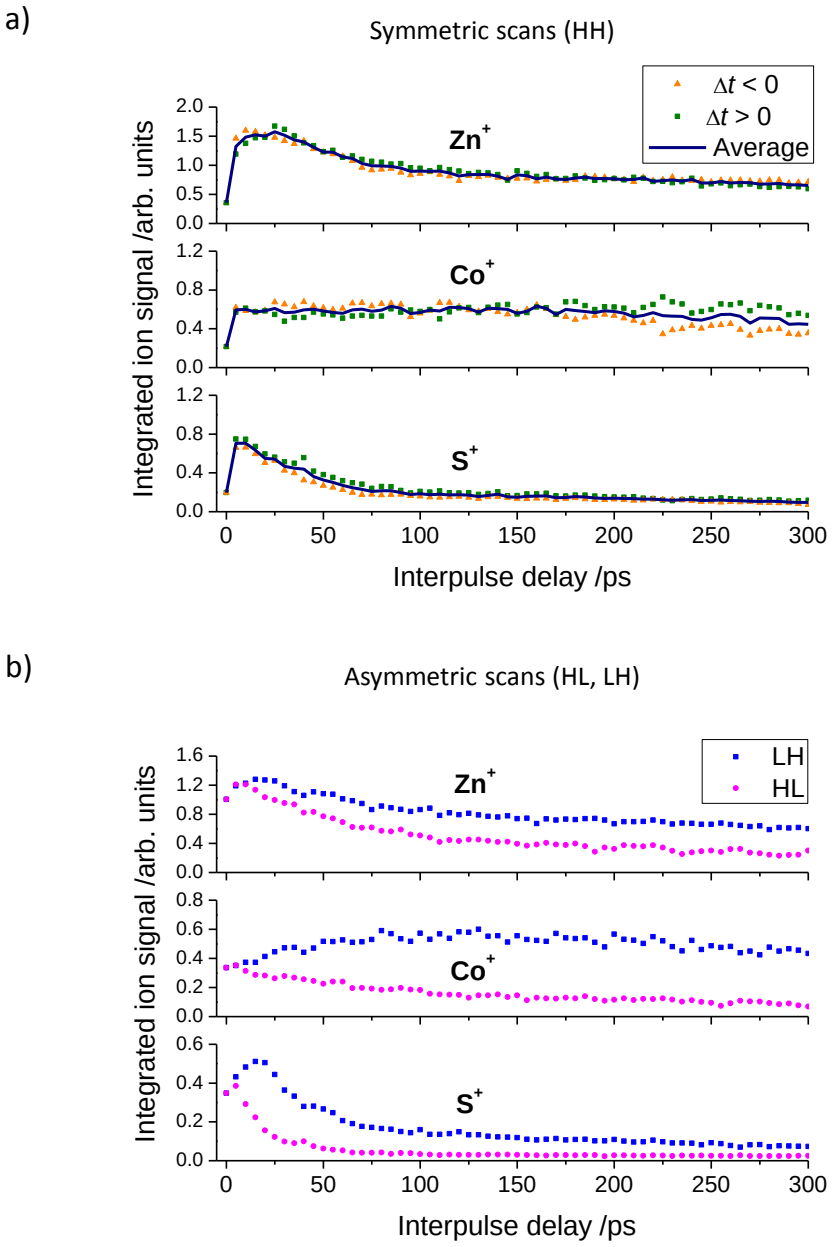


Figure 4.28 Integrated signal intensities for $Zn^+$, $Co^+$ and $S^+$ mass peaks as a function of the interpulse delay. a) Symmetric scans (HH) corresponding to the positive (green squares) and negative (orange triangles) branches. The dark blue line is the average of both negative and positive branches. b) Asymmetric scans corresponding to LH (blue squares) and HL (magenta) configurations. Fluences of H and L are ~ 0.2 and ~ 0.1 J $cm^{-2}$ respectively.

For asymmetric DP ablation, shown in figure 4.28b, $Zn^+$ and $S^+$ signals decay faster for HL than for LH situation. Furthermore, $Co^+$ signal exhibits the most asymmetric behaviour. For HL case, the $Co^+$ signal rises up to 5 ps and then decreases with the interpulse delay, while for LH ablation it rises up to 90-150 ps and then decays at longer times.

A similar dynamics upon DP femtosecond ablation was observed in experiments performed in pure Co and ZnS targets and in targets of Co/ZnS containing 10 % of Co.

### 4.2.2 Characterization of the double pulse femtosecond laser ablation plasma of Co/ZnS targets by optical emission spectroscopy

OES was used to characterize the spontaneous plasma emission upon ablation of Co/ZnS targets containing 10 % of Co in similar experimental conditions than those used in the PLD experiments described later in this chapter. To that purpose, the femtosecond ablation set-up (laser system, interferometer and ablation chamber) and OES detection system (spectrograph and ICCD camera), described in pages 51 and 48 of the experimental section respectively, were combined. In the experiments, ablation was carried out using 800 nm pulses of equal fluence and duration of ~ 100 fs. The laser radiation was driven to the target at an incidence angle of about 60°.

For the first measurements, under-threshold conditions were chosen as in TOF-MS and PLD experiments. For that purpose, the fluence of each individual pulse was set to a value which resulted in a negligible OES signal. This threshold value was found to be around 0.1 J $cm^{-2}$. In these irradiation conditions, only the combination of the two pulses yielded a measurable signal.

Figure 4.29 shows the emission spectra corresponding to symmetric DP ablation with under-threshold pulses separated by 300 ps. In the spectrum, intense emission lines assigned to neutral Zn(I) are observed. Neutral Co(I) emissions, although they are relatively weak and not well resolved, are also observed. Table 4.2 displays the measured emission wavelengths together with the reference values [63].[10] Under the irradiation conditions herein, emission of ionic species was not detected.

[10] Due to the limited resolution, only the most intense Co(I) lines, falling in the region shown, are displayed in table 4.2. Differences between the observed and reference wavelength values are due to the calibration of the spectrometer.

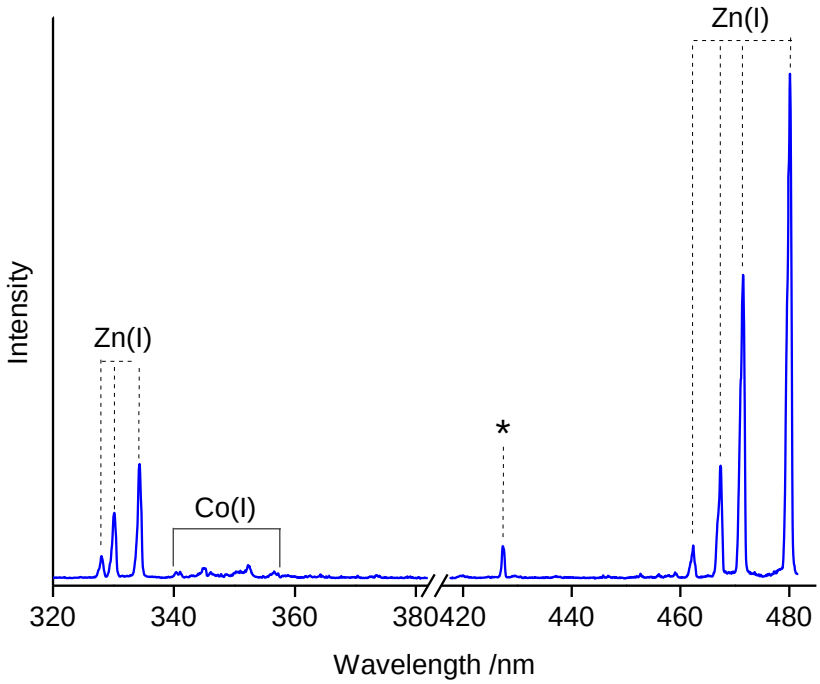


Figure 4.29 Optical emission spectra obtained by DP femtosecond ablation of Co/ZnS targets under vacuum ($10^{-5}$ mbar) at an interpulse delay of 300 ps. The fluence was set to 0.1 J $cm^{-2}$ for the individual pulses. Signal acquisition was performed at zero delay with respect to the delayed pulse in a temporal gate of 1 µs and by accumulation of 125 spectra. The main features observed in the spectrum correspond to emission of Zn(I) and Co(I) species (wavelength values are listed in table 4.2). The line marked with the star sign corresponds to the second diffraction order of Zn(I) 213.856 nm.

Table 4.2 Observed emission lines in DP and SP femtosecond ablation of Co/ZnS targets.

| Species | Wavelength (nm) | Reference line (nm)[b] |
|---|---|---|
| Zn(I) | 328.0 | 328.233 |
| | 330.1 | 330.258 |
| | 334.3 | 334.557 |
| | 427.3[a] | 213.856 |
| | 462.4 | 462.981 |
| | 467.3 | 468.014 |
| | 471.5 | 472.215 |
| | 480.1 | 481.053 |
| Co(I) | 340.6 | 340.512 |
| | 344.9 | 344.364 |
| | 345.0 | 345.350 |
| | 346.1 | 346.580 |
| | 352.3 | 352.685 |
| | 356.5 | 356.938 |

[a] Second diffraction order of Zn(I) emission at 213.856 nm. [b] From [63].

The dependence of Co and Zn emission intensities on the interpulse delay was studied. Figure 4.30 depicts the emission spectra obtained by DP ablation with under-threshold pulses separated by delays of 1 ps, 10 ps and 300 ps. It can be observed that SP irradiation did not yield a measurable signal, as spectral features are within the noise level. For DP ablation, Zn(I) and Co(I) signal intensities increase up to two orders of magnitude when the interpulse delay is varied from 1 ps to 300 ps.

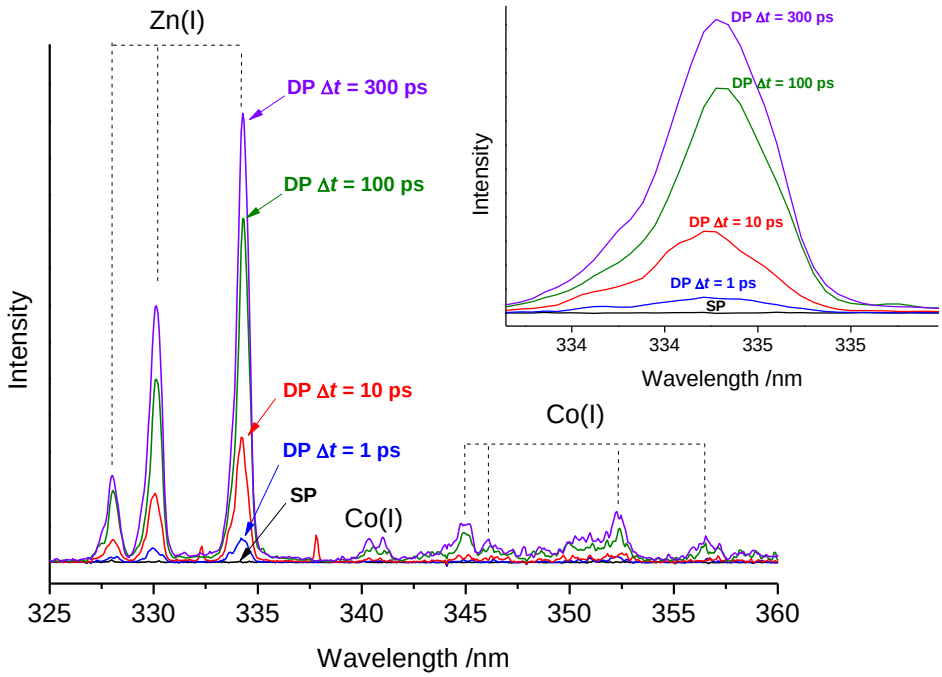


Figure 4.30 Optical emission spectra obtained by SP and DP femtosecond irradiation of Co/ZnS targets showing a spectral region containing several Zn and Co emission lines. Ablation was performed under vacuum ($10^{-5}$ mbar) with pulses of ~ 0.1 J cm$^{-2}$. Double pulse spectra were acquired at different interpulse delays between 1 and 300 ps. Acquisition was performed at zero delay with respect to the probe pulse in a temporal gate of 1 µs.

In the ablation dynamic experiments described previously in section 4.2.1, it is noted that in the time delay region below 10 ps the results of the TOF-MS analysis of the plasma with symmetric DP ablation yielded a rising signal. Here the region of shorter interpulse delays up to 10 ps, was studied by OES using pulses of fluence comparable to that used for PLD experiments described later in this chapter (~0.2 J cm$^{-2}$) and also close to that used in the ablation dynamics experiments. Figure 4.31 shows the obtained spectra corresponding to SP and DP ablation at interpulse delays of 250 fs, 500 fs, 1 ps, 5 ps and 10 ps.

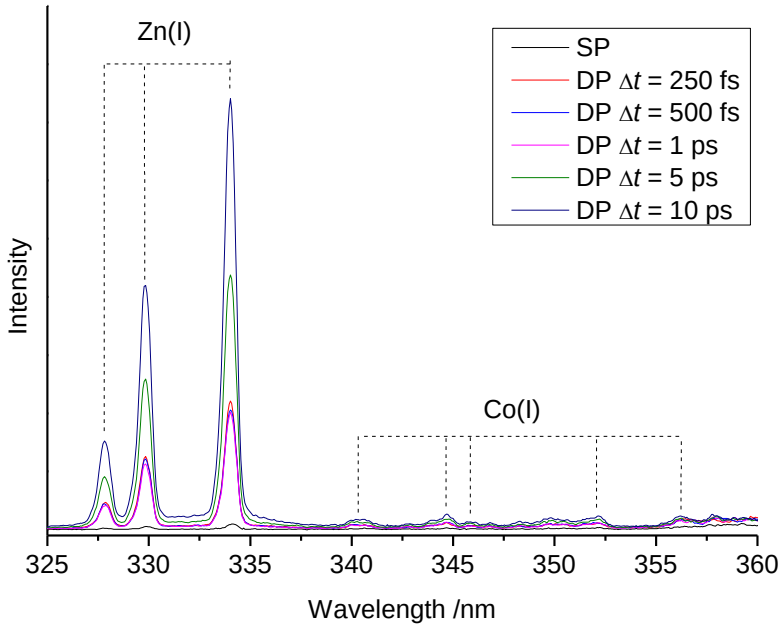


Figure 4.31 Optical emission spectra corresponding to SP and DP femtosecond ablation of Co/ZnS targets at different interpulse delays. Ablation was performed using a fluence of ~0.2 J $cm^{-2}$ for each individual pulse. The spectra were obtained after 125 accumulations acquired at zero delay with respect to the pump pulse during a time window of 1 μs.

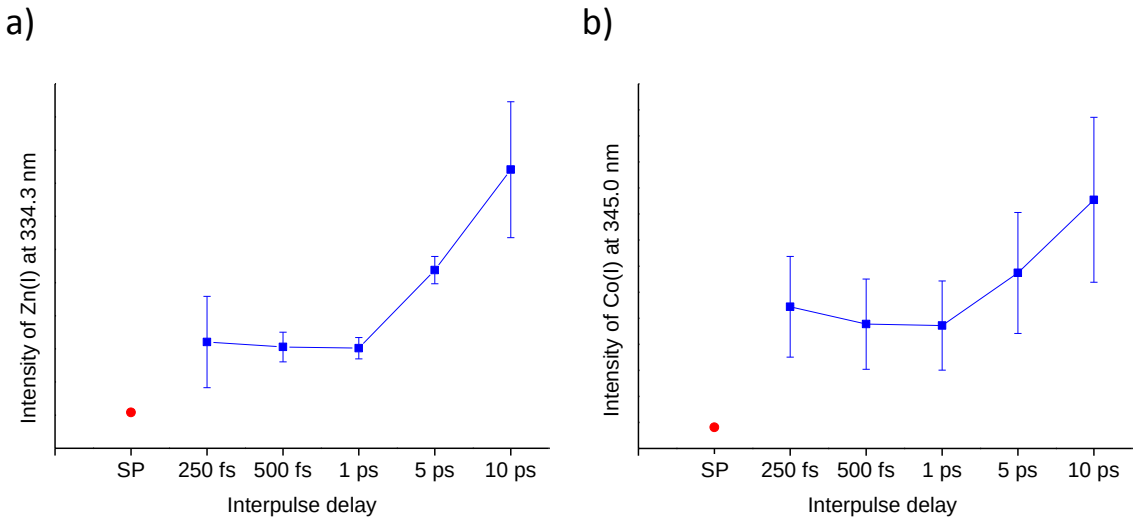


Figure 4.32 Intensity values of the Zn(I) 334.3 nm (a) and Co(I) 345.0 nm emission lines of figure 4.31 as a function of the interpulse delay for SP (red dots) and DP (blue squares) irradiation.

The signal intensity of the most intense Zn(I) line at 334.3 nm is plotted against the interpulse delay in figure 4.32a. Two different regimes are observed. For interpulse delays shorter than 1 ps, the intensity of Zn remains nearly constant, while at delays over 1 ps, the Zn signal intensity increases. Similar behaviour is observed in figure 4.32b for the Co(I) signal. The same trend is observed for the most intense emission lines of Zn(I) and Co(I) in the spectral region explored.

The presence of nanoparticles in the plasma plume was assessed by observing the plasma emission at longer times with respect to the pump pulse triggering. Figure 4.33 shows a broad emission centred around 525 nm, observed 1 µs after the arrival of the pump pulse, attributed to the emission of hot nanoparticles. Ablation was performed using the symmetric DP configuration with a fluence of about 0.2 J $cm^{-2}$ for each individual pulse.

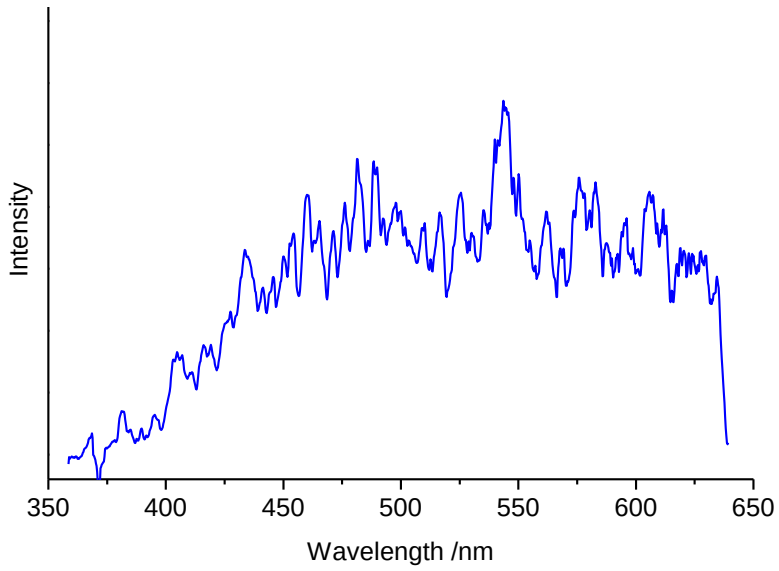


Figure 4.33 Broad emission of nanoparticles detected in Co/ZnS DP femtosecond ablation plasma. The spectrum corresponds to an interpulse delay Δ*t* of 250 fs. The fluence of each individual pulse was set to ~0.2 J $cm^{-2}$. Detection was performed at a delay time of 1 µs after the arrival of the probe pulse during a time window of 10 µs. The spectrum is the result of accumulating 125 individual spectra.

### 4.2.3 Double pulse femtosecond pulsed laser deposition of Co/ZnS

As mentioned, the final objective pursued in this part of the thesis is to transfer the same femtosecond DP approach to a PLD experiment in order to assess the possibilities of controlling the composition of nanostructured Co/ZnS deposits in which a fraction of Zn atoms are replaced by Co atoms in the semiconductor lattice.

For that purpose, the same laser system and double pulse optical arrangement used for TOF-MS studies was combined with a PLD chamber, described in more detail in the experimental section (see Chapter 2, pages 51 and thereafter).

The effect of the interpulse delay on the composition of thin films was studied by fabricating sets of deposits at different interpulse delays. Ablation of Co/ZnS targets containing 10% in weight of Co was carried out using the symmetric DP configuration described previously in TOF-MS experiments, this is, with pulses of equal fluence. In PLD experiments, due to the chamber configuration, the incidence angle of the ablation beam was 55°. Deposits were fabricated under vacuum conditions (< $10^{-5}$ mbar) at room temperature using a variable number of laser shots, typically ranging from 0.5 to 2 × $10^{6}$ individual pulses or sequences of double pulses at 1 kHz repetition rate.

The morphology and composition of the obtained deposits was studied *ex situ* via different characterization techniques (see section 2.2.3). Additionally, the deposition process was monitored *in situ* using a method based on reflectance measurements of the deposited layer (see section 2.2.2.4 for more details).

#### Morphological characterization of Co/ZnS deposits prepared by DP femtosecond PLD

The morphology of the obtained deposits was characterized by SEM, TEM and AFM. Figure 4.34a shows the typical aspect of the deposits obtained by PLD of Co/ZnS on silicon substrates. For the analysis of the deposit thickness by AFM, a portion of the substrate surface was masked before the deposition.

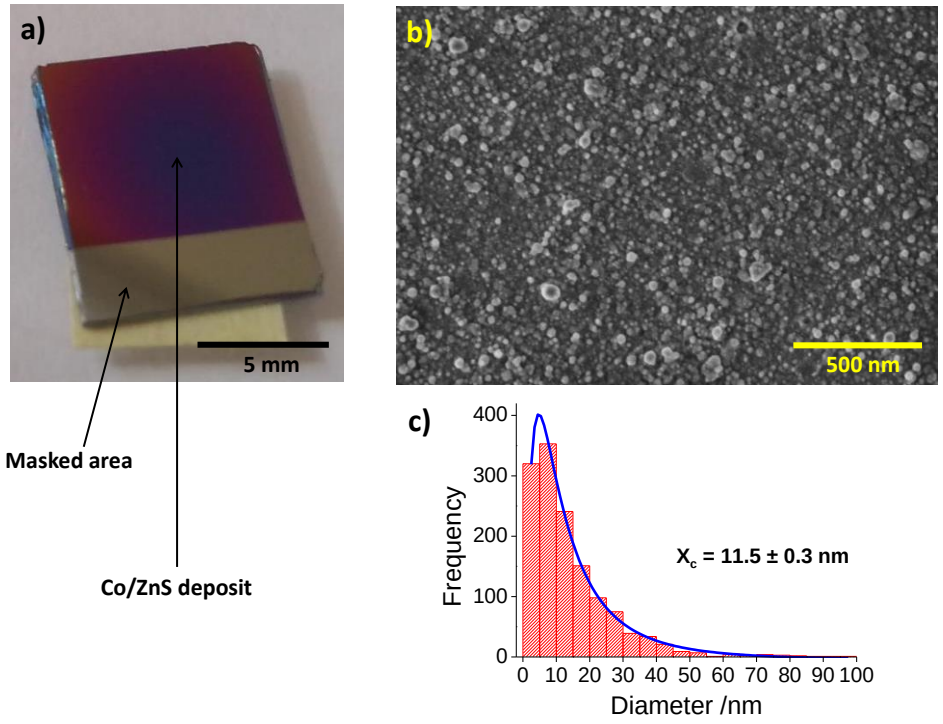


Figure 4.34 Images showing the aspect of deposits obtained by DP femtosecond PLD of Co/ZnS on Si (100) substrates: a) photograph showing one of the obtained deposits and a masked area of the Si substrate, b) HR-SEM image showing the nanoparticles present in the obtained films, c) histogram showing the nanoparticles size distribution corresponding to the deposit shown in panel b. The blue curve represents the log-normal fitting of the data.

Figure 4.34b shows a HR-SEM image of one of the deposits prepared by DP femtosecond ablation of Co/ZnS. The deposit morphology can be described as a nanoparticle-assembled thin film with an estimated nanoparticle mean size of ~ 12 nm.

As mentioned previously, deposits were also prepared by PLD directly on TEM grids. Figure 4.35 includes several images showing their aspect. In the images, spherical nanoparticles can be observed. The crystalline nature of these nanoparticles is confirmed by the observation of the crystalline planes in the high magnification images of figures 4.35b (see inset) and 4.35d.

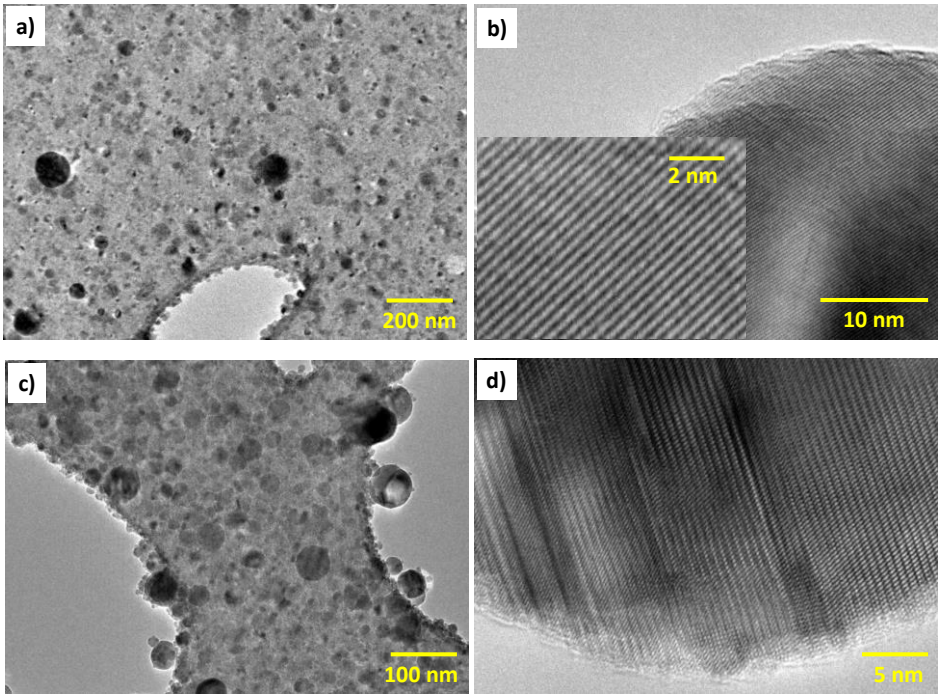


Figure 4.35 TEM images of deposits obtained on TEM grids by DP PLD of Co/ZnS. In panels b and d crystalline nanoparticles are shown in more detail.

TEM-XEDX analysis of individual nanoparticles reveals the presence of Co in the crystalline material. The compositional analysis of the deposits will be discussed in more detail later in this chapter.

### *In situ* reflectance measurements in pulsed laser deposition experiments

In order to follow the evolution of the deposition process, *in situ* measurements of the reflectance of a *p*-polarized He-Ne laser beam impinging on the substrate surface at an incidence angle $\theta_1$ = 80° were used. More details on this methodology can be found in the experimental section in Chapter 2. These *in situ* measurements proved to be crucial during the PLD experiments, as they served us to choose irradiation parameters comparable to the under-threshold conditions used in our previous TOF-MS experiments, and provided an estimation of the thickness variation as the deposit grows. In the following, the way in which the reflectance variation is related to the deposit thickness for transparent thin layers at the irradiation wavelength is explained.

Figure 4.36 depicts an schematic representation of the incident, reflected and transmitted beams together with their respective $\theta$ angles, in a system composed by

three media of different refractive index (medium 1 = vacuum, medium 2 = deposit and medium 3 = substrate). In the scheme, the letter *d* denotes the deposit thickness.

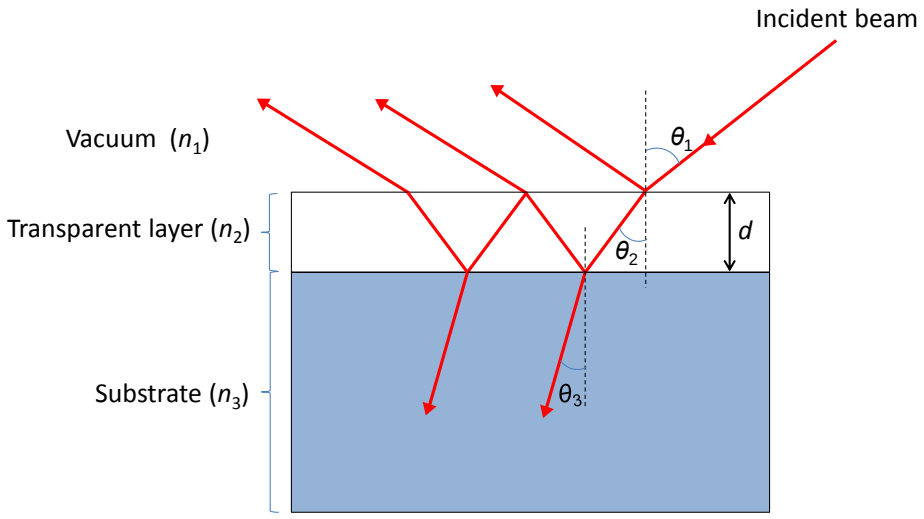


Figure 4.36 Schematic representation of the, incident, reflected and transmitted beams and corresponding angles in a system composed by three media with different refractive index *n*: vacuum, transparent deposit and substrate. The deposit layer thickness is denoted by the letter *d*.

Under the assumption of the Co/ZnS deposit being transparent at the wavelength of the incident radiation, $\lambda$ = 633 nm, the intensity of the reflected radiation, *R*, can be calculated from the Fresnel coefficients. The total intensity of the reflected beam is given by:

$$R = |r|^2 \tag{4.2}$$

In the scheme depicted in figure 4.36, it can be seen that the total reflected radiation is the result of several contributions: the reflected beam in the first interface (12) and the sum of infinite contributions due to reflection on the second interface (23). The reflexion coefficient *r* takes into account the sum of all contributions:

$$r = \frac{r_{12}+r_{23}e^{i2\beta}}{1+r_{12}r_{23}e^{i2\beta}} \tag{4.3}$$

where $\beta$ is a correction factor introduced to compensate for the phase shift due to the different optical path of each beam.

The parameter $\beta$ is given by the expression:

$$\beta = \frac{2\pi d}{\lambda}(p_2 + iq_2) \tag{4.4}$$

where $d$ is the aforementioned thin layer thickness, $\lambda$ is the incident radiation wavelength, and $p_2 = n_2 \cos \theta_2$ and $q_2 = 0$ for transparent media.

Therefore, for transparent thin layers, the variation of the reflectance $R$ with the deposit thickness $d$ results in a modulated signal (see figure 4.37). This is due to interferential effects between the beam reflected on the first interlayer and the beam reflected on the second interlayer. The maximum reflectance is achieved when there is constructive interference and the minimum reflectance is obtained in the case of destructive interference between both reflected beams. By plotting the theoretical reflectance values as a function of the deposit thickness $d$, the first maximum will be reached at a $d$ value corresponding to $\lambda/4n_2$.

Figure 4.37 shows an example of the variation of the experimental reflectance during a PLD process, fitted to the theoretical reflectance curve expected for an incidence angle $\theta_1 = 82.7°$. The data correspond to DP ablation at an interpulse delay of 2 ps.

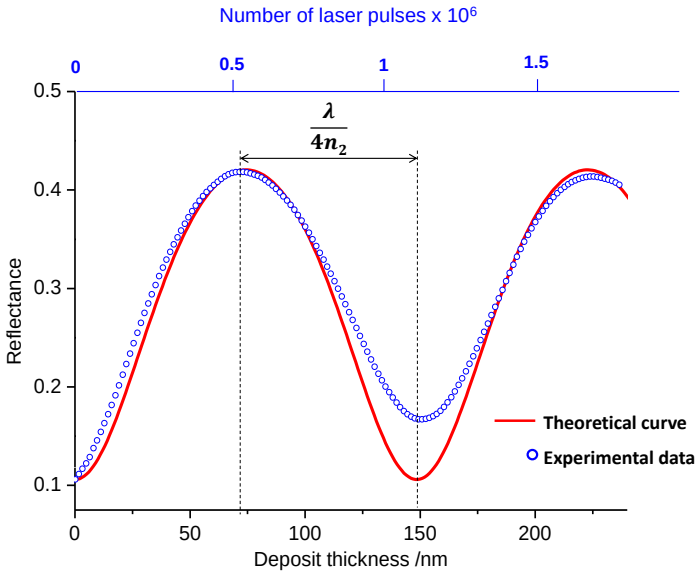


Figure 4.37 Variation of the reflectance as a function of the deposit thickness. The red line represents the theoretical reflectance curve. The blue circles represent the experimental reflectance data obtained during the deposition of Co/ZnS on a silicon substrate by DP ablation at $\Delta t$ = 2 ps using a fluence of ~0.8 J cm$^{-2}$ for each individual pulse.

The deviation of the experimental data with respect to the predicted reflectance curve at the first minimum shown around 150 nm can be related to variations in the optical properties of the deposit.

Similarly to TOF-MS analysis, where DP ablation was performed using a fluence for each individual pulse below the ion detection threshold, in PLD experiments was the variation of the reflectance, measured on the substrate surface as the deposit grows, what served to assess the under-threshold conditions for the DP deposition experiments.

The reflectance curves shown in Figure 4.38 exemplify this situation. In the figure, the evolution of the reflectance is plotted against the number of laser pulses, or double pulse sequences, for SP and DP ablation respectively, to evaluate the deposit growth. Single pulse ablation was performed in two different regimes: under-threshold conditions using 8 μJ of pulse energy (SP E) and above-threshold conditions using twice this energy value (SP 2E = 16 μJ) for comparison. Double pulse ablation was performed using under-threshold pulses of 8 μJ at different interpulse delays (0.5-300 ps).

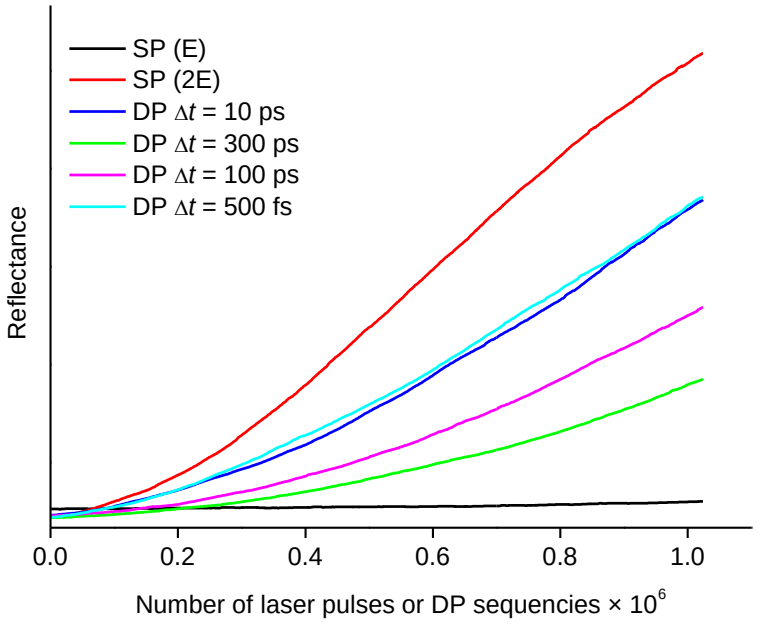


Figure 4.38 Evolution of the reflectance during the deposition process as a function of the number of laser pulses (or DP sequences) for SP with fluence ~0.2 J cm$^{-2}$ (SP E) and SP at twice this fluence value (SP 2E) and DP ablation at interpulse delays of 0.5, 10, 100 and 300 ps at a fluence of ~0.2 J cm$^{-2}$ for each individual pulse.

As can be observed, the reflectance of the deposit obtained by SP irradiation at $E$ = 8 μJ, remains close to the initial value after irradiation with 1 × $10^6$ pulses. On the contrary, the reflectance corresponding to deposits obtained with over-threshold pulses (SP, 2E), increases with the number of laser shots. In deposits obtained by DP ablation, the rate at which the reflectance increases with the number of laser pulse sequences is much higher than that expected for deposition with sequences of two uncoupled pulses of the same energy. In this case, the deposition rate is found to decrease with the interpulse delay, as can be seen in the figure, that is, the deposition rate of deposits prepared at short interpulse delays (500 fs and 10 ps) is higher than that corresponding to deposits prepared at the longer interpulse delays of 100 ps and 300 ps.

### Effect of interpulse delay on the deposit thickness and composition

Different sets of deposits were prepared at different interpulse delays by DP-PLD directly on TEM grids. Ablation was performed using pulses of equal fluence of about 0.2 J $cm^{-2}$, and a variable number of double pulse sequences from 0.5 to 2 × $10^6$. TEM-XEDX analysis was used to determine the composition of deposits prepared in the explored conditions. In the following, four sets of measurements, representative of the results obtained under different DP ablation conditions, are described.

#### Set 1

Figure 4.39 shows TEM images of deposits prepared by DP ablation of Co/ZnS targets at interpulse delays of 1 ps (figure 4.39a) and 300 ps (figure 4.39b). Double pulse ablation was performed with a total number of double pulse sequences of 0.5 × $10^6$ and the fluence of each individual pulse was set to ∼0.2 J $cm^{-2}$. Regarding the morphology of the deposits prepared at different interpulse delays, no significant differences were found. In both cases, deposits are characterized by the presence of spherical nanoparticles with sizes ranging from few nanometres to ∼100 nm diameter. In figure 4.39c, a high magnification image shows one of the nanoparticles exhibiting crystalline planes.

Figure 4.39d shows the reflectance curves obtained during the deposition of these samples by DP ablation at Δ$t$ = 1 ps (black curve), Δ$t$ = 300 ps (red curve) and by SP ablation (blue curve). As can be observed, the deposition rate (defined as the deposit thickness divided by the number of DP sequences) of DP ablation at Δ$t$ = 1 ps is higher than that obtained at Δ$t$ = 300 ps.

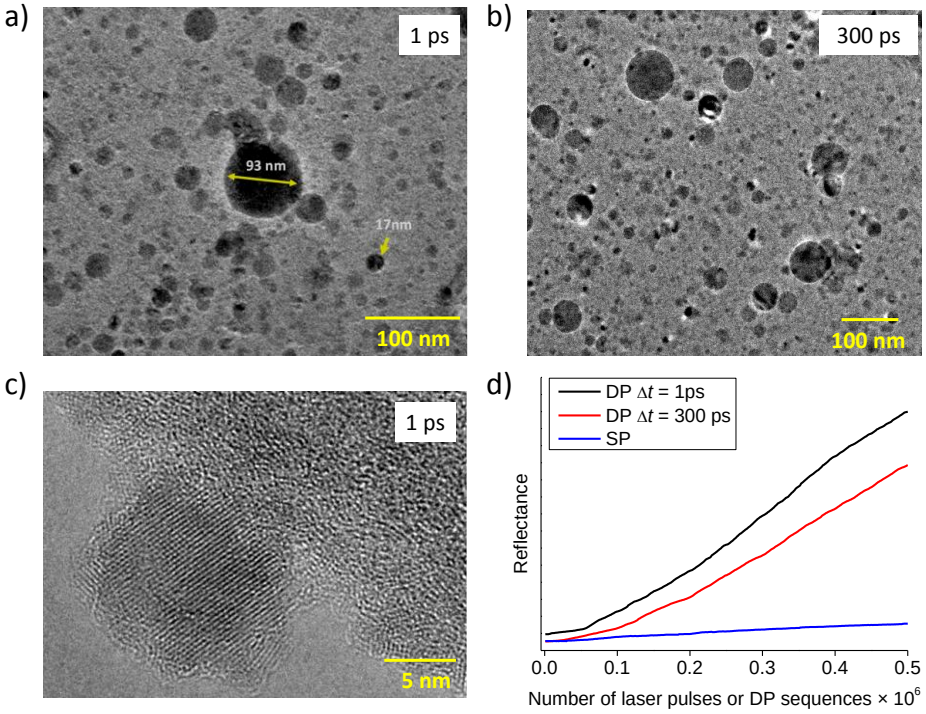


Figure 4.39 TEM images of deposits obtained directly on TEM grids by DP ablation of Co/ZnS targets at interpulse delays of: a) 1 ps and b) 300 ps. Panel c) shows a high magnification image of a crystalline nanoparticle. The diameter of some nanoparticles is indicated in panel a) to evidence the large dispersion of particle size in the deposits. Panel d) shows the corresponding reflectance curves obtained during the deposition of samples prepared by SP and DP ablation. The fluence of each individual pulse was set to ~0.2 J $cm^{-2}$ and the total number of single pulses or double pulse sequences was $0.5 \times 10^6$.

As previously mentioned, the thickness of the obtained deposits was assessed by AFM measurements. Figure 4.40a shows the corresponding AFM images. The obtained AFM profiles of deposits prepared by DP and SP ablation are shown in figure 4.40b. As can be observed in the table of figure 4.40c, the thickness values of deposits prepared by DP ablation at 1 and 300 ps are very similar. Nonetheless, these values are larger than the expected thickness of a deposit prepared by SP ablation with an equivalent number of uncoupled pulses.

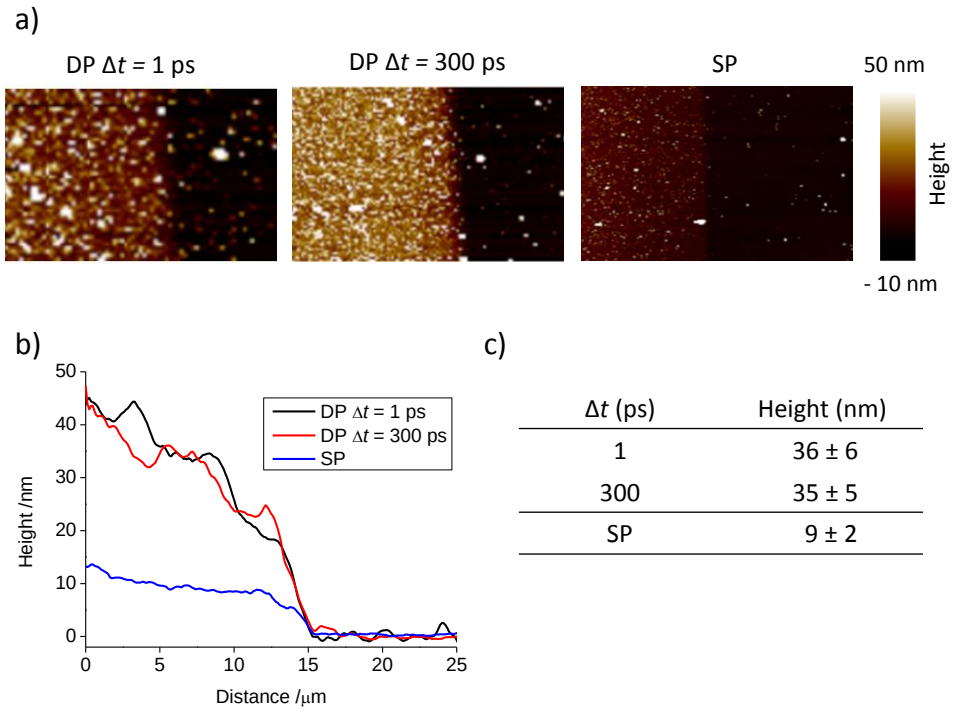


Figure 4.40 AFM data obtained after the analysis of deposits prepared on Si substrates by SP and DP ablation of Co/ZnS targets: a) AFM images of the studied deposits, b) AFM profiles of deposits prepared upon SP ablation and DP ablation at interpulse delays of 1 ps and 300 ps, c) thickness values of the corresponding deposits.

The substitution of Zn atoms by Co atoms in the ZnS lattice is one of the main objectives sought in these experiments and it was confirmed by the presence of Co atoms in crystalline nanoparticles. Therefore, the Co/Zn ratio is chosen as figure of merit to evaluate the compositional differences between deposits prepared at different interpulse delays. The results of the TEM-XEDX analysis of several individual nanoparticles present in each deposit are shown in table 4.3. The provided Co/Zn and S/Zn ratios are calculated from the averaged composition of the analysed nanoparticles in atomic percentage.

Table 4.3 Co/Zn and S/Zn atomic % ratios obtained by TEM-XEDX analysis of a collection of individual nanoparticles present in deposits prepared by DP ablation of Co/ZnS targets at interpulse delays of 10 ps and 300 ps.

| Interpulse delay (ps) | Co/Zn | | S/Zn | |
|---|---|---|---|---|
| | Mean | SD | Mean | SD |
| 1 | 0.10 | 0.07 | 1.04 | 0.07 |
| 300 | 0.04 | 0.03 | 0.92 | 0.09 |

Attending to the results of this first set of deposits, the Co/Zn ratio obtained at the longest interpulse delay of 300 ps decreases with respect to that of deposits fabricated at 1 ps delay.

### Set 2

A second set of deposits was prepared at interpulse delays of 10 ps and 300 ps by DP ablation with 0.5 × $10^6$ double pulse sequences and pulses of about 0.2 J $cm^{-2}$. The general aspect of the deposits obtained in these conditions can be seen in figure 4.41a and 4.41b. Once again, the morphology of the deposited material is very similar at both interpulse delays. The corresponding reflectance curves are plotted in figure 4.41c together with the curve obtained during SP ablation and deposition in similar conditions.

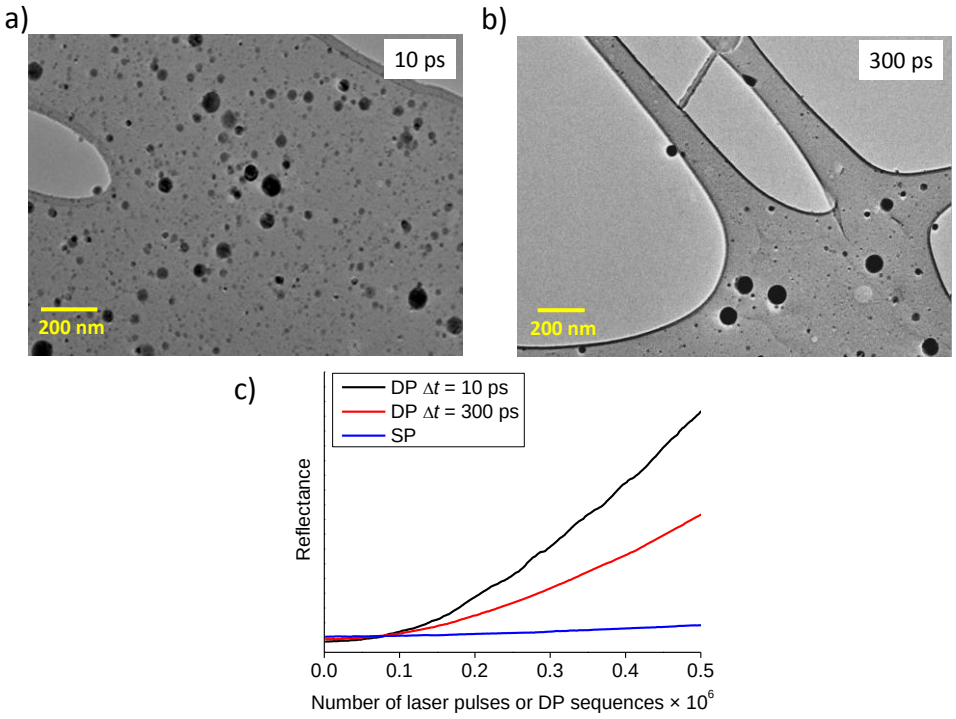


Figure 4.41 TEM images of deposits obtained directly on TEM grids by DP ablation of Co/ZnS targets at interpulse delays of: a) 10 ps, b) 300 ps. Panel c) shows the corresponding reflectance curves obtained during the deposition of samples prepared by SP and DP ablation. The fluence of each individual pulse was set to ~0.2 J $cm^{-2}$ and the total number of double pulse sequences was 0.5 × $10^6$.

As in the first set of deposits, the reflectance curves indicate that DP ablation at the shortest interpulse delay of 10 ps yields a faster increase of the deposit thickness compared to that obtained during deposition at 300 ps delay.

The corresponding AFM images and profiles are shown in figure 4.42a and 4.42b respectively. The values shown in the table of figure 4.42c reveal that, in this particular case, the thickness differences between deposits prepared by DP ablation at different interpulse delays are not so evident. As can be seen, the deposit obtained at 300 ps has a slightly lower thickness compared to that of the deposit obtained at an interpulse delay of 10 ps.

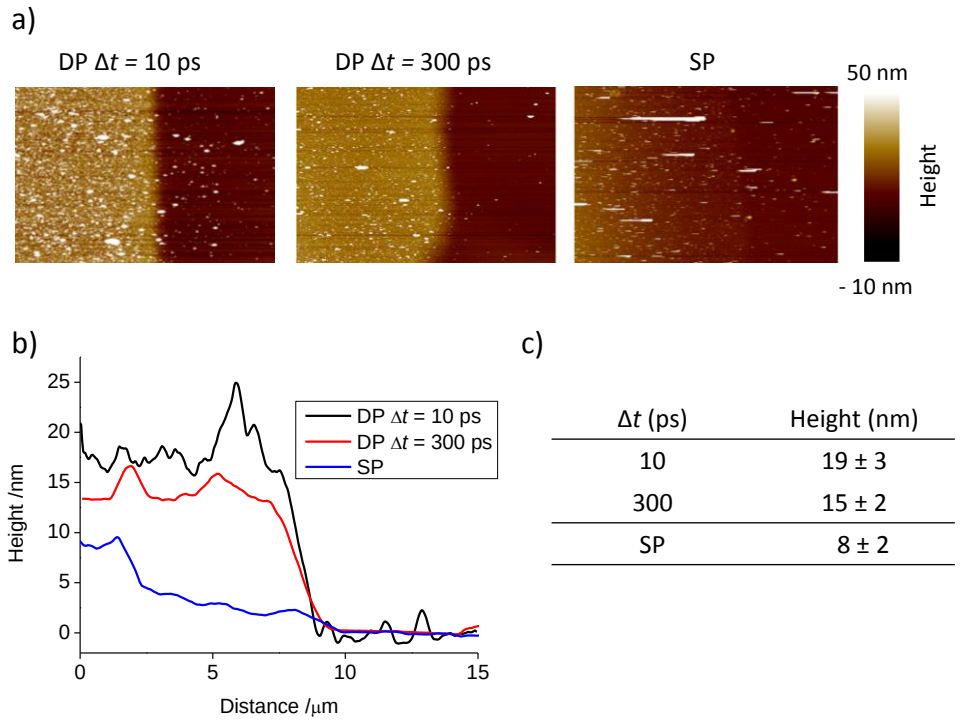


Figure 4.42 AFM data obtained after the analysis of deposits prepared on Si substrates by SP and DP ablation of Co/ZnS targets: a) AFM images of the studied deposits, b) AFM profiles of deposits prepared upon SP ablation and DP ablation at interpulse delays of 10 ps and 300 ps, c) thickness values of the corresponding deposits.

Table 4.4 shows the composition data from the TEM-XEDX analysis of individual nanoparticles present in deposits of prepared by DP at the different interpulse delays studied. The obtained data match those obtained in set 1. Samples prepared at the longer interpulse delay of 300 ps exhibit a lower Co/Zn ratio compared to that corresponding to 10 ps delay.

Table 4.4 Co/Zn and S/Zn atomic % ratios obtained by TEM-XEDX analysis of a collection of individual nanoparticles present in deposits prepared by DP ablation of Co/ZnS targets at interpulse delays of 10 ps and 300 ps.

| Interpulse delay (ps) | Co/Zn | | S/Zn | |
|---|---|---|---|---|
| | Mean | SD | Mean | SD |
| 10 | 0.10 | 0.06 | 1.20 | 0.06 |
| 300 | 0.04 | 0.02 | 1.07 | 0.07 |

## Set 3

In a third set, intermediate delays were explored by preparing deposits at 10, 100 and 300 ps with $1 \times 10^6$ double pulse sequences and pulses of about 0.2 J $cm^{-2}$. The corresponding TEM images are displayed in figures 4.43a, 4.43b and 4.43c respectively. The reflectance curves shown in figure 4.43d corroborate the trend observed in the first set, that is, the deposition rate decreases as the interpulse delay is increased. As observed previously, the reflectance values remain roughly constant for SP ablation.

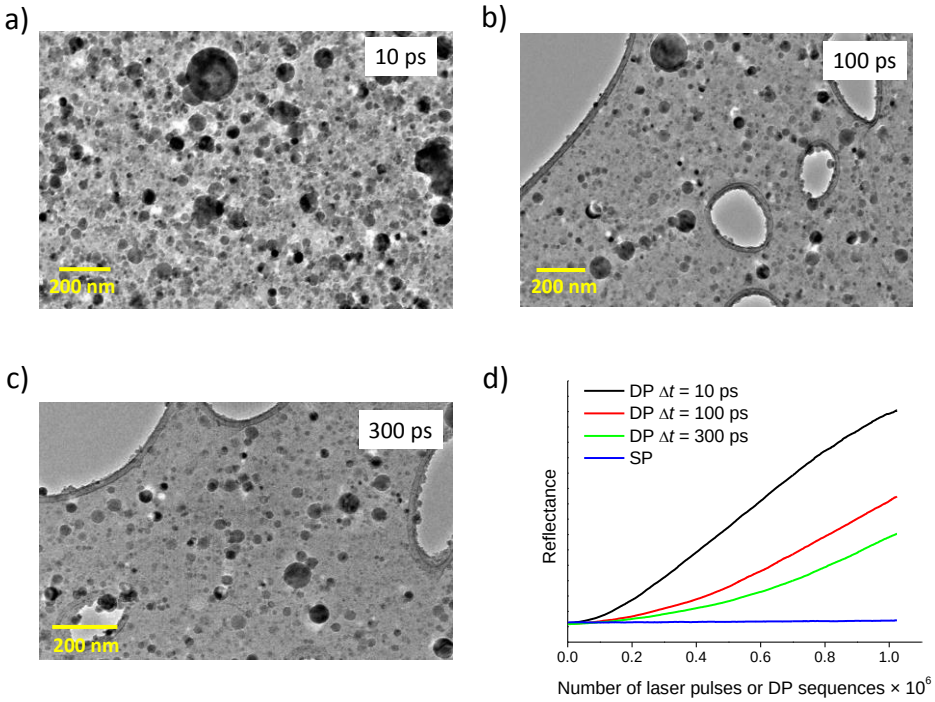


Figure 4.43 TEM images of deposits obtained directly on TEM grids by DP ablation of Co/ZnS targets at interpulse delays of: a) 10 ps, b) 100 ps and c) 300 ps. Panel d) shows the corresponding reflectance curves obtained during deposition of samples prepared by SP and DP ablation. The fluence of each individual pulse was set to ~0.2 J $cm^{-2}$ and the total number of single pulses or double pulse sequences was $1 \times 10^6$.

The AFM images corresponding to deposits prepared by DP ablation at $\Delta t$ = 10 ps, $\Delta t$ = 100 ps and $\Delta t$ = 300 ps are shown in figure 4.44a together with data from a SP ablation sample. The obtained AFM profiles are shown in figure 4.44b and the corresponding thickness values are listed in the table displayed figure 4.44c.

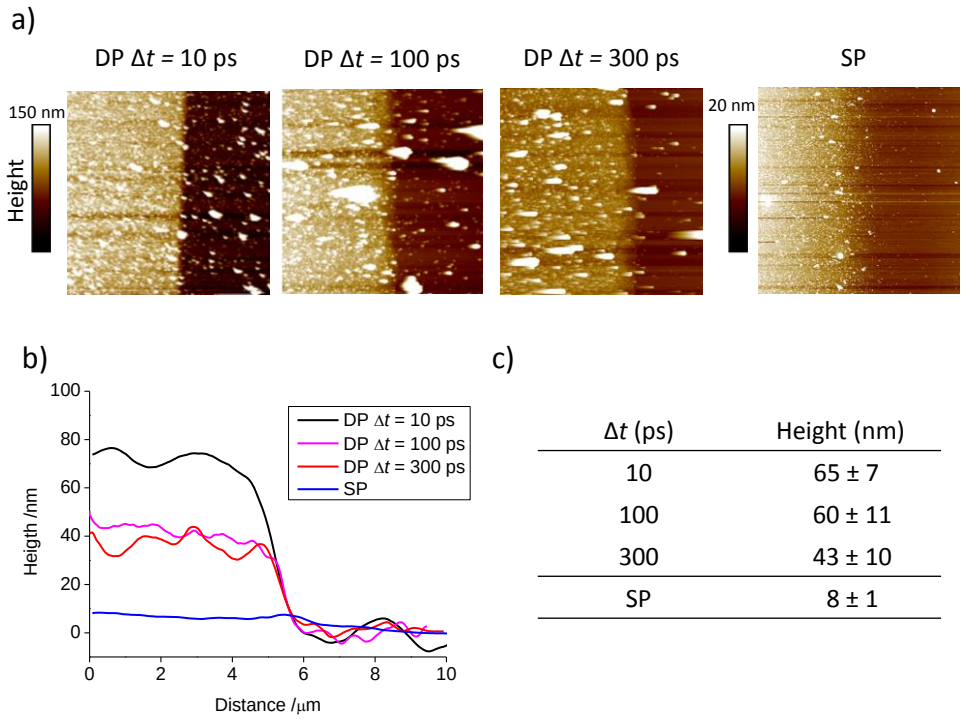


| Δt (ps) | Height (nm) |
|---|---|
| 10 | 65 ± 7 |
| 100 | 60 ± 11 |
| 300 | 43 ± 10 |
| SP | 8 ± 1 |

Figure 4.44 AFM data obtained after the analysis of deposits prepared on Si substrates by SP and DP ablation of Co/ZnS targets: a) AFM images of the studied deposits, b) AFM profiles of deposits prepared upon SP ablation and DP ablation at interpulse delays of 10 ps, 100 ps, 300 ps, c) thickness values of the corresponding deposits.

Table 4.5 lists the averaged compositional ratios of individual nanoparticles present in samples prepared at 10 ps, 100 ps and 300 ps. Differently to the trend observed in the previous two sets, where the Co/Zn ratio decreased with the interpulse delay, the results indicate an increase of the Co/Zn ratio at the longest interpulse delay studied, while values obtained from deposits prepared at 10 ps and 100 ps have comparable ratios.

Table 4.5 Co/Zn and S/Zn atomic % ratios obtained by TEM-XEDX analysis of a collection of individual nanoparticles present in deposits prepared by DP ablation of Co/ZnS targets at interpulse delays of 10 ps, 100 ps and 300 ps.

| Interpulse delay (ps) | Co/Zn | | S/Zn | |
|---|---|---|---|---|
| | Mean | SD | Mean | SD |
| 10 | 0.019 | 0.005 | 1.02 | 0.09 |
| 100 | 0.015 | 0.009 | 1.22 | 0.07 |
| 300 | 0.041 | 0.018 | 0.88 | 0.07 |

## Set 4

TEM images of the deposits obtained by DP ablation at interpulse delays of 10 ps, 100 ps and 300 ps prepared with $2 \times 10^6$ laser pulse sequences and fluence of about 0.2 J $cm^{-2}$ are shown in figure 4.45a, figure 4.45b and figure 4.45c respectively.

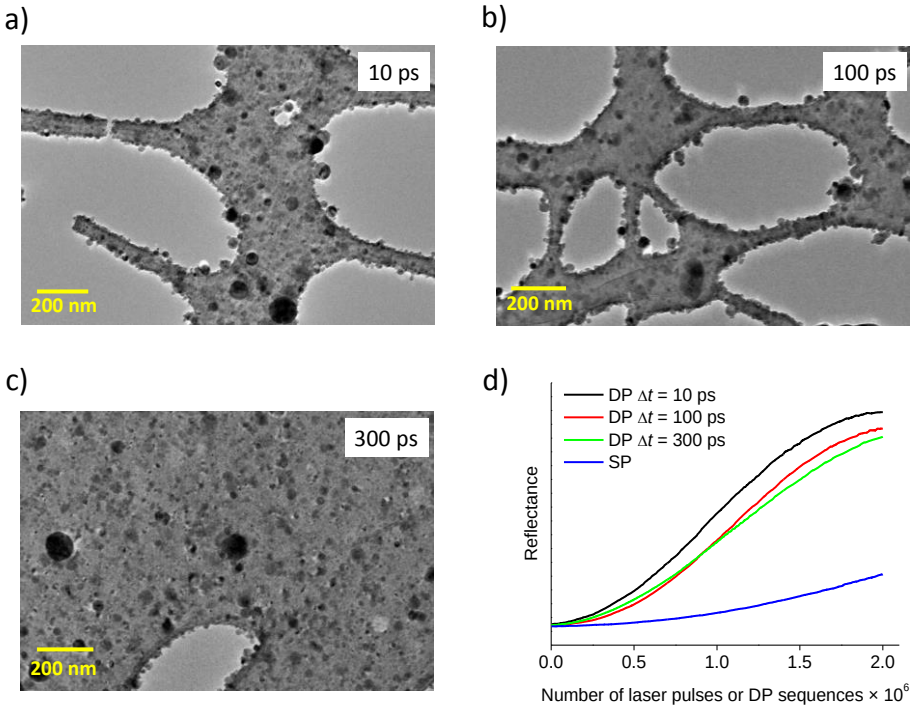


Figure 4.45 TEM images of deposits obtained directly on TEM grids by DP ablation of Co/ZnS targets at interpulse delays of: a) 10 ps, b) 100 ps and c) 300 ps. Panel d) shows the corresponding reflectance curves obtained during the deposition of samples prepared by SP and DP ablation. The fluence of each individual pulse was set to ~0.2 J $cm^{-2}$ and the total number of single pulses or double pulse sequences was set to $2 \times 10^6$.

The same trend observed in the previous sets is also patent in figure 4.45d. Reflectance of deposits prepared at short interpulse delays increases faster than in the case of deposits prepared at longer delays and it is remarkably larger than that observed for SP at a given number of laser pulses. As can be seen in the figure, in this particular case, the reflectance curve obtained during SP deposition (blue curve) increases significantly if compared with previous experiments, where SP reflectance values remained roughly constant. The corresponding AFM data are reported in the table of figure 4.46d.

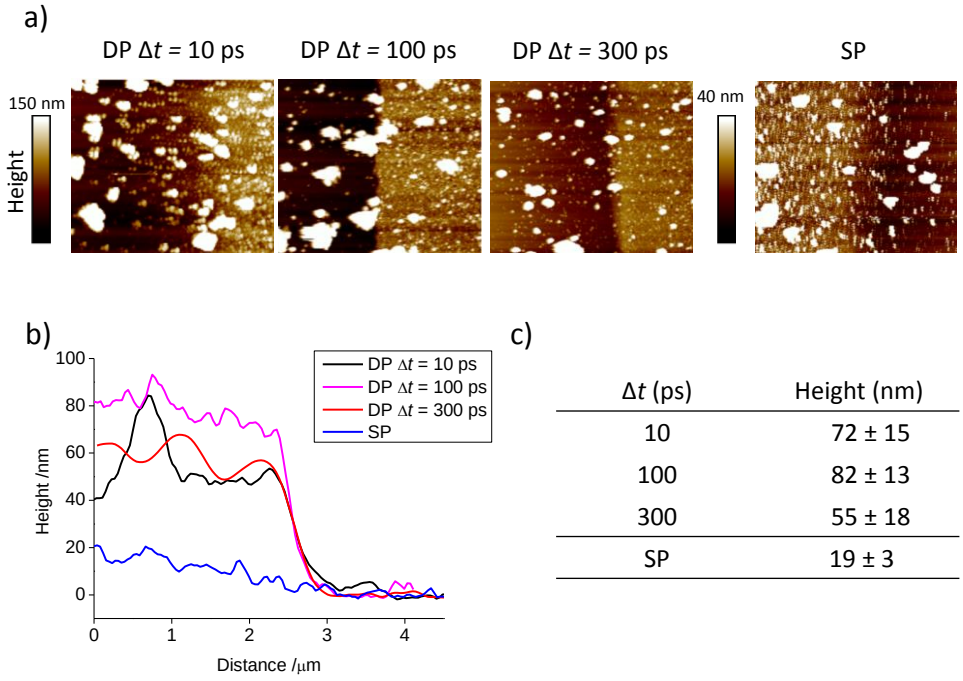


| Δt (ps) | Height (nm) |
|---|---|
| 10 | 72 ± 15 |
| 100 | 82 ± 13 |
| 300 | 55 ± 18 |
| SP | 19 ± 3 |

Figure 4.46 AFM data obtained after the analysis of deposits prepared on Si substrates by SP and DP ablation of Co/ZnS targets: a) AFM images of the studied deposits, b) AFM profiles of deposits prepared upon SP ablation and DP ablation at 10 ps, 100 ps and 300 ps, c) thickness values of the corresponding deposits.

The Co/Zn and S/Zn ratios found after TEM-XEDX analysis of individual nanoparticles in the three deposits obtained by DP ablation at the different interpulse delays are presented in table 4.6. The results are very similar to those obtained in the previous set.

Table 4.6 Co/Zn and S/Zn atomic % ratios obtained by TEM-XEDX analysis of a collection of individual nanoparticles present in deposits prepared by DP ablation of Co/ZnS targets at interpulse delays of 10 ps, 100 ps and 300 ps.

| Interpulse delay (ps) | Co/Zn | | S/Zn | |
|---|---|---|---|---|
| | Mean | SD | Mean | SD |
| 10 | 0.032 | 0.022 | 1.14 | 0.08 |
| 100 | 0.037 | 0.013 | 1.05 | 0.11 |
| 300 | 0.041 | 0.021 | 0.91 | 0.11 |

In order to reduce the large dispersion of the data obtained in the analyses of individual nanoparticles, several TEM-XEDX measurements were performed in areas of about 1.3 µm of diameter in samples of sets 3 and 4, thus including a larger number of particles. A TEM image of the analysed area can be seen in figure 4.47. The obtained Co/Zn and S/Zn ratios are listed in table 4.7 below.

Table 4.7 Co/Zn and S/Zn atomic % ratios obtained by TEM-XEDX analysis of areas of about 1.3 µm diameter in the corresponding deposits of set 3.

| | Interpulse delay (ps) | Co/Zn | | S/Zn | |
|---|---|---|---|---|---|
| | | Mean | SD | Mean | SD |
| Set 3 | 10 | 0.06 | 0.01 | 1.21 | 0.08 |
| | 100 | 0.04 | 0.01 | 1.29 | 0.05 |
| | 300 | 0.062 | 0.003 | 1.10 | 0.21 |
| Set 4 | 10 | 0.115 | 0.046 | 1.07 | 0.02 |
| | 100 | 0.074 | 0.015 | 1.09 | 0.05 |
| | 300 | 0.071 | 0.018 | 0.87 | 0.08 |

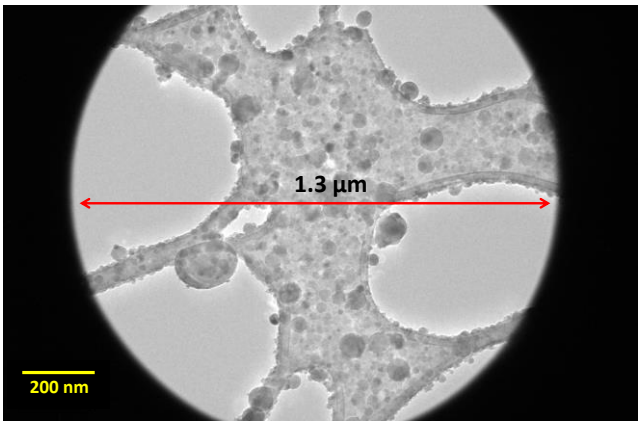


Figure 4.47 TEM image showing the analyzed area in one of the PLD deposits.

As expected, the dispersion of the data decreases with respect to the previous measurements. However, the results of these averaged analyses do not evidence a clear trend. A better comparison of the results can be made by plotting all the compositional data together. In figure 4.48, the Co/Zn and S/Zn ratios obtained from the TEM-XEDX analysis of individual nanoparticles (sets 1 and 2) and areas (sets 3 and 4) are plotted as a function of the interpulse delay. In all, the obtained data on the dependence of the Co/Zn ratio on interpulse delay do not show a clear trend. Some discussion on this fact will be included in the next section.

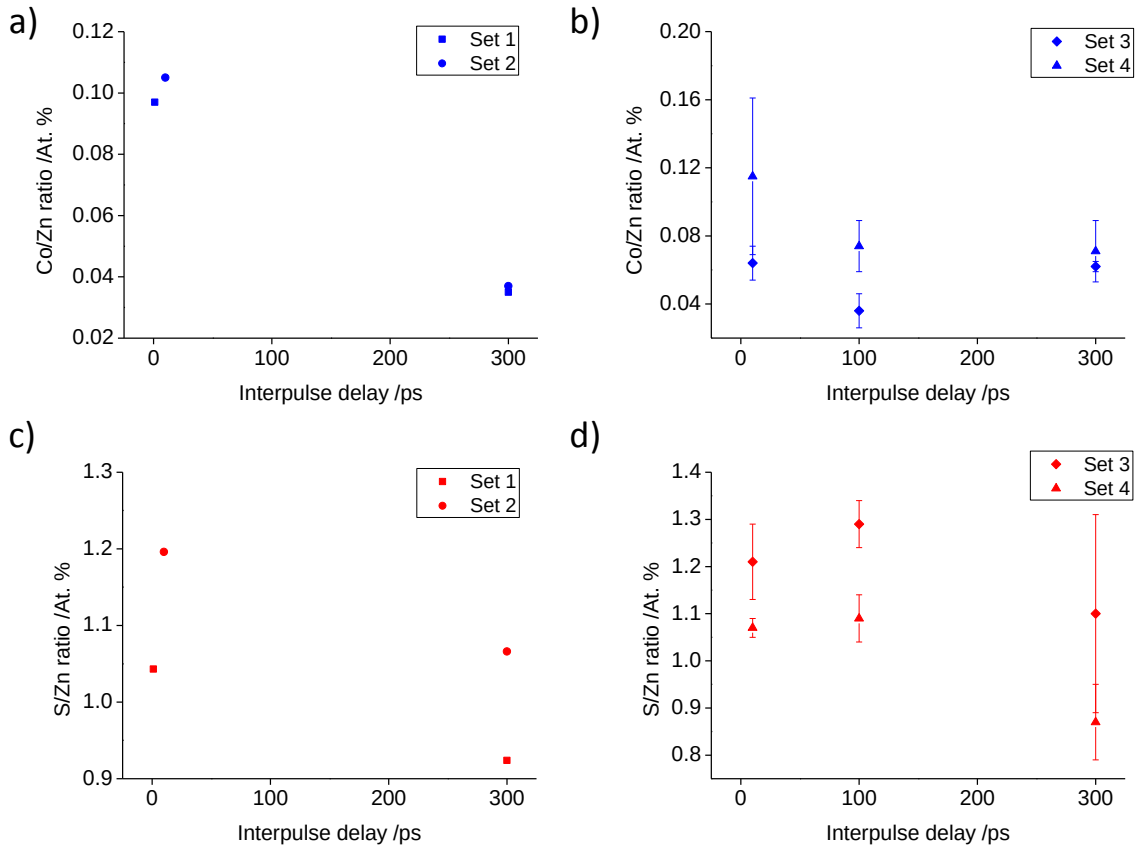


Figure 4.48 Atomic percentage ratios obtained by TEM-XEDX analysis of individual nanoparticles (sets 1 and 2) and areas (sets 3 and 4) obtained in deposits prepared by DP ablation of Co/ZnS targets at different interpulse delays: a) and b) Co/Zn ratio and c) and d) S/Zn ratio. Error bars have been omitted in Sets 1 and 2 for clarity but the large standard deviation of data (displayed in tables 4.3 and 4.4) should be noted.

## 4.2.4 Discussion of results

### Ablation dynamics of Co/ZnS targets

As already mentioned, the main characteristic of ultrafast laser irradiation of materials resides in the fact that excitation of electrons or free carriers is completed in the femtosecond time scale, while the material lattice can remain at its initial density and temperature for times in the picosecond range.

In DP ultrafast laser ablation, the properties of the irradiated layer are modified by the first pulse and evolve with time, causing enhanced or reduced coupling of the second pulse at the different time delays. Some insight into the processes driving the ablation dynamics of Co and ZnS can be gained by the comparison between the symmetric and asymmetric DP configurations, shown in figure 4.28. Comparison between DP HH and HL, both at the same pump pulse fluence, can inform on the response of the irradiated skin layer to probe pulses with the different fluences H and L. On the other hand, comparison between HH and LH can help to assess how the different transient modifications in the skin layer, induced respectively at the H and L pump pulse fluences, affect the coupling efficiency of the H probe pulse.

It will be also assumed throughout this discussion that in the HL configuration, ($F_{probe} << F_{pump}$), the DP ablation dynamics mainly reflects the time evolution of the layer irradiated by the pump pulse.

Due to the different mechanisms involved in the ablation of metals and semiconductors, the interaction of the laser radiation with the two components of the target, Co and ZnS, will be treated separately. The constant values used in the following discussion are listed in table 4.8.

Table 4.8 Values of the physical constants of Co and ZnS relevant for the discussion of results on PLD experiments in Co/ZnS material.

| | Constant | Symbol | Value | Reference |
|---|---|---|---|---|
| Co | Optical penetration depth | $\alpha^{-1}$ | 13.2 nm[a] | [64] |
| | Reflectivity | $R$ | 0.72[a] | [64] |
| | Transmittance | $T'$ | 0.37 | [64] |
| | Electronic specific heat | $A_e$ | 704 J $m^{-3}$ $K^{-2}$ | [65] |
| | Electron-phonon coupling | $G$ | $9.3\times10^{17}$ W $m^{-3}$ $K^{-1}$ | [65] |
| ZnS | Reflectivity | $R$ | 0.16[a] | [64] |
| | 3-photon absorption coefficient | $\alpha_{3PA}$ | $1.7\times10^{-21}$ $cm^3$ $W^{-2}$ | [66] |

[a] at 800 nm and normal incidence

### Double pulse ablation of Co

The estimation of the energy absorbed by the electronic subsystem and of the time scale in which this energy is transferred to the metal lattice can provide information on the modifications produced in the material by the pump pulse.

The maximum electron temperature $T_e$ reached in the irradiated layer and the electron-phonon coupling time $\tau_{e\text{-}ph}$ can be calculated under the assumptions of the two temperature model (TTM) for metals [67]. This model considers the electron subsystem as a hot bath of electrons in a cold lattice, both at separated temperatures $T_e$ and $T_L$ for the electrons and the lattice respectively. The TTM can be expressed as in (4.5).

$$C_e \frac{\delta T_e}{\delta t} = \frac{\delta}{\delta z} K_e \frac{\delta T_e}{\delta z} - G(T_e - T_L) + A(z,t) \tag{4.5}$$

where $K$ is the thermal conductivity of electrons, $G$ is the electron-phonon coupling constant and $A(z, t)$ is the heat source term.

On the other hand, the heat transfer towards deeper layers of the lattice can be expressed by (4.6) [68, 69].

$$C_L \frac{\delta T_L}{\delta t} = \frac{\delta}{\delta z} K_L \frac{\delta T_L}{\delta z} + G(T_e - T_L) \tag{4.6}$$

where $C_L$ and $K_L$ are the lattice specific heat and thermal conductivity respectively.

The first and the last terms of the TTM equation account for the electron conductivity due to electron diffusion towards deeper layers of the material and for the absorption rate of the laser pulse respectively. As both processes are completed in a time scale close

to that of the laser pulse, much shorter than the relatively slow electron-phonon energy transfer (typically in the picoseconds range); the latter can be treated separately as:

$$\left(C_e \frac{\delta T_e}{\delta t}\right)_{e-ph} = -G(T_e - T_L) \tag{4.7}$$

The maximum electron temperature $T_e$ reached after the absorption of the femtosecond laser pulse can be obtained from:

$$\left(\frac{\delta Q_e}{\delta T_e}\right) = C_e \tag{4.8}$$

where $Q_e$ is the density of energy absorbed by the electron subsystem and $C_e$ is the electronic specific heat, which for metals can be approximated by the expression given in (4.9).

$$C_e = A_e T_e \tag{4.9}$$

being $A_e$ the electronic specific heat constant. Thus:

$$\left(\frac{\delta Q_e}{\delta T_e}\right) = A_e T_e \tag{4.10}$$

Integration of (4.10) yields the expression:

$$Q_e = \frac{1}{2} A_e (T_e^2 - T_{ei}^2) \tag{4.11}$$

from which $T_e$ is obtained:

$$T_e = \sqrt{\frac{2Q_e}{A_e} + T_{ei}^2} \tag{4.12}$$

The initial value for the electron temperature of the system, $T_{ei}$, can be neglected against the final electron temperature expected upon irradiation and $T_e$ can be obtained as:

$$T_e = \sqrt{\frac{2Q_e}{A_e}} \tag{4.13}$$

In the case of cobalt ablation, when the pump pulse has the highest fluence (HH and HL DP configurations), the energy density $Q_e$ deposited in an irradiated layer of thickness equal to the optical penetration depth ($l_s = \alpha^{-1}$) can be estimated using:

$$Q_e = F_{pump}(1 - R)(1 - T')\alpha \tag{4.14}$$

where $\alpha$ is the absorption coefficient, $F_{pump}$ is the fluence of the pump pulse ($F_{pump}$ = 0.2 J cm$^{-2}$), $R$ is the reflectance of cobalt for 800 nm radiation at normal incidence and $T'$ is the transmittance at the given optical penetration depth [64]. With these values, the calculated energy density is $Q_e$ = 2.5×10$^{10}$ J m$^{-3}$. Diffusion of hot electrons should also be considered. In the case of Co, the layer thickness heated by electron diffusion is in the order of the optical penetration depth [65]. Substituting expression (4.14) into (4.13) the final expression shown in (4.15) for the electron maximum temperature is obtained.

$$T_e = \sqrt{\frac{2F_{inc}(1-R)(1-T')}{A_e l_s}} \tag{4.15}$$

For $F_{inc}$ = 0.2 J cm$^{-2}$ the calculated value for the maximum electron temperature reached after irradiation with the H pump pulse is ~8500 K.

The time evolution of the electron temperature can be assumed to be proportional to the difference between the electron and lattice temperatures:

$$\frac{\delta T_e}{\delta t} = \frac{T_e - T_L}{\tau_{e-ph}} \tag{4.16}$$

where $\tau_{e\text{-}ph}$ represents the electron cooling time constant. Combining (4.7), (4.9) and (4.16) the final expression for the electron-phonon coupling time $\tau_{e\text{-}ph}$ is given by:

$$\tau_{e-ph} = \frac{1}{G} A_e T_e \tag{4.17}$$

For the values $A_e$ and $G$ provided in table 4.8, the estimated electron phonon coupling time is ~6 ps.

Using the same equations, similar estimations can be made for the L pump pulse. In this case the obtained values for the electron temperature and electron-phonon coupling time are ~6000 K and ~5 ps respectively.

It should be noted that transient changes in the thermophysical properties of the irradiated layer can affect the maximum electron temperature reached at a given absorbed fluence. This was found to be the case in calculations for *d*-band metals as Ni and Cu [68, 70, 71]. However, the expressions used above are generally considered to hold at the relatively low fluences of the individual pulses used in our experiment.

It can be assumed that the signal obtained at delays shorter than 10 ps in HL DP ablation reflects the growth of the Co lattice temperature, that is, the process of energy transfer via electron-phonon coupling. The fast rise of $Co^+$ signal up to approximately 5 ps

observed in figure 4.28b for HL ablation is therefore compatible with electron-phonon coupling times in the range of few picoseconds as the $\tau_{e\text{-}ph}$ value estimated above. This electron-phonon coupling rate would also be consistent with the fast rise of the Co signal observed in the HH scans obtained with higher temporal resolution shown in figure 4.26.

At times longer than ~10 ps the coupling of the probe pulse can be affected by the evolution of the non-equilibrium melting of the irradiated layer. The density of energy ($Q_e$ = 2.5×10$^{10}$ J m$^{-3}$) deposited by the pump pulse is high enough to rise the lattice temperature above the melting point of Co ($mp_{Co}$ = 1780 K) [72].

The optical conductivity at 800 nm of the liquid Co is reported to be about twice higher than that of the bulk solid [73, 74]. Taking this fact into account, the differences between the ablation dynamics observed at interpulse delays above ~10 ps for HH, HL and LH (shown in figure 4.28) will be discussed under the assumption that the layer irradiated by the pump pulse melts and therefore this process will affect the absorption of the probe pulse by the skin layer.

In LH DP ablation, $Co^+$ signal intensity rises up to delays around 100 ps (see figure 4.28b). This increase in the signal could be explained by the slow solid-liquid transition after the absorption of the pump pulse. As the melting front propagates from the surface to the inner layers of the bulk material the coupling of the probe pulse would increase with the interpulse delay due to the growing depth of the molten layer. The observed rising time of the signal would be compatible with the dynamics of heterogeneous melting, governed by the propagation velocity of the melting front [75].

The slow rise of the $Co^+$ signal observed in LH DP ablation in the range of 10-100 ps, can be compared with the fast rise of the signal intensity obtained by HH DP ablation. In the latter due to the higher fluence of the pump pulse (about twice than that in the LH scheme), a large overheating (temperature of the lattice in excess over the melting temperature) is expected. The velocity of the solid-liquid interface increases with the degree of overheating and above a certain level, homogeneous melting occurs [69]. At short delay times (~10 ps) the H probe pulse would couple to the fast developed molten layer reaching the maximum ion signal intensity, at variance with the LH case. At the successive pump-probe delays, thermal loses lead to a flow of energy out of the pump pulse irradiated layer and the probe pulse would be absorbed by a progressively cooler material; however, the nearly constant ion signal intensity observed suggests that the energy delivered by the H probe pulse is high enough to sustain the ion ejection efficiency up to ~100 ps, to slowly decrease at longer times.

Finally, the comparison between the dynamics of HH and HL DP ablation suggests that at the lower fluence of the probe pulse in the HL case, the energy delivered on the skin layer is not enough to sustain a similar ion ejection efficiency at long and short delays, leading to the observed slow decay of the $Co^+$ signal intensity.

### Double pulse ablation of ZnS

As in the case of cobalt, DP ablation of ZnS will be discussed assuming that the HL DP ablation dynamics reflects the temporal evolution of the layer after absorption of the H pump pulse. Therefore the absorption of the pump pulse and the main subsequent processes affecting the evolution of the carrier energy and density will be considered in the following.

ZnS is a direct band gap semiconductor with an energy gap ($E_{gap}$) of 3.7 eV [76] for its most stable cubic structure. At the laser pump pulse wavelength of 800 nm and intensity $I = 2\times10^{12}$ W cm$^{-2}$ (for the H pump pulse), the absorption mechanism is mainly a three-photon process. Carrier excitation mainly involves transitions between *p* band states of S in the valence band to *s* and *p* states of Zn in the conduction band [77]. The excitation process converts the absorbed energy to kinetic energy of the free carriers, and "potential" energy stored in the electron-hole pairs.

The initial kinetic energy of the carriers ($E_{k(e)}$) upon irradiation at 800 nm is:

$$E_{k(e)} = 3h\nu - E_{gap} \tag{4.18}$$

This results in a kinetic energy $E_{k(e)}$ = 0.95 eV, which evolves in the femtosecond time scale to an equilibrium energy distribution characterized by a temperature $T_e$ which can be calculated using (4.19), where the specific heat of free carriers is assumed to be $3k_B/2$.

$$T_e = \left(\frac{2}{3k_B}\right) E_{k(e)} \tag{4.19}$$

The obtained value for $T_e$ is ~7500 K.

The carrier density $N_{e\text{-}h}$ produced upon absorption of the H pump pulse can be estimated from:

$$\left(\frac{\delta N_{e-h}}{\delta t}\right)_{abs} = \frac{\alpha_{3PA} I^3 (1-R)^3}{3h\nu} \tag{4.20}$$

where $\alpha_{3PA}$ is the three-photon absorption (3PA) coefficient and $R$ is the reflectance of ZnS at 800 nm. For the values given in table 4.8 and integrating over the laser pulse duration the carrier density results in a value of $\sim 1 \times 10^{21}$ cm$^{-3}$.

Besides the kinetic energy gained through 3PA, part of the pump pulse energy can be absorbed by the growing population of free carriers, resulting in an increase of their kinetic energy. It has been reported that free carrier absorption (FCA) in ZnS is not negligible at pump intensities above $9\times10^{10}$ W cm$^{-2}$, being the estimated FCA cross section $\alpha_{FCA} = 1.5 \times 10^{-18}$ cm$^2$ [78].

As the pump pulse propagates in the material, the intensity variation due to the three photon and free carrier absorption processes can be written as:

$$\frac{dI}{dz} = I[\alpha z] \tag{4.21}$$

where $z$ is the depth into the target and $\alpha$ has the meaning of an effective linear absorption coefficient defined as:

$$\alpha = [\alpha_{3PA} I^2 (1-R)^2 + \alpha_{FCA} N_{e-h}] \tag{4.22}$$

From the data given in table 4.8 the contributions of 3PA and FCA to the effective linear absorption coefficient can be calculated. It is obtained that the 3PA contribution is much higher than that due to FCA, even at the end of the pump pulse, when the growing population of free carriers reaches its maximum number density and FCA can take place upon irradiation by the trailing part of the pump pulse. Therefore, neglecting the term due to FCA, the effective linear absorption coefficient for the H pump pulse is:

$$\alpha = \alpha_{3PA} I^2 (1-R)^2 = 5 \times 10^3 cm^{-1} \tag{4.23}$$

from which the optical penetration depth can be calculated as $\alpha^{-1} = 2$ µm.

In photoexcited semiconductors, the temporal evolution of the irradiated layer is affected by the free carriers relaxation dynamics, which involves a combination of competing processes, as phonon emission, radiative and non-radiative recombination and carrier diffusion [79, 80]. The relative importance of these processes in ZnS after the absorption of the pump pulse will be discussed in the following.

In direct-gap semiconductors radiative channels dominate the recombination of carriers at low carrier densities while at high densities Auger recombination rates increase [81]. For instance, in GaAs it is known that Auger recombination becomes dominant at carrier

densities of $10^{21}$ $cm^{-3}$ [80, 81]. It is also reported that three-centre Auger recombination mechanisms involving impurity centres in ZnS, compete with radiative transitions [82], suggesting that these Auger processes can be also efficient ways to increase the kinetic energy of the carriers generated in ZnS upon absorption of the H pump pulse, at the expense of the reduction of the carrier number density. The kinetic energy is subsequently transferred to the lattice.

In polar semiconductors, carrier-phonon coupling times are known to be dependent on carrier density, thus relaxation times can be in the range of sub-picoseconds to tens of picoseconds, depending on whether the carrier density is below or above a critical value. This critical carrier density scales with the carrier effective mass and phonon energy for direct-gap polar semiconductors [81]. For GaAs the reported critical density is $N_c \approx 10^{18}$ $cm^{-3}$. Comparison of this value with the carrier density of $10^{21}$ $cm^{-3}$, achieved upon irradiation with the H pump pulse, suggests that in the present conditions the expected critical carrier density for ZnS is exceeded and therefore the carrier to lattice energy transfer times are expected to be in the picosecond range.

Under the assumption that the HL DP ablation dynamics follows the time evolution of the energy and carrier density of the layer irradiated by the pump pulse, an approximate description of this evolution can be made.

According to the results shown in figure 4.28b, the delay range in which $S^+$ and $Zn^+$ signal intensities rise, would be compatible with 5-10 ps carrier kinetic energy transfer times. This increase in the $S^+$ and $Zn^+$ signal was followed by a two-component decay. The fast-lived component, observed up to ~150 ps, could be explained by energy and carrier depletion due to non-radiative recombination processes which take place in time ranges of several tens of picoseconds [83]. The long-lived component observed in the range of 150-300 ps, can be related to the return to the equilibrium of the remaining free carriers through radiative recombination processes, which take place in the sub- to few-nanosecond time scale.

The comparison between symmetric and asymmetric DP ablation shows that $S^+$ and $Zn^+$ signal intensities are higher for the HH configuration than for HL independently of the interpulse delay. This would be consistent with the higher total DP fluence deposited in the HH ablation. In contrast, in the LH case, also at a total DP fluence smaller than that of the HH, the signal intensities for the symmetric configuration are only higher at delays shorter than ~50 ps, becoming nearly equal at longer times.

Some explanation for the latter behaviour can be obtained comparing the relative efficiency of the 3PA and FCA mechanisms in the coupling of the H probe pulse with the material heated either by the L or by the H pump pulses. Owing to the cubic dependence on laser intensity of the 3PA process, the carrier density produced by absorption of the L pump pulse in the LH configuration is nearly one order of magnitude lower than that for the HH case. In this conditions the contribution of the FCA mechanism to the total absorption of the H probe pulse, is much lower in the LH than in the HH case. Then, the different DP ablation dynamics observed for both configurations could be explained through the competition of FCA and 3PA mechanisms at the different delays of the probe pulse. In the HH case, FCA can contribute to the absorption at delays up to hundreds of picoseconds [78, 84], but carrier depletion mechanisms becomes progressively important with time, thus FCA is expected to maximize at short delays. Therefore, at long delays, 3PA can be considered the main mechanism which couples the probe pulse to the irradiated ZnS layer, both in the HH and LH configurations. The cubic dependence on laser intensity of three photon processes strongly discriminates against the DP configuration with the lowest probe pulse intensity, resulting in a lower ablation yield in the HL case.

The faster decay observed for $S^+$ compared to that of $Zn^+$ (see figure 4.28b) could attend to different processes. It was stated before that photoexcitation of zinc monochalcogenides, in particular ZnS, involves electron transitions from the chalcogen *p* states in the valence band to *s* and *p* states of zinc in the conduction band. In simple terms, the promotion of a large number of electrons to the valence band implies that in a fraction of the $S^{2-}$ and $Zn^{2+}$ ions in lattice sites, the charge state changes to singly charged chalcogen anion and zinc cation respectively (resulting in weakening of the bonding and lattice destabilization). A simple conclusion is that, regardless of the mechanism of ion ejection, the formation of $Zn^+$ from the electron-hole plasma should be more cost effective than that of $S^+$. Therefore, while the total energy remaining in the DP irradiated layer is above the threshold for $Zn^+$ ejection in the whole range of delays, the threshold for $S^+$ is only attained in the short delay region, above which, the energy delivered by the probe pulse cannot balance the progressive cooling of the surface irradiated by the pump pulse.

Ion-neutral reactions between $S^+$ and Co atoms in the plasma plume can lead to the formation of $Co_nS_m^+$ clusters, consuming a fraction of $S^+$ ions which would not be detected in the TOF-MS measurements. The temporal dependence of this $S^+$ depletion process can be related to the different overlapping between the velocity distributions of $S^+$ and Co resulting from the different ablation conditions (interpulse delay).

Other possible source of differences between the ablation dynamics observed for $S^+$ and $Zn^+$ could be related to the complex equilibrium between ZnS and S- or Zn-rich liquid phases, attained at different temperatures, at normal pressure conditions [85]. Disproportionated phases might also occur upon the far from equilibrium conditions of ultrafast ablation.

### Optical emission spectroscopy

OES analysis of plasma plumes generated in similar conditions than those used for symmetric DP PLD experiments points toward the same "pump-probe" effect observed in TOF-MS (figure 4.23) and PLD experiments. While a SP with fluence below the OES signal detection threshold does not produce a measurable signal, the combination of both pulses used in the DP configuration produces a noticeable signal, independently of the interpulse delay within the studied temporal range of 1-300 ps (see inset in figure 4.30). This enhancement in the ablation yield was also observed by the analysis of the deposits obtained by PLD (figure 4.38).

The threshold fluence for the detection of light emission in OES experiments was found to be around 0.1 J $cm^{-2}$, lower than that for ion signal detection in the TOF-MS experiments (∼0.2 J $cm^{-2}$). In atomic species, the energy of the electronically excited states converges to that of the ionization limit. Therefore, regardless of the specific mechanism responsible for the formation of ions and neutrals in the DP laser ablation, it is reasonable to assume that the ionization of the observed atoms require more energy than that of the excited neutrals. It is important to notice that emission from sulfur is not observed in the OES experiments here described. It is known that detection of sulfur is difficult in OES (LIBS) mainly due to its high excitation energy [86, 87].

The temporal dependence of the OES signal intensity with the interpulse delay can be discussed taking into account the main characteristics of optically thin plasmas. In plasmas of small dimensions, most of the radiation emitted by the excited atoms escapes without being reabsorbed and the population of the higher levels cannot be described by a Boltzmann distribution. In this case, if the density of electrons in the plasma is high enough, the processes of excitation, de-excitation, ionization and recombination in atoms and ions are controlled by electron collisions [88]. Therefore, the OES signal is due to collision-induced transitions, mainly from a low lying energy level to the next higher level. The most important factors affecting the collisional transition rate in a given state are the electron density, which has to be above a critical value, and the kinetic energy of the electrons, which has to be larger, but close to the difference in energy of the two atom

levels involved in the transition. Besides that, the interaction time with the atom has to be long enough to allow the electron and atom to reach the distance below which a collision-induced transition can take place.

Despite the rather simplified description of the plasma processes given above, the latter can provide some basis to discuss the dependence of the OES intensities on the interpulse delay observed in the present thesis. The electron density and velocity of species in the ablation plasma can be related to the degree of heating reached by the material upon DP irradiation (discussed in the previous sections). At delays of tens of picoseconds, the density of charged species and electron energy in the ablation plasma can be expected to be higher than that at longer delays. The highest OES signal intensity observed at 300 ps delay would indicate that the range of electron energies in the DP ablation plasma at longer delays suits better the conditions for efficient collision-induced excitation than at shorter delays.

### Pulsed laser deposition of Co/Zn/S

Pulsed Laser Deposition performed in Co/ZnS targets using a DP femtosecond ablation scheme yielded nanoparticle-assembled deposits with typical mean size in the range of tens of nanometers. The analysis of these nanoparticles by TEM revealed the nanocrystalline nature of the deposited material (see figures 4.35b and 4.35d). The analysis of individual crystallites by TEM-XEDX indicates that Co doping of the ZnS lattice occurs upon ablation and deposition. To the best of our knowledge, this is the first demonstration of metal doping of semiconductors by a double pulse ultrafast laser ablation process.

Despite having similar fluence values than those used in TOF-MS experiments, carried out under the ion detection threshold, the deposit thickness measured by AFM in SP deposits indicates that some material is being transferred to the substrate. At this point, it is important to bear in mind that PLD experiments are sensitive to all kind of species, in contrast with TOF-MS, where only the ions present in the plasma plume are being detected. The deposition of a certain amount of material can be related to the ejection of neutral species in SP ablation. This fact is supported by the optical emission spectra acquired at similar ablation fluence, which evidence the presence of neutral species in the plasma plume (see figure 4.31).

The analysis of the deposited layer by AFM revealed that the thickness of deposits obtained by DP ablation is larger than that expected for SP ablation with twice the

number of uncoupled laser pulses. This observation corroborates the pump and probe effect observed in TOF-MS experiments and OES analysis of the plasma, where the probe pulse interacts with the already modified material by the pump pulse, and the better coupling of the former results in an different ablation efficiency depending on the interpulse delay. The thickness values of deposits obtained at 300 ps are found to be somewhat lower than those of deposits prepared at shorter interpulse delays. This fact is compatible with the results on DP ablation dynamics of ZnS (the majority component of the target mixture) discussed above.

As regards to the composition of the deposited material, although compositional differences have been found between deposits prepared at different interpulse delays, a clear trend cannot be inferred from the obtained data. The low concentration of Co in the targets (10 % in weight) and the large dispersion of the composition values obtained in TEM-XEDX measurements lead to ambiguous results. Similar high dispersion of the Co/Zn ratio was obtained in SEM-XEDX measurements on deposits prepared on Si substrates (not shown). Analysis of areas containing several nanoparticles, although exhibited a smaller dispersion do not show a clear evidence of a relationship between the interpulse delay and the composition of deposits.

Alternative analysis techniques could shed some more light on the deposits composition and its dependence with the interpulse delay in the DP approach. One of the limitations found regarding the analysis of the obtained deposits is related to the high response of the silicon substrate in SEM-XEDX, which hindered the detection of Co. Preparation of thicker deposits by increasing the number of double pulse sequences would minimize the response of the crystalline Si in the XEDX analysis. This limitation can be also overcome by performing cross-sectional TEM-XEDX analysis of the deposited layer.

## 4.4 References


1. I. Lopez-Quintas, M. Oujja, M. Sanz, A. Benitez-Cañete, R.J. Chater, M.V. Cañamares, J.F. Marco, M. Castillejo, *Micrometric rods grown by nanosecond pulsed laser deposition of boron carbide,* Applied Surface Science, **328** (2015) p. 170.
2. I. Lopez-Quintas, V. Loriot, D. Ávila, J.G. Izquierdo, E. Rebollar, L. Bañares, M. Castillejo, R. de Nalda, M. Martin, *Ablation Dynamics of Co/ZnS Targets under Double Pulse Femtosecond Laser Irradiation,* Physical Chemistry Chemical Physics, **18** (2016) p. 3522.
3. V. Domnich, S. Reynaud, R.A. Haber, M. Chhowalla, *Boron Carbide: Structure, Properties, and Stability under Stress,* Journal of the American Ceramic Society, **94** (2011) p. 3605.
4. K.M. Reddy, P. Liu, A. Hirata, T. Fujita, M.W. Chen, *Atomic structure of amorphous shear bands in boron carbide,* Nat Commun, **4** (2013) p. 2483.
5. A.C. Ferrari, *Raman spectroscopy of graphene and graphite: Disorder, electron–phonon coupling, doping and nonadiabatic effects,* Solid State Communications, **143** (2007) p. 47.
6. D.R. Tallant, T.L. Aselage, A.N. Campbell, D. Emin, *Boron carbide structure by Raman spectroscopy,* Physical Review B, **40** (1989) p. 5649.
7. E. Yu Zarechnaya, L. Dubrovinsky, N. Dubrovinskaia, N. Miyajima, Y. Filinchuk, D. Chernyshov, V. Dmitriev, *Synthesis of an orthorhombic high pressure boron phase,* Science and Technology of Advanced Materials, **9** (2008) p. 044209.
8. H. Werheit, V. Filipov, U. Kuhlmann, U. Schwarz, M. Armbrüster, A. Leithe-Jasper, T. Tanaka, I. Higashi, T. Lundström, V.N. Gurin, and M.M. Korsukova, *Raman effect in icosahedral boron-rich solids,* Science and Technology of Advanced Materials, **11** (2010) p. 023001.
9. P.V. Zinin, L.C. Ming, I. Kudryashov, N. Konishi, S.K. Sharma, *Raman spectroscopy of the $BC_3$ phase obtained under high pressure and high temperature,* Journal of Raman Spectroscopy, **38** (2007) p. 1362.
10. R. Brüning, J.B. Galbraith, K.E. Braedley, J. Johnstone, J. Robichaud, S. Balaji, Y. Djaoued, *X-Ray Diffraction and Micro-Raman Study of Structural Transformations in $(B_2O_3)_{1-x}(H_2O)_x$ Glasses and Liquids,* Journal of the American Ceramic Society, **93** (2010) p. 3745.
11. C.D. Wagner, L.E. Davis, M.V. Zeller, J.A. Taylor, R.H. Raymond, L.H. Gale, *Emprical Atomic Sensitivity Factors for Quantitative Analysis by Electron Spectroscopy for Chemical Analysis,* Surface and Interface Analysis, **3** (1981) p. 211.
12. W. Cermignani, T.E. Paulson, C. Onneby, C.G. Pantano, *Synthesis and characterization of boron-doped carbons,* Carbon, **33** (1995) p. 367.
13. C. Vincent, H. Vincent, H. Mourichoux, J. Bouix, *Characterization by XPS and SEM of reactive chemical vapour deposited boron carbide on carbon fibre,* Journal of Materials Science, **27** (1992) p. 1892.
14. R.B. Kaner, J. Kouvetakis, C.E. Warble, M.L. Sattler, N. Bartlett, *Boron-carbon-nitrogen materials of graphite-like structure,* Materials Research Bulletin, **22** (1987) p. 399.

15. M.W. Chen, A. Goto, T. Hirai, *State of boron in chemical vapour-deposited SiC-B composite powders,* Journal of materials science letters, **9** (1990) p. 997.
16. R. Ma, Y. Bando, *Investigation on the Growth of Boron Carbide Nanowires,* Chemistry of Materials, **14** (2002) p. 4403.
17. C. Pallier, J.-M. Leyssale, L.A. Truflandier, A.T. Bui, P. Weisbecker, C. Gervais, H.E. Fischer, F. Sirotti, F. Teyssandier, G. Chollon, *Structure of an Amorphous Boron Carbide Film: An Experimental and Computational Approach,* Chemistry of Materials, **25** (2013) p. 2618.
18. B. Zeng, Z. Feng, S. Li, Y. Liu, L. Cheng, L. Zhang, *Microstructure and deposition mechanism of CVD amorphous boron carbide coatings deposited on SiC substrates at low temperature,* Ceramics International, **35** (2009) p. 1877.
19. A.O. Sezer, J.I. Brand, *Chemical vapor deposition of boron carbide,* Materials Science and Engineering: B, **79** (2001) p. 191.
20. O. Conde, A.J. Silvestre, J.C. Oliveira, *Influence of carbon content on the crystallographic structure of boron carbide films,* Surface and Coatings Technology, **125** (2000) p. 141.
21. Z. Guan, T. Gutu, J. Yang, Y. Yang, A.A. Zinn, D. Li, T.T. Xu, *Boron carbide nanowires: low temperature synthesis and structural and thermal conductivity characterization,* Journal of Materials Chemistry, **22** (2012) p. 9853.
22. L.G. Jacobsohn, R.D. Averitt, C.J. Wetteland, R.K. Schulze, M. Nastasi, L.L. Daemen, Z. Jenei, P. Asoka-Kumar, *Role of intericosahedral chains on the hardness of sputtered boron carbide films,* Applied Physics Letters, **84** (2004) p. 4173.
23. T. Szörényi, R. Stuck, F. Antoni, E. Fogarassy, *Number density and size distribution of droplets in KrF excimer laser deposited boron carbide films,* Applied Surface Science, **247** (2005) p. 45.
24. D. Zemsky, R. Shneck, P.J. Dagdigian, I. Bar, *Structure and morphology of pulsed laser depos ited boron carbide films: Influence of deposition geometry,* Journal of Applied Physics, **102** (2007) p. 104309.
25. R. Dietsch, T. Holz, D. Weissbach, R. Scholz, *Large area PLD of nanometer-multilayers,* Applied Surface Science, **197-198** (2002) p. 169.
26. R. Dietsch, T. Holz, H. Mai, C.-F. Meyer, R. Scholz, B. Wehner, *High precision large area PLD of X-ray optical multilayers,* Applied Surface Science, **127-129** (1998) p. 451.
27. J. Sun, H. Ling, W.J. Pan, N. Xu, Z.F. Ying, W.D. Shen, J.D. Wu, *Chemical structure and micro-mechanical properties of ultra-thin films of boron carbide prepared by pulsed-laser deposition,* Tribology Letters, **17** (2004) p. 99.
28. S. Zhang, Z. He, X. Ji, W. Lu, C. Wang, Q. Shen, L. Zhang, *Understanding the deposition mechanism of pulsed laser deposited B-C films using dual-targets,* Journal of Applied Physics, **115** (2014) p. 154906.
29. O. Derkach, S. Pentzien, W. Kautek, *Pulsed laser deposition of boron carbide: spectroscopic study of the laser ablation plasma,* SPIE proceedings, **2991** (1997) p. 48.
30. W. Kautek, S. Pentzien, A. Conradi, J. Krüger, K.-W. Brzezinka, *Pulsed-laser deposition and boron-blending of diamond-like caron (DLC) thin films,* Applied Surface Science, **106** (1996) p. 158.

31. T. Csákó, J. Budai, T. Szörényi, *Property improvement of pulsed laser deposited boron carbide films by pulse shortening,* Applied Surface Science, **252** (2006) p. 4707.
32. S. Aoqui, H. Miyata, T. Ohshima, T. Ikegami, K. Ebihara, *Preparation of boron carbide thin film by pulsed KrF excimer laser deposition process,* Thin Solid Films, **407** (2002) p. 126.
33. H.A. Castillo, E. Restrepo-Parra, J.M. Vélez, W. de la Cruz, *Substrate temperature influence on boron carbide coatings grown by the PLD technique,* Surface and Coatings Technology, **205** (2011) p. 3607.
34. F. Kokai, M. Taniwaki, K. Takahashi, A. Goto, M. Ishihara, K. Yamamoto, Y. Koga, *Laser ablation of boron carbide: thin-film deposition and plume analysis,* Diamond and Related Materials, **10** (2001) p. 1412.
35. F. Kokai, M. Taniwaki, M. Ishihara, Y. Koga, *Effect of laser fluence on the deposition and hardnessof boron carbide thin films,* Applied Physics A: Materials Science & Processing, **74** (2002) p. 533.
36. H. Werheit, *On excitons and other gap states in boron carbide,* Journal of Physics: Condensed Matter, **18** (2006) p. 10655.
37. G. Koren, A. Gupta, R.J. Baseman, M.I. Lutwyche, R.B. Laibowitz, *Laser wavelength dependent properties of $YBa_2Cu_3O_7$–δ thin films deposited by laser ablation,* Applied Physics Letters, **55** (1989) p. 2450.
38. P.T. Murray, D.T. Peeler, *Pulsed Laser Deposition of Carbon Films: Dependence of Film Properties on Laser Wavelength,* Journal of Electronic Materials, **23** (1994) p. 855.
39. S. Fähler, K. Sturm, H.-U. Krebs, *Resputtering during the growth of pulsed-laser-deposited metallic films in vacuum and in an ambient gas,* Applied Physics Letters, **75** (1999) p. 3766.
40. W. An, X. Zhao, Z. Zhang, R. Su, *Carbon dendrite formation induced by pulsed laser irradiation,* Applied Surface Science, **256** (2010) p. 2304.
41. P.M. Ossi, A. Miotello, *Control of cluster synthesis in nano-glassy carbon films,* Journal of Non-Crystalline Solids, **353** (2007) p. 1860.
42. I. Lopez-Quintas, M. Oujja, M. Sanz, M. Martín, R.A. Ganeev, M. Castillejo, *Low-order harmonic generation in nanosecond laser ablation plasmas of carbon containing materials,* Applied Surface Science, **278** (2013) p. 33.
43. T. Scharf, H.U. Krebs, *Influence of inert gas pressure on deposition rate during pulsed laser deposition,* Applied Physics A: Materials Science & Processing, **75** (2002) p. 551.
44. A.V. Bulgakov, N.M. Bulgakova, *Gas-dynamic effects of the interaction between a pulsed laser-ablation plume and the ambient gas: analogy with an underexpanded jet,* Journal of Physics D: Applied Physics, **31** (1998) p. 693.
45. F. Claeyssens, A. Cheesman, S.J. Henley, M.N.R. Ashfold, *Studies of the plume accompanying pulsed ultraviolet laser ablation of zinc oxide,* Journal of Applied Physics, **92** (2002) p. 6886.
46. K.L. Saenger, *On the origin of spatial nonuniformities in the composition of pulsed-laser-deposited films,* Journal of Applied Physics, **70** (1991) p. 5629.
47. M. Jazirehpour, H.-R. Bahahrvandi, A. Alizadeh, N. Ehsani, *Facile synthesis of boron carbide elongated nanostructures via a simple in situ thermal evaporation process,* Ceramics International, **37** (2011) p. 1055.

48. M. Carlsson, J. García-García, M. Johnsson, *Synthesis and characterization of boron carbide whiskers and thin elongated platelets,* Journal of Crystal Growth, **236** (2002) p. 466.
49. A.M. Morales, C.M. Lieber, *A Laser Ablation Method for the Synthesis of Crystaline Semiconductor Nanowires,* Science, **279** (1998) p. 208.
50. R.S. Wagner, W.C. Ellis, *The Vapor-Liquid-Solid Mechanism of Crystal Growth and Its Application to Silicon,* Transactions of the metallurgical society of AIME, **233** (1965) p. 1053.
51. K. Kolasinski, *Catalytic growth of nanowires: Vapor–liquid–solid, vapor–solid–solid, solution–liquid–solid and solid–liquid–solid growth,* Current Opinion in Solid State and Materials Science, **10** (2006) p. 182.
52. S.H. Yun, J.Z. Wu, A. Dibos, X. Gao, U.O. Karlsson, *Growth of inclined boron nanowire bundle arrays in an oxide-assisted vapor-liquid-solid process,* Applied Physics Letters, **87** (2005) p. 113109.
53. A. Umar, S.H. Kim, Y.S. Lee, K.S. Nahm, Y.B. Hahn, *Catalyst-free large-quantity synthesis of ZnO nanorods by a vapor–solid growth mechanism: Structural and optical properties,* Journal of Crystal Growth, **282** (2005) p. 131.
54. Y. Sun, G.M. Fuge, M.N.R. Ashfold, *Growth mechanisms for ZnO nanorods formed by pulsed laser deposition,* Superlattices and Microstructures, **39** (2006) p. 33.
55. J.F. Conley, L. Stecker, Y. Ono, *Directed assembly of ZnO nanowires on a Si substrate without a metal catalyst using a patterned ZnO seed layer,* Nanotechnology, **16** (2005) p. 292.
56. D. Maestre, A. Cremades, J. Piqueras, *Growth and luminescence properties of micro- and nanotubes in sintered tin oxide,* Journal of Applied Physics, **97** (2005) p. 044316.
57. D. Maestre, PhD Thesis: *Crecimiento y caracterización mediante técnicas de microscopía de nano- y microestructuras de $SnO_2$ y $TiO_2$*, Departamento de Física de Materiales, Complutense University, Madrid, 2007.
58. F. Thévenot, *Boron carbide—A comprehensive review,* Journal of the European Ceramic Society, **6** (1990) p. 205.
59. D. Emin, T.L. Aselage, *A proposed boron-carbide-based solid-state neutron detector,* Journal of Applied Physics, **97** (2005) p. 013529.
60. S. Sasaki, M. Takeda, K. Yokoyama, T. Miura, T. Suzuki, H. Suematsu, W. Jiang, K. Yatsui, *Thermoelectric properties of boron-carbide thin film and thin film based thermoelectric device fabricated by intense-pulsed ion beam evaporation,* Science and Technology of Advanced Materials, **6** (2005) p. 181.
61. A. Cebollada, J.M. García Martín, C. Clavero, L. Balcells, S. Estradé, J. Arbiol, F. Peiró, C. Smith, R. Clarke, L. Martínez, Y. Huttel, E. Román, N.D. Telling, and G. van der Laan, *Growth and magnetic characterization of Co nanoparticles obtained by femtosecond pulsed laser deposition,* Physical Review B, **79** (2009) p. 014414.
62. M. Sanz, M. López-Arias, J.F. Marco, R. de Nalda, S. Amoruso, G. Ausanio, S. Lettieri, R. Bruzzese, X. Wang, M. Castillejo, *Ultrafast Laser Ablation and Deposition of Wide Band Gap Semiconductors,* The Journal of Physical Chemistry C, **115** (2011) p. 3203.
63. *NIST Atomic Spectra Database*, Available from: http://physics.nist.gov/PhysRefData/ASD/lines_form.html.

64. M.N. Polyanskiy, *Refractive Index Database*, Available from: http://refractiveindex.info.
65. J. Hohlfeld, S.-S. Wellershoff, J. Güdde, U. Conrad, V. Jähnke, E. Matthias, *Electron and lattice dynamics following optical excitation of metals,* Chemical Physics, **251** (2000) p. 237.
66. J. He, Y. Qu, H. Li, J. Mi, W. Ji, *Three-photon absorption in ZnO and ZnS crystals,* Optics Express, **13** (2005) p. 9235.
67. S.I. Anisimov, B.L. Kapeliovich, T.L. Perel´man, *Electron emission from metal surfaces exposed to ultrashort laser pulses,* Soviet Physics-Journal of Experimental and Theoretical Physics, **39** (1975) p. 375.
68. Z. Lin, L.V. Zhigilei, V. Celli, *Electron-phonon coupling and electron heat capacity of metals under conditions of strong electron-phonon nonequilibrium,* Physical Review B, **77** (2008) p. 075133.
69. D.S. Ivanov, L.V. Zhigilei, *Combined atomistic-continuum modeling of short-pulse laser melting and disintegration of metal films,* Physical Review B, **68** (2003) p. 064114.
70. V. Recoules, J. Clérouin, G. Zérah, P.M. Anglade, S. Mazevet, *Effect of Intense Laser Irradiation on the Lattice Stability of Semiconductors and Metals,* Physical Review Letters, **96** (2006) p. 055503.
71. E. Bévillon, J.P. Colombier, V. Recoules, R. Stoian, *Free-electron properties of metals under ultrafast laser-induced electron-phonon nonequilibrium: A first-principles study,* Physical Review B, **89** (2014) p. 115117.
72. C.S. Yoo, P. Söderlind, H. Cynn, *The phase diagram of cobalt at high pressure and temperature: the stability of $\gamma$ (fcc)-cobalt and new $\varepsilon'$(dhcp)-cobalt,* Journal of Physics: Condensed Matter, **10** (1998) p. L311.
73. J.H. Weaver, E. Colavita, D.W. Lynch, R. Rosei, *Low-energy interband absorption in bcc Fe and hcp Co,* Physical Review B, **19** (1979) p. 3850.
74. V.S. Stashchuk, O.P. Poljanska, S.I. Stashenko, *Optical and electronic properties of metallic cobalt in various structural states,* Ukranian Journal of Physics, **55** (2010) p. 388.
75. D.S. Ivanov, L.V. Zhigilei, *Kinetic Limit of Heterogeneous Melting in Metals,* Physical Review Letters, **98** (2007) p. 195701.
76. J. Camassel, D. Auvergne, *Temperature dependence of the fundamental edge of germanium and zinc-blende-type semiconductors,* Physical Review B, **12** (1975) p. 3258.
77. R. Khenata, A. Bouhemadou, M. Sahnoun, A.H. Reshak, H. Baltache, M. Rabah, *Elastic, electronic and optical properties of ZnS, ZnSe and ZnTe under pressure,* Computational Materials Science, **38** (2006) p. 29.
78. B. Gu, J. He, W. Ji, H.-T. Wang, *Three-photon absorption saturation in ZnO and ZnS crystals,* Journal of Applied Physics, **103** (2008) p. 073105.
79. D.M. Duffy, S.L. Daraszewicz, J. Mulroue, *Modelling the effects of electronic excitations in ionic-covalent materials,* Nuclear Instruments and Methods in Physics Research Section B: Beam Interactions with Materials and Atoms, **277** (2012) p. 21.

80. J.P. Callan, A.M.-T. Kim, L. Huang, E. Mazur, *Ultrafast electron and lattice dynamics in semiconductors at high excited carrier densities,* Chemical Physics, **251** (2000) p. 167.
81. E.J. Yoffa, *Screening of hot-carrier relaxation in highly photoexcited semiconductors,* Physical Review B, **23** (1981) p. 1909.
82. H. Przybylinska, M. Godlewski, *Three-center Auger-type nonradiative recombination mechanism in the ZnS lattice,* Physical Review B, **36** (1987) p. 1677.
83. S.K. Sundaram, E. Mazur, *Inducing and probing non-thermal transitions in semiconductors using femtosecond laser pulses,* Nature Materials, **1** (2002) p. 217.
84. J. He, W. Ji, J. Mi, Y. Zheng, J.Y. Ying, *Three-photon absorption in water-soluble ZnS nanocrystals,* Applied Physics Letters, **88** (2006) p.
85. R.C. Sharma, Y.A. Chang, *The S-Zn (Sulfur-Zinc) System,* Journal of Phase Equilibria, **17** (1996) p. 261.
86. B. Sallé, J.-L. Lacour, E. Vors, P. Fichet, S. Maurice, D.A. Cremers, R.C. Wiens, *Laser-Induced Breakdown Spectroscopy for Mars surface analysis: capabilities at stand-off distances and detection of chlorine and sulfur elements,* Spectrochimica Acta Part B: Atomic Spectroscopy, **59** (2004) p. 1413.
87. L. Dudragne, P. Adam, J. Amouroux, *Time-resolved Laser-Induced Breakdown Spectroscopy: Application for Qualitative and Quantitative Detection of Fluorine, Chlorine, Sulfur and Carbon in Air,* Applied Spectroscopy, **52** (1998) p. 1321.
88. H.R. Griem, *Validity of Local Thermal Equilibrium in Plasma Spectroscopy,* Physical Review, **131** (1963) p. 1170.

# Chapter 5

# Conclusions

# 5. Conclusions

Given the described results it can be stated that the main goals of this thesis have been achieved and the following conclusions can be extracted:

1. Near-infrared laser ablation plasmas of graphite, boron carbide and zinc sulfide proved to be suitable nonlinear media for the generation of coherent short wavelength radiation. Efficient third and fifth harmonic generation of 1064 nm nanosecond laser pulses was demonstrated in plasmas of graphite and $B_4C$. Plasmas of the latter material also served to efficiently generate 266 nm radiation through a frequency mixing process involving 1064 and 532 nm driving beams. In ZnS plasmas generation of odd-harmonics up to the $9^{th}$ order was demonstrated.

2. Low-order harmonic generation in laser ablation plasmas served to obtain complementary information regarding the plasma composition and dynamics. The temporal behaviour of the nonlinear response of the studied plasmas revealed the presence of two distinct populations of plasma species contributing in different manners to the harmonic generation process. The early component of the harmonics signal, observed at short delays after the ablation event (in the range of few hundreds of nanoseconds), is attributed to the direct contribution of fast atomic and small molecular species. The broad delayed component in the range of several microseconds, observed under inert gas atmosphere in the case of graphite and $B_4C$ plasmas and under vacuum in ZnS plasmas, is constituted by nanoparticles which, upon fragmentation by the driving beam, are in turn precursors of the atomic species responsible for harmonic generation at longer delays.

3. The results reveal that the efficiency of the nonlinear process changes considerably when the position of the driving beam is moved within the plasma volume. This finding allows discussing about the influence of plasma conditions, including density, phase mismatch and absorption of the newly generated light, on the amplitude of the harmonic signal.

4. Nanosecond pulsed laser ablation at 1064 nm of boron carbide targets resulted in the growth of deposits containing micrometric columnar structures on silicon substrates at room temperature. The morphological analysis of the structures revealed typical crystalline features with faceted tips, sharp edges and square section and, in some cases, a hollow core. The growth of these regular elongated structures was observed in a narrow range of conditions involving 1064 nm ablation and high-vacuum. Irradiation at 266 nm led to the growth of smaller and less regular structures, while inert gas atmosphere led to the formation of spherical particles or dendritic structures.

5. For the growth of micrometric columnar structures by nanosecond pulsed laser ablation of boron carbide, a vapour-solid mechanism is proposed, where the deposited nanoparticle-assembled films constitute a background of nucleation sites.

6. Characterization of the deposits obtained by PLD of $B_4C$ using micro-Raman spectroscopy, XPS and FIB-SIMS revealed a complex composition of the microcolumns, based mainly on boron, carbon and oxygen. The presence of oxygen in the structures is attributed to contamination of the target material. The presence of peaks in the grazing incidence X-ray diffractograms of deposits is indicative of their crystallinity although assignment of those remains unclear.

7. Double pulse femtosecond irradiation of Co/ZnS mixed material with under-threshold pulses proved to be a valid approach to influence the material ablation dynamics. The ablation dynamics was found to be highly dependent on the relative energy and delay between the pump and probe pulses. The experimental observations with pairs of pulses of different energy indicated that the coupling of the probe pulse is more effective when the pump pulse ahead in time is that of lower energy.

8. Time-of-flight mass spectrometric analysis of plasmas, generated by double pulse femtosecond ablation of Co/ZnS mixed targets, revealed that the relative composition of $Co^+$, and $Zn^+$ ions in the plasma obeys distinctive ablation dynamics under different double pulse configurations, showing a possible new route for tailoring the composition of deposits prepared by PLD.

9. Double pulse femtosecond PLD of Co/ZnS served to prepare nanoparticle-assembled thin films on silicon substrates and TEM grids. As demonstrated by TEM and XEDX analyses of the obtained deposits, the growth of Co-doped crystalline nanoparticles was achieved using this approach.

10. The TEM-XEDX analyses of the atomic composition of crystalline nanoparticles prepared on TEM grids at different interpulse delays, showed a high dispersion of the Co/Zn ratios. Similar high dispersion was obtained from the SEM-XEDX analysis of the thin deposits obtained on silicon substrates (typically below 100 nm). This is attributed to the small amount of Co atoms in the deposits. It is concluded that the present results cannot assess the effect of the interpulse delay on the deposits composition. It is proposed that the analysis of thicker deposits fabricated with a large number of double pulse sequences would overcome the above limitations.

## Contributions and perspectives

This thesis provides an insight into the ablation process of different types of materials and explores conditions in which their laser ablation plasmas can be used in two fields: harmonic generation and pulsed laser deposition.

The main contributions of this thesis can be summarized as follows:

- It provides a better understanding of the composition and dynamics of laser ablation plasmas through the study of their nonlinear response.

- It sets the conditions to obtain novel micrometric structures by pulsed laser deposition of boron carbide with high potential for technological applications.

- It demonstrates the growth of deposits containing crystalline nanoparticles of Co-doped ZnS through a femtosecond double pulse ablation and deposition scheme.

In the framework of this thesis, several scientific contributions have been published. A list of those can be found in Appendix II.

As mentioned in the introduction chapter, laser ablation is a highly complex process. This work, together with the findings revealed and understood, has also opened new questions that should be addressed in the future in order to use laser ablation plasmas in a more efficient way.

In the realm of laser ablation plasmas used as nonlinear media, further experiments can help to better identify the species contributing to the nonlinear process, allowing to fine tune the plasma conditions in processes like harmonic generation or pulsed laser deposition.

Regarding the pulsed laser deposition technique, further investigation of the structure, composition and physical properties of the microcolumns obtained by pulsed laser deposition of boron carbide will help to guide future applications. Finally, the study of the neutral species in Co/ZnS plasmas generated by double pulse femtosecond ablation by post-ionization time-of-flight mass spectrometry can add deeper understanding of the ablation dynamics, providing guidelines to influence the deposition process.

# Appendix I

## List of Acronyms

| | |
|---|---|
| 3H | Third harmonic |
| 3PA | Three photon absorption |
| 4H | Fourth harmonic |
| 5H | Fifth harmonic |
| 7H | Seventh harmonic |
| 9H | Ninth harmonic |
| AFM | Atomic Force Microscopy |
| CCD | Charged Coupled Device |
| CMOS | Complementary Metal-oxide Semiconductor |
| CPA | Chirped Pulsed Amplification |
| CVD | Chemical Vapour Deposition |
| CW | Continuous wave |
| DG | Delay generator |
| DMS | Diluted magnetic semiconductors |
| DP | Double pulse |
| FCA | Free carrier absorption |
| FIB-SIMS | Focused Ion Beam-Secondary Ion Mass Spectrometry |
| FIB-SEM | Focused Ion Beam-Scanning Electron Microscopy |
| FWHM | Full width at half maximum |
| GIXRD | Grazing Incidence X-ray Diffraction |

| | |
|---|---|
| GPIB | General Purpose Interface Bus |
| HG | Harmonic Generation |
| HHG | High-order Harmonic Generation |
| HR-SEM | High-resolution Scanning Electron Microscopy |
| IB | Inverse *Bremsstrahlung* |
| ICCD | Intensified Charged Coupled Device |
| IR | Infrared |
| KDP | Potassium Dihydrogen Phosphate |
| LA-ICP-MS | Laser ablation-Inductively Coupled Plasma-Mass Spectrometry |
| LHG | Low-order Harmonic Generation |
| LIBS | Laser-induced Breakdown Spectroscopy |
| LIF | Laser-induced Fluorescence |
| LIFT | Laser-induced Forward Transfer |
| MALDI | Matrix-assisted Laser Desorption and Ionization |
| MCP | Microchannel Plates |
| Nd:YAG | Neodymium: Yttrium-Aluminium Garnet |
| Nd:YLF | Neodymium: Yttrium-Lithium Fluoride |
| NIR | Near-infrared |
| OES | Optical Emission Spectroscopy |
| PLD | Pulsed Laser Deposition |
| PMT | Photomultiplier tube |
| RETOF | Reflectron Time-of-flight |
| SEM | Scanning Electron Microscopy |
| SHG | Second Harmonic Generation |

| | |
|---|---|
| SLS | Solid-Liquid-Solid |
| SP | Single Pulse |
| TEM | Transmission Electron Microscopy |
| TTM | Two-temperature Model |
| THG | Third Harmonic Generation |
| TOF-MS | Time-of-flight Mass Spectrometry |
| UV | Ultraviolet |
| VLS | Vapour-Liquid-Solid |
| VS | Vapour-Solid |
| VUV | Vacuum Ultraviolet |
| XEDX | X-ray Energy Dispersive Spectroscopy |
| XPS | X-ray Photoelectron Spectroscopy |
| XRD | X-ray Diffraction |
| XUV | Extreme Ultraviolet |

# Appendix II

## List of related publications

- M. Oujja, I. Lopez-Quintas, A. Benítez-Cañete, R. de Nalda, M. Castillejo, *Harmonic generation by atomic and nanoparticle precursors in a ZnS laser ablation plasma*, (submitted to Applied Surface Science).

- I. Lopez-Quintas, V. Loriot, D. Ávila, J.G. Izquierdo, E. Rebollar, L. Bañares, M. Castillejo, R. de Nalda, M. Martin, *Ablation Dynamics of Co/ZnS Targets under Double Pulse Femtosecond Laser Irradiation*, Physical Chemistry Chemical Physics, 18 (2016) p. 3522.

- I. Lopez-Quintas, M. Oujja, M. Sanz, A. Benitez-Cañete, R.J. Chater, M.V. Cañamares, J.F. Marco, M. Castillejo, *Micrometric rods grown by nanosecond pulsed laser ablation of boron carbide*, Applied Surface Science, 328 (2014) p. 170-176.

- M. Oujja, A. Benitez-Cañete, M. Sanz, I. Lopez-Quintas, M. Martín, R. de Nalda, M. Castillejo, *Frequency mixing in boron carbide laser ablation plasmas*, Applied Surface Science, 336 (2014) p. 53-58.

- I. Lopez-Quintas, M. Oujja, M. Sanz, A. Benitez-Cañete, C. Hutchison, R. de Nalda, M. Martin, R.A. Ganeev, J.P. Marangos, M. Castillejo, *Characterization of laser-induced plasmas of nucleobases: uracil and thymine*, Applied Surface Science, 302 (2014) p. 299-302.

- R.A. Ganeev, T. Witting, C. Hutchison, V.V. Strelkov, F. Frank, M. Castillejo, I. Lopez-Quintas, Z. Abdelrahman, J.W.G. Tisch, J.P. Marangos, *Comparative studies of resonance enhancement of harmonic radiation in indium plasma using multi-cycle and few-cycle pulses*, Physical Review A, 88 (2013) p. 033838.

- R.A. Ganeev, C. Hutchison, I. Lopez-Quintas, F. McGrath, D.Y. Lei, M. Castillejo, J.P. Marangos, *Ablation of nanoparticles and efficient harmonic generation using 1-kHz laser*, Physical Review A, 88 (2013) p. 033803.

- C. Hutchison, R.A. Ganeev, M. Castillejo, I. Lopez-Quintas, A. Zair, S. Weber, F. McGrath, Z. Abdelrahman, M. Oppermann, M. Martín, D.Y. Lei, S.A. Maier, J.W. Tisch, J.P. Marangos, *Comparison of high-order harmonic generation in uracil and thymine ablation plumes*. Physical Chemistry Chemical Physics, **15** (2013) p. 12308.

- I. Lopez-Quintas, M. Oujja, M. Sanz, M. Martín, R.A. Ganeev, M. Castillejo, *Low-order harmonic generation in nanosecond laser ablation plasmas of carbon containing materials*. Applied Surface Science, **278** (2013) p. 33-37.

- R.A. Ganeev, C. Hutchison, T. Witting, F. Frank, W.A. Okell, A. Zaïr, S. Weber, R.V. Redkin, D.Y. Lei, S.A. Maier, I. Lopez-Quintas, M. Martín, M. Castillejo, J.W.G. Tisch, J.P. Marangos, *High-order harmonic generation in graphite plasma plumes using ultrashort laser pulses: a systematic analysis of harmonic radiation and plasma conditions*. Journal of Physics B: Atomic and Molecular Optical Physics, **45** (2012) p. 165402.